U.PORTO
FACULDADE DE CIÊNCIAS
UNIVERSIDADE DO PORTO

FCT
FACULDADE DE
CIÊNCIAS E TECNOLOGIA
UNIVERSIDADE NOVA DE LISBOA

PhD

Functional electroactive materials: towards novel saving and conversion energy systems

Marta Susete da Silva Nunes

PhD thesis submitted to
Faculdade de Ciências da Universidade do Porto,
Faculdade de Ciências e Tecnologia da Universidade Nova de Lisboa,
Chemistry

2016

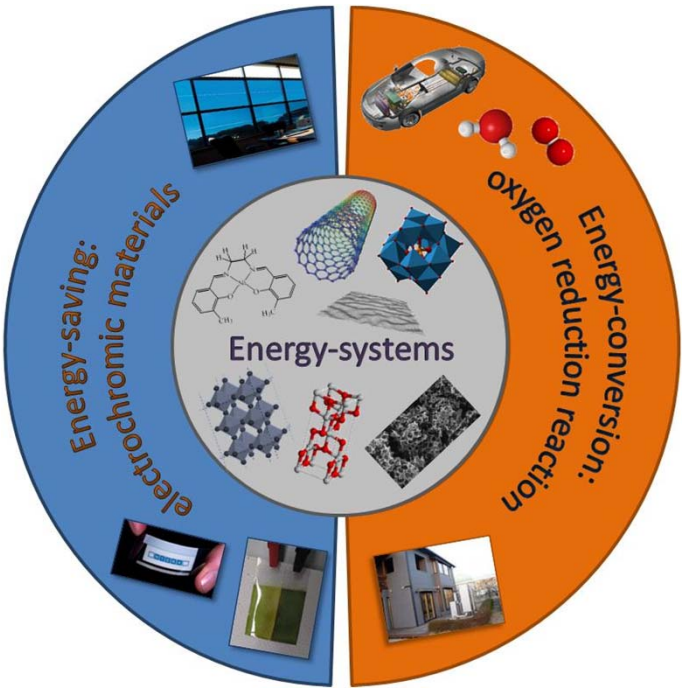

Functional electroactive materials: towards novel saving and conversion energy systems

Marta Susete da Silva Nunes
Doutoramento em Química Sustentável
Departamento de Química e Bioquímica
2016

Supervisor
Ana Cristina Freire, Full Professor,
Faculdade de Ciências da Universidade do Porto

Acknowledgements

To Fundação para a Ciência e a Tecnologia (FCT) for my PhD Grant with reference SFRH/BD/79171/2011.

To Departamento de Química e Bioquímica, Faculdade de Ciências, Universidade do Porto, for provide me the facilities for the development of my project.

To my supervisor, Professor Cristina Freire, for the opportunity to develop this project, for the dedication, knowledge sharing and valuable suggestions; thanks for the crucial advices and support at the beginning of this journey.

To Doctor Diana Fernandes, for helping me in the incursion into the world of electrocatalysis.

To Professor Fernando Pereira and Doctor Inês Rocha from Laboratório de Catálise e Materiais, Departamento de Engenharia Química, Faculdade de Engenharia, Universidade do Porto, for providing me the access to their laboratory facilities and readiness to help.

To Professor Pedro de Oliveira and Doctor Israel-Martyr Mbomekalle from Laboratoire de Chimie Physique, Université Paris-Sud in France, for welcoming me so well during my work with polyoxometalates and constant availability.

To all my colleagues of laboratory, for the pleasant moments spent and in particular to Mariana Araújo by shared discussions about the electrochromic studies.

To my friends Mariana Rocha and Paula Costa for the friendship and constant support.

To my Mother, my Father and my brother, for their unconditional love, encouragement and understanding and for support me in all my decisions.

To Pedro, for being present in all moments, for the motivation and patience and for always believe in me, even when I no longer believe.

This work had the financial support from FCT/MEC through national funds and was co-financed by FEDER, under the Partnership Agreement PT2020 (Projects UID/QUI/50006/2013 – POCI/01/0145/FERDER/007265). Also thanks the COST CM1203 "Polyoxometalate Chemistry for Molecular Nanoscience (PoCheMoN)" by the STSM action.

FCT Fundação para a Ciência e a Tecnologia
MINISTÉRIO DA CIÊNCIA, TECNOLOGIA E ENSINO SUPERIOR

COMPETE QUADRO DE REFERÊNCIA ESTRATÉGICO NACIONAL UNIÃO EUROPEIA

Abstract

The present thesis is focused on the development of novel efficient systems for application in energy saving and conversion technologies.

In the framework of saving-energy technologies, novel electrochromic (EC) materials based in poly[Ni(*salen*)]-type polymer films were explored. The Ni-*salen* metallopolymers, poly[Ni(3-Mesalen)] and poly[Ni(3-MesaltMe)] (poly[1] and poly[2], respectively) were electropolymerised from the respective [Ni(*salen*)] complexes and the influence of the supporting electrolytes – $LiClO_4/CH_3CN$ and $LiClO_4$/propylene carbonate (PC) - in their electrochemical, compositional, morphological, electronic and electrochromic properties were evaluated. Both films exhibited interesting EC properties, with colour changes between yellow, green and russet, accordingly to the oxidation state and with superior long-term electrochemical stability in $LiClO_4$/PC; the most promising results were obtained for poly[1], allowing the assemblage of electrochromic devices with very good performances.

In order to obtain new materials with improved EC performances, several nanocomposites were prepared through the electropolymerisation of poly[1] films in the presence of (i) WO_3 and (ii) TiO_2 nanoparticles (NPs) and (iii) nitrogen-doped graphene (N-FLG). All nanocomposites showed a positive effect in some EC properties: the nanocomposite with WO_3 showed faster responses and higher optical contrasts and colouration efficiencies, while the composite with TiO_2 showed an excellent electrochemical stability; the nanocomposite prepared with N-FLG showed simultaneous outstanding enhancement of all EC parameters.

In the field of energy-conversion, carbon-based materials were studied as electrocatalysts for the oxygen reduction reaction (ORR) in alkaline and acidic media. Two activated carbons prepared from sucrose, SC800 and SH800, were tested as metal-free ORR electrocatalysts. The SH800 showed the best electrocatalytic performance, as a consequence of its higher surface area. Moreover, several nanocomposites prepared through the immobilisation of a polyoxometalate, tetrabutylammonium salt of vanadium(V)-substituted phosphomolybdate ($PMo_{11}V$), into several carbon nanomaterials (carbon black, carbon nanotubes and graphene (GF)) were studied. A strong dependency between the carbon support and the ORR electrocatalytic activity was found, with $PMo_{11}V$@GF nanocomposite showing the best electrocatalytic performance. The prepared nanocomposites also showed electrocatalytic activity towards H_2O_2 reduction.

Keywords: Electrochromic materials, Oxygen reduction reaction, Metal-*salen* polymers, Metal oxides, Carbon-based materials, Polyoxometalates.

Resumo

O trabalho de investigação descrito nesta tese focou-se no desenvolvimento de novos materiais, para aplicação em tecnologias relacionadas com poupança e conversão de energia.

No âmbito da temática poupança de energia, foram desenvolvidos novos materiais electrocrómicos baseados em filmes poliméricos do tipo poli[Ni(*salen*)]. Os metalopolímeros, poli[Ni(3-Mesalen)] e poli[Ni(3-MesaltMe)] (poli[1] e poli[2], respectivamente) foram electropolimerizados a partir dos respectivos complexos [Ni(*salen*)], e foi estudada a influência dos electrólitos de suporte - $LiClO_4/CH_3CN$ e $LiClO_4$/carbonato de propileno (PC) – nas suas propriedades electroquímicas, electrónicas e electrocrómicas e na sua composição e morfologia. Ambos os filmes exibiram propriedades electrocrómicas interessantes, com mudanças de cor entre o amarelo, verde e castanho-avermelhado de acordo com o estado de oxidação, e com maior estabilidade electroquímica em $LiClO_4$/PC; os resultados mais promissores foram obtidos para o poli[1], o que permitiu a construção de dispositivos electrocrómicos com bom desempenho electrocrómico.

De modo a obter novos materiais com melhor desempenho electrocrómico, foram preparados vários nanocompósitos através da electropolimerização do poli[1] na presença de nanopartículas (NPs) de (i) WO_3 e (ii) TiO_2 e (iii) grafeno dopado com azoto (N-FLG). Todos os nanocompósitos mostraram um efeito positivo em alguma das propriedades electrocrómicas: o nanocompósito com NPs de WO_3 exibiu respostas mais rápidas e maior contraste óptico e eficiência de coloração, enquanto o compósito com NPs de TiO_2 mostrou uma excelente estabilidade electroquímica; o nanocompósito preparado com o N-FLG apresentou um notável melhoramento de todos os parâmetros electrocrómicos em simultâneo.

No domínio da conversão de energia, foram estudados materiais de carbono como electrocatalisadores para a reacção de redução do oxigénio (ORR), em meio alcalino e ácido. Foram testados dois carvões activados preparados a partir da sacarose, SC800 e SH800, como electrocatalisadores sem metais. O SH800 apresentou o melhor desempenho electrocatalítico, como consequência da sua elevada área superficial. Foram ainda estudados vários nanocompósitos preparados através da imobilização de um polioxometalato, sal de tetrabutilamónio de vanado-fosfomolibdato ($PMo_{11}V$), em vários materiais de carbono (negro de carbono, nanotubos de carbono e grafeno (GF)). Observou-se uma forte dependência entre o suporte de carbono usado e a actividade electrocatalítica para ORR, com o nanocompósito $PMo_{11}V$@GF exibindo o melhor desempenho electrocatalítico. Os

nanocompósitos preparados também apresentaram actividade electrocatalítica para a redução de H_2O_2.

Palavras-chave: Materiais electrocrómicos, Reacção de redução do oxigénio, Polímeros metal-*salen*, Óxidos metálicos, Materiais de carbono, Polioxometalatos.

Contents

List of Figures

List of Tables

List of Abbreviations and Symbols

A	Electrode area
a*	CIELAB coordinate
A_{BET}	Specific surface area
Abs	Absorbance
ACs	Activated carbons
AFC	Alkaline Fuel Cell
a.u.	Arbitrary units
b*	CIELAB coordinate
CB	Carbon black
CBV	Carbon black Vulcan
CNTs	Carbon nanotubes
C	Concentration of the specie
C_{O_2}	Bulk concentration of O_2
CPs	Conducting polymers
CT	Charge-transfer
CV	Cyclic voltammetry
CVs	Cyclic voltammograms
CVD	Chemical vapour deposition
DC	Direct current
DMF	N,N'-dimethylformamide
DMFC	Direct Methanol Fuel Cell
D_{O_2}	Diffusion coefficient of O_2
D_x	Diffusion coefficient of the specie
E	Electric potential
EC	Electrochromic
ECD	Electrochromic device
EDS	Energy-dispersive X-ray Spectroscopy
E_g	Energy of the band gap
E_{onset}	Onset potential
E_{pa}	Potential of the anodic peak
E_{pc}	Potential of the cathodic peak
EPR	Electron Paramagnetic Resonance
F	Faraday's constant
FTIR	Fourier Transform Infrared Spectroscopy
FTO	Fluorine-doped tin oxide
FWHM	Full width at half maximum
GCE	Glassy carbon electrode
GF	Graphene
HER	Hydrogen evolution reaction
HET	Heterogeneous electron transfer
HOMO	Highest occupied molecular orbital
HOR	Hydrogen oxidation reaction
i	Peak current intensity
i_{pc}	Intensity of the cathodic peak current
i_{pa}	Intensity of the anodic peak current
ITO	Indium tin oxide
j	Current density
j_0	Exchange current density
j_k	Kinetic current density
j_L	Diffusion limiting current density
k_{HET}	HET rate constant
K-L	Koutecky-Levich
L*	CIELAB coordinate
LSV	Linear sweep voltammetry
LUMO	Lowest unoccupied molecular orbital
MCFC	Molten Carbonate Fuel Cell
MWCNTs	Multi-walled nanotubes
n	Doping level
N-FLG	Nitrogen-doped few layer graphene
n_{O_2}	Number of electrons transferred per O_2 molecule
NPs	Nanoparticles
OER	Oxygen evolution reaction
ORR	Oxygen reduction reaction
PAFC	Phosphoric Acid Fuel Cell
PANI	Polyaniline
PB	Prussian Blue
PC	Propylene carbonate
PEDOT	Poly(3,4-ethylenedioxythiophene)

PEDOT: PSS	Poly(3,4-ethylenedioxythiophene): poly(styrene sulfonic acid)
PEMFC	Polymer Electrolyte Membrane Fuel Cell
PET	Poly(ethylene terephthalate)
POMs	Polyoxometalates
PMMA	Poly(methyl methacrylate)
PNCs	Polymeric nanocomposites
PPO	Poly(propylene glycol)
Q	Charge
Q_d	Density of charge
R	Gas constant
RDE	Rotating disk electrode
RHE	Reversible hydrogen electrode
salen	*N,N'*-bis(salicylidine)-ethylenediamine dianion
salen	N_2O_2 tetradentate Schiff base ligands
SEM	Scanning Electron Microscopy
SOFC	Solid Oxide Fuel Cell
SWCNTs	Single-walled nanotubes
T	Temperature
TEM	Transmission Electron Microscopy
T_{ox}	Oxidised-state transmittance value
T_{red}	Reduced-state transmittance value
TTIP	Titanium (IV) isopropoxide
UV-Vis	Ultraviolet-Visible
v	Scan rate
V_{meso}	Mesoporous volume
V_{total}	Total pore volume
$V_{\alpha\ super}$	Supermicropore volume
$V_{\alpha\ total}$	Total volume
$V_{\alpha\ ultra}$	Ultra volume
W_1	Transition from the valence band to the bonding polaron level
W_2	Transition from the valence band to the antibonding polaron level
W_3	Transition from the bonding to the antibonding polaron level
W_I	Intervalence band transition
XAS	X-ray absorption spectroscopy
XPS	X-ray photoelectron spectroscopy
XRD	X-ray diffraction
α	Transfer coefficient
Γ	Electroactive surface coverage
ΔA	Optical absorbance change
ΔE*	Total colour difference
ΔE_p	Peak-to-peak separation
ΔOD	Change of the optical density
ΔT	Optical contrast
ε	Molar extinction coefficient
η	Colouration efficiency
θ	X-ray diffraction angle
λ	Wavelength
τ	Response times or switching times
υ	Kinematic viscosity of the electrolyte
Ψ	Charge transfer parameter
ω	Angular velocity

Chapter 1

Introduction

1

Introduction

The world's population has increased from approximately 2.5 billion in 1950 to about seven billion in 2014 and it is estimated to keep growing to 10 billion or more in 2100.[1] In parallel with the population increase, there has been an improvement in overall living standards, being desirable that in the next years people in the poorer countries can enjoy of the same quality of life and amenities existing in the more prosperous countries. The result of this evolution is that the strains on the global resources are growing steeply and that there is an unsustainable demand in resources such as energy, water and minerals.

Currently, energy is mainly derived from the burning of fossil fuels (coal, oil and gas) with ensuing injection of carbon dioxide, a greenhouse gas, into the air. This changes the atmosphere and leads to global warming, rising sea level, harsher weather and shifts in the Earth's biosphere. The increase in sea levels is well documented and rises approximately 3.2 mm per year,[2] as consequence of the melting of glaciers and ice caps and thermal expansion of warming water.[3] Among the environmental changes, one main point is the ocean acidification with damage of calcifying organisms such as corals and foraminifera.[4] The effect of global warming due to greenhouse gases, such as CO_2, is yet aggravated by the fact that about half of the world's population lives in cities or mega-cities lead to "urban heat islands" with temperatures several degrees above those of the surrounding countryside, which can cause cardiovascular, cerebrovascular and respiratory human diseases.[5] Furthermore, it is undoubted that the fossil fuels will be depleted in near future.[6]

Taking into account the combination of all these factors, the society has been confronted with two major challenges: (i) to find efficient methods to reduce the consumption of energy without impairing the actual life standards or (ii) to replace fossil fuels with sustainable alternative sources of energy.

The first option has been widely pursued by researchers, in order to find methods for energy saving. The electrochromic materials and devices have been appointed as a promising energy-saving and environmental protection technology, due to their low power requirement and several potential applications such as in electronic paper-like displays, antiglare rear-view mirrors and energy-saving smart windows. In particular, the use of smart windows (that allow to control the amount of light that enters in a building) in the called "green architecture" is a promising application, mainly considering that approximately 40 % of the total world energy consumption is spent in buildings for heating, cooling, lighting and ventilation[7] and that, in richest countries, we spend 80 – 90 % of our time indoors and a high level of comfort and convenience is desirable.

On the other hand, finding environmentally-friendly, secure and sustainable alternative sources of energy to reduce our dependence on fossil fuels, has become an important challenge. Over the last few years, several technologies that provide electrical energy from renewable sources (e.g. solar photovoltaics and wind power generation) have been increasingly implemented. However, the supply of energy from such sources is intermittent whereby, to provide an integrated solution, they must be coupled with advanced energy conversion and storage processes.[8] Electrochemical devices such as fuel cells, water electrolysis, batteries and supercapacitors are recognised as very feasible and efficient technologies.[9] In particular, fuel cells have attracted a lot of attention due to their ability to efficiently generate electricity from the energy in chemical bonds of fuels such as hydrogen and simple hydrocarbons. Hydrogen is the most attractive fuel, as it can be produced through the environmental-benign electrochemical splitting of water.[10]

The core of these energy-related technologies is a series of electrochemical processes, which can include the hydrogen oxidation and evolution reactions (HOR and HER) and the oxygen reduction and evolution reactions (ORR and OER).[11] The ORR, in particular, is the reaction that occurs at the cathode of fuel cells and metal-air batteries and strongly influences the devices performance, whereby has been the focus of an extensive research.

In the next sections of this chapter it is provided an overview on the topics of electrochromic materials and electrocatalytic oxygen reduction reaction, as solutions for the saving- and conversion-energy approaches, respectively.

1.1 Energy saving

As a promising green-technology for the energy-saving, electrochromic (EC) materials have the ability to adjust their optical properties upon applying external voltage, which renders important applications in the fields of smart windows, electronic displays and automotive industry. The pursuit for EC materials is because they are relatively cheap and require a low power use once, after the optical change has been effected, the new redox state exists with little or no input of power (memory effect). In addition, some materials can be switched between several shades or colours, simplifying devices that might otherwise need to use colour filters.[12] In this section, it is made a foray into the world of electrochromism, highlighting the class of EC conducting polymers and their nanocomposites, as well as the incorporation of EC materials in practical devices (electrochromic devices, ECDs).

1.1.1 Electrochromism

Chromism is defined as a reversible colour change of a substance, in the most of cases based in a modification of the electron states of molecules caused by some form of stimulus, such as temperature, light or solvent effect.[13,14] In particular, the electrochromism phenomenon is characterised by a change, evocation or bleaching of colour of a material, induced by an electron-transfer (redox) process.[15] The observed colour change can be between a transmissive state and a coloured state or between multiple coloured states. In the last case the EC materials are referred as polyelectrochromic materials.[16]

Even though, although a material to be regarded as electrochromic when modulate light, by reflectance or absorbance, in the visible region of the electromagnetic spectrum, recently the definition was also extended to materials with multispectral energy modulation (in infrared and microwave regions).[15]

The term “electrochromism” has its origin in Latinized Greek roots *elektro*- and *khroma*, the first root referring to electricity and the second root to colour.[17] Although it was first introduced in 1961 by Platt,[18] the colour switching in materials by electron gain (reduction) or loss (oxidation) has been known since the early 19th century and, so, a revised of its history can be interesting.

In 1815, Berzelius observed the electrochromic properties of tungsten oxide (WO_3), reporting that pure pale-yellow WO_3 changed of colour when reduced under a flow of hydrogen gas; a similar effect was observed by Wöhler in 1824, through the chemical reduction of WO_3 with sodium metal.[19] In 1929, in a London patent, the chemical oxidation of a dye precursor by molecular iodine was reported, thus forming a

bright colour.[12] The colour change (colourless to blue) of WO_3 induced by its electrochemical reduction was first reported in 1930 by Kobosew and Nekrassow.[19] In the meantime, several other works were developed and, in 1942, Talmey patented a paper impregnated with particulate MoO_3 and/or WO_3 (called "electrolytic writing paper"), whose colour changed when it was in contact with an electrode.[19] However, none of these studies attracted much attention and therefore it is widely accepted that the first suggestion of an electrochromic device was performed in 1969 by Deb,[20] a researcher at the American Cyanamid Corporation in the U.S.A. In this work, the electrochromic behaviour was generated by the application of an electrical field across a thin film of WO_3, deposited on quartz. Some authors also cite the Deb's later paper,[21] dated from 1973, as the true birth of the electrochromic technology, once it describes the first "true" electrochromic device, with a film of WO_3 immersed in an ion-containing electrolyte. Poorly known, or at least rarely cited, are the parallel developments in the Soviet Union, related to the electrochromism of the niobium oxide and reported in 1974.[22] Both these works were motivated by the development of devices for information displays. Since then, several works were done and, in 1978, Mohapatra of the Bell Laboratoires in New Jersey, published the first description of the reversible electro-insertion of lithium for WO_3 electrochromism.[23] Meanwhile, the electrochromism of organic materials was also investigated: in 1974 Parker *et al.*[24] studied methoxybiphenyl species and later Kaufman *et al.*,[25] of IBM in New York, published the first report of an electrochromic polymer. The first account of an electrochromic conducting polymer came in 1979, when Diaz *et el.*,[26] of IBM in California, announced the electrosynthesis of a poly(pyrrole) thin-film. From the 1980s to now, John Reynolds and his co-workers have been working in the development of conjugated conducting polymers, through the manipulation of the composition of thiophene-based polymers to create soluble materials with a whole gamut of possible colours.[27,28]

1.1.2 Electrochromic materials

Nowadays, a great diversity of EC materials is known, from inorganic to the organic materials. In general, five main classes of EC materials are considered: metal oxides, viologen derivatives, metal coordination complexes, Prussian Blue (PB) and conducting polymers.[15,19]

As EC metal oxides, are considered the thin-films of several (transition) metal oxides, such as the oxides of tungsten, molybdenum, vanadium, chromium, iridium, palladium, ruthenium, titanium and nickel.[15] These films can be reversibly electrochemically switched between a near colourless and a highly coloured states (generally the reduced form),[12] being the most prominent example of this class the

WO_3, studied since decades ago. In its maximum oxidation state, W^{VI}, thin films of WO_3 are pale yellow and switch to a deep blue colour when a low fraction of W^{V} sites are generated during the electrochemical reduction.[12]

On the other hand, viologens are salts of 4,4'-bipyridine, with the main EC prototype being the methyl viologen. These compounds are intensely coloured due to the charge transfer between the nitrogen atoms.[15] The metal coordination complexes are similar to viologens but involve a 2,2'-bypyridine molecule binds to a central metal atom.[15]

Prussian blue was first prepared in early 1700s and used as synthetic pigment. Its synthesis is based in the hexacyanoferrate anion and the pigment is a mixed-valence compound, as the iron atoms exist in more than one oxidation state (Fe^{III} and Fe^{II}). The charge transfer between these ions gives rise to the intense blue colour of this compound, and the oxidation or reduction generates green-yellow and bleached colour states.[12]

Lastly, the conducting polymers are characterised by an extended conjugated system, which allows them to combine the mechanical flexibility of the traditional polymers with the electrical properties typical of the semiconducting materials.[16] These materials have gained increasing popularity both from the academia and the industry owing their interesting EC behaviour, with multiple redox states, rich colour changes and easy of colour tuning via structural modifications of the monomers, allied with a simple processability.[29] Due to its importance in the development of this work, the topic of conducting polymers is addressed in more detail below.

Considering the huge diversity of EC materials, Chang *et al.*[30] developed a classification system (materials of type I-III), based in the solubility of EC materials in each redox state.[15,19] Thus, in a given electrolyte solution, EC materials of type I are soluble in both the reduced and oxidised states (e.g. methyl viologen), while type II EC materials are soluble in one redox state but form a solid film on the surface of electrode following electron transfer (*e.g.* heptyl viologen). In type III EC materials, all redox states are solid and these materials are studied as thin films on electrode surfaces, which is the case of WO_3, Prussian Blue and conducting polymers.

1.1.3 Conducting polymers

The history of conducting polymers (CPs, or synthetic metals) can be traced back to 1862, when Letheby, a professor of chemistry in the College of London Hospital, reported the electrochemical synthesis of a "thick layer of dirty bluish-green pigment" (probably, a form of polyaniline) by oxidation of aniline in sulphuric acid at a platinum electrode.[19] However, the real interest for these fascinating materials started after

1977, with the discovery of the metallic properties of poly(acetylene) by Shirakawa, Heeger and MacDiarmid, which lead to the attribution of 2000 Nobel Prize in Chemistry.[31,32]

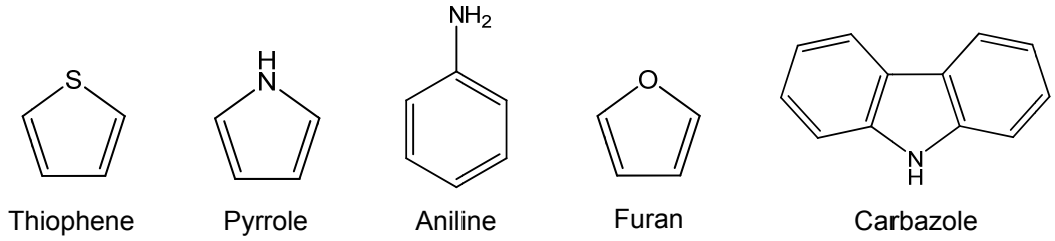

Figure 1.1 Aromatic molecules structures.

The CPs are produced through the chemical or electrochemical oxidation of resonance-stabilised molecules, such as thiophene, pyrrole, aniline, furan and carbazole (see structures in Figure 1.1). These molecules are characterised by have alternating single and double bonds, with the electron orbital of their constituent atoms connected in such way that the electrons are delocalised, moving freely throughout the molecule and stabilising the structure.[12] The oxidative electropolimerisation process of CPs (exemplified in Figure 1.2 for thiophene) is initiated by monomer oxidation to yield monomer radical-cation; then, conducting polymer generation follows via a mechanism that is believed to involve either coupling between radical-cations or attack of radical-cation on neutral monomer, with removal of two protons, forming a dimer. Further oxidation of the dimer and coupling produces oligomers that, as their chains grow long enough, become insoluble and form the conducting polymer deposit at the electrode surface.[33,34]

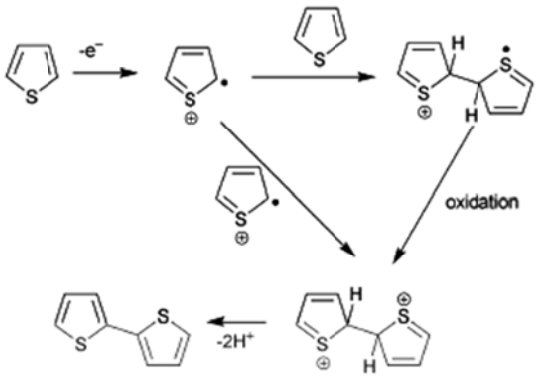

Figure 1.2 Oxidative electropolimerisation process of thiophene. Reproduced from Ref. [33].

CPs have the interesting ability to interconvert between an insulator form (undoped / neutral state) and a conductor form (most commonly, the doped oxidised state), which is similar to the behaviour of a typical semiconductor material. In the neutral state, the polymer has insulator properties due to the energy difference (band gap, E_g) between the highest-occupied π-electron band (HOMO/valence band) and the lowest-unoccupied band (LUMO/conduction band) that difficult the electron movement. Nonetheless, at low oxidation levels, electrons are removed from the valence band and it is formed a radical cation that behaves as a polaronic charge carrier and remains delocalised over a polymer segment (exemplified in Figure 1.3 (b) for thiophene). This process is accompanied by a relaxation of the aromatic structure geometry of the polymer chain toward a quinoid-like structure. The removal of the electrons cause the emergence of new electronic levels at the band gap (polaronic levels), which allow new electronic transitions at lower energies.[16] The positive charge carriers introduced in polymer film during the oxidation are charge compensated by the introduction of counter-anions from electrolyte into polymeric film (p-doping). The electrochemical reduction is accompanied by the concurrent counter-anions egress to (or cation ingress from, n-doping) electrolyte.[19]

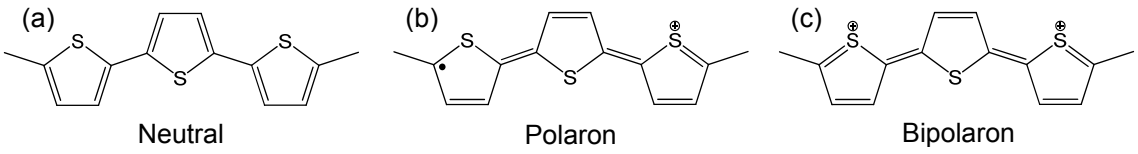

Figure 1.3 Structure of thiophene trimer in (a) neutral, (b) polaron and (c) bipolaron states. Adapted from Ref. [16].

The charge transport mechanism in the CPs can be explained by the polaronic model, developed for organic conductors with non-degenerate ground states.[35] During the oxidation, the polaronic levels (bonding and antibonding) formed within the band gap generate three new allowed electronic transitions with energies below that of the intervalence band transition, as depicted in Figure 1.4: W_1 from the valence band to the bonding polaron level, W_2 from the valence band to the antibonding polaron level and W_3 from the bonding to the antibonding polaron level. The energies of these transitions are related to each other and to the intervalence band (W_I) as follows: $W_1+W_3=W_2$ and $W_1+W_2=W_I$ (assuming symmetrical distribution of the gap-state energy levels).[36]

As the polymer is further oxidised, a second electron is removed and two situations can occur: (i) removal of the electron from the valence band with formation of other polaron or (ii) removal of the electron from the polaronic level with formation of a

bipolaron (dication delocalised over the same polymer segment, Figure 1.3 (c)). The situation that occurs is dependent of the energy associated to each of them, whereby a system can present one or both types of charge carriers.[16]

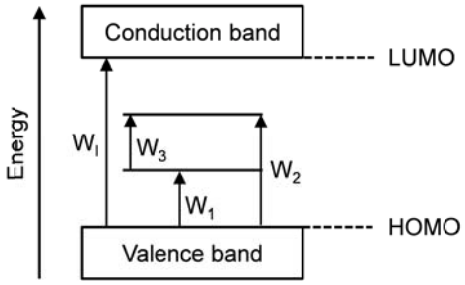

Figure 1.4 Schematic representation of the electronic structure of a conducting polymer accordingly to the polaronic model.

CPs are typically electrochromic as thin films, showing a change of colour between the neutral and the doped states. The intrinsic optical properties are determined by the polymer's band gap[15,12] and the change of colour is the result of the new electronic levels created between the valence and the conduction bands during the oxidation, which shift the absorption maximum of electronic transitions to higher wavelengths.[16] Generally, CPs that are transmissive in its undoped state and strongly coloured in its oxidation state are classified as *anodically colouring polymers*, while the *cathodically colouring polymers* are highly absorbing in the undoped state (e.g. poly(3,4-ethylenedioxythiophene), PEDOT). CPs with an intermediate behaviour have distinct optical changes throughout the visible region of the electromagnetic spectrum, and can switch between several colours.[19] In recent years, derivatives of poly(thiophene),[37,38] poly(pyrrole)[39,40] and poly(aniline)[41,42] have received the most attention as promising EC polymers. Figure 1.5 illustrates the EC ability of some EC polymers studied by Reynolds's group.

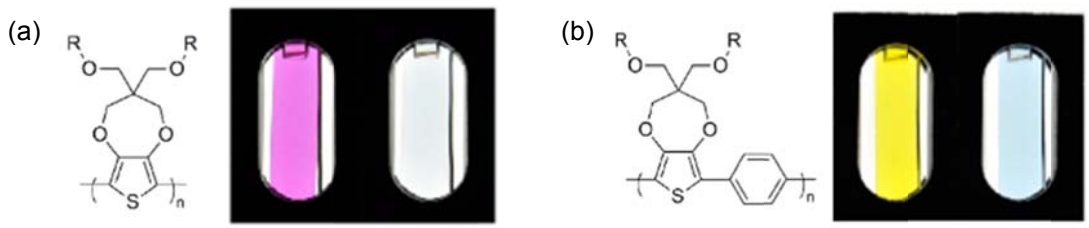

Figure 1.5 Structures and photographs of representative EC films studied by Reynolds's group. Adapted from Ref. [38].

The electric conductivity in organic-based polymers can be limited by the existence of structural defects which interrupt the mobility of charge carriers. A possible solution to minimize this effect is the incorporation of transition metals as functional groups or as units within the polymer backbone. The latter can be achieved by the preparation of transition metal complexes, as monomers in the preparation of supramolecular systems.[43] [M(*salen*)]-type complexes (M = transition metal) have been studied in this context due to the robustness and easy functionalization of the *salen* ligand and its ability to coordinate several transition metal centers.[44]

1.1.4 [M(*salen*)] complexes

In 1864, Hugo Schiff described the condensation between an aldehyde and an amine, leading to a compound denominated Schiff base.[45] A particular class of Schiff bases are obtained through the condensation of salicylaldehyde with the ethylenediamine, which are the so-called "salen" (*N,N'*-bis(salicylidine)ethylenediamine dianion) ligand.[46] Nonetheless, the acronym "*salen*-type" is widely used in literature to denominate the class of all N_2O_2 tetradentate Schiff base ligands.[47] The [M(*salen*)]-type complexes (see general molecular structure in Figure 1.6) result from the complexation of these *salen*-type ligands with almost all transition metals.

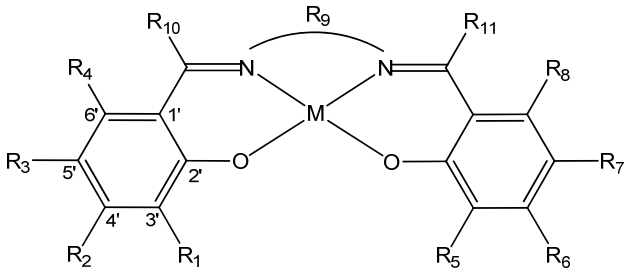

Figure 1.6 General molecular structure of the [M(*salen*)]-type complexes (M = transition metal, R_1–R_{11} = -H or functional groups).

In moderately/weak donor solvents (e.g. acetonitrile) the [M(*salen*)]-type complexes are oxidatively polymerised at the electrode surfaces, generating electroactive films.[48]

Modified electrodes with [M(*salen*)]-based polymers were studied for the first time by Goldsby and co-workers,[49,50] who electropolimerised several nickel-*salen* complexes on platinum and indium-doped tin oxide-coated glass electrodes and characterised the resulting polymers by cyclic voltammetry, electronic spectroscopy and scanning electron microscopy. Several similar studies with metal-*salen* complexes of nickel and

copper were subsequently performed by Devynck,[51] Audebert and collaborators[52-55] and Dahm and co-workers,[56-58] using electrochemical, spectroscopic and microscopic techniques. Despite the detailed studies performed, no consensus concerning the mechanism of electronic conduction and structural information was obtained. Some of these aspects were clarified later, by some studies performed by Freire's group.[48,59,60]

Throughout a combination of electrochemical and spectroscopic (*in situ* FTIR and UV-Visible and *ex-situ* Electron Paramagnetic Resonance (EPR)) techniques, Vilas-Boas *et al.*[48] revealed that the electropolimerisation of [Ni(salen)] is a ligand-based process that probably takes place through a mixture of *o*- and *p*-linking of the phenyl ring. Although based in a coordination compound, the study revealed that poly[Ni(salen)] behaves like a polyphenylene compound, with the electroactivity based on *salen* ligand and the metal ion acting as a bridge between the biphenylene moieties. Analogous to a conducting organic polymer, the polarons were appointed as the main charge carriers. Later, by X-ray absorption spectroscopy (XAS) measurements, Tedim *et al.*[59] showed that, in a poly[Ni(*salen*)]-based film, the nickel atom is covalently bonded to the nitrogen and oxygen atoms of the *salen* moiety in a square planar environment, such as in the monomer; the structure is unaltered by the film redox switching, which corroborate the assumption of ligand-based film redox process. During the oxidation, the uptake of counter ions for maintaining the electroneutrality of the *salen* film, accompanied by a significant solvent entry (as result of a concentration gradient or a physical opening of the polymer structure) and consequent polymer swelling, was described by Vilas-Boas *et al.*[60] The supramolecular structure of the *salen* polymers plays a key role in the control of the movement of these mobile species between the film and the solution during the redox switching, whereby polymers based in complexes with aliphatic chains in imine bridge tend to facilitate the anion ingress and solvent swelling, once have a less compact structure.[61,62]

The potential application of these poly[M(*salen*)]-type films as EC materials have also been evaluated by Freire's group;[63,64] the materials have shown promising EC properties, with several and interesting colour changes (Figure 1.7). The main achievements about the EC performances of these polymers are given in more detail in Chapter 2 of this work.

Although the general promising EC properties of CPs, some drawbacks associated mainly with an insufficient electrochemical stability and larger response times due to the slow transport of counter anions into the EC layer (see below typical parameters used for the evaluation of the EC behaviour of a material) limits their successful commercial application, whereby the improvement of these properties remain priority demands.[65] In order to achieve these goals, the combination of CPs with

other polymers, organic molecules (e.g. dyes) and inorganic nanomaterials has been attracted a lot of attention.[16] The latter approach is addressed in this work.

Figure 1.7 Photographs of several poly[M(*salen*)]-type films in different oxidation states. Adapted from Ref. [64].

1.1.5 Polymeric nanocomposites

The polymeric nanocomposites (PNCs) are functional hybrid materials characterised by a polymer matrix reinforced by a nanometric filler, and show considerable improved properties due to the synergic effects of both counterparts.[29,33] These hybrid materials result of the combination of the CPs with different types of nanomaterials, namely metal oxides[66] and carbon-based[67,68] nanostructures.

a) Metal oxides

The nanohybridisation of CPs with metal oxides has the advantages of receive the individual semiconducting functions of the polymer and of the metal oxide (p/n junction)[66] and of to take benefit of the high surface-to-volume ratio, short diffusion distances for ion/electron transport and high thermal and chemical stabilities of the metal oxides.[66,69]

Among the several metal oxides that have been combined with CPs (e.g. ZnO, V_2O_5 and Fe_3O_4), TiO_2 and WO_3 semiconductors are probably the most commonly employed. Titanium dioxide (TiO_2) is a versatile material, whose properties depend of the particle size, crystal structure, morphology and crystallinity. It has three main polymorphs: rutile, anatase and brookite (Figure 1.8 (a), (b) and (c)), with band gaps of 3.02, 3.20 and 2.96 eV, respectively.[70,71] The WO_3 has a band gap of 2.7 eV and show the particularity of having genuine colour switching. One of the possible structures of WO_3 is the monoclinic (Figure 1.8 (d)).[72] Both materials are typically synthesized by wet chemistry[73], employing methods such as coprecipitation,[74] sol-gel,[75] microemulsion[76] and hydrothermal.[77]

In Chapters 3 and 4, are provided a large overview about the preparation of nanocomposites between CPs and WO_3 and TiO_2 nanoparticles (NPs), respectively.

b) Carbon-based nanomaterials

The interest in the combination of CPs with carbon-based nanomaterials started with the discovery of carbon nanotubes due to the remarkable electrical, chemical, physical, mechanical and structural properties of these 1D materials. More recently, graphene emerged as an alternative very promising material. With a two-dimensional (2D) sp^2-hybridised carbon structure in a single-atom-thick sheet, graphene shows interesting physicochemical properties, such as a large theoretical specific surface area, high carrier mobility at room temperature, good thermal conductivity, high Young's modulus and good optical transmittance.[78] The properties of pristine graphene can be tailored the chemical doping, which can be a promising approach. Typical methods for the preparation of these materials are exfoliation (chemical, mechanical, ultra-sound assisted) of graphite[79] and the chemical vapor deposition (CVD),[80] for instance.

An overview on the preparation of nanocomposites between CPs and graphene / nitrogen-doped graphene is provided in Chapter 5.

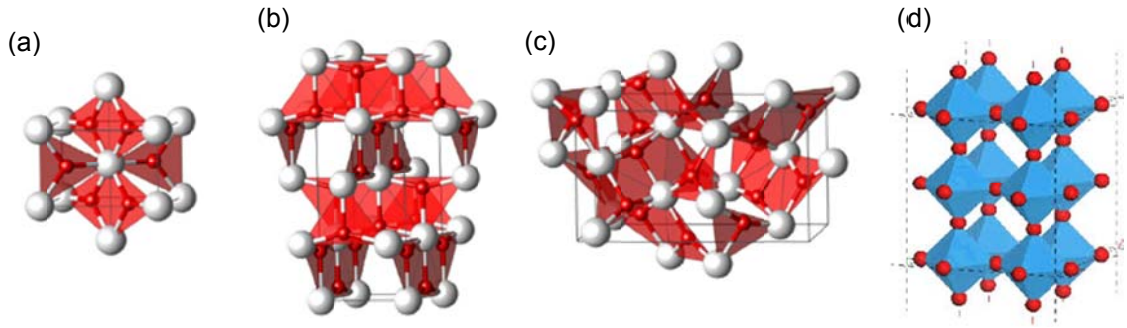

Figure 1.8 Structures of the TiO_2 polymorphs: (a) rutile, (b) anatase and (c) brookite; (d) monoclinic structure of WO_3.

In a general way, the synergistic combination of the merits of CPs and inorganic nanostructures results in a hybrid material with improved performances in comparison with the pristine CPs. From an EC point of view, a new hybrid material with improved EC properties can be obtained, in which the colouration change is induced by the CPs redox reactions and the nanomaterial has an important role in the electronic transport and surface area.[81]

The higher colouration efficiency, sometimes observed in hybrids, is attributed to the reduced charge transfer resistance brought by the bridging effect of the conductive nanomaterials between crystalline domains of CPs, while the faster response is due to the shorter diffusion length brought by the highly porous structure formed by the

inorganic nanofillers.[14] The improved stability can be related to the hybrid architecture, with the nanomaterials acting as a skeleton that keep the polymer intact and avoid its detachment.[82]

c) Preparation methods

There is a large pool of preparation methods that can be employed to prepare PNCs, once the components can be synthesised separately prior or concurrently (in the presence of the other counterpart) and the polymer can be obtained through chemical or electrochemical polymerisation (Figure 1.9).

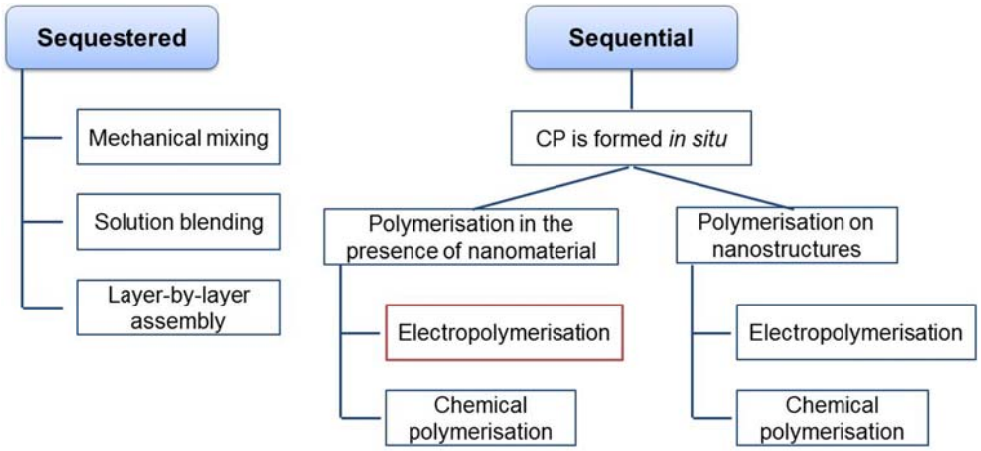

Figure 1.9 Summary of some routes employed in PNCs preparation.

In the sequestered route, the CP and the nanocomponent are prepared separately and the hybrid is assembled in a subsequent step, by simple or more sophisticated blending of two components. However, these methods are limited by the processability of the CPs (e.g. insolubility of poly[M(*salen*)]-type polymers in common solvents and difficult chemical synthesis). Thus, the *in situ* polymerisation of CPs in the presence of the nanomaterial can be a promising first approach for the preparation of PNCs[33]. Depending of the polymerisation method employed, composite particles (typical of chemical polymerisation) or thin-films with the nanomaterial incorporated (typical of electropolimerisation) are obtained. The one-step electropolimerisation method has clear advantages, once (i) the composite is directly formed as a thin-film on the electrode surface, facilitating the application as a chemically modified electrode, (ii) the film thickness, porosity and morphological features can be precisely controlled by the electrochemical procedures and (iii) the film has strong adherence to the

underlying supporting electrode and improved high mechanical stability.[82] This is the route employed for the preparation of PNCs in this work.

Through the electrochemical approach, the nanomaterial can be incorporated in polymeric matrix by physical interactions between both counterparts (entrapment) and chemical interactions (dipole-dipole or electrostatic bonds). The electrostatic interaction can occur when the nanofiller are surface negatively charged and are incorporated in polymer as dopant, compensating the positive charges generated during anodic electropolimerisation.[33]

The *in situ* (electro)polymerisation of CPs on nanostructured modified electrodes, although not explored in this work, is an attractive route as future work perspective due to the interesting nanoarchitectures that can be obtained.

1.1.6 Electrochromic properties

The common parameters that define the performance of an EC material include the colour change (sometimes characterised through the CIELAB coordinates), the optical contrast, colouration efficiency, response times and the long-term switching stability.[83]

The optical contrast (ΔT) is an essential parameter to evaluate an EC material and is used to quantitatively measure the intensity of the colour change. It is generally defined as the difference in transmittance between the redox states, at a given wavelength.[14,27] Transmittance values are generally recorded upon application of square-wave potential steps to the electroactive film placed in the beam of a spectrophotometer.

The colouration efficiency, η or CE, relates the optical absorbance change (ΔA, also designated by change of the optical density, ΔOD) of an electrochrome at a given wavelength to the density of injected / ejected electrochemical charge necessary to induce a full switch (Q_d).[27] It can be estimated through the Equation (1.1).

$$\eta = \frac{\Delta OD}{Q_d} = \frac{\log\left(\frac{T_{red}}{T_{ox}}\right)}{Q_d} \qquad (1.1)$$

where η is in cm^2 C^{-1}, Q_d in C cm^{-2} and T_{ox} and T_{red} are the oxidised- and reduced-state transmittance values, respectively.[27] Experimentally, the studies can be performed by tandem chronocoulometry / chronoabsorptometry, during which variations of film transmittance and charge density are simultaneously monitored, while the potential is repeatedly stepped from one redox state to the other.

The response time (τ), sometimes also referred as switching time, is defined as the time needed for an electrochrome to switch from one redox state to other.[27] It depends of several parameters, such as the ability of the electrolyte to conduct ions, the ease of diffusion of the counterbalancing ionic species across the EC active layer (related with the film thickness and morphology) and the magnitude of applied potential.[14] Considering that the majority of the redox reactions occur in the beginning of the switch (caused by the faster movement of charges and charges balancing ions when the electric field is first established) and that the human eye is fairly insensitive to the small colour shifts beyond this point, response times are commonly determined for 90 % of full switch.[84,85]

It is desirable that EC systems undergo stable redox processes with its EC behaviour being reproducible upon repeated switching. Nonetheless, the degradation of one of the redox components can affect the overall performance of the system, resulting in rapid loss of EC contrast. Typical degradation processes encompass irreversible redox behaviour under high potentials, water and oxygen redox interferences, degradation of electrode materials and evaporation of the electrolyte. Long-term switching stability experiments are commonly carried out in a three-electrode electrochemical cell via repeated potential cycling or applying potential steps over around 10^3 cycles.[27]

Thus, on the basis of a function oriented to selection of practical applications, it is desirable to prepare the EC materials with long-term cyclic stability, high colouration efficiency, large optical modulation and short switching time under a low DC voltage.[86] Depending on the desired application, some of these variables can assume more importance than others: for instance, a short response time is necessary for antiglare rear view mirrors, but is less relevant for architectural windows.[83,85]

1.1.7 Electrochromic devices and applications

Although the usefulness of a liquid cell setup to test the functionality of EC materials at a laboratory scale, it is not appropriate for a commercial usage. Thus, the suitable integration of EC materials into colour-switchable solid-state electrochemical cell, called electrochromic device (ECD), is the ultimate goal to take advantage of these materials in commercial applications. Nowadays, EC technologies are facing a brighter future, as a consequence of promising results reported by several laboratories.[85]

A stand-out commercial success of EC devices is Gentex Corporation's automatically dimming "Night Vision Safety" (NVS) mirrors for glare elimination (Figure 1.10 (a)). This EC system is widely applied in car rear view mirrors, allowing attenuate the head-light glare of cars coming from behind.[19,87] In combination with PPG

Aerospace, Gentex is also expanded its technology to interactive windows for use in aircraft (Figure 1.10 (b)). Under the name of Alteos Interactive Window system, the technology was applied in 2011 in Boeing's 787 Dreamliner and Hawker Beechcraft King Air 350i aircrafts as a substitute of the manually operated window blinds, allowing the passenger to switch the window from a bright clear state to an extremely dark state or to a confortable intermediate level, by pushing a button.[87]

Other commercial application of EC materials is in dimmable windows for applications in buildings (green architecture), known as smart windows (Figure 1.10 (c)). These windows allow to control the input of solar irradiation into the building through them colouration/discolouration processes, reducing significantly the energy consumption (e.g. in illumination and air-conditioning systems) and improving the office comfort.[88] Several companies have been worked in this technology, namely Gesimat GmbH in Germany,[89] Sage Electrochromics in USA[90] and ChromoGenics AB in Sweden.[91]

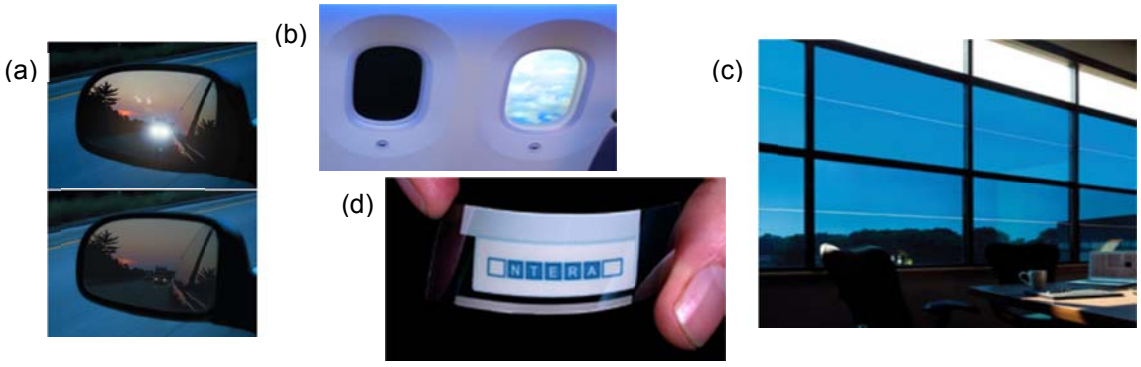

Figure 1.10 Applications of EC materials: (a) car rear view mirrors with glare elimination (adapted from Ref. [12]), (b) airplane windows with EC technology (adapted from Ref. [87]), (c) EC smart window (adapted from Ref. [90]) and (d) EC flexible display.

Cost-effective flexible multicoloured displays (Figure 1.10 (d)) for use as electronic paper,[92] eyewear,[93] clocks[94] and reusable price labels[12] are also possible applications. The Portuguese company Ynvisible created inclusively cards, advertisement in prints and even promotional airline tickets.[95]

Camaleonic materials for use as adaptative camouflage, wearable displays, or simply for fashion are other target applications for electrochromics. Some EC polymers can be stenciled onto flexible fabric substrates and the low power requirements mean that flexible electrodes could be used to switch the colours. Gregory A. Sotzing and his

group have been working on an EC spandex and on EC fibers and threads for direct weaving of fabrics.[96]

ECDs, that serve the basis for these applications, operate as rechargeable solid-state electrochemical cells, containing typically two electrodes, wherein at least one of them is optically transparent and is coated with a layer of an EC material, separated by an ion conductor electrolyte (Figure 1.11 (a)).[15,97]

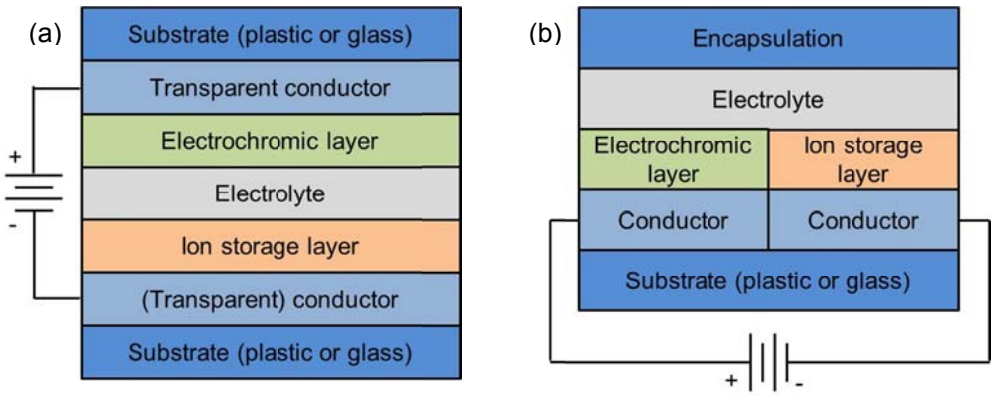

Figure 1.11 Schematic structure of an electrochromic device with (a) vertical and (b) lateral configurations.

a) Electrodes and EC layer

The transparent electrodes comprise an electrical conducting film coated on a rigid – glass – or flexible – poly(ethylene terephthalate), PET - substrate. The conducting films optically transparent are, generally, of indium tin oxide (ITO), fluorine-doped tin oxide (FTO) or antimony-doped tin oxide.[15] When the auxiliary electrode does not have to be transparent, is common to use as electrical conductor a silver or platinum electrode.

As mentioned, while one of the electrodes, the main electrode, is necessarily covered with an EC material, the auxiliary electrode is covered by an electroactive layer that can or not exhibit EC behaviour. In the former case, the EC system can be based (i) in the same material of the main EC system or (ii) in a different EC material but that generally exhibit complementary EC behaviour to the main system, i.e. while one EC system is cathodically colouring, the other system is anodically colouring.[27] Examples of developed complementary colouring ECDs are those with PB (colourless to blue on oxidation) as anodically colouring material and WO_3 (colourless to blue on reduction),[98] PEDOT (light-blue to deep blue on reduction)[99] and poly(butyl viologen) (colourless to purple on reduction)[100] as cathodically colouring materials. In those cases, the ECD is denominated by *dual electrochromic device*, once is based in more

than one EC material. In comparison with ECDs composed by just one EC material (*single electrochromic device*), the *dual ECDs* offer the advantage of exhibit several colour changes in a small electrical potential window.[14]

b) Electrolyte

The electrolyte is also an indispensable ECDs component, being responsible for the ionic conduction between the electrodes.[14] The electrolyte has to be an electronic insulator, transparent in the wavelength range used and has a wide electrochemical window and low volatility.[15] In general, the electrolytes are liquid, gel or solids. The liquid electrolytes are important when the EC material is dissolved in electrolyte (types I and II EC materials) and can be aqueous (acids and bases as H_2SO_4 or KOH) or polar organic solvents (such as acetonitrile and propylene carbonate (PC)), in which can be dissolved a salt (e.g. lithium perchlorate, $LiClO_4$).[15] The solid electrolytes are used with type III EC and predominantly are based in solid organic polymers, which can be subdivided in two categories: polyelectrolytes and polymer electrolytes. The polyelectrolytes contain ion-labile moieties along the backbone (e.g. Nafion®), while polymer electrolytes are effectively "solutions" of ionic salts (e.g. $LiClO_4$) with neutral macromolecules, such as poly(methyl methacrylate) (PMMA) and poly(propylene glycol) (PPO) as the immobile solvent. The viscosity / rigidity of the electrolyte depend of the molecular weight of the macromolecules employed.[15] In order to increase the conductivity of the polymer electrolytes,[101] an organic solvent is added.

To prevent leakage of electrolyte and to promote easy handling of the device after the assemblage, the ECDs must be sealed with epoxy or other types of sealants.[14]

c) ECD configurations and operation

Besides the vertical configuration, outlined in Figure 1.11 (a), the ECDs can also be assembled in a lateral configuration (Figure 1.11 (b)) that, although less common, offers an interesting potential. In this configuration, the working and auxiliary electrodes are in the same substrate, which decrease the number of layers and simplify the device assemblage. Nonetheless, as the charge transport between both electrodes occurs laterally, the response times can be larger than in ECDs with vertical configuration.[102]

In general, to ensure the working of the device, two redox couples must be involved between the two electrodes. Applying a voltage difference to the ECD, one species, for example the EC material in the main electrode, is oxidised (or reduced, according with the potential applied), while the other one is reduced (or oxidised). In consequence, the system switches from one coloured state to another.[14,97] When the

auxiliary electrode is also coated with an EC material, the anodic and cathodic colouration processes are simultaneously driven.

In terms of light propagation, ECDs can operate in (i) an absorption / transmission or (ii) reflective modes. In absorption / transmission ECDs, both electrodes are transparent, and the system switch reversibly between a state of high optical density (coloured) and a more transmissive state (ideally transparent);[27] smart windows, spectacles and visors are typical examples of this operation mode. In reflective ECDs, one of the electrodes is transparent and the other is a silver or platinum electrode, which acts as a mirror;[15] displays and anti-glare mirrors are more common examples.

1.2 Energy conversion

As the worldwide demand for energy supplies continues to increase, the development of alternative clean energy conversion (and storage) technologies has been a prior demand. Fuel cells and also metal-air batteries have been recognised as efficient alternative technologies, very useful for portable, stationary and transportation applications.[9] The core of these energy-related technologies is a series of electrochemical processes that include the occurrence of the oxygen reduction reaction (ORR) at the cathode. This reaction has a strong influence in devices performance, affecting the power output, charge-discharge rate, energy efficiency and cycle life.[103,104] For this reason, most of the research around fuel cells, and also around metal-air batteries, is focused in finding an efficient ORR electrocatalyst, very stable and cost-effective. In this section, the fundamental aspects of the current-state ORR electrocatalysis are present; the carbon-based materials are also introduced as alternative ORR electrocatalysts.

1.2.1 Oxygen Reduction Reaction

In aqueous electrolytes, oxygen gas molecule can be reduced with two different pathways, as summarised in Table 1.1. One pathway is the 4-electron process, in which oxygen molecules directly gets four electrons, generating water (in acidic electrolytes) or hydroxyl group (in basic electrolytes), and the other is the two-step 2-electron process, in which H_2O_2 (in acidic electrolytes) or HO_2^- (in basic electrolytes) is generate as intermediate.[6,105] In practical applications, namely in fuel cells, the 4-electron pathway is preferred in order to get high efficiency and also because the hydrogen peroxide production can lead to the corrosion of the device components;[106] nonetheless, the 2-electron process is useful for industrial H_2O_2 production.[11]

Table 1.1 Reactions pathways of ORR in aqueous electrolytes (potentials vs. NHE).

Electrolyte	Reaction pathway
Alkaline	*4-electron:* $O_2 + 4e^- + 2H_2O \rightarrow 4OH^-$ (E = 0.401 V)
	2-electron: $O_2 + H_2O + 2e^- \rightarrow HO_2^- + OH^-$ (E = -0.065 V) $HO_2^- + H_2O + 2e^- \rightarrow 3OH^-$ (E = 0.867 V)
Acid	*4-electron:* $O_2 + 4e^- + 4H^+ \rightarrow 2H_2O$ (E = 1.229 V)
	2-electron: $O_2 + 2H^+ + 2e^- \rightarrow H_2O_2$ (E = 0.695 V) $H_2O_2 + 2H^+ + 2e^- \rightarrow 2H_2O$ (E = 1.763 V)

The detailed ORR mechanism involves multistep and multiple adsorbed intermediates, which primary depend of the properties of the electrode surface.[11] An important step is the initial O_2 adsorption, followed by O=O bond breaking, and formation of oxygen adsorbed species (such as O^{ads} or OOH^{ads}, depending mainly of the initial O_2 dissociating energy barrier on a given surface).[8,11]

However, due to the high energy of the O=O bond (498 kJ mol^{-1}), the ORR kinetics is very slow and the reaction is not easily activated electrochemically, which implies the application of high reduction potentials and decreases the device performance.[105] In order to overcome these obstacles, the use of a cathode ORR catalyst is crucial. Platinum nanoparticles supported on carbon materials (Pt/C) are the most effective known ORR catalyst, leading to low ORR overpotential and large current densities, with selectivity toward a direct 4-electron pathway.[107] Nevertheless, the required high Pt loading (40-80 %)[108] associated with its high cost, scarcity, declining activity and possible Pt-deactivation by methanol crossover or carbon monoxide poisoning have limited the large-scale application of fuel cells with Pt-based electrocatalysts.[103] Therefore, research efforts have been devoted to developing alternative ORR electrocatalysts, with a competitive activity with the Pt/C catalysts but more stables and cost-effectives.[109]

Basically, two paths have been pursued to partly/completely replace Pt catalysts: (i) development of alloys with Pt[110,111] and (ii) replacing of Pt-based electrocatalysts by non-precious metal catalysts.[112,113] With Pt-alloys, the difficulties in terms of durability still remain due to decomposition, agglomeration and sintering of metal particles,[103] whereby the non-precious metal catalysts seems to be the most promising alternative. Actually, such electrocatalysts are predominantly carbon-based

materials, whose research has been driven by the recent advances in nanotechnology and synthetic chemistry.[11]

1.2.2 Carbon-based ORR electrocatalysts

Carbon is a wide available material, with unique characteristics that make it ideal for electrochemical applications. Carbon materials are characterised by high chemical and thermal stabilities, good electrical properties and high surface areas and porosity.[6] Furthermore, carbon has the ability to adopt several allotropic forms:[114] graphite, diamond, fullerenes, carbon nanotubes (CNTs) and graphene (Figure 1.12).

Graphene is the basic structure of all allotropic forms, except of the diamond. It is characterised by a single tightly packed layer of carbon atoms, bonded together in a hexagonal honeycomb lattice with sp^2 hybridisation. Several layers of graphene stacked on top of each other in a well-organized crystalline structure led to graphite, while CNTs consist of graphene layer(s) rolled into cylinders and can be single- (SWCNTs) or multi- (MWCNTs) walled nanotubes, with diameters of few nanometers and lengths in the order of micrometers.[114] These materials have been applied in ORR as metal-free electrocatalysts itself and also as catalyst supports in functional composites (hybrids).

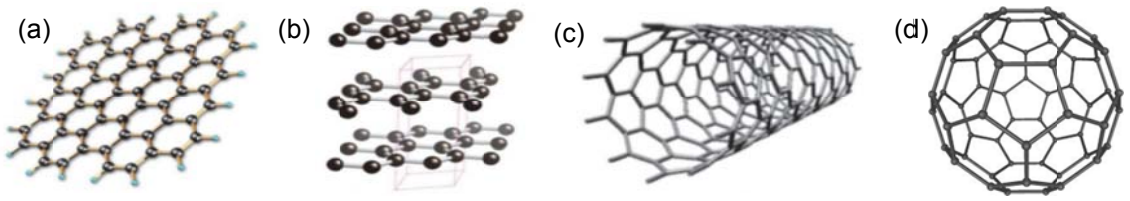

Figure 1.12 Structures of (a) graphene, (b) graphite, (c) carbon nanotube and (d) fullerene.

As metal-free ORR electrocatalysts, several works have reported the application of graphite,[115] carbon nanotubes,[116,117] and graphene[118]. Among these catalysts, the heteroatom-doped carbon nanostructures involving nitrogen, sulfur and phosphorous[103,112] are the most promising alternatives, demonstrating enhanced durability over the metal-catalysts; N-doped graphene exhibited the best ORR electroactivity. On the other hand, the ORR conducted in carbon electrocatalysts without doping, functionalization or lattice substitution generally exhibits the 2-electron peroxide pathway.[6]

Activated carbon, a common amorphous carbonaceous material that differs from graphite by having a random structure, has also been applied as ORR electrocatalyst.

This material takes advantage of its high surface area and well developed pore structure,[114] which are favourable conditions for a high ORR electrocatalytic activity, once increase the number of active sites exposed to the electrolyte.[119,120] Furthermore, superactivated carbons can be obtained from renewable sources, which is an advantageous green approach.[119,121] In the introduction of Chapter 6, it is provided an overview about the preparation of activated carbons from several biomass sources and their application as ORR electrocatalysts.

As catalyst support, carbon materials maximize the electroactive surface area, enhance the conductivities and bring the catalyst particles close to the reactants, improving the catalytic activity and durability.[104] Carbon black (CB), a synthetic carbon material based on spherical particles (diameter < 50 nm) of graphitic layers that may form agglomerates with a para-crystallite structure,[114] is the most commonly used support catalyst due to its low cost. Unfortunately, this material is susceptible to oxidation under fuel cells operating conditions,[114] sometimes resulting in active surface area loss and alteration of the pore surface characteristics. CNTs and graphene supports, although more expensive than carbon black, normally result in high catalyst utilization, due to the high crystallinity and surface area of those materials.

Several composites of these materials with conducting polymers,[122] non-precious metals,[123,124] metal oxides[125] and metallic complexes[126] have been applied as ORR electrocatalysts. Between the metal oxides, polyoxometalates (POMs) can be very attractive ORR electrocatalysts owing to their ability to mediate electron, proton and oxygen transfer reactions.[127]

1.2.3 Polyoxometalates

POMs are a class of early transition metal-oxygen clusters, mostly anionic in nature, based on building blocks with the general formula $(MO_x)_n$, where M is generally molybdenum (Mo^{VI}), tungsten (W^{V}) or vanadium (V^{V}) and x = 4-7.[128] The metal atoms (M) are called addenda atoms and are surrounded by bridging or terminal oxygen atoms. Different combinations and orientations of these building blocks lead to thousands of possible compounds with the POM denomination, with metal ions from 6 to 368 in a single molecule and monodisperse size from several angstroms up to 10 nm.[129]

POMs can be broadly classified into three main categories: heteropolyanions, isopolyanions and molybdenium blue and molybdenium brown reduced POM cluster.[130] Heteropolyanions are the most widely studied class and are characterised by containing, apart from M and O, other type of atoms, X, which are called primary heteroatoms. The Keggin and Wells-Dawson structures and their derivatives are

among the most common heteropolyanion species. In particular, the Keggin structure, $[XM_{12}O_{40}]^{n-}$ (Figure 1.13), involves four 3-fold M_3O_{13} groups. Each MO_6 octahedron therein shares two edges with other MO_6 and the four M_3O_{13} groups are attached to one another by corner sharing. The total assemblage contains 40 close-packed oxygens and has a tetrahedral pocket in its center for the heteroatom.

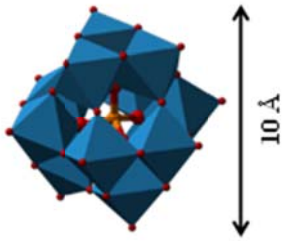

Figure 1.13 Polyhedral representation of Keggin polyoxometalate molecule.

The electrochemical behaviour of the Keggin-type anions has been studied in aqueous medium by electrochemical techniques, such as cyclic voltammetry.[131,132] These heteropolyanions undergo several rapid one and two-electron reversible reduction and further irreversible multi-electron reductions with concomitant decomposition. The electrons are accepted by the addenda ions of the heteropolyanion and, in general, the polyanion structure is not significantly altered when the number of electrons is lower or equal to four in Keggin heteropolytungstates and six in Keggin heteropolymolybdates.[133]

The pH has a large influence on the reduction of these polyanions; generally, there is a linear dependence between the redox potentials attributed to the reduction of addenda atoms and the pH value, as result from the protonation of the reduced species.[134] The slopes of the plots *E* vs. pH depend on the number of the protons and electrons exchanged in the redox process and change when the pH approaches the pK_a values of the oxidised or reduced forms, unless the pK_a values of both forms are similar.

The redox properties of POM clusters can be tailored by changing their addenda atoms. The substitution of one or more tungsten (W^{VI}) or molybdenum (Mo^{VI}) ions by another addenda ion such as W^{VI}, Mo^{VI} and V^{V} give rise to the mixed-addenda anions. The POM addenda atoms can be order by increasing oxidising ability as follows: $W^{VI} < Mo^{VI} < V^{V}$.[135]

Sometimes, the utilization of POMs as functional materials for practical applications is hampered by their low specific surface area and solubility in water.

Thus, their immobilization onto high surface supports, such as carbon materials, is expected to overcome their difficult processability and leads to significant improvements in electrochemical properties and electrocatalytic performances.

In Chapter 7 is provided a more detailed overview about the application of POMs itself and of POM@carbon-based nanocomposites as ORR electrocatalysts.

1.2.4 ORR electrocatalytic activity evaluation

Linear sweep voltammetry (LSV) is the most widely used technique to investigate the performance of potential ORR electrocatalysts. This technique can be complemented by cyclic voltammetry (CV), which can provide information on the redox behaviour of the electrocatalysts in the presence of O_2 or other molecules, including potential poisoning species.

The electrochemical parameters that are being used to benchmark the electrocatalysts with the state-of-the-art Pt/C electrocatalyst are: the onset potential (E_{onset}), the diffusion limiting current density (j_L) and the number of electrons transferred per O_2 molecule (n_{O_2}).[106] These parameters can be determined from the LSV plots measured with a rotating disk electrode (RDE). The E_{onset} is the potential at which the reaction starts, the limiting current density is the current density reached when the reaction at the electrode is totally controlled by mass transport (current is determined by the rate of diffusion of the reactant to the electrode and becomes independent of the applied potential, whereby a plateau is reached and $j = j_L$); the kinetic current density is the current in the absence of mass-transfer limitations.

LSV data are analysed through Koutecky-Levich (K-L), Equation (1.2):[121,136]

$$\frac{1}{j} = \frac{1}{j_L} + \frac{1}{j_k} = \frac{1}{B\omega^{1/2}} + \frac{1}{j_k} \tag{1.2}$$

where j is the experimentally measured current density, j_k is kinetic current density, and ω is the angular velocity; B is related to the diffusion limiting density, as expressed by the Equation (1.3):

$$B = 0.2\, n_{O_2} F (D_{O_2})^{2/3} \upsilon^{-1/6} C_{O_2} \tag{1.3}$$

where F is the Faraday constant (96 485 C mol^{-1}), C_{O_2} is the bulk concentration of O_2, υ is the kinematic viscosity of the electrolyte and D_{O_2} is the diffusion coefficient of O_2. The constant 0.2 is adopted when the rotating speed is in rpm. j_k and n_{O_2} can be determined from the intercept and the slope of the plot of j^{-1} *vs.* $\omega^{-1/2}$, respectively.[106] The values of n_{O_2} provides information about the selectivity of the electrocatalysts. For

the ORR, n_{O_2} = 2 corresponds to the reduction of O_2 to H_2O_2 (2-electron pathway), while n_{O_2} = 4 corresponds to the reduction of O_2 to H_2O (4-electron pathway). Higher ORR activity of electrocatalysts can be paired with higher (less negative) E_{onset} and with higher limiting current densities. However, as the limiting current density depends of the n_{O_2}, a lower limiting current density does not necessarily mean that the catalyst is less active, as it might be observed with a catalyst that is very active but selective to the 2-electron ORR pathway.[106]

The kinetics ORR evaluation can be made from the Tafel plots. An effective electrocatalyst reduces the electrode overpotential, η, defined as the deviation of the applied potential from the equilibrium potential, which is related to the current density (when it is limited solely by the kinetics of the electrode reaction) by the Tafel equation (Equation 1.4):[10,137]

$$|\eta| = \frac{2.3RT}{\alpha nF} log \frac{j}{j_0} \quad (1.4)$$

where j_0 is the exchange current density, α is the transfer coefficient, n is the number of electrons involved in the electrode reaction, T is temperature and R is the gas constant. The slop of the η *vs.* log j plot ($2.3RT/\alpha nF$) is called the Tafel slope. For an electrochemical reaction, to obtain a high current at low overpotential, the reaction should exhibit a low Tafel slope.[11]

Apart from promising ORR electrocatalytic performance, it is also desirable that the electrocatalyst exhibit high stability/durability, resistance to CO poisoning and tolerance to fuel (e.g. methanol) cross-over. The stability can be evaluated by investigating the current loss after prolonger operation by means of chronoamperometric measurements or by observing if no relevant changes occur in cyclic voltammograms after a sufficiently large number of cycles. It has to be noted that the stability can be separated into a physical and a chemical component.[106] The physical stability is related with the preservation of the structure of the material in different environments, while the chemical stability is associated with alterations of the functional groups (e.g. due to possible protonation or oxidation of groups).

1.2.5 ORR-involved electrochemical devices

The ORR is the cathode reaction in fuel cells and metal-air batteries.[103,104] For these electrochemical devices, the energy conversion/storage relies on the controllable oxidation of fuel molecules or metals, respectively.[138] This section provides an overview on both technologies.

Fuel cells are electrochemical energy conversion devices that directly convert chemical energy into electric power, with much higher efficiency and lower greenhouse gases emissions than the conventional technologies based on fossil fuel combustion.[139] Their operation is based in two electrochemical half-reactions, one occurring at the cathode (ORR) and the other taking place at the anode (fuel oxidation); other main component of the cell is the electrolyte (Figure 1.14).[106]

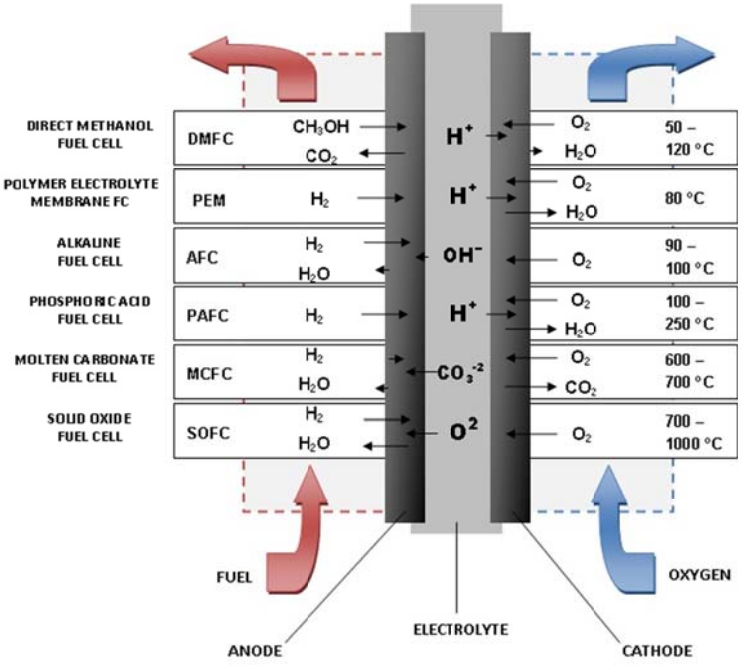

Figure 1.14 Schematic structures of several fuel-cells types.

According with the electrolyte employed and the operating temperature, the fuel cells can be divided in several classes.[140] The high temperature fuel cells operate at 600 – 1000 ºC and are classified into two different types:

(i) Molten Carbonate Fuel Cell (MCFC);

(ii) Solid Oxide Fuel Cell (SOFC).

Low temperature fuel cells are particularly attractive and are considered the main power source candidate for the next generation light-duty vehicles and portable electronics.[141] They can be subdivided into four fuel cells-types:

(iii) Alkaline Fuel Cell (AFC);

(iv) Polymer Electrolyte Membrane Fuel Cell (PEMFC, also called Proton Exchange Membrane Fuel Cell);

(v) Direct Methanol Fuel Cell (DMFC);

(vi) Phosphoric Acid Fuel Cell (PAFC).

With the exception of DMFC that uses methanol as fuel, in all of these fuel cells the hydrogen oxidation is the reaction that occurs in the anode. The AFC is characterised by use an alkaline electrolyte (generally KOH), which is an advantage once the ORR kinetics is faster in alkaline than in acidic electrolytes. Nonetheless, the requirement for very pure gases limits its large-scale application. On the other hand, in PEMFC is used a proton-conducting polymer membrane (e.g. Nafion®) as electrolyte;[142] the DMFC is a special form of fuel cell based in PEM technology. The PAFC also used an acidic electrolyte based in phosphoric acid.

All of these fuel cells are sensitive to the CO poisoning that occurs due to the adsorption of the specie (coming as contaminant in fuel stream) to the active site of the catalyst, blocking the sites available for reaction.[140] Particularly in DMFC, the methanol cross-over can poison the ORR electrocatalysts, since methanol at the cathode causes a mixed potential due to its oxidation and, consequently, decrease the cell performance.[108]

The metal-air battery is composed of a metal anode and an air cathode in which the active material, oxygen, is accessed from the environment (Figure 1.15).[143] The performance of the battery is strongly influenced by the ORR during discharge and by the oxygen evolution reaction (OER) during charge. The oxygen reduction is accompanied by the formation of metal oxides or hydroxides (e.g. Li_2O_2 or LiOH, depending of the electrolyte).[144]

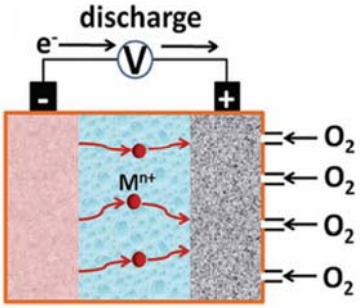

Figure 1.15 Schematic structure of a metal-air battery.

The main promise of this technology over traditional batteries is its cost-effectiveness and high theoretical energy density (5200 Wh kg^{-1}), which make of them hopeful for automotive applications (electrical vehicles).[145] Among all metal-air batteries, Li-air and Zn-air batteries have attracted the most attention, with the first

having the potential to deliver the highest energy density.[144] Nowadays, the performance and applicability of these batteries are limited by the sensitivity to contaminants from air (e.g. CO_2) and electrolyte evaporation due to their open cathode structure.

1.3 Objectives

This thesis was devoted to the development of novel efficient systems in the context of new technologies for energy saving and conversion. In the framework of saving-energy technologies, the novel EC systems were based in poly[Ni(*salen*)]-type polymer films and nanocomposites with inorganic nanomaterials. In the field of energy-conversion, novel carbon-based materials were developed for the ORR electrocatalysis.

The main objectives of the work were:

(i) to evaluate the EC behaviour of novel nickel *salen*-type polymers in order to find promisor EC materials to assemble a prototype solid-state electrochromic cell;

(ii) to investigate the effect of the incorporation of (a) metal oxides – WO_3 and TiO_2 NPs – and (b) nitrogen-doped graphene in the electronic, optical and morphological properties of a poly[Ni(*salen*)]-type polymer film, with the final purpose to improve the EC properties of the pristine film;

(iii) to explore the potentialities of activated carbons prepared from a renewable biomass source as novel efficient ORR electrocatalysts;

(iv) to examine the effect of different carbon-based supports on the ORR electrocatalytic activity of several POM@carbon-based nanocomposites.

The Figure 1.16 illustrates the foray into the world of energy-related materials within the framework of the present thesis, highlighting the possible applications of electrochromic materials for energy-saving (Chapters 2 to 5) and the role of the oxygen reduction reaction in the development of alternative efficient energy-conversion technologies (Chapters 6 and 7), with practical impact in the human daily life. Several materials, from the traditional nickel-*salen* complexes and polyoxometalates (Keggin-type) to the metal oxides nanostructures and carbon-based materials (including carbon nanomaterials), were considered as the core for the development of the new energy-related systems and technologies.

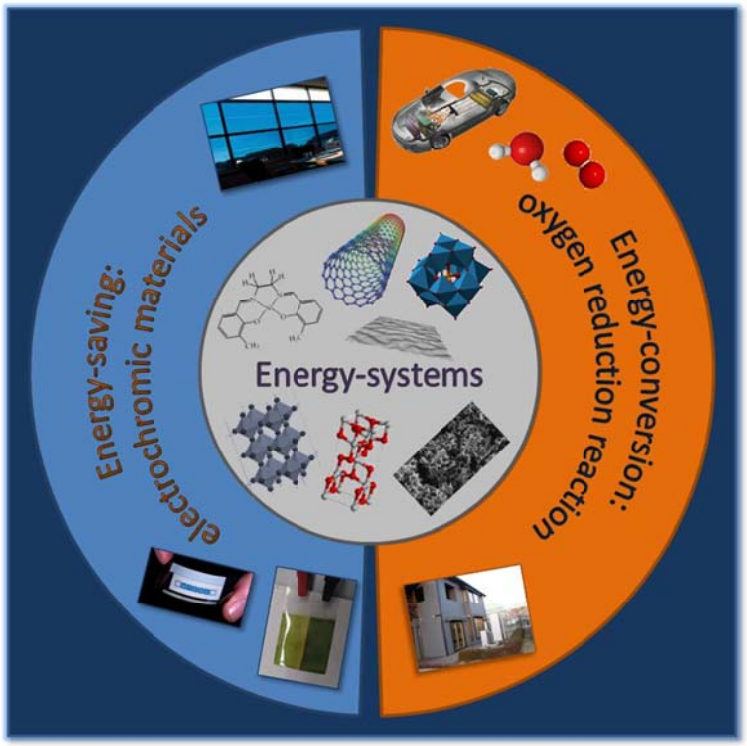

Figure 1.16 Energy-related materials within the framework of the present thesis: application of EC materials for energy-saving and of new ORR electrocatalysts for alternative efficient energy-conversion technologies.

Apart from the Chapter 1, which aims at giving an overall introduction on the reported themes, the thesis is divided into more 7 chapters.

Chapter 2 comprises the preparation, characterisation and exploration of the EC behaviour of two novel poly[Ni(*salen*)]-type polymers, as well as the assemblage of electrochromic devices.

Chapter 3 relates to the synthesis and characterisation of WO_3 NPs and to the preparation and characterisation (electrochemical and optical) of the nanocomposite based in the incorporation of WO_3 NPs onto a poly[Ni(*salen*)] film.

Chapter 4 describes the preparation of TiO_2 NPs and investigates the effect of their incorporation in the properties of the nickel *salen*-film, with emphasis for the EC properties of the resulting nanocomposite.

Chapter 5 comprises the preparation of a nanocomposite between the nickel *salen*-film and nitrogen-doped few layer graphene and the improvements on the electrical / optical properties induced by the nanomaterial incorporation.

Chapter 6 corresponds to the application of two activated carbons, prepared from sucrose, as metal-free electrocatalysts for ORR in acidic and alkaline media, as well as to their electrochemical characterisation in the presence of several redox probes.

Chapter 7 describes the electrochemical characterisation of several POM@carbon-based hybrids, prepared through the incorporation of a polyoxometalate ($PMo_{11}V$) on carbon black, CNTs and graphene, and the influence of the carbon support in the electrocatalytic activity of the hybrids for ORR.

Chapter 8 is devoted to the overall conclusions and future perspectives.

The thesis also includes the Appendices A, B and C, in which the experimental details on the electrochemical, spectroelectrochemical and other most common characterisation techniques used are described.

The results described in Chapters 2 to 7 are based on 6 scientific papers, one of which has been already published in refereed journals and the remaining have been submitted.

List of publications

Chapter 2

M. Nunes, M. Araújo, J. Fonseca, C. Moura, A. R. Hillman, C. Freire, "High-performance electrochromic device based on poly[Ni(*salen*)]-type polymer films". Submitted.

Chapter 3

M. Nunes, C. Moura, A. R. Hillman, C. Freire, "Novel hybrid based in poly[Ni(*salen*)] film and WO_3 nanoparticles with electrochromic properties". Submitted.

Chapter 4

M. Nunes, C. Moura, A. R. Hillman, C. Freire, "Multicolour electrochromic film based in a TiO_2@poly[Ni(*salen*)] nanocomposite with excellent electrochemical stability". Submitted.

Chapter 5

M. Nunes, M. Araújo, R. Bacsa, R. V. Ferreira, E. Castillejos, P. Serp, A. R. Hillman, C. Freire, "N-doped graphene@poly[Ni(*salen*)] nanocomposite with outstanding electrochromic properties". Submitted.

Chapter 6

M. Nunes, I. M. Rocha, D. M. Fernandes, A. S. Mestre, C. N. Moura, A. P. Carvalho, M. F. R. Pereira, C. Freire, "Sucrose-derived activated carbons: electron transfer properties and application as oxygen reduction electrocatalysts", *RSC Adv.* **2015**, *5*, 102919-102931. DOI: 10.1039/c5ra20874b.

Chapter 7

M. Nunes, D. Fernandes, I. Rocha, M. F. R. Pereira, I.-M. Mbomekalle, P. de Oliveira, C. Freire, "Phosphomolybdate@carbon-based nanocomposites as electrocatalysts for oxygen reduction". Submitted.

References

[1] *World Population Prospects: the 2015 revision*; United Nations: New York, USA, http://esa.un.org/unpd/wpp/publications/files/key_findings_wpp_2015.pdf, accessed in January 2016.

[2] ocean.nationalgeographic.com/oceancritical-issues-sea-level-rise/, accessed in January 2016.

[3] Jacob, T.; Wahr, J.; Pfeffer, W. T.; Swenson, S. *Nature* **2012**, *482*, 514.

[4] Harrould-Kolieb, E. R.; Herr, D. *Clim. Policy* **2012**, *12*, 378.

[5] Basu, R.; Samet, J. M. *Epidemiol. Rev.* **2002**, *24*, 190.

[6] Wang, D. W.; Su, D. S. *Energy Environ. Sci.* **2014**, *7*, 576.

[7] Shi, L.; Chew, M. Y. L. *Renew. Sust. Energ. Rev.* **2012**, *16*, 192.

[8] Katsounaros, I.; Cherevko, S.; Zeradjanin, A. R.; Mayrhofer, K. J. J. *Angew. Chem.-Int. Edit.* **2014**, *53*, 102.

[9] Zhou, X. J.; Qiao, J. L.; Yang, L.; Zhang, J. J. *Adv. Energy Mater.* **2014**, *4*, 25.

[10] Faber, M. S.; Jin, S. *Energy Environ. Sci.* **2014**, *7*, 3519.

[11] Jiao, Y.; Zheng, Y.; Jaroniec, M. T.; Qiao, S. Z. *Chem. Soc. Rev.* **2015**, *44*, 2060.

[12] Mortimer, R. J. *Am. Scientist* **2013**, *101*, 38.

[13] Caglar, A.; Cengiz, U.; Yildirim, M.; Kaya, I. *Appl. Surf. Sci.* **2015**, *331*, 262.

[14] Thakur, V. K.; Ding, G. Q.; Ma, J.; Lee, P. S.; Lu, X. H. *Adv. Mater.* **2012**, *24*, 4071.

[15] Mortimer, R. J. *Annu. Rev. Mater. Res.* **2011**, *41*; 241.

[16] Skotheim, T. A.; Reynolds, J. R. *Conjugated Polymers - Theory, Synthesis, Properties and Characterization*; Third ed.; CRC Press, Taylor & Francis Group: USA, **2007**.

[17] Fletcher, S. *J. Solid State Electrochem.* **2015**, *19*, 3305.

[18] Platt, J. R. *J. Chem. Phys.* **1961**, *34*, 862.

[19] Monk, P. M. S.; Mortimer, R. J.; Rosseinsky, D. R. *Electrochromism and Electrochromic Devices*; Cambridge University Press: New York, **2007**.

[20] Deb, S. K. *Appl. Opt.* **1969**, *8 Suppl 1*, 192.

[21] Deb, S. K. *Philos. Mag.* **1973**, *27*, 801.

[22] Granqvist, C. G. *Sol. Energy Mater. Sol. Cells* **2012**, *99*, 1.

[23] Mohapatra, S. K. *J. Electrochem. Soc.* **1978**, *125*, 284.

[24] Ronlan, A.; Coleman, J.; Hammeric.O; Parker, V. D. *J. Am. Chem. Soc.* **1974**, *96*, 845.

[25] Kaufman, F. B.; Schroeder, A. H.; Engler, E. M.; Patel, V. V. *Appl. Phys. Lett.* **1980**, *36*, 422.

[26] Kanazawa, K. K.; Diaz, A. F.; Geiss, R. H.; Gill, W. D.; Kwak, J. F.; Logan, J. A.; Rabolt, J. F.; Street, G. B. *J. Chem. Soc.-Chem. Commun.* **1979**, 854.

[27] Beaujuge, P. M.; Reynolds, J. R. *Chem. Rev.* **2010**, *110*, 268.

[28] Beaujuge, P. M.; Vasilyeva, S. V.; Liu, D. Y.; Ellinger, S.; McCarley, T. D.; Reynolds, J. R. *Chem. Mat.* **2012**, *24*, 255.

[29] Yang, C.; Wei, H.; Guan, L.; Guo, J.; Wang, Y.; Yan, X.; Zhang, X.; Wei, S.; Guo, Z. *J. Mater. Chem. A* **2015**, *3*, 14929.

[30] Chang, I. F.; Gilbert, B. L.; Sun, T. I. *J. Electrochem. Soc.* **1975**, *122*, 955.

[31] MacDiarmid, A. G. *Rev. Mod. Phys.* **2001**, *73*, 701.

[32] Hall, N. *Chem. Commun.* **2003**, 1.

[33] Li, C.; Bai, H.; Shi, G. *Chem. Soc. Rev.* **2009**, *38*, 2397.

[34] Zmija, J.; Matachowski, M. J. *Journal of Achievements in Materials and Manufacturing Engineering* **2011**, *48*, 14

[35] Bredas, J. L.; Scott, J. C.; Yakushi, K.; Street, G. B. *Phys. Rev. B* **1984**, *30*, 1023.

[36] Tedim, J.; Patricio, S.; Fonseca, J.; Magalhaes, A. L.; Moura, C.; Hillman, A. R.; Freire, C. *Synth. Met.* **2011**, *161*, 680.

[37] Dyer, A. L.; Craig, M. R.; Babiarz, J. E.; Kiyak, K.; Reynolds, J. R. *Macromolecules* **2010**, *43*, 4460.

[38] Bulloch, R. H.; Kerszulis, J. A.; Dyer, A. L.; Reynolds, J. R. *ACS Appl. Mater. Interfaces* **2015**, *7*, 1406.

[39] Kurtay, G.; Ak, M.; Gullu, M.; Toppare, L.; Ak, M. S. *Synth. Met.* **2014**, *194*, 19.

[40] Chang, K. H.; Wang, H. P.; Wu, T. Y.; Sun, I. W. *Electrochim. Acta* **2014**, *119*, 225.

[41] Yang, C. H.; Chih, Y. K.; Wu, W. C.; Chen, C. H. *Electrochem. Solid State Lett.* **2006**, *9*, C5.

[42] Xiong, S. X.; Wei, J.; Jia, P. T.; Yang, L. P.; Ma, J.; Lu, X. H. *ACS Appl. Mater. Interfaces* **2011**, *3*, 782.

[43] Fonseca, J.; Tedim, J.; Biernacki, K.; Magalhaes, A. L.; Gurman, S. J.; Freire, C.; Hillman, A. R. *Electrochim. Acta* **2010**, *55*, 7726.

[44] Holliday, B. J.; Swager, T. M. *Chem. Commun.* **2005**, 23.

[45] Schiff, H. *Ann. Suppl.* **1864**, *3*, 343.

[46] Baleizao, C.; Garcia, H. *Chem. Rev.* **2006**, *106*, 3987.

[47] Cozzi, P. G. *Chem. Soc. Rev.* **2004**, *33*, 410.

[48] VilasBoas, M.; Freire, C.; deCastro, B.; Christensen, P. A.; Hillman, A. R. *Inorg. Chem.* **1997**, *36*, 4919.

[49] Goldsby, K. A. *J. Coord. Chem.* **1988**, *19*, 83.

[50] Goldsby, K. A.; Blaho, J. K.; Hoferkamp, L. A. *Polyhedron* **1989**, *8*, 113.

[51] Bedioui, F.; Labbe, E.; Gutierrezgranados, S.; Devynck, J. *J. Electroanal. Chem.* **1991**, *301*, 267.

[52] Audebert, P.; Capdevielle, P.; Maumy, M. *New J. Chem.* **1991**, *15*, 235.

[53] Audebert, P.; Capdevielle, P.; Maumy, M. *Synth. Met.* **1991**, *43*, 3049.

[54] Audebert, P.; Capdevielle, P.; Maumy, M. *New J. Chem.* **1992**, *16*, 697.

[55] Audebert, P.; Hapiot, P.; Capdevielle, P.; Maumy, M. *J. Electroanal. Chem.* **1992**, *338*, 269.

[56] Dahm, C. E.; Peters, D. G. *Anal. Chem.* **1994**, *66*, 3117.

[57] Dahm, C. E.; Peters, D. G. *J. Electroanal. Chem.* **1996**, *406*, 119.

[58] Dahm, C. E.; Peters, D. G.; Simonet, J. *J. Electroanal. Chem.* **1996**, *410*, 163.

[59] Tedim, J.; Carneiro, A.; Bessada, R.; Patricio, S.; Magalhaes, A. L.; Freire, C.; Gurman, S. J.; Hillman, A. R. *J. Electroanal. Chem.* **2007**, *610*, 46.

[60] Vilas-Boas, M.; Henderson, M. J.; Freire, C.; Hillman, A. R.; Vieil, E. *Chem.-Eur. J.* **2000**, *6*, 1160.

[61] Vilas-Boas, M.; Freire, C.; de Castro, B.; Christensen, P. A.; Hillman, A. R. *Chem.-Eur. J.* **2001**, *7*, 139.

[62] Vilas-Boas, M.; Santos, I. C.; Henderson, M. J.; Freire, C.; Hillman, A. R.; Vieil, E. *Langmuir* **2003**, *19*, 7460.

[63] Pinheiro, C.; Parola, A. J.; Pina, F.; Fonseca, J.; Freire, C. *Sol. Energy Mater. Sol. Cells* **2008**, *92*, 980.

[64] Branco, A.; Pinheiro, C.; Fonseca, J.; Tedim, J.; Carneiro, A.; Parola, A. J.; Freire, C.; Pina, F. *Electrochem. Solid State Lett.* **2010**, *13*, J114.

[65] Reddy, B. N.; Deepa, M.; Joshi, A. G.; Srivastava, A. K. *J. Phys. Chem. C* **2011**, *115*, 18354.

[66] Janaky, C.; de Tacconi, N. R.; Chanmanee, W.; Rajeshwar, K. *J. Phys. Chem. C* **2012**, *116*, 4234.

[67] Guo, F. J.; Mi, H. Y.; Zhou, J. P.; Zhao, Z. B.; Qiu, J. S. *Carbon* **2015**, *95*, 323.

[68] Abdulla, S.; Mathew, T. L.; Pullithadathil, B. *Sens. Actuator B-Chem.* **2015**, *221*, 1523.

[69] Eren, E.; Celik, G.; Uygun, A.; Tabaciarova, J.; Omastova, M. *Synth. Met.* **2012**, *162*, 1451.

[70] Choi, M.; Yong, K. *Nanoscale* **2014**, *6*, 13900.

[71] Silva, E.; La Porta, F. A.; Liu, M. S.; Andres, J.; Varela, J. A.; Longo, E. *Dalton Trans.* **2015**, *44*, 3159.

[72] Wei, H. G.; Yan, X. R.; Wu, S. J.; Luo, Z. P.; Wei, S. Y.; Guo, Z. H. *J. Phys. Chem. C* **2012**, *116*, 25052.

[73] Cushing, B. L.; Kolesnichenko, V. L.; O'Connor, C. J. *Chem. Rev.* **2004**, *104*, 3893.

[74] Pereira, C.; Pereira, A. M.; Fernandes, C.; Rocha, M.; Mendes, R.; Fernandez-Garcia, M. P.; Guedes, A.; Tavares, P. B.; Greneche, J. M.; Araujo, J. P.; Freire, C. *Chem. Mat.* **2012**, *24*, 1496.

[75] Kulal, A. B.; Dongare, M. K.; Umbarkar, S. B. *Appl. Catal. B-Environ.* **2016**, *182*, 142.

[76] Zhang, W. X.; Wang, H.; Zhang, Y. M.; Yang, Z. H.; Wang, Q.; Xia, J. F.; Yang, X. N. *Electrochim. Acta* **2013**, *113*, 63.

[77] Zhang, Z. G.; Huang, Z. F.; Cheng, X. D.; Wang, Q. L.; Chen, Y.; Dong, P. M.; Zhang, X. W. *Appl. Surf. Sci.* **2015**, *355*, 45.

[78] Wang, L.; Lu, X. P.; Lei, S. B.; Song, Y. H. *J. Mater. Chem. A* **2014**, *2*, 4491.

[79] Novoselov, K. S.; Geim, A. K.; Morozov, S. V.; Jiang, D.; Zhang, Y.; Dubonos, S. V.; Grigorieva, I. V.; Firsov, A. A. *Science* **2004**, *306*, 666.

[80] Reina, A.; Jia, X. T.; Ho, J.; Nezich, D.; Son, H. B.; Bulovic, V.; Dresselhaus, M. S.; Kong, J. *Nano Lett.* **2009**, *9*, 30.

[81] Takagi, S.; Makuta, S.; Veamatahau, A.; Otsuka, Y.; Tachibana, Y. *J. Mater. Chem.* **2012**, *22*, 22181.

[82] Janaky, C.; Rajeshwar, K. *Prog. Polym. Sci.* **2015**, *43*, 96.

[83] Padilla, J.; Osterholm, A. M.; Dyer, A. L.; Reynolds, J. R. *Sol. Energy Mater. Sol. Cells* **2015**, *140*, 54.

[84] Amb, C. M.; Dyer, A. L.; Reynolds, J. R. *Chem. Mat.* **2011**, *23*, 397.

[85] Jensen, J.; Hosel, M.; Dyer, A. L.; Krebs, F. C. *Adv. Funct. Mater.* **2015**, *25*, 2073.

[86] Zhang, J. H.; Tu, J. P.; Zhou, D.; Tang, H.; Li, L.; Wang, X. L.; Gu, C. D. *J. Mater. Chem. C* **2014**, *2*, 10409.

[87] www.gentex.com, accessed in January 2016.

[88] Granqvist, C. G. *Thin Solid Films* **2014**, *564*, 1.

[89] www.gesimat.de, accessed in January 2016.

[90] www.sageglass.com/technology/, accessed in January 2016.

[91] www.chromogenics.com, accessed in January 2016.

[92] Heinkenfeld, J.; Drzaic, P.; Yeo, J.-S.; Koch, T. *J. Soc. Inf. Display* **2011**, *19*, 129.

[93] Österholm, A. M.; Shen, D. E.; Kerszulis, J. A.; Bullock, R. H.; Kuepfert, M.; Dyer, A. L.; Reynolds, J. R. *ACS Appl. Mater. Interfaces* **2015**, *7*, 1413.

[94] Remmele, J.; Shen, D. E.; Mustonen, T.; Fruehauf, N. *ACS Appl. Mater. Interfaces* **2015**, *7*, 12001.

[95] www.ynvisible.com, accessed in January 2016.

[96] Invernale, M. A.; Ding, Y.; Sotzing, G. A. *ACS Appl. Mater. Interfaces* **2010**, *2*, 296.

[97] Carpi, F.; De Rossi, D. *Opt. Laser Technol.* **2006**, *38*, 292.

[98] Kraft, A.; Rottmann, M. *Sol. Energy Mater. Sol. Cells* **2009**, *93*, 2088.

[99] Tung, T. S.; Ho, K. C. *Sol. Energy Mater. Sol. Cells* **2006**, *90*, 521.

[100] Kuo, T. H.; Hsu, C. Y.; Lee, K. M.; Ho, K. C. *Sol. Energy Mater. Sol. Cells* **2009**, *93*, 1755.

[101] Agnihotry, S. A.; Pradeep; Sekhon, S. S. *Electrochim. Acta* **1999**, *44*, 3121.

[102] Tehrani, P.; Isaksson, J.; Mammo, W.; Andersson, M. R.; Robinson, N. D.; Berggren, M. *Thin Solid Films* **2006**, *515*, 2485.

[103] Kim, D. W.; Li, O. L.; Saito, N. *Phys. Chem. Chem. Phys.* **2015**, *17*, 407.

[104] Zhu, C. Z.; Dong, S. J. *Nanoscale* **2013**, *5*, 1753.

[105] Shi, H.; Shen, Y. F.; He, F.; Li, Y.; Liu, A. R.; Liu, S. Q.; Zhang, Y. J. *J. Mater. Chem. A* **2014**, *2*, 15704.

[106] Daems, N.; Sheng, X.; Vankelecom, I. F. J.; Pescarmona, P. P. *J. Mater. Chem. A* **2014**, *2*, 4085.

[107] Panomsuwan, G.; Saito, N.; Ishizaki, T. *Phys. Chem. Chem. Phys.* **2015**, *17*, 6227.

[108] Tao, G. J.; Zhang, L. X.; Chen, L. S.; Cui, X. Z.; Hua, Z. L.; Wang, M.; Wang, J. C.; Chen, Y.; Shi, J. L. *Carbon* **2015**, *86*, 108.

[109] Guo, C. Z.; Liao, W. L.; Li, Z. B.; Chen, C. G. *Carbon* **2015**, *85*, 279.

[110] Wang, C.; Markovic, N. M.; Stamenkovic, V. R. *ACS Catal.* **2012**, *2*, 891.

[111] Stephens, I. E. L.; Bondarenko, A. S.; Gronbjerg, U.; Rossmeisl, J.; Chorkendorff, I. *Energy Environ. Sci.* **2012**, *5*, 6744.

[112] Qu, L. T.; Liu, Y.; Baek, J. B.; Dai, L. M. *ACS Nano* **2010**, *4*, 1321.

[113] Chen, S.; Bi, J. Y.; Zhao, Y.; Yang, L. J.; Zhang, C.; Ma, Y. W.; Wu, Q.; Wang, X. Z.; Hu, Z. *Adv. Mater.* **2012**, *24*, 5593.

[114] Trogadas, P.; Fuller, T. F.; Strasser, P. *Carbon* **2014**, *75*, 5.

[115] Shen, A.; Zou, Y.; Wang, Q.; Dryfe, R. A. W.; Huang, X.; Dou, S.; Dai, L.; Wang, S. *Angew. Chem.-Int. Ed.* **2014**, *53*, 10804.

[116] Tuci, G.; Zafferoni, C.; Rossin, A.; Milella, A.; Luconi, L.; Innocenti, M.; Phuoc, L. T.; Cuong, D. V.; Cuong, P. H.; Giambastian, G. *Chem. Mat.* **2014**, *26*, 3460.

[117] Vikkisk, M.; Kruusenberg, I.; Ratso, S.; Joost, U.; Shulga, E.; Kink, I.; Rauwel, P.; Tammeveski, K. *RSC Adv.* **2015**, *5*, 59495.

[118] Wu, J. J.; Ma, L. L.; Yadav, R. M.; Yang, Y. C.; Zhang, X.; Vajtai, R.; Lou, J.; Ajayan, P. M. *ACS Appl. Mater. Interfaces* **2015**, *7*, 14763.

[119] Song, M. Y.; Park, H. Y.; Yang, D. S.; Bhattacharjya, D.; Yu, J. S. *ChemSusChem* **2014**, *7*, 1755.

[120] Li, J. P.; Wang, S. G.; Ren, Y. Q.; Ren, Z. H.; Qiu, Y. J.; Yu, J. *Electrochim. Acta* **2014**, *149*, 56.

[121] Chen, P.; Wang, L. K.; Wang, G.; Gao, M. R.; Ge, J.; Yuan, W. J.; Shen, Y. H.; Xie, A. J.; Yu, S. H. *Energy Environ. Sci.* **2014**, *7*, 4095.

[122] Yuan, Y.; Zhou, S. G.; Zhuang, L. *J. Power Sources* **2010**, *195*, 3490.

[123] Charreteur, F.; Jaouen, F.; Ruggeri, S.; Dodelet, J. P. *Electrochim. Acta* **2008**, *53*, 2925.

[124] Cheng, Y. H.; Li, W. Y.; Fan, X. Z.; Liu, J. G.; Xu, W. G.; Yan, C. W. *Electrochim. Acta* **2013**, *111*, 635.

[125] Liang, Y. Y.; Li, Y. G.; Wang, H. L.; Zhou, J. G.; Wang, J.; Regier, T.; Dai, H. J. *Nat. Mater.* **2011**, *10*, 780.

[126] Jiang, Y. Y.; Lu, Y. Z.; Wang, X. D.; Bao, Y.; Chen, W.; Niu, L. *Nanoscale* **2014**, *6*, 15066.

[127] Fernandes, D. M.; Barbosa, A. D. S.; Pires, J.; Balula, S. S.; Cunha-Silva, L.; Freire, C. *ACS Appl. Mater. Interfaces* **2013**, *5*, 13382.

[128] Long, D. L.; Burkholder, E.; Cronin, L. *Chem. Soc. Rev.* **2007**, *36*, 105.

[129] Liu, S. Q.; Tang, Z. Y. *Nano Today* **2010**, *5*, 267.

[130] Long, D. L.; Tsunashima, R.; Cronin, L. *Angew. Chem.-Int. Edit.* **2010**, *49*, 1736.

[131] Fernandes, D. M.; Simoes, S. M. N.; Carapuca, H. M.; Cavaleiro, A. M. V. *Electrochim. Acta* **2008**, *53*, 6580.

[132] Fernandes, D. M.; Freire, C. *ChemElectroChem* **2015**, *2*, 269.

[133] Keita, B.; Nadjo, L. In *Electrochemistry of Polyoxometalates, in Encyclopedia of Electrochemistry*; Bard, A. J., Stratmann, M., Eds.; Wiley-VCH, **2006**.

[134] Couto, F.; Cavaleiro, A. M. V.; de Jesus, J. D. P.; Simao, J. E. J. *Inorg. Chim. Acta* **1998**, *281*, 225.

[135] Sadakane, M.; Steckhan, E. *Chem. Rev.* **1998**, *98*, 219.

[136] Liu, F. F.; Peng, H. L.; You, C. H.; Fu, Z. Y.; Huang, P. Y.; Song, H. Y.; Liao, S. J. *Electrochim. Acta* **2014**, *138*, 353.

[137] Bard, A. J.; Faulkner, L. R. *Electrochemical Methods: Fundamentals and Applications*; Wiley: New York, **2001**.

[138] Yuan, C. Z.; Wu, H. B.; Xie, Y.; Lou, X. W. *Angew. Chem.-Int. Edit.* **2014**, *53*, 1488.

[139] Zheng, Y.; Jiao, Y.; Jaroniec, M.; Jin, Y. G.; Qiao, S. Z. *Small* **2012**, *8*, 3550.

[140] Carrette, L.; Friedrich, K. A.; Stimming, U. *ChemPhysChem* **2000**, *1*, 162.

[141] Wang, Y.; Chen, K. S.; Mishler, J.; Cho, S. C.; Adroher, X. C. *Appl. Energy* **2011**, *88*, 981.

[142] Debe, M. K. *Nature* **2012**, *486*, 43.

[143] Laoire, C. O.; Mukerjee, S.; Abraham, K. M.; Plichta, E. J.; Hendrickson, M. A. *J. Phys. Chem. C* **2009**, *113*, 20127.

[144] Cao, R.; Lee, J. S.; Liu, M. L.; Cho, J. *Adv. Energy Mater.* **2012**, *2*, 816.

[145] Li, Q.; Mahmood, N.; Zhu, J. H.; Hou, Y. L.; Sun, S. H. *Nano Today* **2014**, *9*, 668.

In the world of energy-saving…

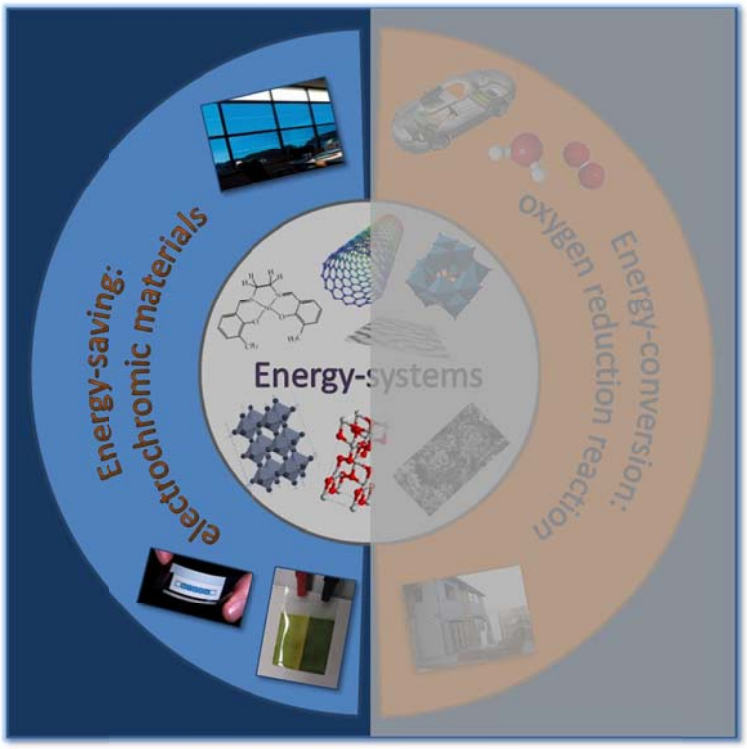

Chapter 2

High-performance electrochromic devices based on poly[Ni(*salen*)]-type polymer films

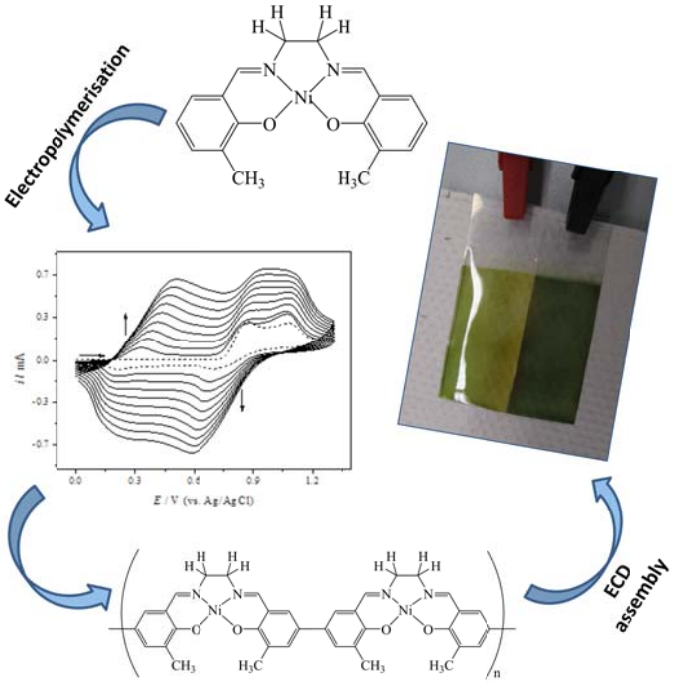

2

High-performance electrochromic devices based on poly[Ni(*salen*)]-type polymer films[1,2,3]

Abstract

In this chapter it is described the application of two poly[Ni(*salen*)]-type electroactive polymer films as new electrochromic materials. The two films, poly[Ni(3-Mesalen)] (poly[1]) and poly[Ni(3-MesaltMe)] (poly[2]), were successfully electrodeposited onto ITO/PET flexible substrates and their voltammetric characterisation revealed that poly[1] showed similar redox profiles in $LiClO_4/CH_3CN$ and $LiClO_4$/propylene carbonate (PC), while poly[2] showed solvent dependent electrochemical responses. Both films showed polyelectrochromic behaviour, exhibiting yellow, green and russet colours according to their oxidation state, and promising electrochromic properties with high electrochemical stability in $LiClO_4$/PC supporting electrolyte. In particular, poly[1] exhibited a very good electrochemical stability changing colour between yellow and green (λ = 750 nm) during 9000 redox cycles, with a charge loss of 34.3 %, an optical contrast of ΔT = 26.2 % and an optical density of ΔOD = 0.49, with a colouration efficiency of η = 75.55 $cm^2\ C^{-1}$. On the other hand, poly[2] showed good optical contrast for the colour change from green to russet (ΔT = 58.5 %), although with moderate electrochemical stability. Finally, poly[1] was used to fabricate electrochromic devices using lateral configuration with two figures of merit: a simple shape (typology 1) and a butterfly shape (typology 2); typology 1 showed the best performance with optical contrast ΔT = 88.7 % (at λ = 750 nm), colouration efficiency η = 130.4 $cm^2\ C^{-1}$ and charge loss of 37.0 % upon 3000 redox cycles.

---

[1] Adapted from: M. Nunes, M. Araújo, J. Fonseca, C. Moura, A. R. Hillman, C. Freire, High-performance electrochromic devices based on poly[Ni(*salen*)]-type polymer films. Submitted.

[2] M. Nunes's contribution to the publication: preparation and characterisation of the poly[Ni(*salen*)] films, evaluation of the electrochromic properties, assemble and characterisation of the electrochromic devices and manuscript preparation.

[3] The experimental details on the electrochemical/spectroelectrochemical and characterisation techniques are indicated in Appendices A and C, respectively.

2.1 Introduction

Among the several known electrochromic materials, conducting polymers have attracted particular attention due to their multichromism, good EC properties, thin film mechanical flexibility and cost effectiveness.[1-3] In fact, several works have been reported the EC behaviour of the polypyrrole,[4-6] polyaniline (PANI),[7] polythiophene[8,9] and their derivatives, as well as the fabrication of efficient complementary ECDs comprising CPs (e.g. polythiophene-derivatives@PANI[10,11] and polypyrrole@polythiophene-derivatives[12]).

Electroactive poly[M(*salen*)]-type films (M = transition metal) are a special class of CPs, formed through the oxidative polymerisation of transition metal complexes with *salen*-type ligands onto the electrode surface,[13] which exhibit poly(phenylene)-like properties, with the transition cations acting as a bridge between the phenyl rings.[14] Their potential application as EC materials has been explored by Freire's group.[15,16] The colorimetric properties of polymers based on *salen*-type complexes of Cu(II), Ni(II) and Pd(II) deposited over transparent flexible electrodes of polyethylene terephthalate coated with indium tin oxide (ITO/PET) were first studied by Pinheiro *et al.*,[15] using the CIELAB coordinates and spectroelectrochemical studies. More recently, Branco *et al.*[16] studied other series of [M(*salen*)]-derived electroactive films and selected materials were chosen to build homemade ECDs, whose preliminary performance was also assessed. The reported results addressed some promising EC properties for the poly[M(*salen*)] films in terms of colour changes and optical contrasts, but they showed moderate electrochemical stabilities which is one of the drawbacks for technological applications. Nevertheless, the results showed that the synthetic versatility of the metal *salen* complexes (by the introduction of different substituents into the *salen* skeleton or by using different metal centres) allowed fine tuning of the final EC features of the resulting polymeric systems, providing important guidelines for film molecular design optimisation.

These observations motivated more detailed studies in order to achieve other poly[M(*salen*)]-type films with improved EC performance and electrochemical stability. Consequently, in this chapter it is described the preparation and study of two novel electrochromic systems based on the electroactive polymers: poly[Ni(3-Mesalen)], poly[1] ([Ni(3-Mesalen)] = *N,N'*-bis(3-methylsalicylideneiminate) nickel(II)), and poly[Ni(3-MesaltMe)], poly[2] ([Ni(3-MesaltMe)] = *N,N'*-2,3-dimethylbutane-2,3-dyil-bis(3-methylsalicylideneiminate) nickel(II)), which differ on the absence/presence of methyl substituents in the imine bridge, respectively. The influence of two electrolyte solutions – $LiClO_4/CH_3CN$ or $LiClO_4$/PC – on the redox and optical properties of the

films was explored. The EC properties (switching times, optical contrasts and densities, colouration efficiencies and electrochemical stabilities) of both films were evaluated in full detail, and used as guidance to choose poly[1] as the polymeric film with the best EC properties for ECD fabrication with flexible substrates, using a lateral configuration with two figures of merit: simple lateral assemblage and butterfly shape. The described work corresponds to a step forward in the design of EC materials and devices fabrication based in poly[M(*salen*)] films, since poly[1] surpassed all the previous EC metallopolymers analogues and are competitive with other EC materials for application in electronic devices.

2.2 Experimental section

2.2.1 Materials and solvents

The complexes *N,N'*-bis(3-methylsalicylideneiminate) nickel(II), [Ni(3-Mesalen)], and *N,N'*-2,3-dimethylbutane-2,3-dyil-bis(3-methylsalicylideneiminate) nickel(II), [Ni(3-MesaltMe)], and respective *salen* ligands were prepared by methods described in the literature.[17] Acetonitrile and propylene carbonate (Romil, pro analysis grade), $LiClO_4$ (Aldrich, purity 99 %) and poly(methylmethacrylate) (PMMA, Aldrich) were used as received.

2.2.2 Preparation and characterisation of polymeric films

The poly[Ni(*salen*)] films were deposited potentiodynamically from corresponding monomer solutions (1.0 mmol dm^{-3} [Ni(*salen*)] in 0.1 mol dm^{-3} $LiClO_4/CH_3CN$), by cycling the potential of the working electrode (ITO/PET 3.0 cm^2) between 0.0 and 1.3 V, at the scan rate of 0.020 V s^{-1}, during 10 cycles; other conditions are specified in the corresponding text and figure legends.

After film deposition, the modified electrodes were rinsed with dry CH_3CN, immersed in monomer-free 0.1 mol dm^{-3} $LiClO_4/CH_3CN$ or $LiClO_4$/PC solutions and cycled voltammetrically in the potential ranges 0.0 – 1.3 V or 0.0 – 1.4 V, at 0.020 V s^{-1}. The electroactive surface coverage, Γ / μmol cm^{-2}, of each film was determined by a coulometric assay,[18,19] using cyclic voltammograms (CVs) obtained in monomer-free 0.1 mol dm^{-3} $LiClO_4/CH_3CN$ solution at the scan rate of v = 0.010 V s^{-1}, to ensure complete film redox conversion. The doping level (n) values used for Γ determination were calculated from comparison of coulometric data for films deposition and cycling, as described in literature,[18,19] and were found to be n = 0.69 and 0.08 for poly[1] and poly[2], respectively.

The monitoring of the redox process by *in situ* UV-Vis spectroscopy was performed with films prepared with 5 electrodeposition cycles. The films were subsequently cycled five times between -0.1 and 1.3 V, at v = 0.020 V s^{-1}, using monomer-free $LiClO_4/CH_3CN$ or $LiClO_4$/PC 0.1 mol dm^{-3} solutions. The UV-Vis spectra were acquired simultaneously at 0.5 s intervals, in the wavelength range of 315 – 1100 nm. The molar extinction coefficients, ε / cm^{-1} mol^{-1} dm^3, of all observed electronic bands were estimated using a combination of the Beer-Lambert and Faraday laws (Equation 2.1):[18-20]

$$Abs(\lambda) = \varepsilon(\lambda)\, Q / nFA \qquad (2.1)$$

where Q is the charge (C), n is the doping level, F is the Faraday constant and A the electrode area (cm^2).

Films for SEM/EDS and XPS analysis were prepared with 10 and 15 cycles and the reduced and oxidised states were achieved by the application of 0.0 or 1.3 V, during 300 s, in a monomer-free $LiClO_4/CH_3CN$ 0.1 mol dm^{-3} solution, after the electrodeposition. For poly[1] were also studied by XPS reduced and oxidised films in $LiClO_4$/PC 0.1 mol dm^{-3}.

2.2.3 Electrochromic properties evaluation

The EC properties of the films were explored by a double potential step method (chronoamperometry) coupled with UV-Vis spectroscopy (chronoabsorptometry). The studies were performed in 0.1 mol dm^{-3} $LiClO_4/CH_3CN$ or $LiClO_4$/PC solutions, considering two possible colour transitions: yellow ↔ green and green ↔ russet. In the double potential step experiment, the potential was set at the initial potential value (E = 0.0 or 0.7 V, according to the colour change) for a period of time of 50 s and was stepped to a second potential (E = 0.7, 1.3 or 1.15 V) for another period of 50 s, being after switched back to the initial potential. The simultaneous chronoabsorptometric measurements were performed at the fixed wavelengths of λ = 510 nm (green ↔ russet) and λ = 750 nm (yellow ↔ green), acquiring the UV-Vis spectra at intervals of 1 s, during 4 redox cycles. The films used in these studies were electrodeposited using 5 potentiodynamic cycles.

Electrochemical stability tests were performed by chronoamperometry, using the same experimental conditions, but over extended time intervals (400 – 9000 redox cycles, ca. 11 hours – 11 days). The films used in these studies were prepared with 10 electrodeposition cycles.

The colouration efficiency, η, and the change of the optical density, ΔOD, parameters were estimated through Equation 1.1. The switching times were determined considering 90 % of the full switch.[1,21]

2.2.4 Fabrication and characterisation of electrochromic devices

ECDs were built using as EC material poly[1] films electrodeposited on flexible substrates of ITO/PET (4.5 x 3.0 cm^2). The devices were assembled in lateral configuration, with the electrodes side-by-side, in two different typologies: typology 1, with a simple shape, and typology 2, with a butterfly shape. Both electrodes are based in the same EC material and, in case of the device of typology 2, one of the electrodes corresponds to the butterfly inside area, while the other corresponds to the butterfly outside area.

Following film deposition, the ECDs were assembled by making a cut under the film and ITO surface, in order to define the limits of each electrode and prevent electrical contact between each part. The cut is a simple vertical line in case of ECD of typology 1 and corresponds to the butterfly shape for device of typology 2. Then, a layer of a PMMA-based electrolyte was put over both electrodes.

The poly[1] films employed were electrodeposited potentiodynamically in the potential range 0.3 to 1.5 V, at ν = 0.020 V s^{-1}, for 10 cycles and with slow stirring, in the two compartment cell. The electrolyte was a semi-solid polymeric electrolyte based in PMMA, prepared by a procedure adapted from literature.[22] Briefly, a mixture of PMMA (7 %), $LiClO_4$ (3 %), CH_3CN (58 %) and PC (32 %) (% m/m) was stirred during about 20 hours, at room temperature, to yield a translucent and malleable gel.

The ECD of typology 1 was characterised by chronoamperometry, during 3000 redox cycles, applying potential pulses of 200 s, with potential alternating between -1.0 and 1.0 V (colour transition yellow ↔ green). During the first 1000 redox cycles, the experiment was monitored by UV-Vis spectroscopy (chronoabsorptometry), at $\lambda = 750$ nm. The ECD of typology 2 was also characterised by chronoamperometry, but applying potential pulses of 100 s, with potential alternating between -1.1 and -0.25 V (yellow ↔ green). Note that these potential values are, in reality, potential differences between the two electrodes; since there is no reference electrode, potential values are not directly placed on an absolute scale.

2.3 Results and discussion

2.3.1 Electrochemical preparation and characterisation of polymeric films

The voltammetric responses obtained during the electropolymerisation of both [Ni(*salen*)] complexes are depicted in Figure 2.1 and the peak potential values are summarised in Table 2.1.

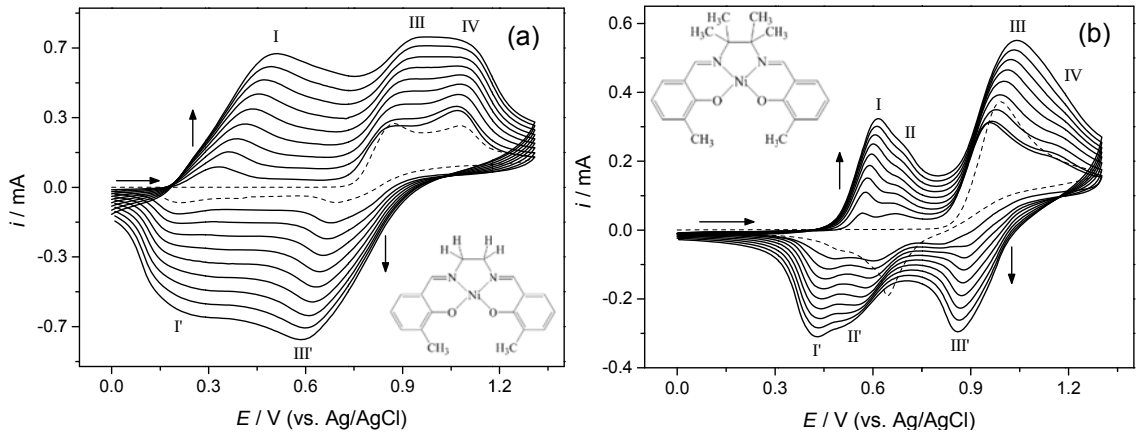

Figure 2.1 CVs of the electrodeposition of (a) [Ni(3-Mesalen)] and (b) [Ni(3-MesaltMe)] complexes, using 1.0 mmol dm^{-3} solutions of complexes in $LiClO_4/CH_3CN$ 0.1 mol dm^{-3}, at 0.020 V s^{-1} during 10 cycles. Inset: chemical structures of the respective [Ni(*salen*)] complex.

In the first anodic half-cycle, two peaks are observed at E_{pa} = 0.87 and 1.08 V and one peak at E_{pa} = 0.99 V for [Ni(3-Mesalen)] and [Ni(3-MesaltMe)] complexes, respectively, which are attributed to the oxidation of monomers, resulting in formation of oligomers/polymer in the vicinity of the working electrode surface.[18] In the reverse scan, two peaks are detected at E_{pc} = 0.69 and 0.20 V for [Ni(3-Mesalen)] and one peak at E_{pc} = 0.64 with a slight inflection at E_{pc} = 0.50 V for [Ni(3-MesaltMe)], which correspond to the reduction of film deposited in the preceding anodic scan.[23,24] In the second and subsequent voltammetric cycles, a new peak appears at $E_{pa} \approx 0.42$ V for the [Ni(3-Mesalen)] system. This is assigned to the oxidation of polymer film, deposited during the previous cycle(s).[23,24] In the case of [Ni(3-MesaltMe)], the two new peaks during the subsequent scans appear at E_{pa} = 0.59 and 0.68 V and the peak attributed to the oxidation of monomer shows now a slight inflexion at E_{pa} = 1.17 V. In cathodic scan it is possible to distinguish three peaks at E_{pc} = 0.87, 0.58 and 0.45 V.

The growth of both polymers is proved by the increasing of current intensity of the peaks corresponding to the oxidation and reduction of film in consecutive cycles, and by the visual inspection of a green film deposited on the electrode surface at the end of the process.

Table 2.1 Peak potentials in CVs during 1st and 5th scans of films electrodeposition.

Films	*E* / V (vs. Ag/AgCl)							
	Scan	E_{paI}	E_{paII}	E_{paIII}	E_{paIV}	$E_{pcI'}$	$E_{pcII'}$	$E_{pcIII'}$
poly[1]	1st	-	-	0.87	1.08	0.20	-	0.69
	5th	0.42	-	0.91	1.08	0.22	-	0.64
poly[2]	1st	-	-	0.99	-	0.50	-	0.64
	5th	0.59	0.68	0.99	1.17	0.45	0.58	0.87

The voltammetric responses of the as-prepared poly[1] and poly[2] films in the supporting electrolytes $LiClO_4/CH_3CN$ and $LiClO_4$/PC 0.1 mol dm^{-3} are depicted in Figure 2.2 and in Table 2.2 are summarised the potential peak values.

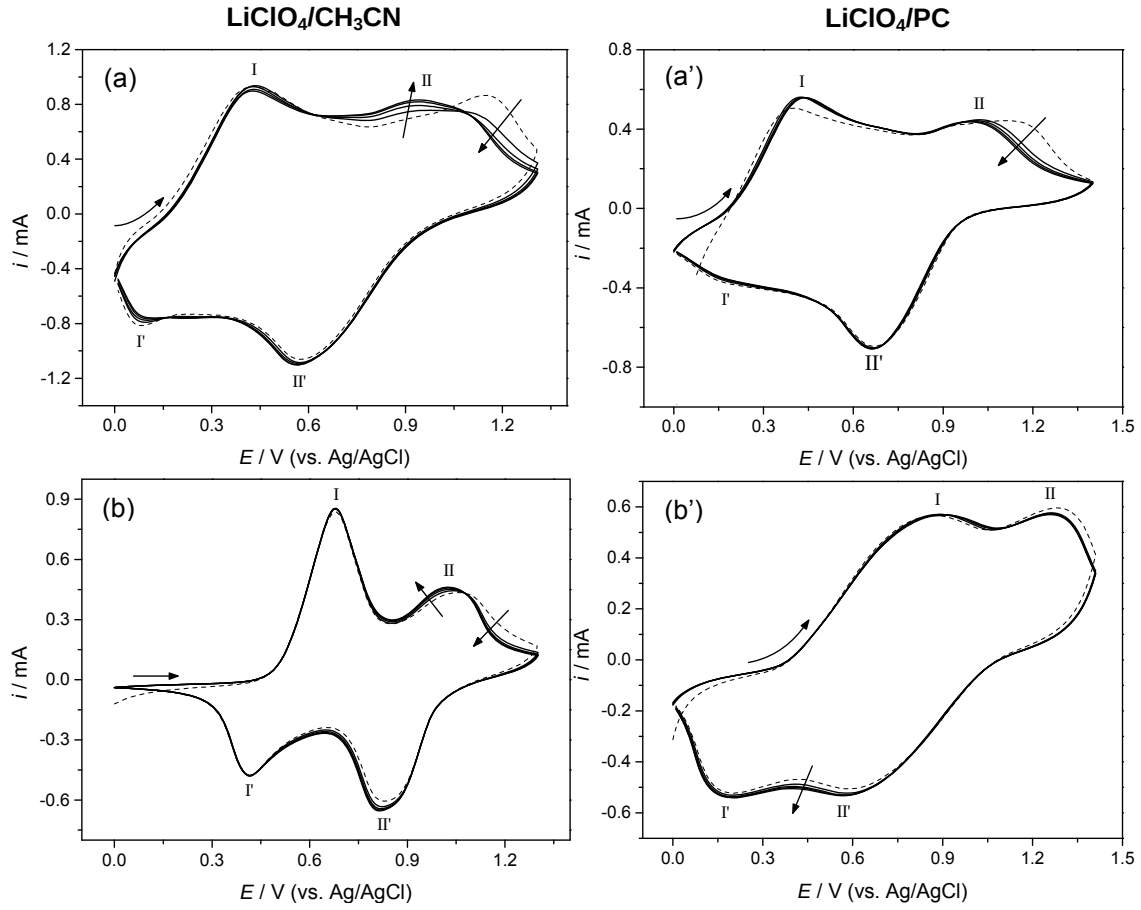

Figure 2.2 Voltammetric responses of (a and a') poly[1] (Γ= 0.31 μmol cm^{-2}) and (b and b') poly[2] (Γ= 1.13 μmol cm^{-2}) films in $LiClO_4/CH_3CN$ and $LiClO_4$/PC 0.1 mol dm^{-3} electrolytes, acquired at 0.020 V s^{-1}.

It is possible to identify two anodic peaks at E_{pa} = 0.39-0.88 V and E_{pa} = 0.94-1.29 V and two cathodic peaks at E_{pc} = 0.17-0.41 V and E_{pc} = 0.56-0.83 V. The results

revealed that poly[1] film showed similar redox profiles either in $LiClO_4/CH_3CN$ or $LiClO_4$/PC electrolytes. In contrast, electrochemical responses of poly[2] obtained in $LiClO_4$/PC present greater peak separation (anodic peaks at more positive potentials and the cathodic peaks at less positive potentials) than those obtained in $LiClO_4/CH_3CN$. In general, the voltammetric responses of polymeric films stabilised after 5 scans, which correspond to the typical "film conditioning".[23,25]

Table 2.2 Peak potentials in CVs during 1st and 5th scans of films redox switching.

Films	Supporting electrolyte	*E* / V (vs. Ag/AgCl)				
		Scan	E_{paI}	E_{paII}	$E_{pcI'}$	$E_{pcII'}$
poly[1]	$LiClO_4/CH_3CN$	1st	0.42	1.16	0.18	0.58
		5th	0.42	0.94	0.17	0.56
	$LiClO_4$/PC	1st	0.39	1.16	0.20	0.66
		5th	0.43	1.00	0.20	0.66
poly[2]	$LiClO_4/CH_3CN$	1st	0.68	1.07	0.41	0.83
		5th	0.68	1.03	0.41	0.81
	$LiClO_4$/PC	1st	0.87	1.29	0.19	0.58
		5th	0.88	1.27	0.19	0.56

The coulometric data revealed Γ = 0.31 and 1.13 μmol cm^{-2} for poly[1] and poly[2], respectively, suggesting greater polymerisation efficiency for poly[2].

2.3.2 Composition and morphology

Surface analysis of poly[Ni(*salen*)] films in reduced and oxidised states (at *E* = 0.0 V and *E* = 1.3 V) was performed by XPS. Surface atomic percentages and atomic ratios are summarised in Table 2.3 for poly[1] in $LiClO_4/CH_3CN$ and $LiClO_4$/PC and for poly[2] in $LiClO_4/CH_3CN$.

For the reduced films in $LiClO_4/CH_3CN$, the XPS-derived atom ratios N/Ni and O/Ni are slightly higher than those expected, based on the Ni:*salen* stoichiometric ratio, N/Ni = O/Ni = 2. Combined with the appearance of Cl, this indicates the presence of ClO_4^- and/or CH_3CN at low levels, as result of the supporting electrolyte trapping in the polymeric matrix during the deposition or cycling processes.[18]

Table 2.3 XPS results for poly[1] and poly[2]: surface atomic percentages and atomic ratios for reduced and oxidised polymeric films in $LiClO_4/CH_3CN$ and $LiClO_4/PC$ (only for poly[1]) 0.1 mol dm^{-3}.

Films		Atomic %					Atomic Ratios		
		Ni	C	N	O	Cl	N/Ni	O/Ni	Cl/Ni
poly[1]	**$LiClO_4/CH_3CN$**								
	Reduced state	3.31	78.60	7.89	10.03	0.16	2.38	3.03	0.05
	Oxidised state	1.76	60.52	6.06	26.33	5.32	3.44	14.96	3.02
	$LiClO_4/PC$								
	Reduced state	2.87	76.41	6.93	12.66	0.87	2.41	4.41	0.30
	Oxidised state	2.51	71.31	6.55	17.39	2.23	2.61	6.93	0.89
poly[2]	**$LiClO_4/CH_3CN$**								
	Reduced state	2.55	76.69	6.13	12.26	0.81	2.40	4.81	0.32
	Oxidised state	1.89	65.98	5.78	22.76	3.28	3.06	12.04	1.74

In comparison, the oxidised films showed higher N/Ni, O/Ni and Cl/Ni atomic ratios. This significant increase, mainly for O/Ni and Cl/Ni ratios, is explained by the presence of CH_3CN and ClO_4^- inside the film as a consequence of charge compensation/solvation during the film oxidation, as observed previously for similar systems[18] (deconvoluted XPS spectra in O1s region for reduced and oxidised poly[1] in Figure 2.3). This assumption is supported by the observation of Cl/O ratio increase in a proportion of ca. 1:4 from the reduced to the oxidised films (in agreement with ClO_4^- composition). For $LiClO_4/PC$, both films showed similar atomic ratio changes on going from reduced to oxidised film states, which can be interpreted as before. It should be mention that the XPS results refer to typically 4-5 nm from the total film thickness.

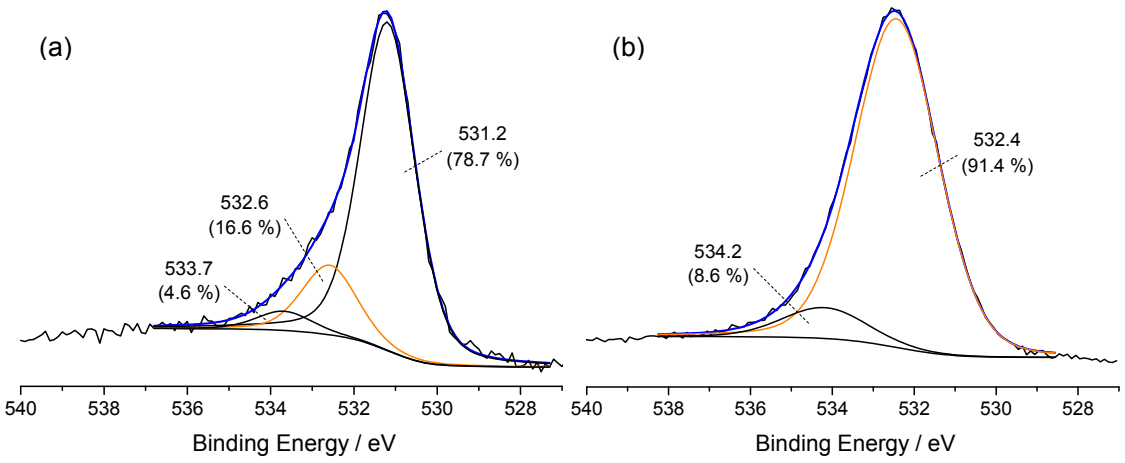

Figure 2.3 High-resolution XPS spectra in O1s region of poly[1] film in (a) reduced and (b) oxidised states in $LiClO_4/CH_3CN$, with respective deconvolutions; — peak assigned to ClO_4^-.

In Figure 2.4 are depicted SEM micrographs and EDS spectra for poly[1] films in reduced and oxidised states; SEM images of the surface of poly[2] films (not shown) revealed a similar morphology.

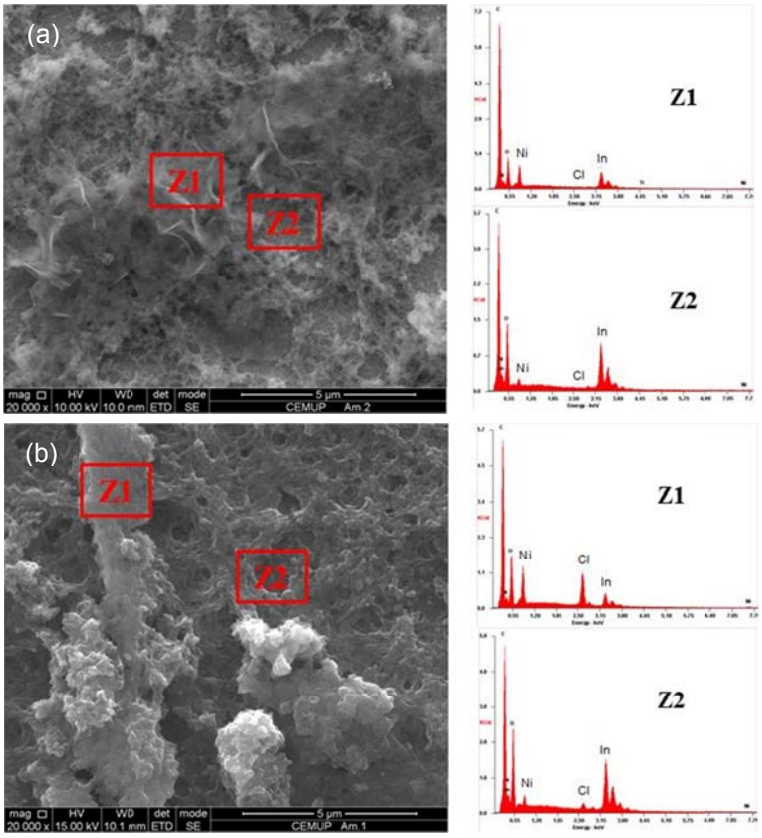

Figure 2.4 SEM micrographs and respective EDS spectra at selected zones for poly[1] films in (a) reduced and (b) oxidised states, with a magnification of 20 000 times.

The films consisted of a continuous layer (Z2), on top of which there are irregular fragments of higher dimensions (Z1). The EDS spectra showed that, in the Z1 regions, the Ni element (from polymeric film) is present in higher quantity than In (from substrate), while, in Z2 regions, the In content increases considerably in comparison to Ni. These results indicate that the film surface and thickness are not uniform. The EDS spectra revealed yet a higher Cl content in oxidised film (in agreement with XPS results) and the respective micrograph showed a bulkier film, possibly due to the ingress of supporting electrolyte into the polymeric matrix.

2.3.3 *In situ* UV-Vis spectroscopy

In Figure 2.5 (a) and (b) are depicted the absolute UV-Vis spectra acquired during the oxidation of poly[1] in $LiClO_4/CH_3CN$ and $LiClO_4$/PC 0.1 mol dm^{-3}, respectively; the equivalent spectra for poly[2] are depicted in Figure 2.6 (a) and (b). The spectra obtained during films reduction showed an inverse behaviour and were omitted for simplicity.

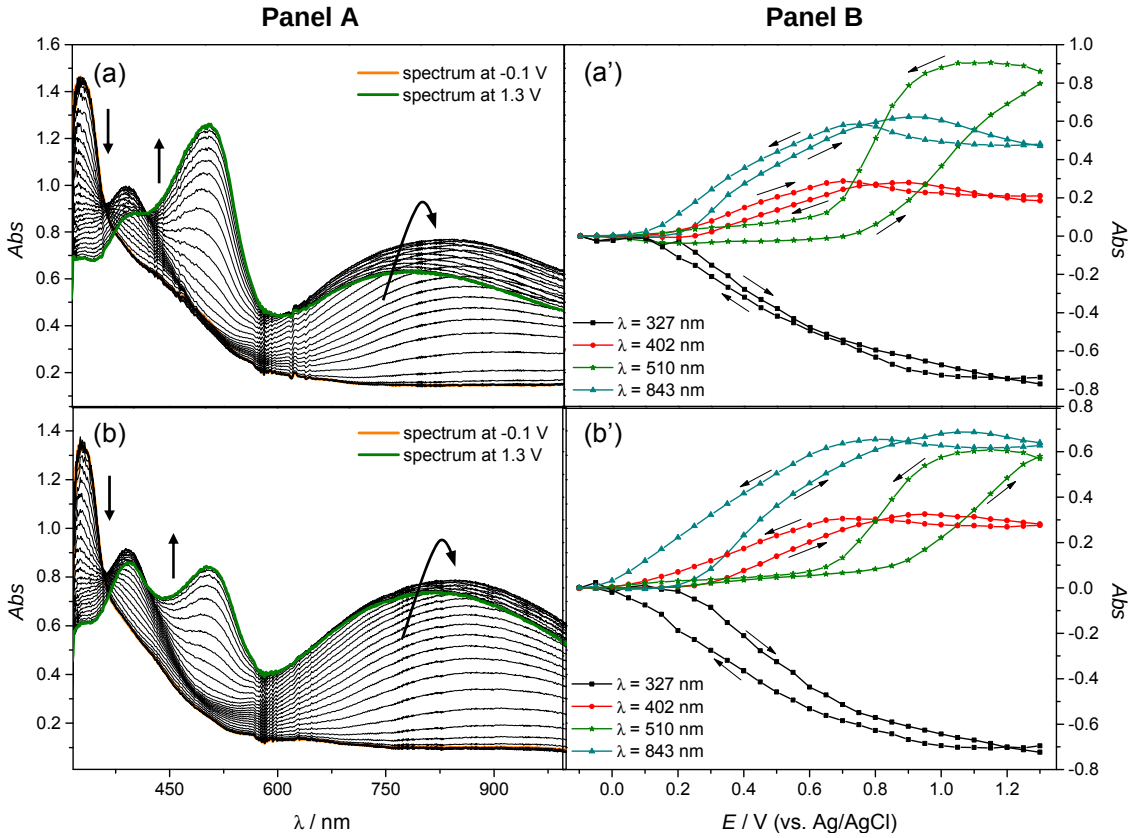

Figure 2.5 Panel A: Absolute UV-Vis spectra of poly[1] (Γ = 0.16 μmol cm^{-2}) acquired during film oxidation in 0.1 mol dm^{-3} (a) $LiClO_4/CH_3CN$ and (b) $LiClO_4$/PC (referenced to the respective electrolyte spectrum). Panel B: *Abs* vs. *E* plots for the electronic bands identified in absolute UV-Vis spectra, referenced to the spectra at *E* = -0.1 V (arrows indicate scan direction).

The poly[1] spectra show four bands in both electrolytes. For poly[2], four electronic bands are observed in $LiClO_4/CH_3CN$, whereas in $LiClO_4$/PC five bands are observed. The bands show different dependences on applied potential and, so, their intricate behaviours are most readily appreciated by depicting the differential spectra, using the responses at selected potentials as reference points, Figures 2.7 and 2.8 for poly[1] and poly[2], respectively.

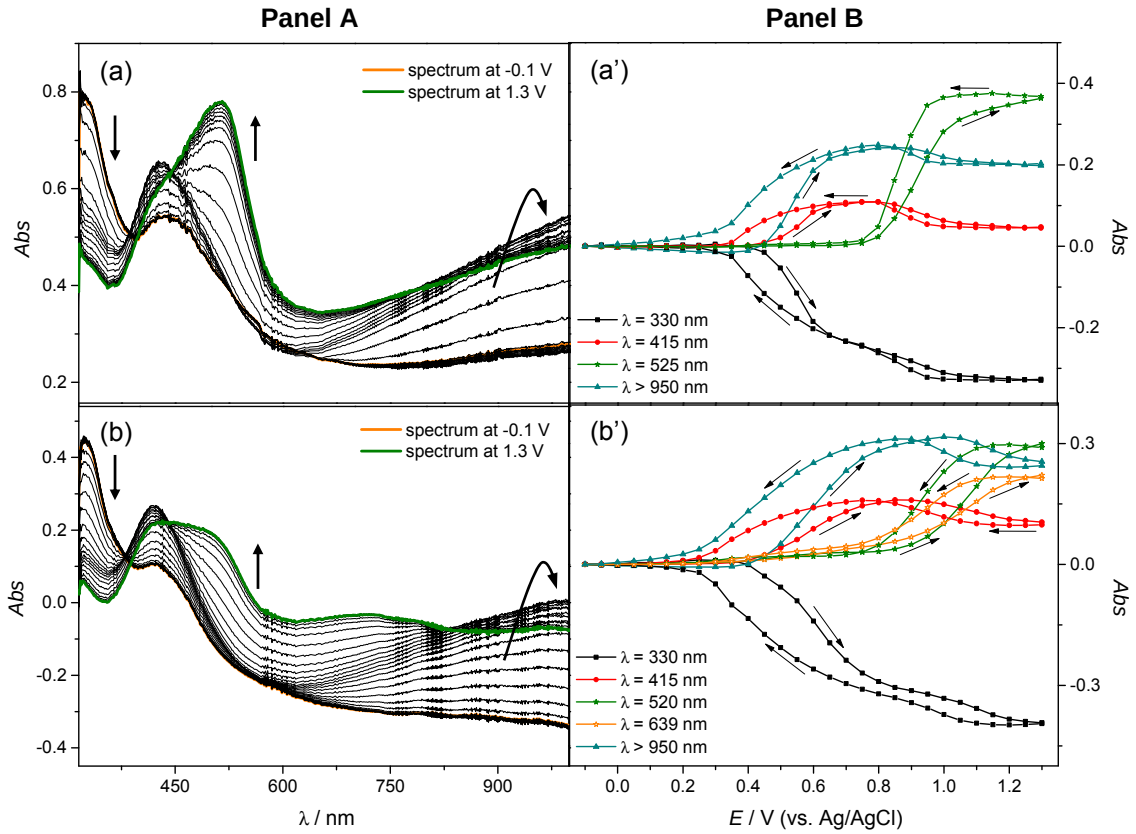

Figure 2.6 Panel A: Absolute UV-Vis spectra of poly[2] (Γ = 0.84 μmol cm^{-2}) acquired during film oxidation in 0.1 mol dm^{-3} (a) $LiClO_4/CH_3CN$ and (b) $LiClO_4$/PC (referenced to the respective electrolyte spectrum). Panel B: *Abs* vs. *E* plots for the electronic bands identified in absolute UV-Vis spectra, referenced to the spectra at *E* = -0.1 V (arrows indicate scan direction).

The absorbance vs. potential profiles (*Abs* vs. *E*) for wavelengths of detected bands (Figure 2.5 (a') and (b') and Figure 2.6 (a') and (b')), allowed the identification of three main band profiles with increasing potential in both electrolytes: (i) bands at λ = 327 and 330 nm for poly[1] and poly[2], respectively, showed a monotonically intensity decrease during the positive half cycle, (ii) bands in the range λ = 402-415 nm and λ = 843->950 nm showed intensity increase until *E* = 0.8-0.9 V and thereafter decreased until the end of the positive half cycle, and (iii) bands in the range λ = 510-525 nm for poly [1] and poly[2] and at λ = 639 nm (poly[2] in $LiClO_4$/PC), showed monotonically intensity increase from *E* = 0.8-0.9 V until the end of the positive half scan. Curiously, the maximum intensity of the electronic bands at λ = 510 nm for poly[1] and at λ = 520 / 525 nm for poly[2], is significantly lower in $LiClO_4$/PC than in $LiClO_4/CH_3CN$.

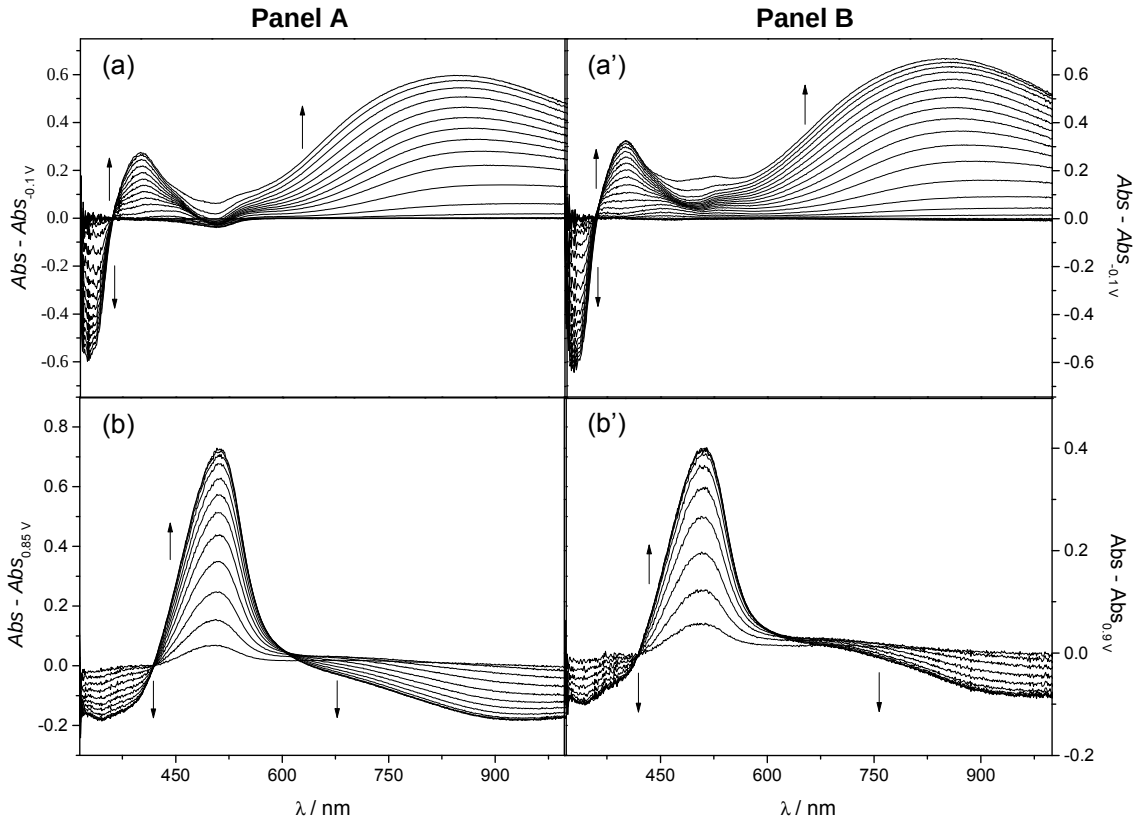

Figure 2.7 UV-Vis spectra of poly[1] (Γ = 0.16 μmol cm^{-2}) acquired during film oxidation in $LiClO_4/CH_3CN$ (Panel A) and $LiClO_4$/PC (Panel B) from (a) -0.1 to 0.85 V and referenced to the spectrum of neutral polymer, (b) 0.85 to 1.3 V and referenced to the spectrum of polymer at E = 0.85 V, (a') -0.1 to 0.9 V and referenced to the spectrum of neutral polymer and (b') 0.9 to 1.3 V and referenced to the spectrum of polymer at E = 0.9 V.

Table 2.4 summarises data for the observed electronic bands for both polymers in the two electrolytes: λ_{max} (nm), energy (eV) and molar extinction coefficients, ε, (estimated from Equation 2.1, through the slopes of *Abs* vs. Q plots, Figure 2.9).

Both polymers showed similar energy values for all the electronic bands as a consequence of their similar monomer structures; furthermore, the electronic band energies for each polymer film are also similar in the two electrolytes, indicating that the polymer structures are comparable in both electrolytes.

The results also revealed that, for each film, all the electronic bands have similar ε-values in $LiClO_4/CH_3CN$ and $LiClO_4$/PC electrolytes, with the exception of the band at λ = 510 nm for poly[1] and λ = 520 / 525 nm for poly[2], which ε-values are lower in $LiClO_4$/PC than in $LiClO_4/CH_3CN$ (for poly[1], the ε-value decreased from 19.7 x 10^3 to 13.6 x 10^3 cm^{-1} mol^{-1} dm^3).

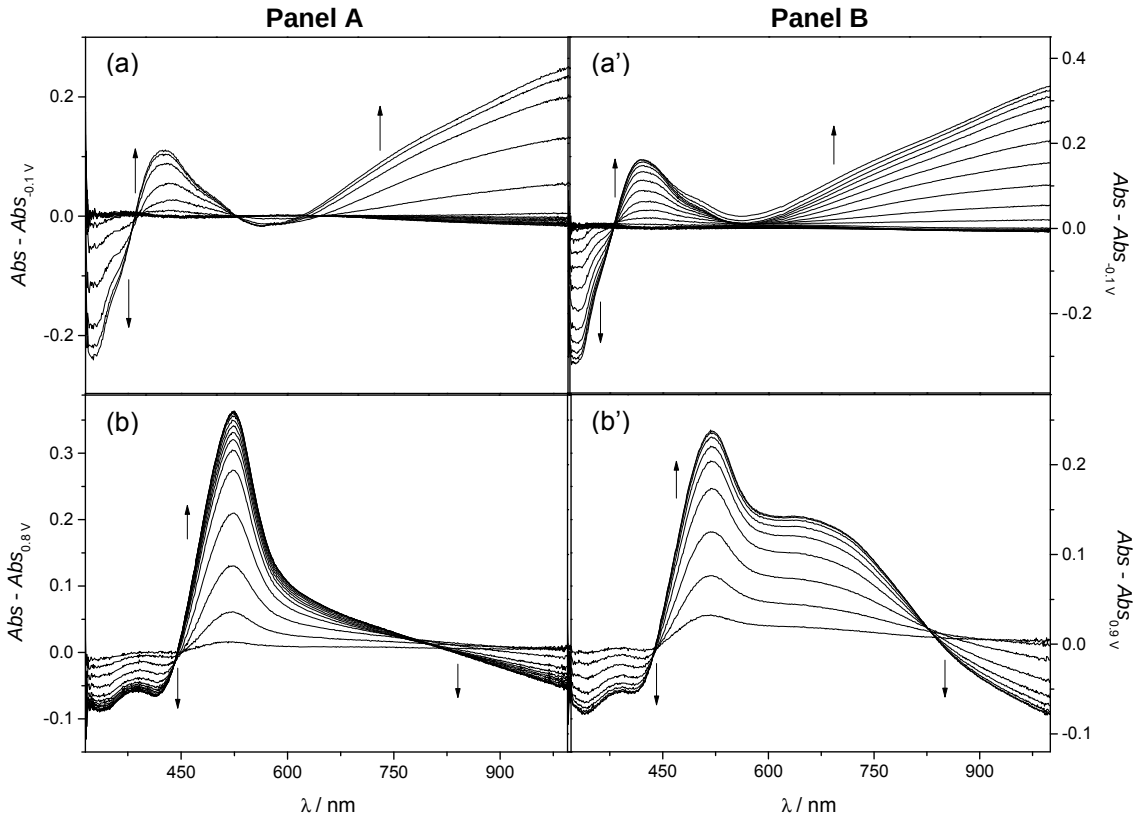

Figure 2.8 UV-Vis spectra of poly[2] (Γ = 0.84 μmol cm^{-2}) acquired during film oxidation in $LiClO_4/CH_3CN$ (Panel A) and $LiClO_4$/PC (Panel B) from (a) -0.1 to 0.8 V and referenced to the spectrum of neutral polymer, (b) 0.8 to 1.3 V and referenced to the spectrum of polymer at *E* = 0.8 V, (a') -0.1 to 0.9 V and referenced to the spectrum of neutral polymer and (b') 0.9 to 1.3 V and referenced to the spectrum of polymer at *E* = 0.9 V.

For both polymers, all the electronic bands ε-values are typical of electronic transitions between states with large contribution from ligand orbitals, which is consistent with the assertion of ligand-based film oxidation.[18,19,26] Consequently, the electronic bands can be assigned according to the polaronic model.[18,19] The electronic bands with the same *Abs* vs. *E* (or *Q*) profiles can be associated with the same charge carriers, whereby the following band assignment is proposed: (i) the electronic bands at λ = 327 / 330 nm (3.79 eV and 3.76 eV) are assigned to the intervalence band (band gap), since they represent the largest energy transition and decrease in intensity upon polymer oxidation; (ii) the bands at λ = 402 / 415 nm (3.09 eV and 2.99 eV) are attributed to the transition between the valence band and the antibonding polaron level and (iii) the bands at λ = 843 nm and λ > 950 nm (1.47 and 1.31 eV) are ascribed to the transition from the bonding to the antibonding polaron levels (or from the valence band to the bonding polaron level). The other band predicted by the polaronic model was estimated to be at λ = 766 and λ = 738 nm (1.62 and 1.68 eV) for poly[1] and

poly[2], respectively; these would most likely be overlapped with the bands at λ = 843 and λ > 950 nm and thus not separately observed.

Table 2.4 Electronic bands and respective molar extinction coefficients (ε) for poly[1] and poly[2] in $LiClO_4/CH_3CN$ and $LiClO_4/PC$.

Film	Supporting Electrolyte	λ_{max} / nm (eV)	ε x 10^{-3} / mol^{-1} dm^3 cm^{-1}
poly[1]	$LiClO_4/CH_3CN$	327 (3.79)	4.99
		402 (3.09)	3.06
		510 (2.43)	19.66
		843 (1.47)	5.21
	$LiClO_4/PC$	327 (3.79)	5.90
		402 (3.09)	3.12
		510 (2.43)	13.64
		843 (1.47)	6.72
poly[2]	$LiClO_4/CH_3CN$	330 (3.76)	0.76
		415 (2.99)	0.42
		525 (2.36)	4.22
		> 950 (1.31)	0.68
	$LiClO_4/PC$	330 (3.76)	0.60
		415 (2.99)	0.31
		520 (2.39)	1.37
		639 (1.94)	0.64
		> 950 (1.31)	0.54

Lastly, the very intense bands at λ = 510 nm (2.43 eV), λ = 520 / 525 nm (2.39 / 2.36 eV) and λ = 639 nm (1.94 eV) (for poly[2] in $LiClO_4/PC$) showed different *Abs* vs. *E* profiles and consequently cannot be assigned to the same charge carriers and explained by the polaronic model. Since they start to increase at high oxidation potentials and their ε-values depend on the solvent (CH_3CN vs. PC), unlike the other observed electronic transitions, they are assigned to charge transfer transitions between the metal and the oxidised ligand.[18,19]

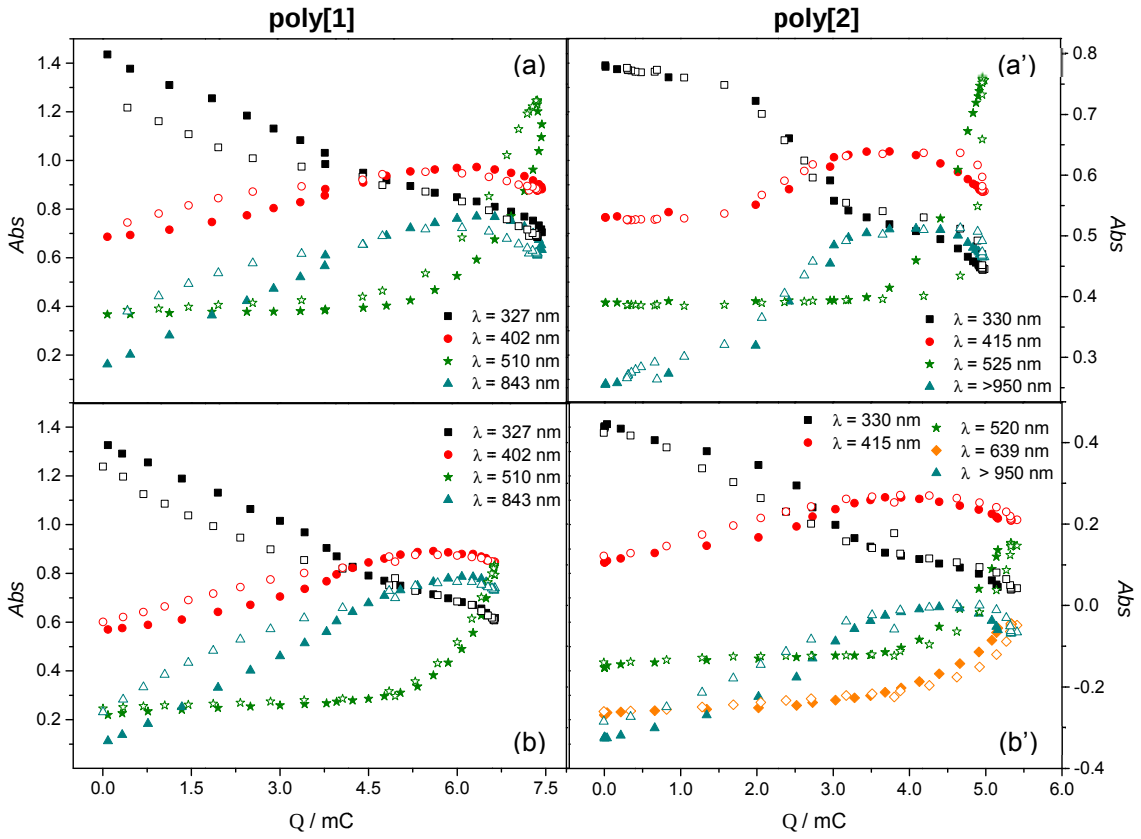

Figure 2.9 Plots of the *Abs* vs. *Q* for selected electronic bands of poly[1] and poly[2] in (a and a') $LiClO_4/CH_3CN$ and (b and b') $LiClO_4$/PC; filled forms correspond to the anodic scan and open forms to the cathodic scan.

2.3.4 Electrochromic properties

The visual inspection of both poly[Ni(*salen*)] films during redox cycling allowed the observation of their colour changes. Figure 2.10 shows photographic images of the film distinct colours as a function of the potential: in the reduced state (E = 0.0 V) the films are yellow, switch to green at E = 0.7 V, and then to russet (reddish-brown) at E = 1.3 V.

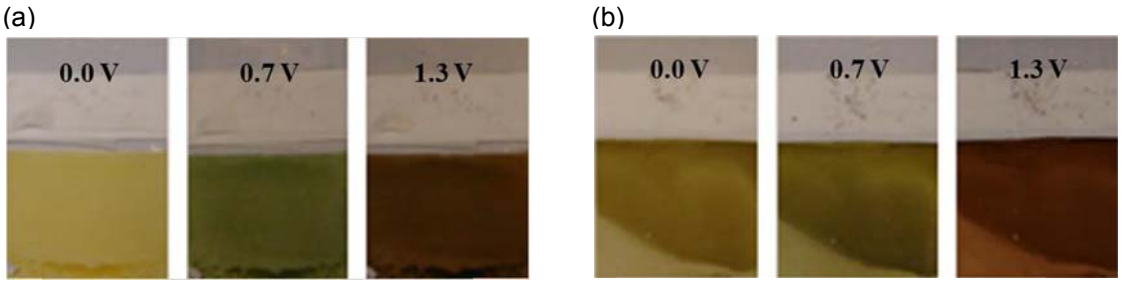

Figure 2.10 Photographs of (a) poly[1] and (b) poly[2] films in different oxidation states (E = 0.0, 0.7 and 1.3 V vs. Ag/AgCl (NaCl / 1.0 mol.dm^{-3})) in $LiClO_4/CH_3CN$ electrolyte.

To explore the potential application of both films as EC materials, a square-wave potential step method coupled with UV-Vis spectroscopy, was used to evaluate their EC properties: switching times, optical contrasts, changes of the optical densities and colouration efficiencies. In Figure 2.11 are depicted the chronoabsorptograms obtained for poly[1] films (Γ = 0.16 μmol cm^{-2}) in $LiClO_4/CH_3CN$ and $LiClO_4$/PC, for two colour changes - yellow ↔ green (λ = 750 nm) and green ↔ russet (λ = 510 nm). The results obtained for poly[2] (Γ = 0.84 μmol cm^{-2}) in a similar study are depicted in Figure 2.12 and, in Figure 2.13, are depicted the UV-Vis spectra for the two films in each colour and in both supporting electrolytes, with identification of the considered wavelengths.

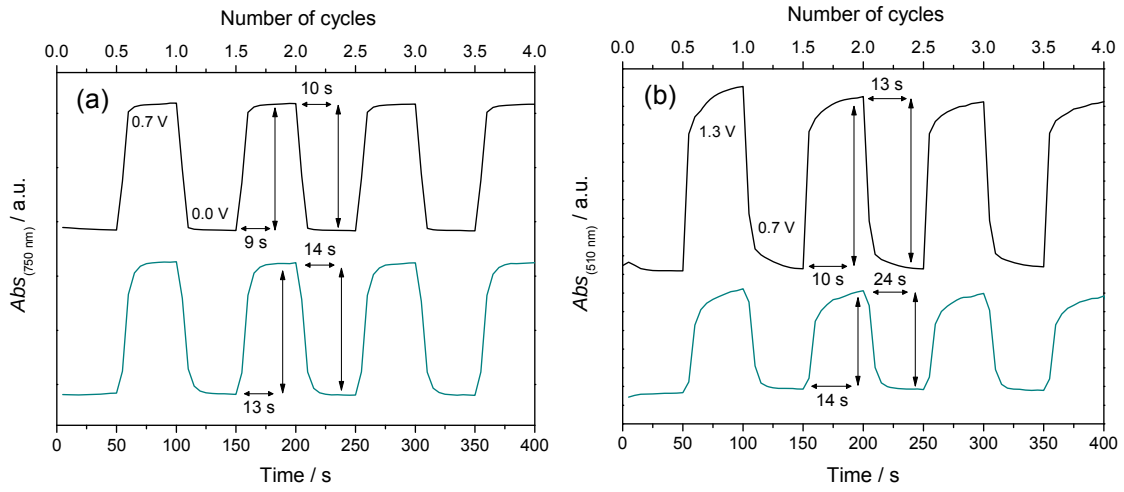

Figure 2.11 Chronoabsorptograms of poly[1] films in $LiClO_4/CH_3CN$ (—) and $LiClO_4$/PC (—), for the colour transitions (a) yellow ↔ green (λ = 750 nm) and (b) green ↔ russet (λ = 510 nm), with indication of the estimated switching times.

The switching time values obtained in $LiClO_4/CH_3CN$ are between τ = 9 - 10 s for the yellow ↔ green transition and τ = 8 - 13 s for the green ↔ russet transition. In $LiClO_4$/PC, the switching time values ranging between τ = 13 - 15 s for the yellow ↔ green transition and τ = 9 - 24 s for the green ↔ russet, being clearly higher than those determined in $LiClO_4/CH_3CN$. This observation is associated with the solvent PC, and maybe related with lower degree of PC film solvation that may hamper ClO_4^- counter-ions ingress, necessary to the charge balance during redox switching. This assumption is in agreement with the XPS results (Table 2.3), which revealed a larger increase in O/Ni (and N/Ni) ratio, from reduced to oxidised state, in $LiClO_4/CH_3CN$ (increase of 79.7 %) than in $LiClO_4$/PC (increase of 36.4 %). Furthermore, independently of the supporting electrolyte employed, the colour transition yellow ↔ green is the fastest for poly[1], while for poly[2] is the green ↔ russet transition.

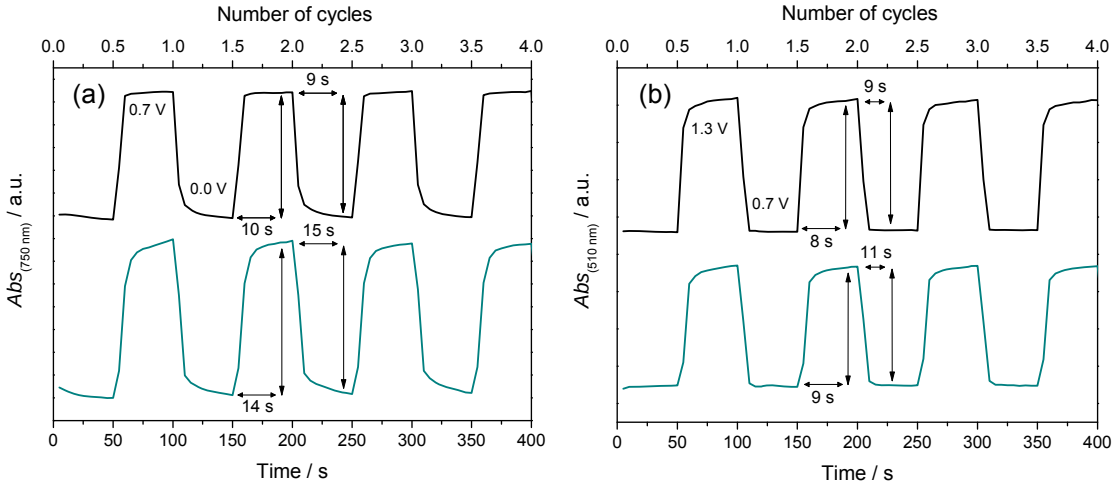

Figure 2.12 Chronoabsorptograms of poly[2] films in $LiClO_4/CH_3CN$ (—) and $LiClO_4$/PC (—), for the colour transitions (a) yellow ↔ green (λ = 750 nm) and (b) green ↔ russet (λ = 510 nm), with indication of the estimated switching times.

The switching time values suggested that these films are especially useful for applications in which the demand for rapid switching is smaller, as in slow-acting electronic devices, such as smart cards or labels.[27]

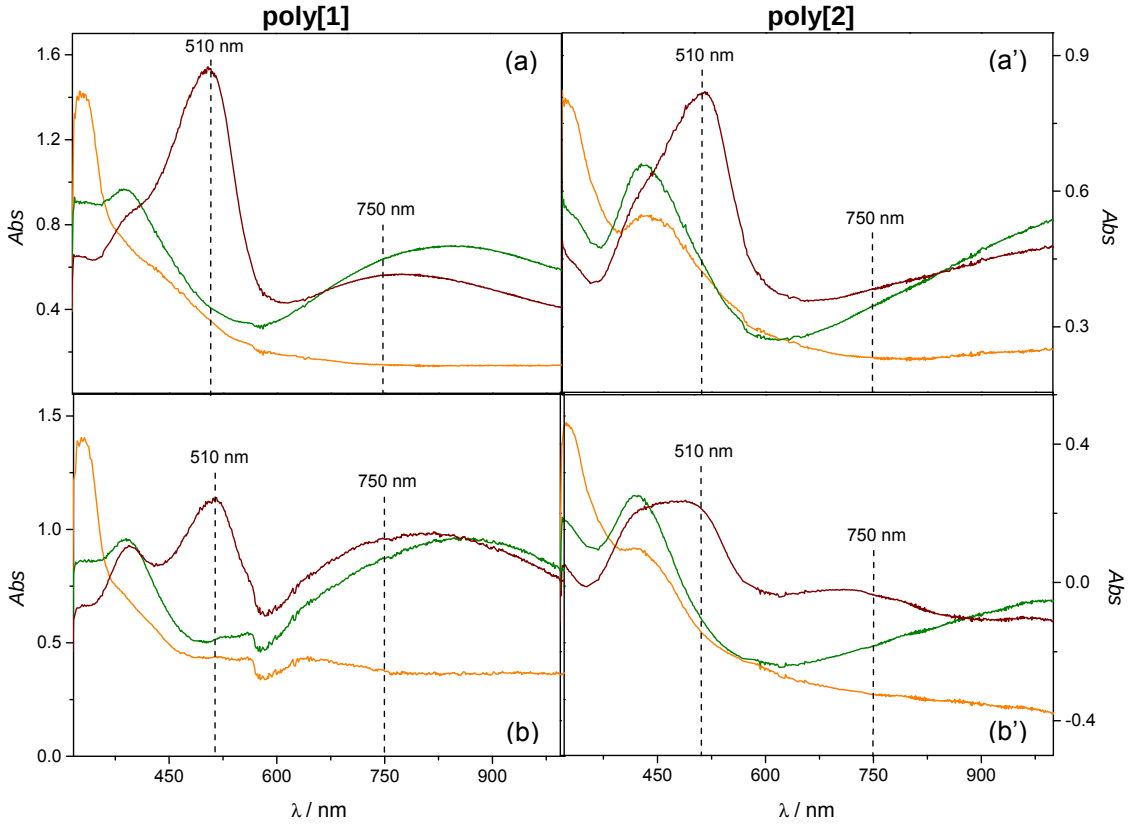

Figure 2.13 UV-Vis spectra of poly[1] and poly[2] films in (a and a') $LiClO_4/CH_3CN$ and (b and b') $LiClO_4$/PC in different oxidation states, corresponding to the colours yellow (E = 0.0 V,—), green (E = 0.7 V,—) and russet (E = 1.3 V, —). The spectra were acquired after applying the indicated potential values during 50 s.

As a complementary result, in Figure 2.14 are depicted, as example, the chronoamperograms/chronocoulograms obtained simultaneously with the chronoabsorptograms for the colour transition yellow ↔ green of poly[1] film in $LiClO_4$/PC. It is possible to see that the switching time values estimated from current intensity and charge are similar to the values determined from absorbance. In fact, from the results, it is seen that the absorbance variation with the redox switching is reflected in the chronoamperograms by a current decay as the potential become constant (indicating that at each time a portion of the film is undergoing a redox process);[1] the charge represents the same information in integrated form. The strong couple between these parameters highlights the possibility of the use of the current intensity / charge profiles as accurate parameters to evaluate the switching times of these polymeric films.

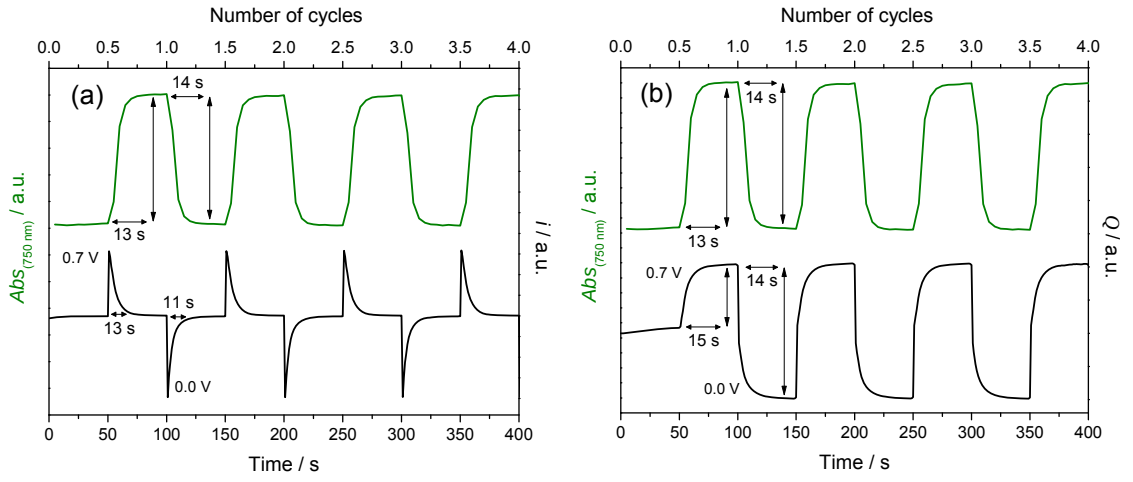

Figure 2.14 Chronoabsorptograms and (a) chronoamperograms or (b) chronocoulograms obtained in simultaneous for poly[1] films in $LiClO_4$/PC, considering the colour transition yellow ↔ green (λ = 750 nm); in chronoamperometric study were applied two potential pulses of 50 s by redox cycle, with potential alternating between 0.0 and 0.7 V.

In Table 2.5 are summarised the optical contrasts, changes of the optical density, charges requirements and colouration efficiencies values, determined for the two films colour changes in both electrolytes. The optical contrast, defined as the transmittance difference, ΔT %, between the reduced and the oxidised states, was measured from the chronoabsorptograms, considering the full optical change. For poly[1] film in $LiClO_4/CH_3CN$, the optical contrast for the colour transition yellow ↔ green is higher than for the green ↔ russet transition (ΔT = 44.9 % vs. 32.7 %). In $LiClO_4$/PC, the optical contrasts decrease for both colour changes (ΔT = 26.2 % and 18.3 %, respectively). The poly[2] film has an opposite behaviour: the colour transition green ↔

russet has a higher contrast than the yellow ↔ green transition (ΔT = 19.4 % vs. 13.0 %), being that in $LiClO_4$/PC the contrasts are enhanced (for ΔT = 58.5 % and 51.2 %). The measured optical contrasts are in accordance with colours difference observed in photographs of Figure 2.10.

Table 2.5 EC parameters for poly[1] and poly[2] films in $LiClO_4/CH_3CN$ and $LiClO_4$/PC: optical contrasts (ΔT %), changes of the optical density (ΔOD), charge requirements (Q_d), and colouration efficiencies (η).

Film	Supporting Electrolyte	Colour transition	ΔT %	ΔOD	Q_d / mC cm^{-2}	η / cm^2 C^{-1}
poly[1]	$LiClO_4/CH_3CN$	yellow ↔ green	44.9	0.47	5.62	83.18
		green ↔ russet	32.7	0.92	6.05	152.04
	$LiClO_4$/PC	yellow ↔ green	26.2	0.49	6.46	75.55
		green ↔ russet	18.3	0.53	4.92	107.36
poly[2]	$LiClO_4/CH_3CN$	yellow ↔ green	13.0	0.11	2.99	36.94
		green ↔ russet	19.4	0.36	2.42	146.86
	$LiClO_4$/PC	yellow ↔ green	51.2	0.13	4.02	33.14
		green ↔ russet	58.5	0.32	3.80	84.12

For both polymeric films, the ΔOD values for the yellow ↔ green colour transition are very similar in $LiClO_4/CH_3CN$ and $LiClO_4$/PC. For the green ↔ russet transitions, on the other hand, the ΔOD are significantly lower in $LiClO_4$/PC (for poly[1], ΔOD = 0.92 in $LiClO_4/CH_3CN$ and ΔOD = 0.53 in $LiClO_4$/PC). These results reflect the behaviour of the obtained UV-Vis spectra represented in Figures 2.5 and 2.6. The smaller ΔOD values in $LiClO_4$/PC are in accordance with the decrease of the intensity of the bands at λ = 510 – 525 from the $LiClO_4/CH_3CN$ to the $LiClO_4$/PC electrolyte (as discussed in section 2.3.3), providing an indication that the green ↔ russet colour change is mainly associated with the appearance of the bands at λ = 510 - 525 nm, attributed to CT transitions. For the remaining UV-Vis bands, no significant differences were observed for behaviour in the two supporting electrolytes, consistent with the similar ΔOD values for the yellow ↔ green colour change.

The power efficiency of the EC films was measured through the colouration efficiency, η, considering the Q_d values obtained from the chronocoulograms, as the represented in Figure 2.14 (b) for poly[1] in $LiClO_4$/PC. The η values measured are in range 33.14 – 83.18 cm^2 C^{-1} for the colour transition yellow ↔ green and 84.12 – 152.04 cm^2 C^{-1} for the green ↔ russet transition. The higher values for the green ↔ russet transition can be explained by the induced higher ΔOD, with similar or even

lower charge requirements. Furthermore, for a same colour change, the films presented smaller η values in $LiClO_4$/PC electrolyte. Comparing both films, poly[1] showed better colouration efficiency. However, it is important to note that Equation 1.1 is typically used for the characterisation of bleached to coloured switching materials, because transitions with significant overlap in the visible region, like is the case of these films, tend to lower the η values, although can reflect into modest optical changes.[27]

The electrochemical stability of poly[Ni(*salen*)] films was evaluated by chronoamperometric observations, investigating the influence of the supporting electrolyte - $LiClO_4/CH_3CN$ or $LiClO_4$/PC – on the cycle life of yellow ↔ green and green ↔ russet colour transitions. The obtained chronoamperograms are depicted in Figure 2.15 for poly[1] and in Figure 2.16 for poly[2]; in the figures are indicated the percentage of charge loss at the number of redox cycles after which no further colour change was observable.

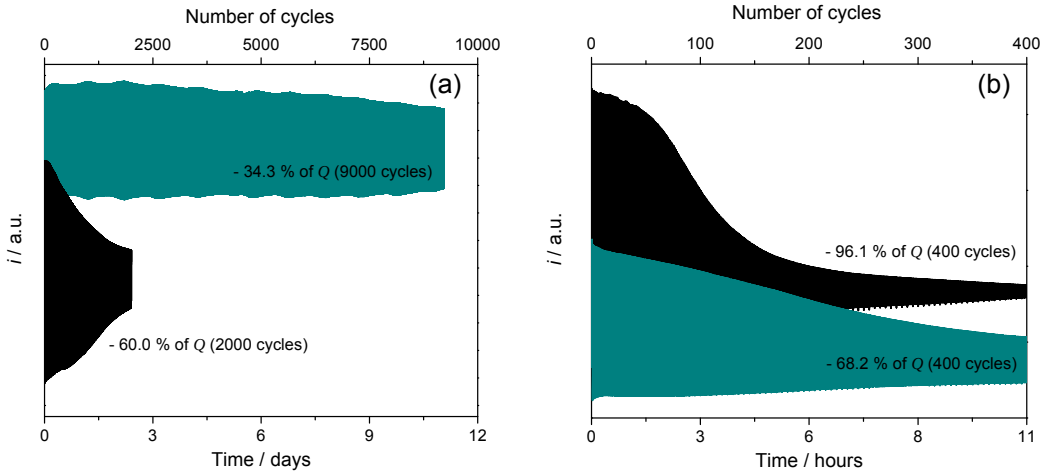

Figure 2.15 Chronoamperograms of poly[1] films in $LiClO_4/CH_3CN$ (—) and $LiClO_4$/PC (—) for the colour changes (a) yellow ↔ green and (b) green ↔ russet, applying two potential pulses of 50 s by redox cycle, with potential alternating between (a) 0.0 - 0.7 V and (b) 0.7 – 1.3 V.

Independently of the colour change, both polymeric films showed greater electrochemical stability in $LiClO_4$/PC than in $LiClO_4/CH_3CN$. The best stability was obtained for poly[1] film in $LiClO_4$/PC that changed of colour between yellow and green during around 9000 redox cycles with a charge loss of 34.3 %. The same film, in $LiClO_4/CH_3CN$, showed colour change only during around 2000 redox cycles, with a charge loss of 60.0 %. The green ↔ russet colour transition was less stable: after 400

redox cycles poly[1] showed a loss in charge of 96.1 % in $LiClO_4/CH_3CN$ and 68.2 % in $LiClO_4$/PC.

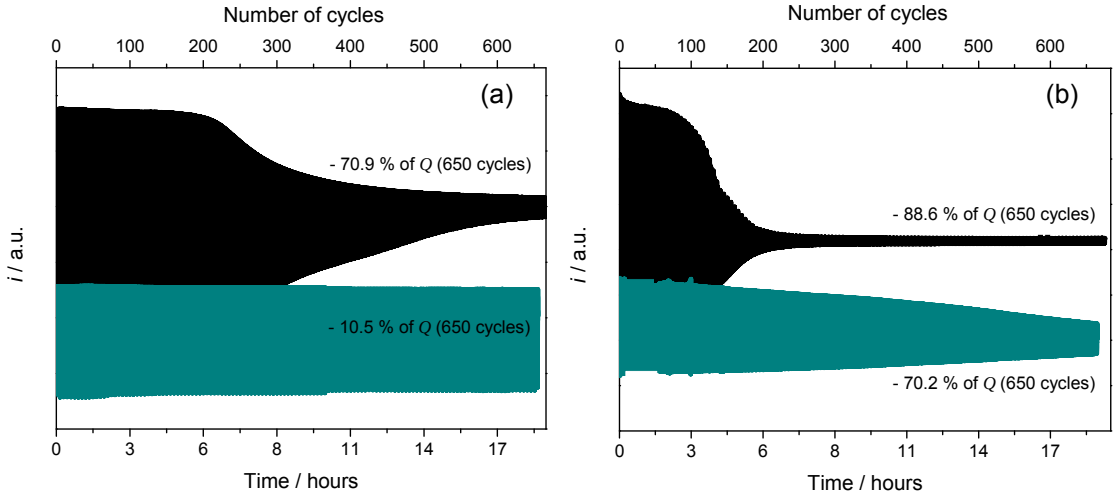

Figure 2.16 Chronoamperograms of poly[2] films in $LiClO_4/CH_3CN$ (—) and $LiClO_4$/PC (—) for the colour changes (a) yellow-green and (b) green-russet, applying two potential pulses of 50 s by redox cycle, with potential alternating between (a) 0.0 - 0.7 V and (b) 0.7 – 1.15 V.

Moreover, for the yellow ↔ green change, poly[2] showed charge losses of 10.5 % and 70.9 % in $LiClO_4$/PC and $LiClO_4/CH_3CN$, respectively, at around 650 redox cycles (taking in account that, for this film, the colour contrast between the yellow and green is low). The green ↔ russet change, although showed the highest contrast for this film, also revealed to be unstable, with charge losses of 70.2 % in $LiClO_4$/PC and 88.6 % in $LiClO_4/CH_3CN$ (at 650 cycles). These results showed that poly[2] has an inferior electrochemical stability than poly[1]. Furthermore, the reasons for the general better stabilities in $LiClO_4$/PC are not well known, but can be related with the less volatility of PC compared to CH_3CN and with degradation of the substrate (PET) over time, when immersed in CH_3CN.

In Table 2.6 are summarised the switching times determined for both poly[Ni(*salen*)] films during the stability studies, along the redox cycles. Note that these response times are in general higher than those indicated in Figures 2.11 and 2.12, once the films used here were deposited during 10 scans ($\Gamma \approx$ 0.31 and 1.13 μmol cm^{-2}, for poly[1] and poly[2], respectively), while the films used in chronoabsorptometric studies were deposited during 5 scans ($\Gamma \approx$ 0.16 and 0.84 μmol cm^{-2}, for poly[1] and poly[2], respectively) and, so, have different thicknesses.

Table 2.6. Switching times measured along the chronoamperometric studies of the poly[1] and poly[2] in $LiClO_4/CH_3CN$ and $LiClO_4/PC$ (Figures 2.15 and 2.16).

Films	Supporting Electrolyte	Switching times / s					
		Number of cycles	yellow - green	green - yellow	Number of cycles	green - russet	russet - green
poly[1]	$LiClO_4/CH_3CN$	0	9.3	8.4	0	6.9	25.0
		1000	11.3	6.4	100	11.7	24.2
		2000	24.0	7.6	200	29.8	17.8
	$LiClO_4/PC$	0	20.6	15.4	0	10.5	36.02
		1000	16.5	16.6	100	9.9	30.37
		2000	16.6	17.2	200	11.8	29.9
		3000	17.5	16.7	300	14.9	30.2
		6000	17.4	13.2			
		9000	17.9	9.9			
poly[2]	$LiClO_4/CH_3CN$	0	9.9	3.3	0	20.78	14.3
		200	10.8	3.7	100	-	11.3
	$LiClO_4/PC$	0	38.8	12.1	0	23.9	30.5
		200	39.1	12.2	100	17.2	24.9
		400	39.5	12.0	200	19.9	24.7
		600	38.8	12.0	300	20.0	22.0

In a general way, the response times for the colour changes yellow – green and green – russet (oxidation processes) tend to increase slightly or remain nearly constant, while the response times for the colour changes green – yellow and russet – green (reduction processes) tend to decrease slightly or remain constant.

The electrochemical stability of poly[1] film in $LiClO_4$/PC was also evaluated by CV during 200 redox cycles (Figure 2.17). The voltammetric responses showed that the anodic peak corresponding to the process associated with the colour change from the yellow to green (E_{pa} = 0.37 V) shifted to more positive potentials along the successive redox cycles, suggesting morphological and/or structural changes in film matrix. On the other hand, the anodic peak corresponding to the process associated with the colour change from green to russet (E_{pa} = 0.99 V) showed a more rapid decrease in current intensity, reaching very low values. At this point, the anodic peak at more positive potential values was overlapped by the peak associated with the yellow to green colour change, such that this became the dominant observed colour change. These observations can justify the lower stability of the green ↔ russet colour change.

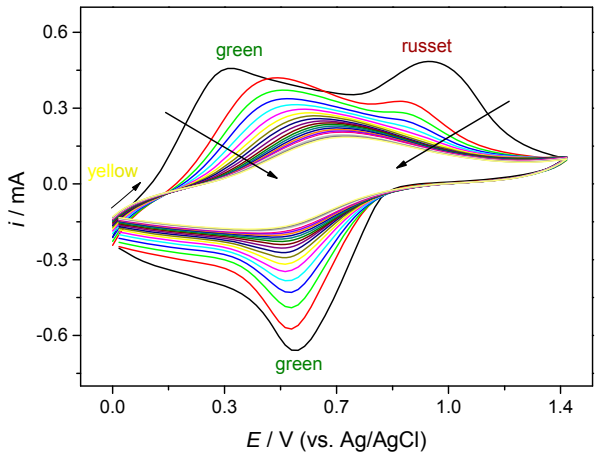

Figure 2.17 Voltammetric responses of poly[1] in $LiClO_4$/PC 0.1 mol dm^{-3}, obtained at the scan rate of 0.020 V s^{-1}, during 200 scans.

The high electrochemical stability obtained for poly[1] in $LiClO_4$/PC medium constitutes a step forward in the electrochemical stability improvement when compared with others poly[M(*salen*)] films,[15,16] and highlights the potentiality of this film as a very stable EC material. Furthermore, when compared with other EC materials, poly[1] in $LiClO_4$/PC showed faster responses (lower switching times) than some inorganic metal oxides (τ = 12-60 s),[22,28] and similar or even higher optical contrasts and colouration efficiencies than some conducting polymers and derived composites.[2,29,30]

2.3.5 ECDs fabrication and characterisation

The high electrochemical stability of the colour change yellow ↔ green of the poly[1], allied with its good optical contrast, makes it the choice for the fabrication of solid-state ECDs. In the case of poly[2], although the high optical contrast associated with the green ↔ russet colour change could be a key issue in the selection for ECD fabrication, its low electrochemical stability remains the highest important drawback. Thereby, ECDs were fabricated employing poly[1] as EC material using a lateral configuration, in two figures of merit: a simple shape (typology 1) and a butterfly shape (typology 2); the latter to exploit the possibility of a future application in smart cards or labels.

In Figure 2.18 are presented the pictures and schematic illustrations of the assembled ECDs. In both typologies, the electrodes are in the same plane and are designated by 1 and 2: the electrode 1 is in the reduced state and shows a yellow colour, while electrode 2 is in the oxidised state and exhibits a green colour.

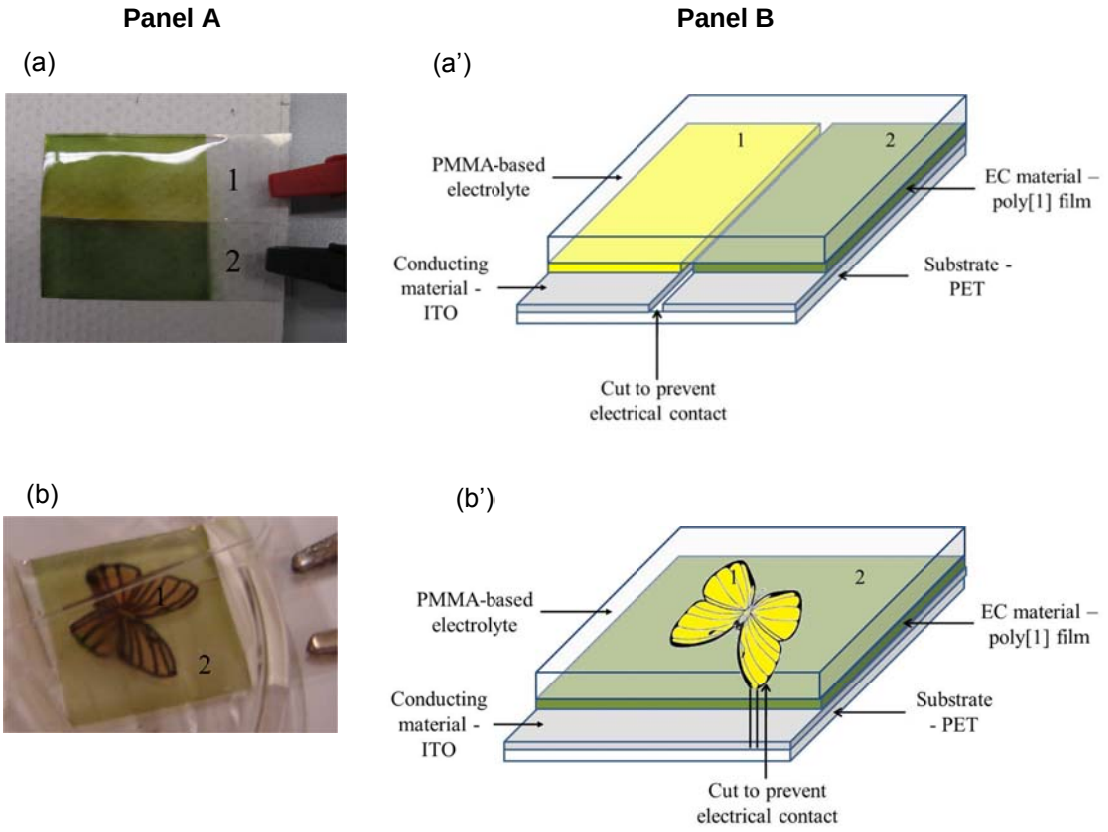

Figure 2.18 Pictures (Panel A) and schematic illustrations (Panel B) of the assembled ECDs of (a and a') typology 1 and (b and b') typology 2, showing the colour contrast between the two electrodes, each one in different oxidation states: electrode 1 in reduced state (E = -1.0 V and -1.1 V) and electrode 2 in oxidised state (E = 1.0 V and -0.25 V).

In Figure 2.19 (a) are depicted the chronoamperograms obtained during the study of the electrochemical stability of the ECD of typology 1, considering the colour change yellow ↔ green. The ECD retained a clear change of colour for ca. 3000 redox cycles, with a loss in charge of 37.0 %.

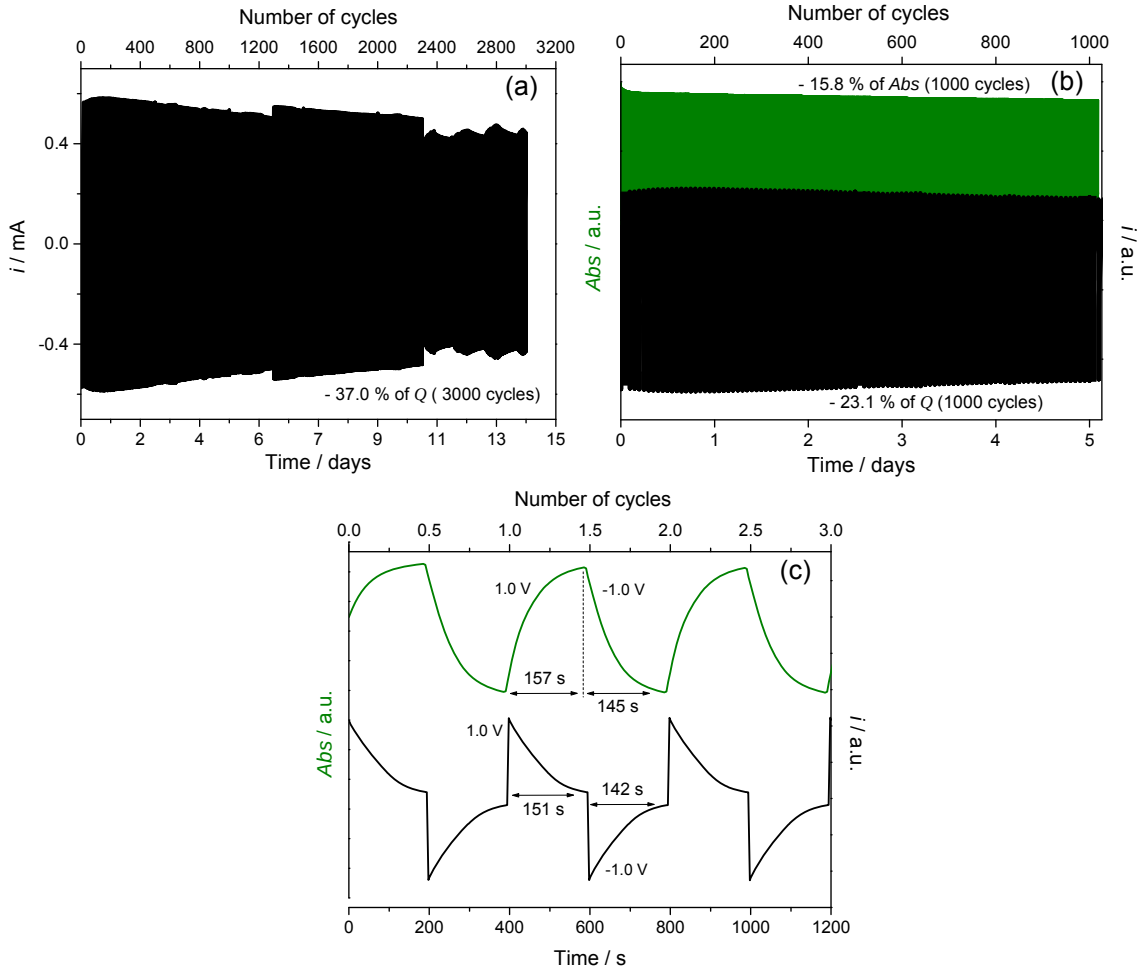

Figure 2.19 ECD of typology 1: (a) chronoamperograms obtained by the application of two potential pulses of 200 s by redox cycle, with potential alternating between -1.0 (yellow) and 1.0 V (green); chronoabsorptograms (at λ = 750 nm) and respective chronoamperograms obtained during (b) the first 1000 redox cycles and (c) the first three redox cycles, with indication of the switching times.

During the first 1000 redox cycles, the process was simultaneously monitored by *in situ* UV-Vis spectroscopy, at λ = 750 nm (Figure 2.19 (b)). At the end of these cycles, the ECD registered a charge loss of 23.1 % and a loss of 15.8 % in absorbance. The estimated τ values are reported in Figure 2.19 (c). From the absorbance – time curves, τ = 157 s for the colour change yellow – green and τ = 145s for the reverse colour change. These times are similar to those determined from the chronoamperograms:

τ = 151 and 142 s to the yellow – green and green – yellow colour changes, respectively. Furthermore, the optical contrast of the assembled ECD was calculated as ΔT = 88.7 % (at λ = 750 nm) and the colouration efficiency as η = 130.4 cm^2 C^{-1}, with ΔOD = 0.84 and a charge requirement of the Q_d = 6.4 mC cm^{-2}.

In order to evaluate the application of this EC system in devices with more sophisticated template forms, a proof-of-concept ECD of typology 2 was assembled. The electrochemical stability of the ECD of typology 2 was determined through the chronoamperograms depicted in Figure 2.20. The ECD changed of colour between yellow and green during around 1250 redox cycles, with a charge loss of 58.9 %. These results indicate the need for a more optimised typology when more sophisticated ECD templates are needed in terms of future applications.

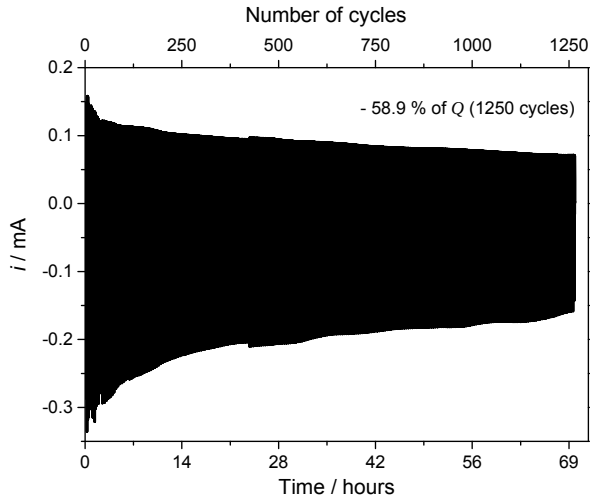

Figure 2.20 Chronoamperograms of the ECD of typology 2, applying two potential pulses of 100 s by redox cycle, with potential alternating between -1.1 (yellow) and -0.25 V (green).

2.4 Conclusions

Poly[1] and poly[2] films were successfully electrodeposited on ITO/PET flexible substrates. Voltammetric characterisation revealed that poly[1] showed similar redox profiles in $LiClO_4/CH_3CN$ and $LiClO_4$/PC, while poly[2] showed solvent dependent electrochemical responses. Both films showed polyelectrochromic behaviour, exhibiting yellow, green and russet colours, according to their oxidation state.

EC properties were firstly studied in solution with both polymer films showing switching times in the range τ = 8 - 24 seconds; this is consistent with their potential application in slow-acting electronic devices, such as smart cards and labels. For poly[1], the yellow ↔ green colour transition showed the best optical contrast, whereas

for poly[2] it was the green ↔ russet transition. Poly[1] also showed the best colouration efficiencies, with the highest values being obtained for the green ↔ russet colour change. Both polymeric films were more electrochemically stable in $LiClO_4$/PC, although the overall poorer electrochemically stability of poly[2]: the highest electrochemical stability was obtained for the yellow ↔ green change of poly[1] in $LiClO_4$/PC, with charge loss of only 34.3 % after 9000 cycles. Consequently, poly[1] was used to fabricate ECD with two figures of merit (typology 1 and 2), with typology 1 showing the best performance: ΔT = 88.7 % (at λ = 750 nm), η = 130.4 cm^2 C^{-1} and charge decrease of 37.0 % after 3000 redox cycles.

The results showed that poly[1] has promising EC properties both in a solution cell and in a solid-state device. Combination of high electrochemical stability, interesting polyelectrochromism and good optical contrast motivate the application of poly[1] as EC material in electronic displays. Furthermore, the combination of these EC properties with a flexible substrate has considerable advantages that may be exploited in paper-like applications.

References

[1] Amb, C. M.; Dyer, A. L.; Reynolds, J. R. *Chem. Mat.* **2011**, *23*, 397.

[2] Yu, W. Y.; Chen, J.; Fu, Y. L.; Xu, J. K.; Nie, G. M. *J. Electroanal. Chem.* **2013**, *700*, 17.

[3] Rende, E.; Kilic, C. E.; Udum, Y. A.; Toffoli, D.; Toppare, L. *Electrochim. Acta* **2014**, *138*, 454.

[4] Chang, K. H.; Wang, H. P.; Wu, T. Y.; Sun, I. W. *Electrochim. Acta* **2014**, *119*, 225.

[5] Jarosz, T.; Brzeczek, A.; Walczak, K.; Lapkowski, M.; Domagala, W. *Electrochim. Acta* **2014**, *137*, 595.

[6] Kurtay, G.; Ak, M.; Gullu, M.; Toppare, L.; Ak, M. S. *Synth. Met.* **2014**, *194*, 19.

[7] Lu, J. L.; Liu, W. S.; Ling, H.; Kong, J. H.; Ding, G. Q.; Zhou, D.; Lu, X. H. *RSC Adv.* **2012**, *2*, 10537.

[8] Sydam, R.; Kokal, R. K.; Deepa, M. *ChemPhysChem* **2015**, *16*, 1042.

[9] Xiong, S. X.; Fu, J. L.; Li, Z. F.; Shi, Y. J.; Wang, X. Q.; Chu, J.; Gong, M.; Wu, B. H. *J. Macromol. Sci. Part B-Phys.* **2015**, *54*, 799.

[10] Kang, J. H.; Oh, Y. J.; Paek, S. M.; Hwang, S. J.; Choy, J. H. *Sol. Energy Mater. Sol. Cells* **2009**, *93*, 2040.

[11] Sydorov, D.; Duboriz, I.; Pud, A. *Electrochim. Acta* **2013**, *106*, 114.

[12] Kraft, A.; Rottmann, M.; Gilsing, H. D.; Faltz, H. *Electrochim. Acta* **2007**, *52*, 5856.

[13] Vilas-Boas, M.; Santos, I. C.; Henderson, M. J.; Freire, C.; Hillman, A. R.; Vieil, E. *Langmuir* **2003**, *19*, 7460.

[14] Martins, M.; Boas, M. V.; de Castro, B.; Hillman, A. R.; Freire, C. *Electrochim. Acta* **2005**, *51*, 304.

[15] Pinheiro, C.; Parola, A. J.; Pina, F.; Fonseca, J.; Freire, C. *Sol. Energy Mater. Sol. Cells* **2008**, *92*, 980.

[16] Branco, A.; Pinheiro, C.; Fonseca, J.; Tedim, J.; Carneiro, A.; Parola, A. J.; Freire, C.; Pina, F. *Electrochem. Solid State Lett.* **2010**, *13*, J114.

[17] Freire, C.; de Castro, B. *J. Chem. Soc.-Dalton Trans.* **1998**, 1491.

[18] Fonseca, J.; Tedim, J.; Biernacki, K.; Magalhaes, A. L.; Gurman, S. J.; Freire, C.; Hillman, A. R. *Electrochim. Acta* **2010**, *55*, 7726.

[19] Tedim, J.; Patricio, S.; Fonseca, J.; Magalhaes, A. L.; Moura, C.; Hillman, A. R.; Freire, C. *Synth. Met.* **2011**, *161*, 680.

[20] Dale, S. M.; Glidle, A.; Hillman, A. R. *J. Mater. Chem.* **1992**, *2*, 99.

[21] Wu, T. Y.; Liao, J. W.; Chen, C. Y. *Electrochim. Acta* **2014**, *150*, 245.

[22] Sapp, S. A.; Sotzing, G. A.; Reynolds, J. R. *Chem. Mat.* **1998**, *10*, 2101.

[23] Tedim, J.; Carneiro, A.; Bessada, R.; Patricio, S.; Magalhaes, A. L.; Freire, C.; Gurman, S. J.; Hillman, A. R. *J. Electroanal. Chem.* **2007**, *610*, 46.

[24] Tedim, J.; Goncalves, F.; Pereira, M. F. R.; Figueiredo, J. L.; Moura, C.; Freire, C.; Hillman, A. R. *Electrochim. Acta* **2008**, *53*, 6722.

[25] Dahm, C. E.; Peters, D. G.; Simonet, J. *J. Electroanal. Chem.* **1996**, *410*, 163.

[26] Vilas-Boas, M.; Freire, C.; de Castro, B.; Christensen, P. A.; Hillman, A. R. *Chem.-Eur. J.* **2001**, *7*, 139.

[27] Beaujuge, P. M.; Reynolds, J. R. *Chem. Rev.* **2010**, *110*, 268.

[28] Kalagi, S. S.; Mali, S. S.; Dalavi, D. S.; Inamdar, A. I.; Im, H.; Patil, P. S. *Synth. Met.* **2011**, *161*, 1105.

[29] Camurlu, P.; Gultekin, C.; Bicil, Z. *Electrochim. Acta* **2012**, *61*, 50.

[30] Xu, G. Q.; Zhao, J. S.; Cui, C. S.; Hou, Y. F.; Kong, Y. *Electrochim. Acta* **2013**, *112*, 95.

Chapter 3

Novel hybrid based in a poly[Ni(*salen*)] film and WO_3 nanoparticles with electrochromic properties

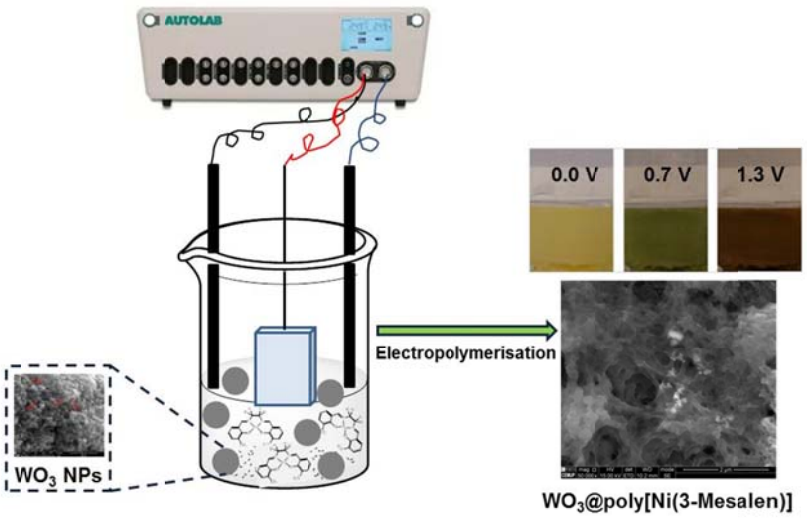

3

Novel hybrid based in a poly[Ni(*salen*)] film and WO_3 nanoparticles with electrochromic properties[1,2,3]

Abstract

The strategy of combining electroactive polymers and inorganic nanomaterials has been widely studied in recent years in order to improve some of their properties, namely electrocatalysis and electrochromism. This chapter focuses on a new composite prepared through the electropolymerisation of the transition metal complex [Ni(3-Mesalen)], designated as [1], in the presence of WO_3 nanoparticles (NPs) and its electrochromic performance.

The WO_3 NPs were prepared using tungsten metal powder and were characterised by several techniques, which indicated quasi-spherical morphology, high crystallinity and sizes of ≈ 34 – 38 nm.

The nanocomposite WO_3@poly[1] films displayed similar electrochemical responses to that of pristine poly[1] film in $LiClO_4/CH_3CN$, but higher electroactive surface coverages, showing the advantage of NPs incorporation in the nanocomposite. The presence of the WO_3 NPs on poly[1] matrix was assessed by X-ray photoelectron spectroscopy and scanning electron microscopy. The nanocomposite presented similar electronic spectra to those of poly[1], indicating that the electronic structure of pristine film is maintained in the nanocomposite, but exhibited lower ε-values for bands associated with charge transfer transitions for high oxidised states, revealing an enhanced stability for ligand over-oxidation.

---

[1] Adapted from: M. Nunes, C. Moura, A. R. Hillman, C. Freire, Novel hybrid based in a poly[Ni(*salen*)] film and WO_3 nanoparticles with electrochromic properties. Submitted.

[2] M. Nunes's contribution to the publication: preparation and characterisation of the WO_3 nanoparticles and of the WO_3@poly[1] nanocomposite and pristine poly[1] films, evaluation of the electrochromic properties and manuscript preparation.

[3] The experimental details on the electrochemical/spectroelectrochemical and remaining characterisation techniques are indicated in Appendices A and C, respectively.

The WO_3@poly[1] nanocomposite showed more favourable EC properties in $LiClO_4/CH_3CN$ than the pristine film, with lower switching times (τ = 1.3 - 3.6 s), higher optical contrasts (improvement of ≈ 40 %) and better colouration efficiencies (improvement of 13.1 - 21.7 %). The results showed unequivocally the advantage of the entrapment of WO_3 NPs on the poly[1] matrix, in the improvement of the EC properties of the pristine film.

3.1 Introduction

In the last years, the continuous research in conducting polymers and the emergence of the nanotechnology boosted the development of several organic/inorganic hybrid assemblies based on the combination of CPs with, for example, metal nanoparticles,[1] carbon nanostructures,[2,3] and inorganic compounds.[4] Among these new composites, combination of CPs with metal oxide semiconductors constitute, undoubtedly, one of the most promising classes,[5,6] once allow to combine the elasticity and functionality of the CPs with the high thermal and chemical stabilities of metal oxides;[7] some examples of these composites have been reported through the incorporation of TiO_2,[8-10] ZnO[11] and MnO_2[12] nanomaterials on CPs-matrixes. In particular, tungsten(VI) oxide (WO_3), an n-type semiconductor with a band gap of 2.7 eV,[13] has been widely employed to assemble WO_3/CPs nanocomposites for applications as sensors[14-16] and electrocatalysts,[17] mainly due to its ability to intercalate electrons and protons.[18] Furthermore, WO_3 is the mostly investigated inorganic electrochromic material[19,20] due to its good chemical stability, strong adherence to substrate and genuine colour switching (cathodic EC material).[21,22] These properties make it very attractive to be combined with CPs and other electroactive polymers for EC applications.

In fact, several EC nanocomposites based in the incorporation of WO_3 nanostructures in several CPs-matrixes, such as polyaniline[21-25] and poly(3,4-ethylenedioxythiophene)[26] has already been reported, taking into account the complementary EC performances of WO_3 and CPs. In a general way, the CPs exhibit interesting optical properties, with rich colour changes due to its multiple redox states, but have small colour switching rates due to the slow transport of charge balance counter ions into the polymer layer; on the other hand, metal oxide nanostructures have high surface-to-volume ratio and organised structures that allow the ion/electron intercalation processes and promote an excellent switching reversibility.[7,27] Thus, the resultant nanocomposites can take advantage of the synergic influence of the WO_3 on

the EC properties of conducting polymer and, generally, present improved EC properties, with more satisfactory switching speeds and colouration efficiencies.[21,23,25]

The similarity of the poly[M(*salen*)]-based electroactive metallopolymers with CPs, namely in the poly(phenylene)-based redox properties and their rich coloured redox states,[28,29] makes them interesting EC polymers. Thus, in this chapter it is described the preparation and characterisation of a novel composite film based in the incorporation of WO_3 NPs on the matrix of a poly[Ni(*salen*)]-based film and the evaluation of its EC properties. The metal *salen* polymer employed was the poly[Ni(3-Mesalen)], designated by poly[1]. The EC performance evaluation of the pristine poly[1] was already described in Chapter 2 and showed promising EC properties, with a good electrochemical stability - a charge loss of 34.3 % after ≈ 9000 cycles - and interesting colour changes, from yellow in neutral state to green and russet (reddish-brown) in oxidised states. Nonetheless, in order to potentiate its commercial application, the EC properties of poly[1] need to be improved, namely in order to achieve lower response times and increase the colouration efficiency. Thus, we took the advantages of WO_3 NPs properties - nanometric size (high surface-to-volume ratio) and semiconductor properties - to incorporate them within poly[1] and to evaluate their influence on the composition, morphology, electrochemical response and spectroelectrochemical properties, with the ultimate goal to potentiate enhanced EC properties. The hybrid films were prepared through the *in situ* electropolymerisation of the respective Ni-*salen* complex in the presence of the WO_3 NPs; this method has several advantages, once allow the formation of the metallo-organic/inorganic interface in one step and because the hybrid film is directly formed on the electrode surface.[27,30] To the best of our knowledge, this is the first time that metallopolymer-nanoparticles hybrid films between this family of M-*salen* polymers and metal oxides are prepared.

3.2 Experimental section

3.2.1 Materials and solvents

Tungsten metal powder (Alfa Aesar, 99.9 %), hydrogen peroxide (Aldrich, 30 wt.% in H_2O), glacial acetic acid (Merck, 100 %), acetonitrile and propylene carbonate (Romil, pro analysis grade) and $LiClO_4$ (Aldrich, 99 %) were used as received; ultra-pure water (resistivity 18.2 MΩ cm at 25 ºC, Millipore) was used. The complex *N,N'*-bis(3-methylsalicylideneiminate) nickel(II), [Ni(3-Mesalen)], and respective *salen* ligand were prepared by methods described in literature.[31]

3.2.2 WO_3 NPs preparation

WO_3 NPs were prepared by a procedure adapted from literature.[32,33] Briefly, 6.5 g of tungsten metal powder were dissolved in 40 mL of 30 wt.% H_2O_2 and 4 mL of millipore water, until a colourless solution was obtained. This solution was filtrated and refluxed at 55 ºC during 17 hours, after the addition of 40 mL of glacial acetic acid. A yellow flaky solid was obtained after solvent evaporation, which was heated to 100 ºC (5 ºC / min) in air, held at this temperature for 1 h, and then brought back to room temperature. Finally, it was annealed at three different temperatures: 250, 450 or 550 ºC during 2 hours, at the same heating rate.

3.2.3 Films preparation and electrochemical studies

The WO_3@poly[1] films were prepared by cyclic voltammetry (CV) from solutions containing 1.0 mmol dm^{-3} [Ni(3-Mesalen)] (complex [1]) and 5 wt.% (WO_3/$LiClO_4$ wt.%) of WO_3 NPs (annealed at 550 ºC) in 0.1 mol dm^{-3} $LiClO_4/CH_3CN$. The potential of the working electrode (ITO/PET 2.25 cm^2) was cycled between 0.0 and 1.3 V at 0.020 V s^{-1}, during 10 scans. Prior to electrodeposition, the starting solutions were (i) sonicated during 10 minutes or (ii) sonicated during 10 minutes followed by reflux during 3 hours. According with the method used, the films obtained were named WO_3@poly[1]_s and WO_3@poly[1]_r, respectively. The pristine poly[1] film was prepared using the same experimental conditions, but in the absence of WO_3 NPs.

Upon film deposition, the modified electrodes were rinsed with dry CH_3CN or PC, immersed in monomer- and WO_3-free 0.1 mol dm^{-3} $LiClO_4/CH_3CN$ or $LiClO_4$/PC solutions and redox cycled in the potential ranges -0.1 to 1.2 V or -0.1 to 1.3 V, respectively, at 0.010 V s^{-1}, during 5 redox cycles. The electroactive surface coverage, Γ / μmol cm^{-2} (cited in terms of monomeric units) of each film was determined by a coulometric assay,[34,35] using CVs obtained in monomer- and WO_3-free 0.1 mol dm^{-3} $LiClO_4/CH_3CN$ solution at the scan rate of 0.010 V s^{-1}, to ensure complete films redox conversion. The doping level value used for Γ determination was calculated from comparison of coulometric data for films deposition and cycling, as described in literature,[34,35] and were found to be n = 0.65.

3.2.4 Composition and morphology characterisation

The composition and morphology characterisations of WO_3@poly[1]_r nanocomposite were performed by XPS and SEM/EDS, respectively. All films were analysed in reduced state. XPS was also used to investigate the influence of the redox cycling in film chemical composition; films were analysed: (i) upon polymerisation and before redox cycling, by application of E = 0.0 V during 200 s in 0.1 mol dm^{-3}

$LiClO_4/CH_3CN$, to ensure the reduced state, and after potential cycling in (ii) $LiClO_4/CH_3CN$ and (iii) $LiClO_4$/PC 0.1 mol dm^{-3}, in the potential ranges -0.1 to 1.2 V or -0.1 to 1.3 V, respectively, at 0.020 V s^{-1}, during 5 redox cycles; poly[1] film was studied in identical conditions for comparison.

3.2.5 Spectroelectrochemical studies

Redox process was also study by *in situ* UV-Vis spectroscopy with films prepared with 3 electrodeposition cycles, at 0.020 V s^{-1}. The films were cycled in 0.1 mol dm^{-3} $LiClO_4/CH_3CN$ and $LiClO_4$/PC supporting electrolytes, in the conditions described in section 3.2.3. The UV-Vis spectra were acquired simultaneously, at intervals of 0.5 s, in the range wavelengths of 315 to 1100 nm, during the 4th redox cycle. The molar extinction coefficients, ε / cm^{-1} mol^{-1} dm^3, of all observed electronic bands were estimated using a combination of the Beer-Lambert and Faraday laws (Equation 2.1).

3.2.6 Electrochromic properties evaluation

The EC parameters – switching times, optical contrast, change of the optical density and colouration efficiency - of the nanocomposites films were obtained by a double potential step method (chronoamperometry) coupled with UV-Vis spectroscopy (chronoabsorptometry). The studies were performed in 0.1 mol dm^{-3} $LiClO_4/CH_3CN$ and $LiClO_4$/PC solutions, considering the colour transition yellow ↔ green, that proved to be the most promising for the pristine poly[1] (Chapter 2). In the double potential step experiment, the potential was set at the initial potential of E = 0.0 V for a period of time of 50 s and was stepped to a second potential E = 0.7 V for another period of 50 s, being after switched back to the initial potential. The simultaneous chronoabsorptometric measurements were performed at the fixed wavelength of λ = 750 nm, acquiring the UV-Vis spectra with intervals of 1 s, during 4 redox cycles. The films studied were electrodeposited during 3 cycles, using the typical experimental conditions. The ΔOD and the colouration efficiency parameters were estimated through Equation 1.1. The switching times were determined considering 90 % of the full switch.[36,37]

The electrochemical stability was evaluated by a chronoamperometric experiment, using the same experimental conditions, but for a long period of time (≈ 9500 redox cycles, ≈ 11 days). The films used were prepared with 10 electrodeposition cycles. All EC parameters were also evaluated for pristine poly[1] film in the same conditions, for comparison.

3.3 Results and discussion

3.3.1 WO_3 NPs characterisation

The XRD patterns of the WO_3 NPs annealed at 450 and 550 ºC are shown in Figure 3.1 (a) and that annealed at 250 ºC is depicted in Figure 3.1 (b).

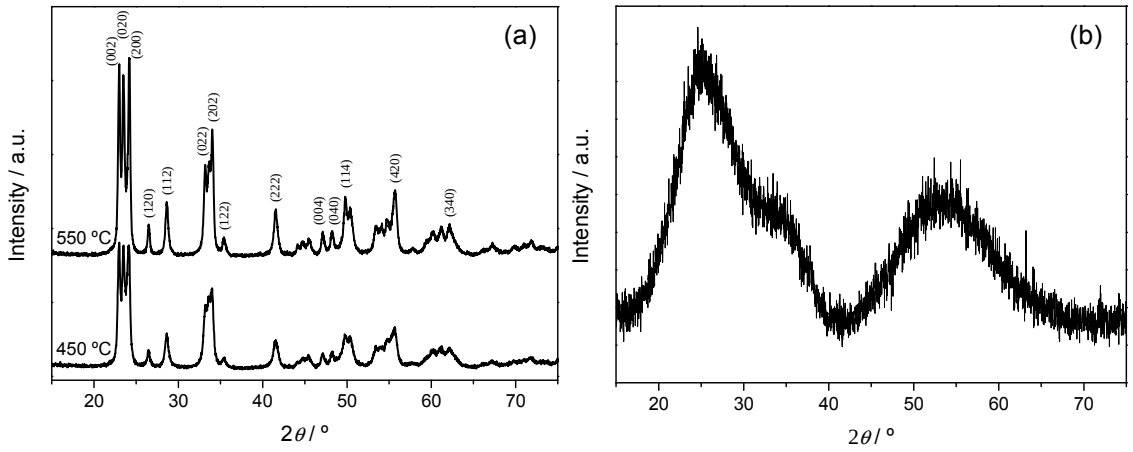

Figure 3.1 XRD patterns of WO_3 NPs annealed at (a) 450 and 550 ºC and (b) 250 ºC.

The XRD pattern of NPs annealed at 250 ºC exhibits two broad peaks in the $2\theta \approx 20 - 39$ º and 42 – 68 º ranges, indicating an amorphous structure.[33] In contrast, the patterns of NPs annealed at 450 and 550 ºC show well defined peaks typical of crystalline NPs. The NPs annealed at 550 ºC, show the highest intense and sharpest peaks, reflecting an enhancement of the crystallinity with the increase of annealing temperature. The XRD peaks of both NPs annealed at 450 and 550 ºC (2θ = 23.0, 23.5, 24.2, 26.5 and 28.6 º) are indexed, respectively, to the (002), (020), (200), (120) and (112) planes and are in accordance with a monoclinic WO_3 structure (JCPDS no. 83-0950); no other peaks were observed pertaining to other WO_3 structures. The crystallite sizes of the NPs annealed at 450 and 550 ºC are, respectively, 33.6 and 36.7 nm.

The SEM and TEM micrographs obtained for WO_3 NPs annealed at 550 ºC are depicted in Figures 3.2 (a) and (b), respectively. Both micrographs show quasi-spherical WO_3 NPs. The particle size distributions were fitted by a log-normal function (Figure 3.2 (c) and (d)), leading to an average particle size of 37.7 nm (± 4.5 nm) by SEM and 35.2 nm (± 7.7 nm) by TEM; the values obtained by the two techniques are similar and are in agreement with those obtained by XRD.

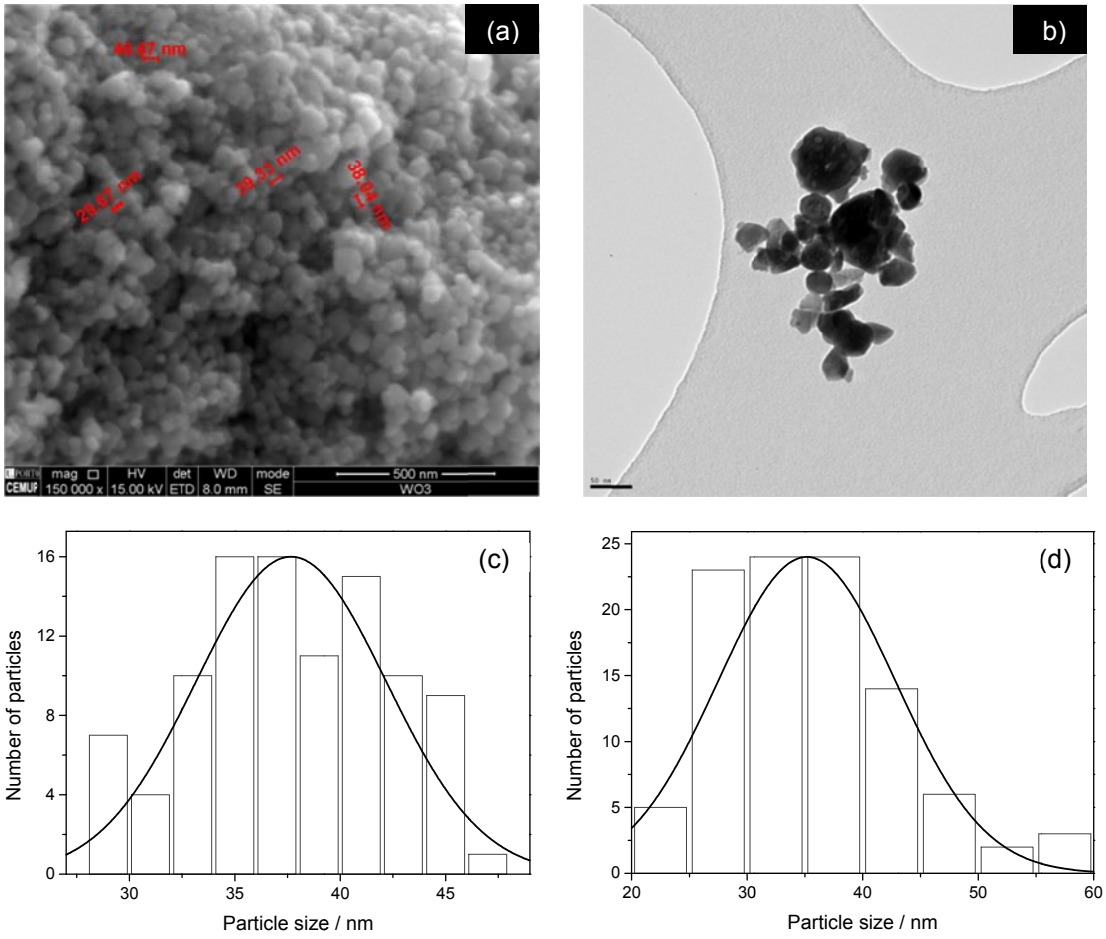

Figure 3.2 (a) SEM and (b) TEM micrographs of WO_3 NPs annealed at 550 ºC; particle size distribution histograms from the analysis of (c) SEM and (d) TEM micrographs (the solid line represents the log-normal distribution fits).

The FTIR spectra of WO_3 NPs annealed at different temperatures are depicted in Figure 3.3. In all spectra there is a large band in the range 1000-500 cm^{-1} that is characteristic of the W-O and O-W-O stretching vibrations.[38,39] The spectra of NPs annealed at the highest temperatures (450 and 550 ºC) exhibit one vibration band at 1037 cm^{-1}, which is assigned to the W=O stretching modes.[40] Furthermore, all the spectra also exhibit a very broad band with a maximum at ≈ 3098 cm^{-1} and a weak band at ≈ 1613 cm^{-1} that correspond to O-H stretching and bending vibrations respectively,[41] due to the presence of adsorbed water and/or hydroxylated W-OH bonds; this broad band is more intense in the spectrum of the WO_3 NPs annealed at 250 ºC and decreases in intensity with the increase of annealing temperature. The vibration bands at 1705 cm^{-1} and 1537-1403 cm^{-1}, clearly seen in the spectrum of the latter NP, are assigned to the C=O stretching vibrations and C-H bending vibrations[42] from acetic acid used in the synthesis, that may still be adsorbed at the lowest annealing temperature. These vibration bands decreased in intensity in the spectra of

NPs annealed at 450 and 550 ºC, which reflect the degradation / elimination of these contaminants at the highest annealing temperatures.

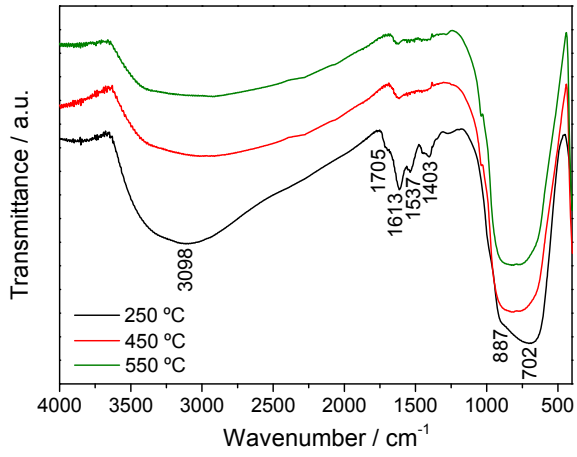

Figure 3.3 FTIR spectra of WO_3 NPs annealed at 250, 450 and 550 ºC.

In Figure 3.4 are depicted the high-resolution XPS spectra in the W4f and O1s regions for the WO_3 NPs annealed at 550 ºC.

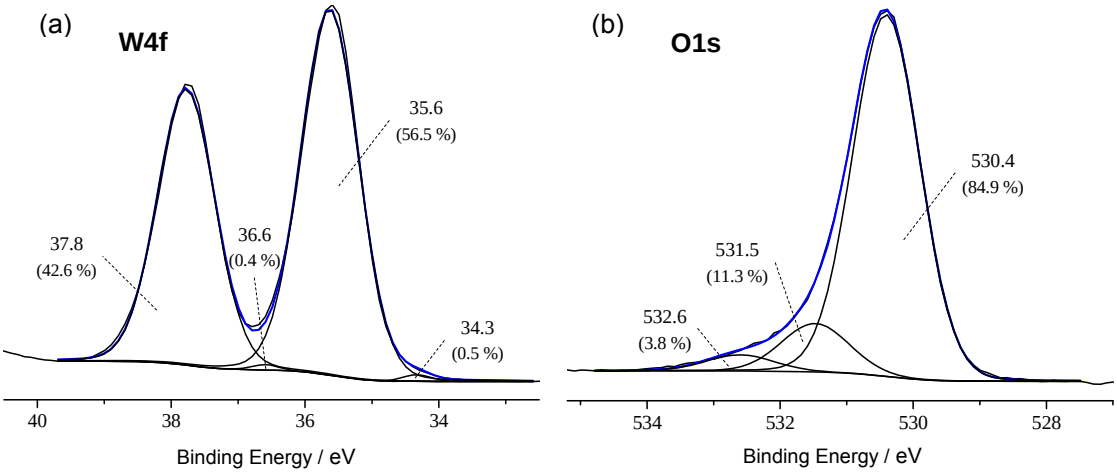

Figure 3.4 High-resolution XPS spectra of WO_3 NPs annealed at 550 ºC in the (a) W4f and (b) O1s regions, with respective deconvolutions.

The spectrum in the W4f region shows two main peaks at 35.6 and 37.8 eV, with a doublet separation of Δ = 2.20 eV and an areas ratio of 0.75, which are assigned to the $W^{(VI)}$ $4f_{7/2}$ and $W^{(VI)}$ $4f_{5/2}$ levels of W in +6 oxidation state in WO_3, respectively.[39,43] The other two peaks with smaller intensities at 34.3 and 36.6 eV are assigned to

$W^{(V)}$ $4f_{7/2}$ and $W^{(V)}$ $4f_{5/2}$ levels, respectively,[44] and indicate the presence of tungsten in a lower oxidation state, $W^{(V)}$, probably as a result of X-ray radiation reduction that may occur during XPS data acquisition. In the O1s region three peaks are observed: a main peak at 530.4 eV assigned to the lattice oxygen bonded to W,[45] a peak at 531.5 eV due to –OH groups and possible C=O groups and a peak at 532.6 eV attributed to C-O bonds, probably from acetic acid residues.[39,44]

The atomic percentages, 19.9 % of W and 80.1 % of O, gives a higher O/W atomic ratio ($O/W_{obtained}$ = 4.0) compared to the expected value ($O/W_{theoretical}$ =3.0), which can be due to some acetic acid contamination, used in the NPs synthesis.

3.3.2 Electrochemical preparation and characterisation of WO_3@poly[1]

The nanocomposite films were prepared from solutions containing the [Ni(3-Mesalen)] complex and 5 wt.% of WO_3 NPs, previously (i) sonicated or (ii) sonicated and refluxed. The WO_3 NPs annealed at 550 ºC were chosen for the preparation of the nanocomposites mainly by their more well-developed crystallinity, once a well-organized structure can be a greater advantage in electrochemical/electrochromic applications.[46]

The CVs obtained during the 1st and 10th electropolymerisation cycles of the WO_3@poly[1]_s and WO_3@poly[1]_r nanocomposite films are depicted in Figure 3.5 (a), along with the same electropolymerisation cycles for the pristine poly[1], for comparison. The voltammetric profiles for the complete film electropolymerisations are shown in Figure 3.6 and the peak potential values are summarised in Table 3.1.

The nanocomposites voltammetric responses for the electropolymerisation are similar to those of pristine poly[1], despite the small shift of the anodic and cathodic peaks for more and less negative potentials, respectively. These results suggest that the presence of the WO_3 NPs did not change the electropolymerisation mechanism of poly[1]. Thus, the two peaks observed in the first anodic half-cycle at E_{pa} = 0.86-0.88 and 1.04-1.08 V are assigned to the [Ni(3-Mesalen)] monomer oxidation and subsequent formation of oligomers/polymer on the working electrode, while the two cathodic peaks in the reverse scan at E_{pc} = 0.20-0.21 and 0.69-0.70 V are attributed to the reduction of the as-formed nanocomposite films. The new anodic peak at E_{pa} = 0.42 V, in second and subsequent polymerisation cycles, corresponds to the oxidation of the as-formed nanocomposite films.[34,35]

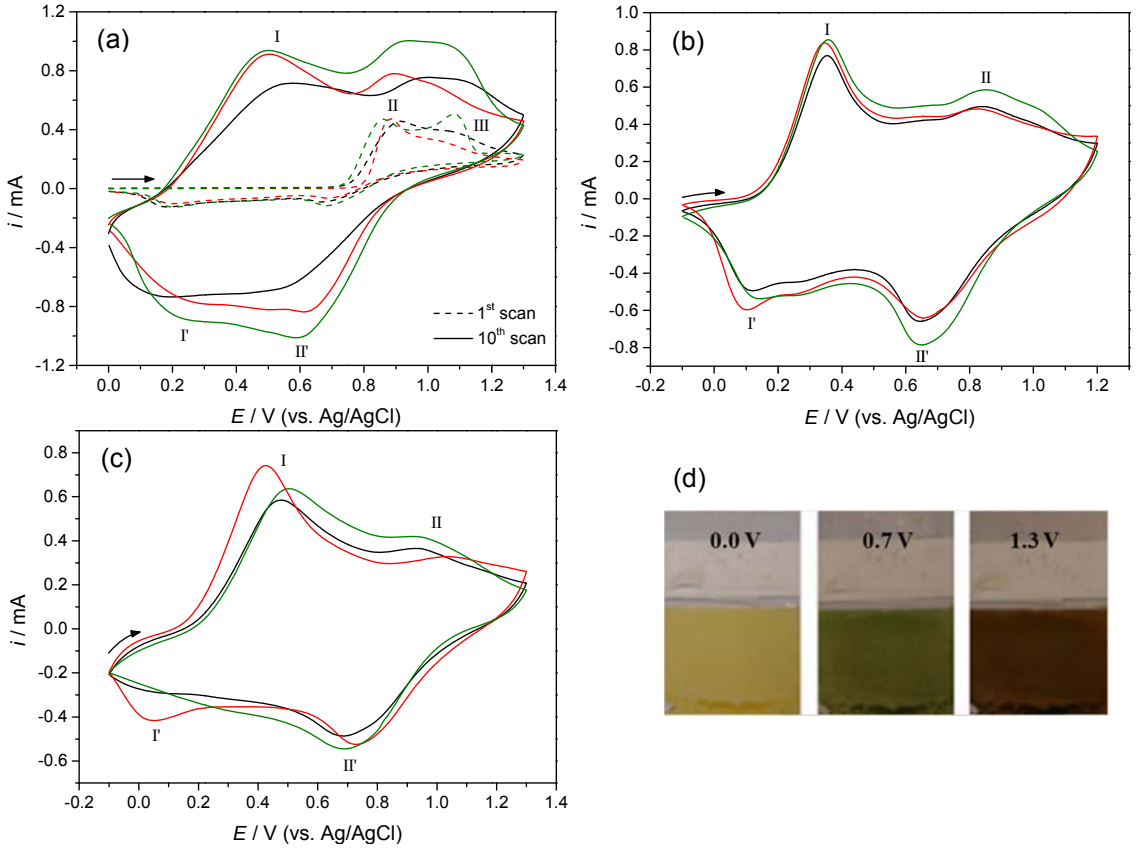

Figure 3.5 CVs obtained during (a) the 1st and 10th scans of electrodeposition, (b) 5th scan of film redox switching in $LiClO_4/CH_3CN$, and (c) 5th scan of film redox switching in $LiClO_4$/PC for: poly[1] (—, Γ = 0.19 μmol cm^{-2}), WO_3@poly[1]_s (—, Γ = 0.22 μmol cm^{-2}) and WO_3@poly[1]_r (—, Γ = 0.27 μmol cm^{-2}); (d) photographs of film in different oxidation states (E = 0.0, 0.7 and 1.3 V).

The nanocomposite and pristine film voltammetric responses during redox cycling (5th scan) in $LiClO_4/CH_3CN$ and $LiClO_4$/PC 0.1 mol dm^{-3} are depicted in Figures 3.5 (b) and (c), respectively; the CVs obtained during the complete films conditioning are shown in Figure 3.7 and, in Table 3.2, are summarised their corresponding peak potential values.

The nanocomposites and pristine films have similar electrochemical responses in both supporting electrolytes; in a general way, the peaks are less defined in $LiClO_4$/PC than in $LiClO_4/CH_3CN$. Moreover, the nanocomposites voltammetric responses exhibit slightly higher current intensities when compared to those of the pristine film, which is attributed to a larger electroactive surface area of the as-prepared nanocomposite films, as result of the incorporation of WO_3 NPs in the polymeric matrix. This is in agreement with the determined electroactive surface coverages: Γ = 0.19 μmol cm^{-2} for poly[1] and Γ = 0.22 and 0.27 μmol cm^{-2} for WO_3@poly[1]_s and WO_3@poly[1]_r nanocomposites, respectively.

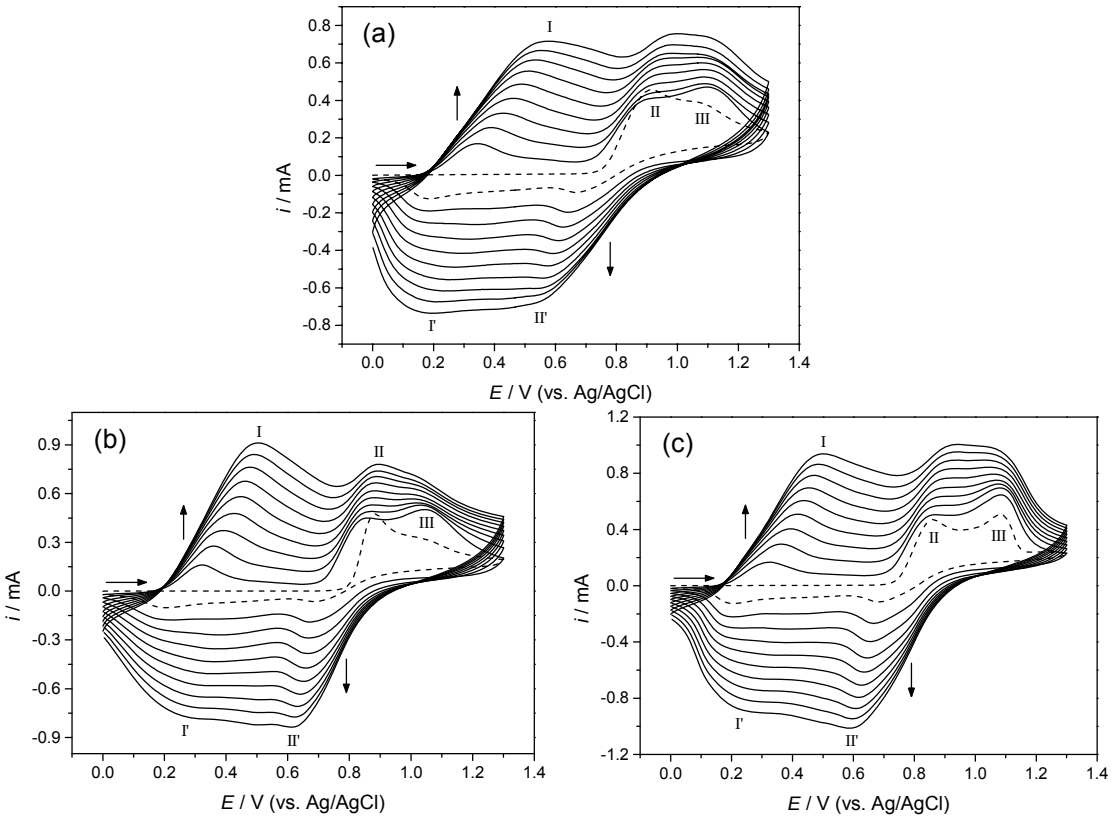

Figure 3.6 CVs of the complete electrodeposition of (a) poly[1], (b) WO_3@poly[1]_s and (c) WO_3@poly[1]_r films at 0.020 V s^{-1}, using 1.0 mmol dm^{-3} monomer solution (with 5 wt.% of WO_3 NPs in (b) and (c)) in $LiClO_4/CH_3CN$ 0.1 mol dm^{-3}.

Table 3.1 Peak potentials in CVs obtained at 1st, 5th and 10th scans of nanocomposites and pristine poly[1] films electrodepositions.

Film	Scan	*E* / V (vs. Ag/AgCl)				
		E_{paI}	E_{paII}	E_{paIII}	$E_{pcI'}$	$E_{pcII'}$
poly[1]	1st	-	0.91	1.08	0.19	0.67
	5th	0.46	0.94	1.08	0.20	0.59
	10th	0.55	0.98	1.06	0.20	0.55
WO_3@poly[1]_s	1st	-	0.88	1.04	0.21	0.70
	5th	0.42	0.88	1.04	0.27	0.66
	10th	0.50	0.90	1.03	0.29	0.61
WO_3@poly[1]_r	1st	-	0.86	1.08	0.20	0.69
	5th	0.42	0.92	1.07	0.22	0.64
	10th	0.50	0.95	1.03	0.27	0.59

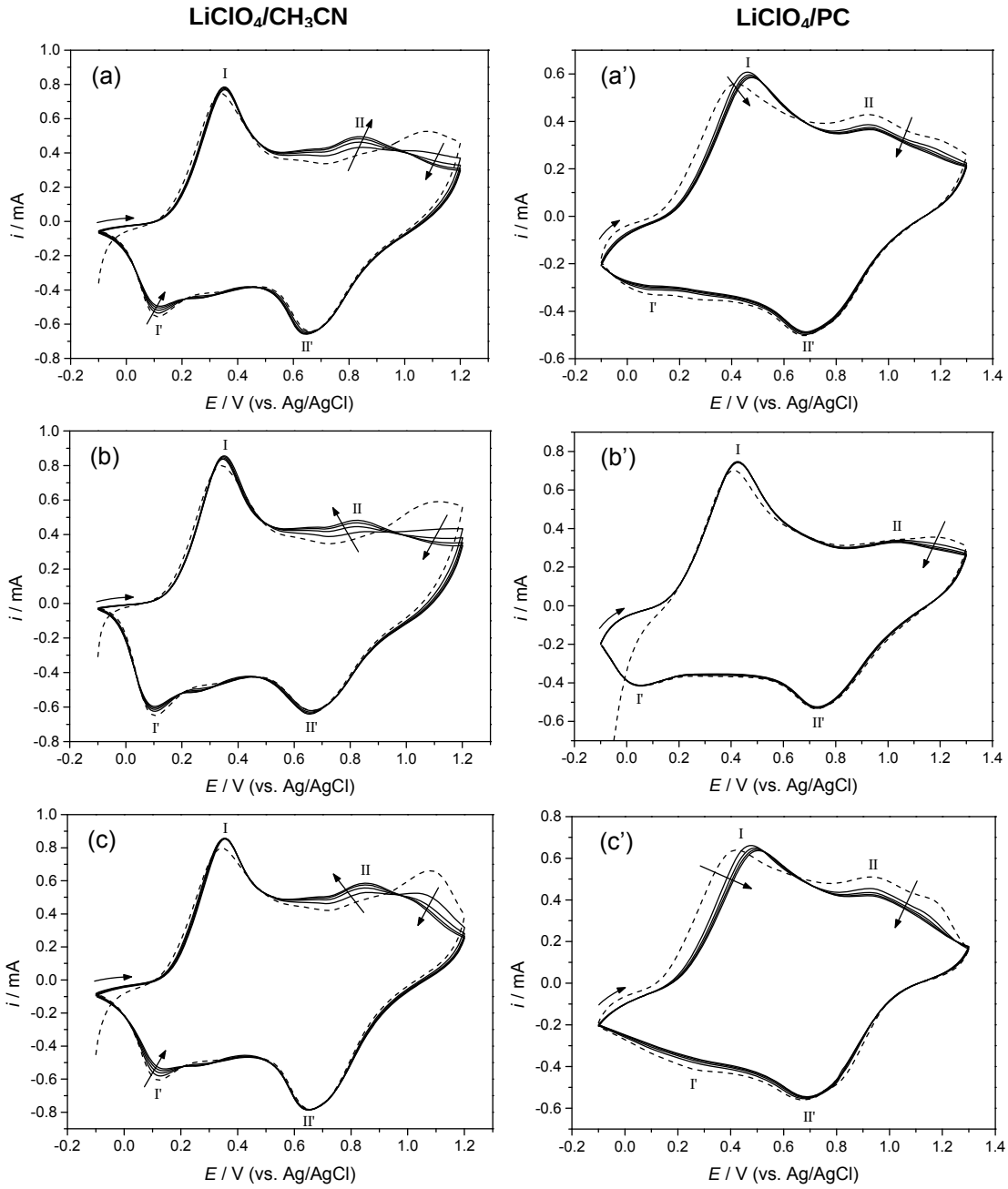

Figure 3.7 CVs of the redox switching of (a and a') poly[1], (b and b') WO_3@poly[1]_s and (c and c') WO_3@poly[1]_r films at 0.010 V s^{-1}, in $LiClO_4/CH_3CN$ and $LiClO_4$/PC 0.1 mol dm^{-3}.

The visual inspection of the WO_3@poly[Ni(*salen*)] nanocomposite films during their redox switching confirm the similarity of their EC behaviour to the pristine poly[1] (Chapter 2). In Figure 3.5 (d), photographs of the nanocomposite films with distinct colours at different oxidation states are presented: yellow (*E* = 0.0 V), green (*E* = 0.7 V) and russet (reddish-brown) (*E* = 1.3 V).

Table 3.2 Peak potentials in CVs obtained during the 1st and 5th scans of the films redox switching in $LiClO_4/CH_3CN$ and $LiClO_4$/PC 0.1 mol dm^{-3}, at 0.010 V s^{-1}.

Film	Supporting electrolyte	Scan	*E* / V (vs. Ag/AgCl)			
			E_{paI}	E_{paII}	$E_{pcI'}$	$E_{pcII'}$
poly[1]	$LiClO_4/CH_3CN$	1st	0.34	1.08	0.11(0.34*)	0.66
		5th	0.35	0.84	0.12(0.28*)	0.65
	$LiClO_4$/PC	1st	0.42	0.93(1.15*)	0.08(0.30*)	0.67
		5th	0.48	0.93	0.12*	0.69
WO_3@poly[1]_s	$LiClO_4/CH_3CN$	1st	0.33	1.12	0.10(0.32*)	0.66
		5th	0.35	0.82	0.11(0.26*)	0.66
	$LiClO_4$/PC	1st	0.41	1.17	0.06	0.73
		5th	0.42	1.04	0.06	0.73
WO_3@poly[1]_r	$LiClO_4/CH_3CN$	1st	0.34	1.08	0.12(0.31*)	0.66
		5th	0.36	0.85(1.01*)	0.15(0.26*)	0.66
	$LiClO_4$/PC	1st	0.42	0.93(1.17*)	0.29	0.67
		5th	0.51	0.91	0.69*	0.69

*inflexion

3.3.3 Composition and morphology

The composition and morphology characterisations were performed for WO_3@poly[1]_r nanocomposite, due to the higher electroactive surface coverage obtained for this nanocomposite film.

The XPS results for WO_3@poly[1]_r indicated the presence of Ni, C, N and O from the pristine film, Cl from the supporting electrolyte (which also contribute to O and N contents), and W due to the incorporated WO_3 NPs (with which also contribute to O).

The deconvoluted high-resolution XPS spectra of nanocomposite in C1s, N1s, O1s, Cl2p, Ni2p and W4f regions are depicted in Figures from 3.8 to 3.13, respectively, along with the spectra of poly[1], for comparison (except in W4f region).

In the C1s region, the high-resolution spectra were deconvoluted with four peaks: a main peak at 284.6 eV attributed to aromatic and aliphatic carbons of the *salen* ligand, a peak at 285.8-286.0 eV assigned to carbon bound to oxygen or nitrogen of the *salen* moiety, a peak at 286.7-287.0 eV ascribed to C≡N (from CH_3CN, Figure 3.8 (a), (a'), (b) and (b')) or to C=O (from PC, Figure 3.8 (c) and (c')) entrapped in the film and a peak at 289.2-290.0 eV assigned to a shake-up satellite associated with π-π^* transitions in the aromatic carbon rings of the ligand.[34,47] The spectrum of the nanocomposite after redox switching in $LiClO_4$/PC (Figure 3.8 (c')) showed a slight different profile, which can indicate different interactions provided by the WO_3 NPs.

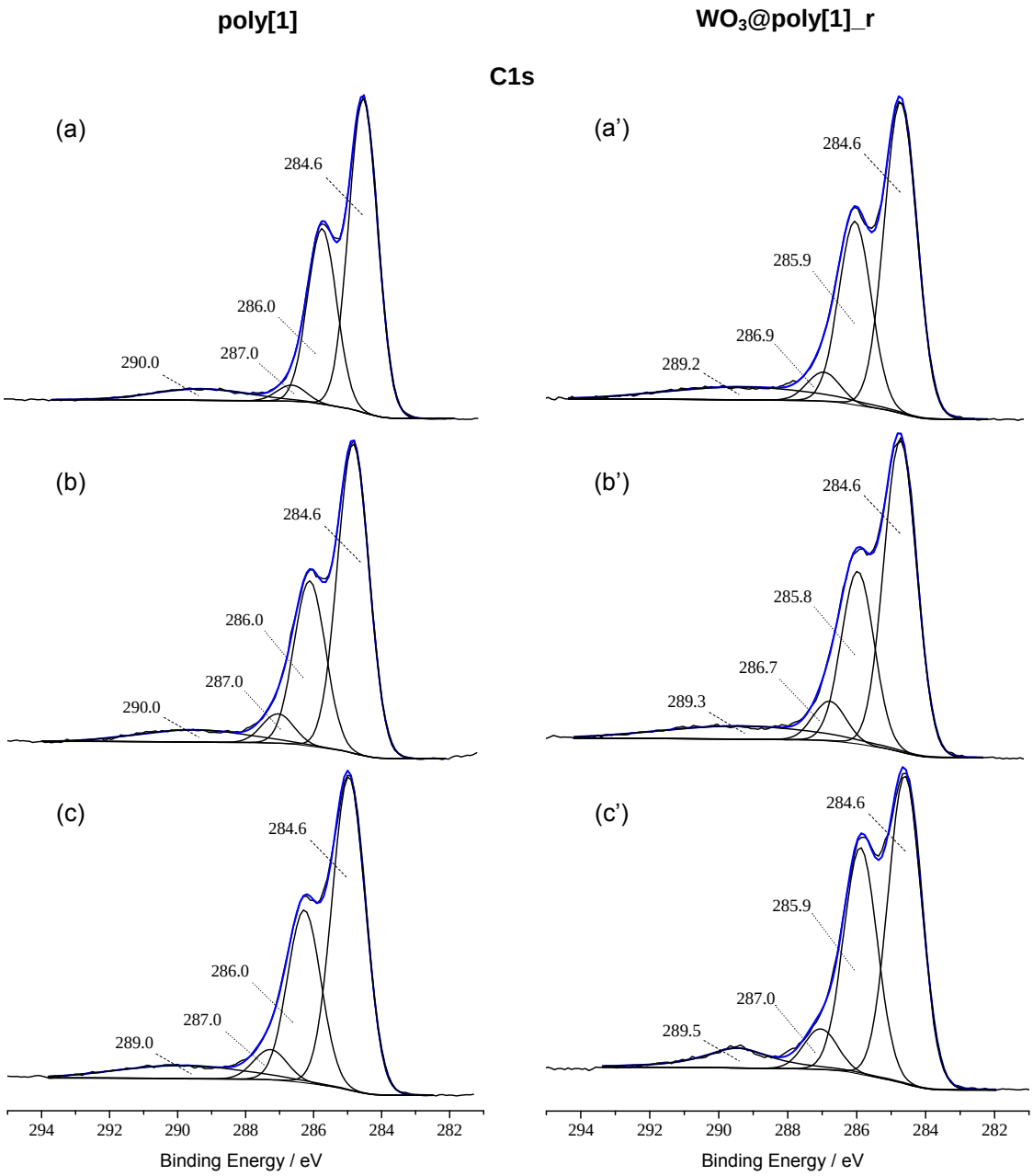

Figure 3.8 High-resolution XPS spectra of pristine poly[1] and WO_3@poly[1]_r in C1s region, with the corresponding deconvolutions, (a and a') before and after redox switching in (b and b') $LiClO_4/CH_3CN$ and (c and c') $LiClO_4$/PC.

The N1s high-resolution spectra of films analysed before redox and after redox in $LiClO_4/CH_3CN$ (Figure 3.9 (a), (a'), (b) and (b')) were deconvoluted with four peaks. The peaks at 399.3-399.5 eV and 400.2-400.4 eV are attributed to the nitrogen from ligand system (N=C and N-C bonds), the peak at higher energy, 401.2-401.5 eV, is assigned to the occluded CH_3CN (N≡C)[34] and the peak at 403.4-403.6 eV is attributed to a shake-up phenomenon.[48] The spectra of the films upon redox switching in $LiClO_4$/PC (Figure 3.9 (c) and (c')) showed equivalent peaks in the ranges 399.4-

399.5 eV, 400.7 eV and 403.0-403.2 eV; as the solvent changed to PC, the peak assigned to CH_3CN was not identified.

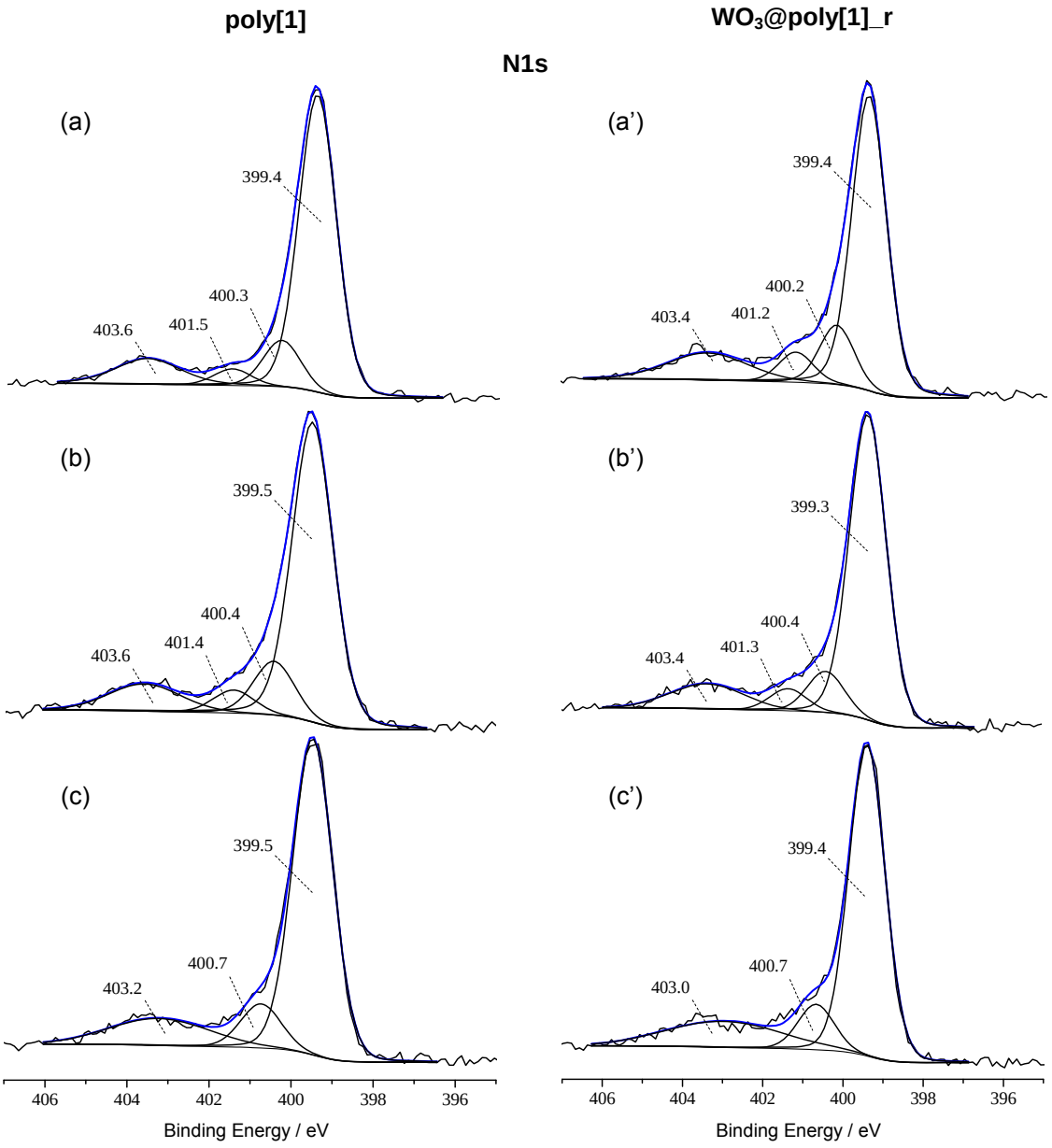

Figure 3.9 High-resolution XPS spectra of pristine poly[1] and WO_3@poly[1]_r in N1s region, with the corresponding deconvolutions, (a and a') before and after redox switching in (b and b') $LiClO_4/CH_3CN$ and (c and c') $LiClO_4$/PC.

The O1s spectra of pristine and nanocomposite films before redox switching (Figure 3.10 (a) and (a')) were deconvoluted with three peaks: a peak at 531.2 eV assigned to the oxygen from *salen* coordination sphere[34] and two other peaks at 532.4-532.6 eV and 533.3-533.4 eV attributed to occluded ClO_4^- with different neighbourhoods. In the nanocomposite spectrum, the peak at 531.2 eV also has the

contribution of O-W bonds from WO_3 and the peaks at higher energy from the –OH groups, C=O and C-O bonds of WO_3 contaminants. The films O 1s spectra after redox switching in $LiClO_4/CH_3CN$ (Figure 3.10 (b) and (b')) exhibit the same peak at 531.1-531.6 eV (O from *salen* coordination sphere)[34] and one peak at 532.7-533.1 eV, assigned to occluded ClO_4^-, in higher amounts, due to charge compensation processes during the redox cycles.[34]

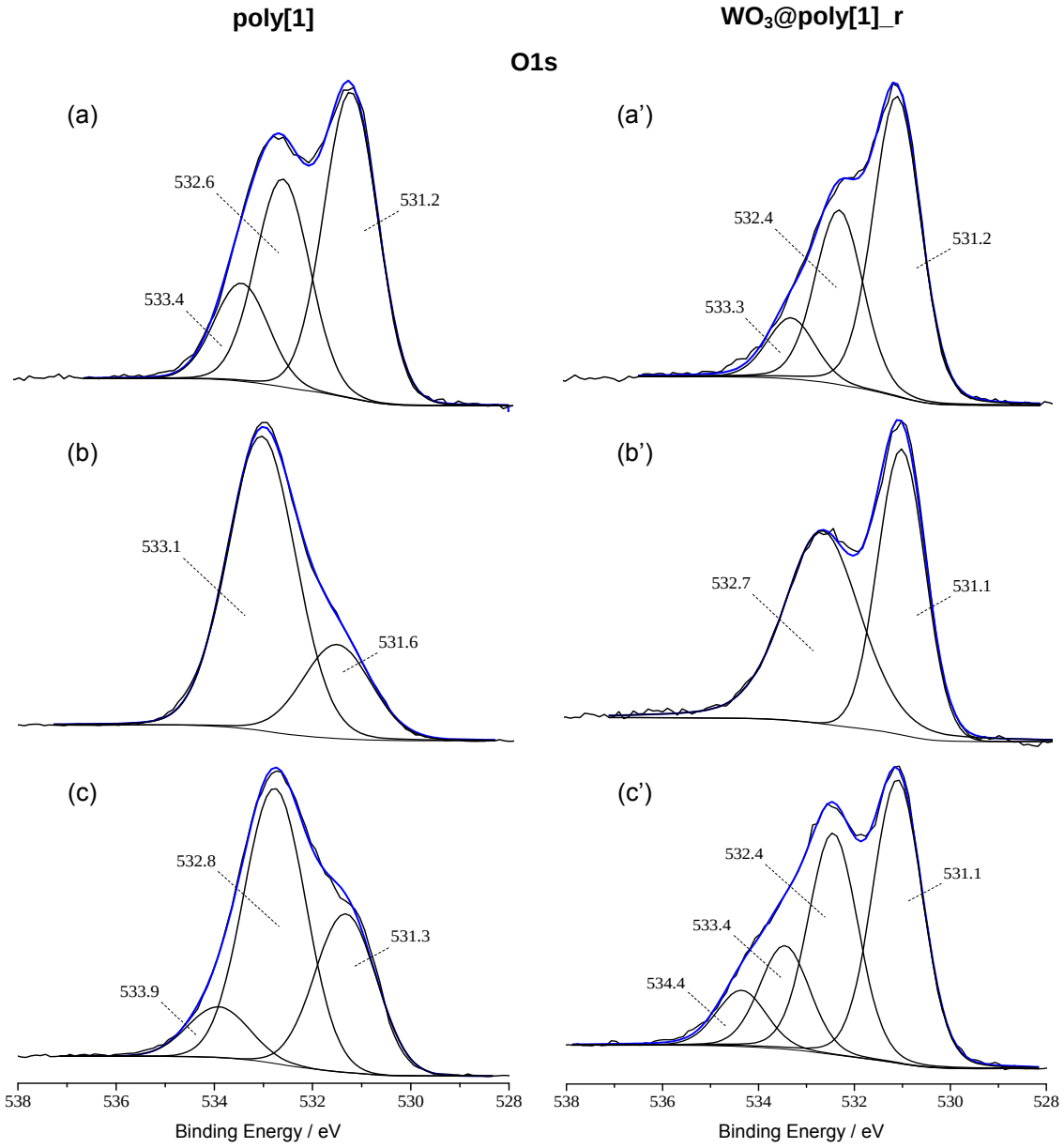

Figure 3.10 High-resolution XPS spectra of pristine poly[1] and WO_3@poly[1]_r in O1s region, with the corresponding deconvolutions, (a and a') before and after redox switching in (b and b') $LiClO_4/CH_3CN$ and (c and c') $LiClO_4$/PC.

After redox switching in $LiClO_4$/PC, the spectra of pristine poly[1] (Figure 3.10 (c)), besides the two peaks at 531.3 eV and 532.8 eV (similarly to redox switching in CH_3CN), also show an additional peak at 533.9 eV, assigned to oxygen-carbon bonds due to occluded PC.[49] In the spectra of WO_3@poly[1]_r after redox in $LiClO_4$/PC (Figure 3.10 (c')) it was also observed these three peaks at 531.1, 532.4 and 534.4 eV and other peak at 533.4 eV, assigned to ClO_4^- trapped on polymeric film during its electropolymerisation.

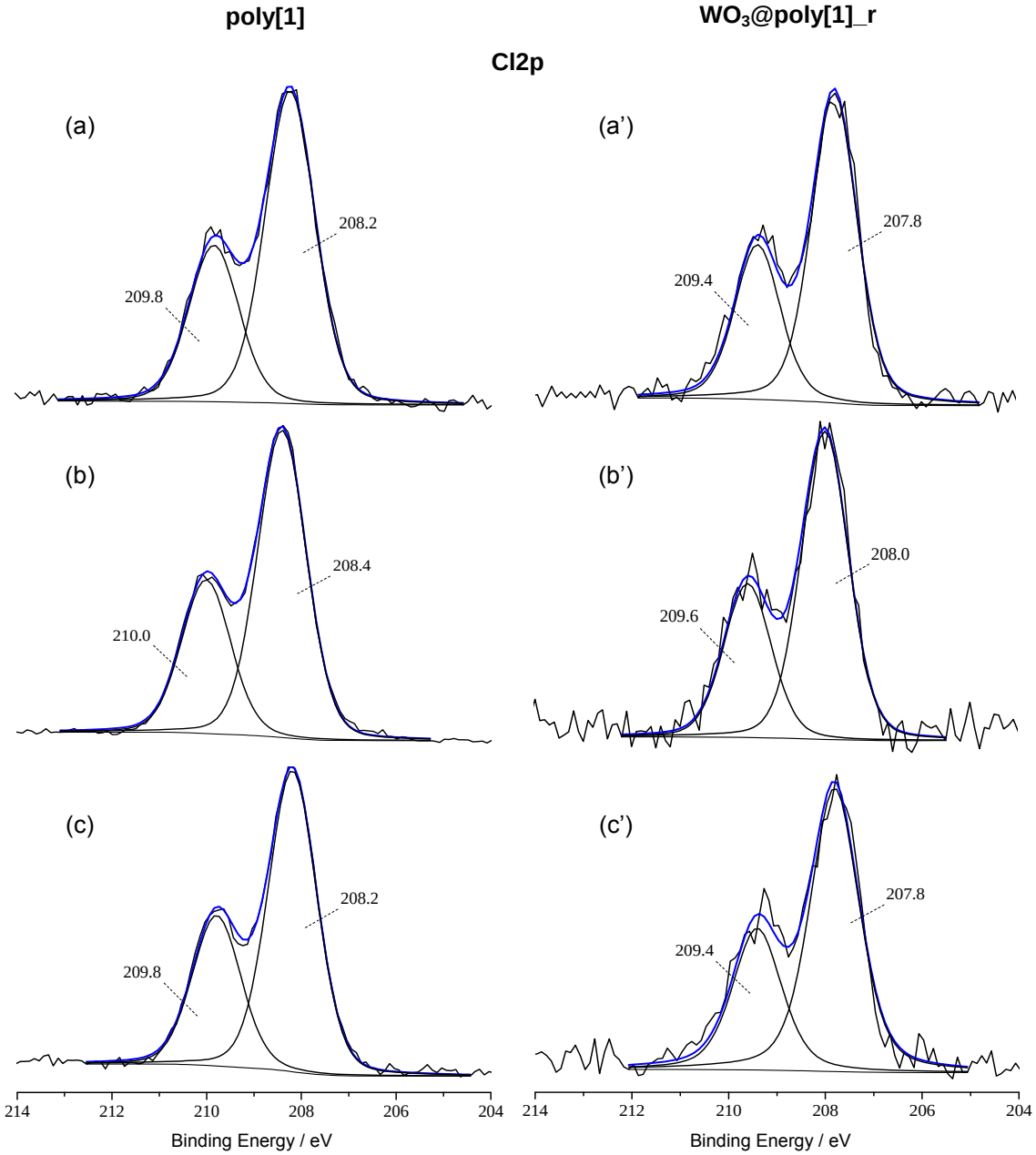

Figure 3.11 High-resolution XPS spectra of pristine poly[1] and WO_3@poly[1]_r in Cl2p region, with the corresponding deconvolutions, (a and a') before and after redox switching in (b and b') $LiClO_4/CH_3CN$ and (c and c') $LiClO_4$/PC.

The high resolution Cl2p spectra (Figure 3.11) show peaks assigned to $Cl2p_{3/2}$ (207.8-208.2 eV) and $Cl2p_{1/2}$ (209.4-210.0 eV) and are consistent with the presence of ClO_4^- from supporting electrolyte occluded within the films. In the Ni2p region (Figure 3.12) the high resolution spectra are characteristic of Ni in a formal +2 oxidation state and the peaks can be assigned to the $Ni2p_{3/2}$ (855.1-855.4 eV), $Ni2p_{3/2}$ satellite (860.1-860.7 eV), $Ni2p_{1/2}$ (872.3-872.5 eV) and $Ni2p_{1/2}$ satellite (877.3-877.8 eV).

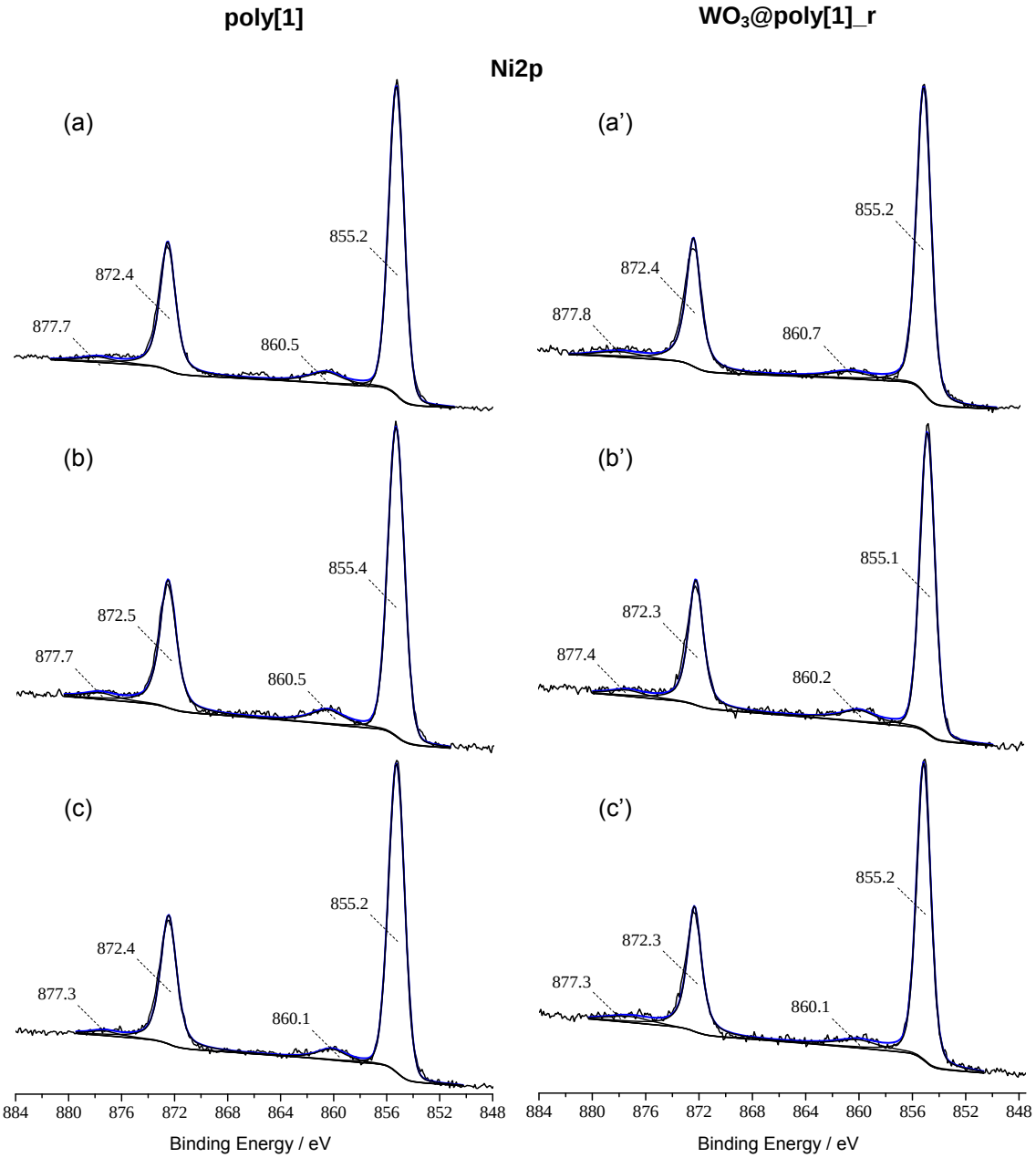

Figure 3.12 High-resolution XPS spectra of pristine poly[1] and WO_3@poly[1]_r in Ni2p region, with the corresponding deconvolutions, (a and a') before and after redox switching in (b and b') $LiClO_4/CH_3CN$ and (c and c') $LiClO_4$/PC.

The deconvoluted spectrum of the nanocomposite film, Figure 3.13, in the W4f region exhibits two peaks at 36.1-36.2 eV and 38.2-38.4 eV, with a doublet separation of $\Delta \approx 2.20$ eV, attributed to the $W^{(VI)}$ $4f_{7/2}$ and $W^{(VI)}$ $4f_{5/2}$ levels of the tungsten in WO_3,[39,43] similarly to the XPS data for free WO_3 NPs.

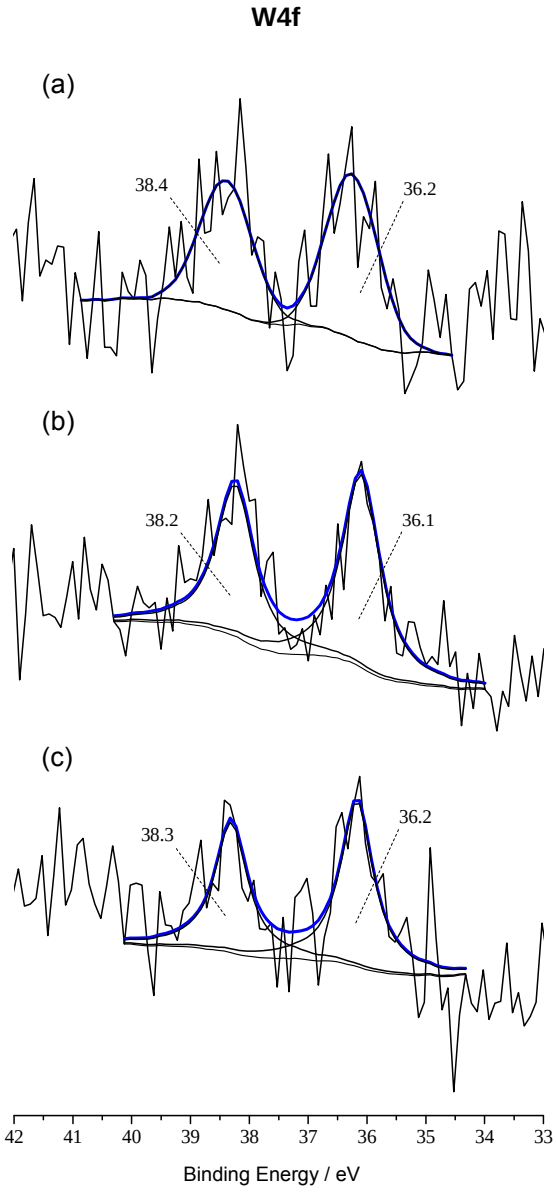

Figure 3.13 High-resolution XPS spectra of WO_3@poly[1]_r in W4f region, with the corresponding deconvolutions, (a) before and after redox switching in (b) $LiClO_4/CH_3CN$ and (c) $LiClO_4$/PC.

In Table 3.3 are summarised the surface atomic percentages of all elements and the calculated atomic ratios for films before and after redox switching in $LiClO_4/CH_3CN$ and $LiClO_4$/PC.

Table 3.3 XPS surface atomic percentages and atomic ratios of relevant elements for poly[1] and WO_3@poly[1]_r nanocomposite films, in their reduced states (*E* = 0.0 V).

Sample	Atomic %						Atomic Ratio		
	Ni	C	N	O	Cl	W	N/Ni	O/Ni	Cl/Ni
poly[1]									
Before redox	3.5	75.5	7.6	12.0	1.3	-	2.2	3.4	0.4
After redox in CH_3CN	2.5	64.8	6.4	22.4	3.9	-	2.6	9.0	1.6
After redox in PC	2.7	72.8	6.6	15.9	2.1	-	2.4	5.9	0.8
WO_3@poly[1]_r									
Before redox	3.5	76.9	8.0	10.6	1.0	0.01	2.3	3.0	0.3
After redox in CH_3CN	2.9	78.6	7.6	10.3	0.6	0.01	2.6	3.5	0.2
After redox in PC	2.8	76.7	6.4	13.3	0.8	0.03	2.3	4.7	0.3

Before the redox switching, the nanocomposite film shows N/Ni, O/Ni and Cl/Ni atomic ratios slightly larger than the expected values considering the [Ni(3-Mesalen)] chemical structure ($N/Ni_{theoretical}$ = $O/Ni_{theoretical}$ = 2.0), due to the presence of WO_3 NPs and trapping of some $LiClO_4/CH_3CN$ on polymeric matrix during the electropolymerisation step.

The WO_3@poly[1]_r films after redox switching in $LiClO_4/CH_3CN$ and $LiClO_4$/PC show only a slightly increase in atomic ratios (most notable for the O/Ni ratio) when compared with the large increase observed for poly[1] in similar conditions. The increase in O, Cl and N contents after redox switching is explained by the accumulation of ClO_4^- and solvent inside the film, as a consequence of the charge compensation/solvation processes along the several redox cycles.[34] For poly[1] submitted to redox switching in $LiClO_4$/PC, the increase in O/Ni and Cl/Ni is less noticeable than in $LiClO_4/CH_3CN$, indicating a smaller incorporation of ClO_4^- with PC, as already observed in Chapter 2. The lower incorporation of ClO_4^- in nanocomposite in comparison to the pristine film can be explained by the presence of the WO_3 NPs, which decrease the polymeric matrix packaging and thus facilitate the ingress / expulsion of supporting electrolyte.

The presence of W from the WO_3 NPs provides an indication of the successful preparation of the WO_3@poly[1]_r nanocomposite. Furthermore, the presence of W in films after redox switching indicate a stable composition for the nanocomposite as-prepared, with the WO_3 NPs remaining incorporated in the polymeric structure after the potential cycling.

In Figure 3.14 it is depicted a representative SEM micrograph of the WO_3@poly[1]_r film and the respective EDS spectrum at a selected region, identified as Z1.

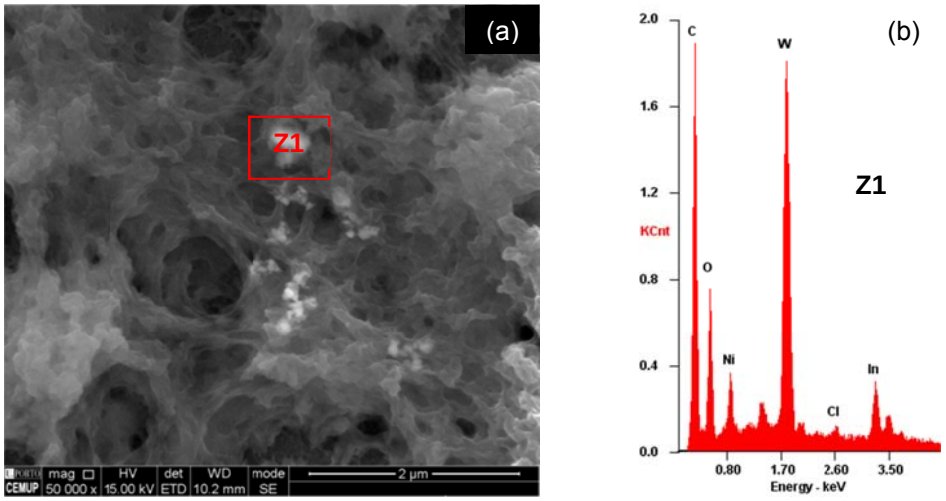

Figure 3.14 (a) Scanning electron micrograph and (b) respective EDS spectrum of WO_3@poly[1]_r film.

The micrograph shows a continuous layer with irregular surface, typical of the pristine poly[1] (see Chapter 2) over which are distinguished small fragments (region Z1). The analysis by EDS of these fragments (Figure 3.14 (b)) revealed that, beyond the compositional elements of the pristine film (C, O, Ni) and from the supporting electrolyte (Cl) and substrate (In), it was detected W, which corroborates the presence of WO_3 NPs occluded on Ni-*salen* polymeric matrix.

3.3.4 *In-situ* UV-Vis spectroscopy

In Figures 3.15 and 3.16 are depicted the absolute UV-Vis spectra acquired during the oxidation of the WO_3@poly[Ni(*salen*)] nanocomposites in $LiClO_4/CH_3CN$ and $LiClO_4$/PC, respectively; for comparison, the equivalent spectra for pristine poly[1] are also depicted. The spectra obtained during films reduction showed an inverse behaviour and were omitted for simplicity.

The nanocomposite spectra show four electronic bands in both supporting electrolytes, similarly to the spectra of the pristine film. The electronic bands profile with the applied potential is most readily appreciated in the differential spectra, depicted using the responses at selected potentials as reference potentials (Figures 3.17 and 3.18), and by the representation of the absorbance vs. potential (*Abs* vs. *E*) profiles, at the wavelength of the detected bands (Figures 3.15 and 3.16 (a'), (b') and (c')).

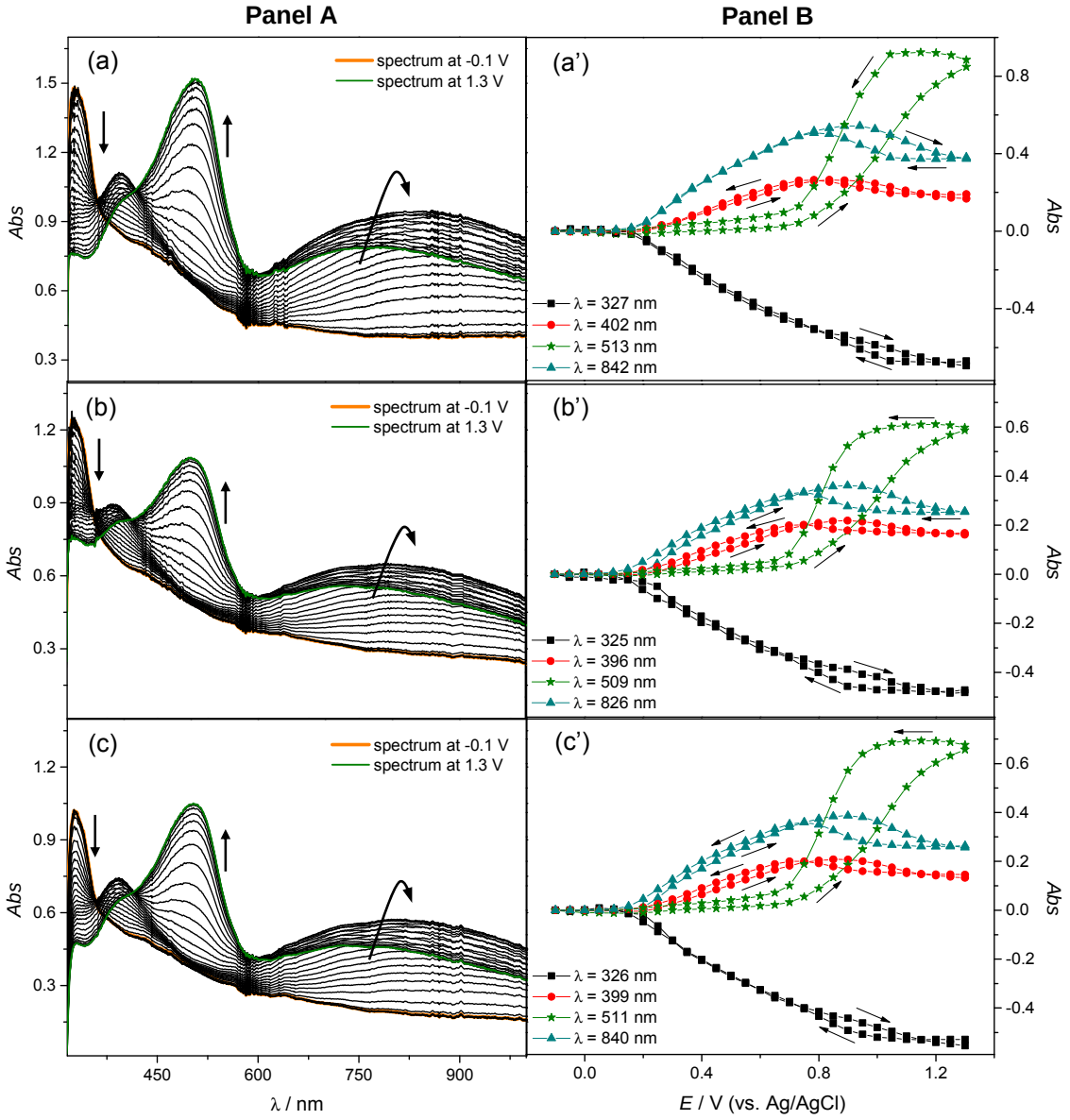

Figure 3.15 Panel A: Absolute UV-Vis spectra of (a) poly[1], (b) WO_3@poly[1]_s and (c) WO_3@poly[1]_r films acquired during films oxidation in 0.1 mol dm^{-3} $LiClO_4/CH_3CN$ (referenced to the electrolyte spectrum; Γ = 0.06-0.10 μmol cm^{-2}). Panel B: *Abs* vs. *E* plots for the electronic bands identified in absolute UV-Vis spectra, referenced to the spectra at *E* = -0.1 V (arrows indicate scan direction).

These representations revealed that the behaviour of the nanocomposites electronic bands as a function of the applied potential are similar to those of poly[1], and show three main band profiles, characteristic of the pristine (as described in Chapter 2) and other similar poly[M(*salen*)] films.[34,35]

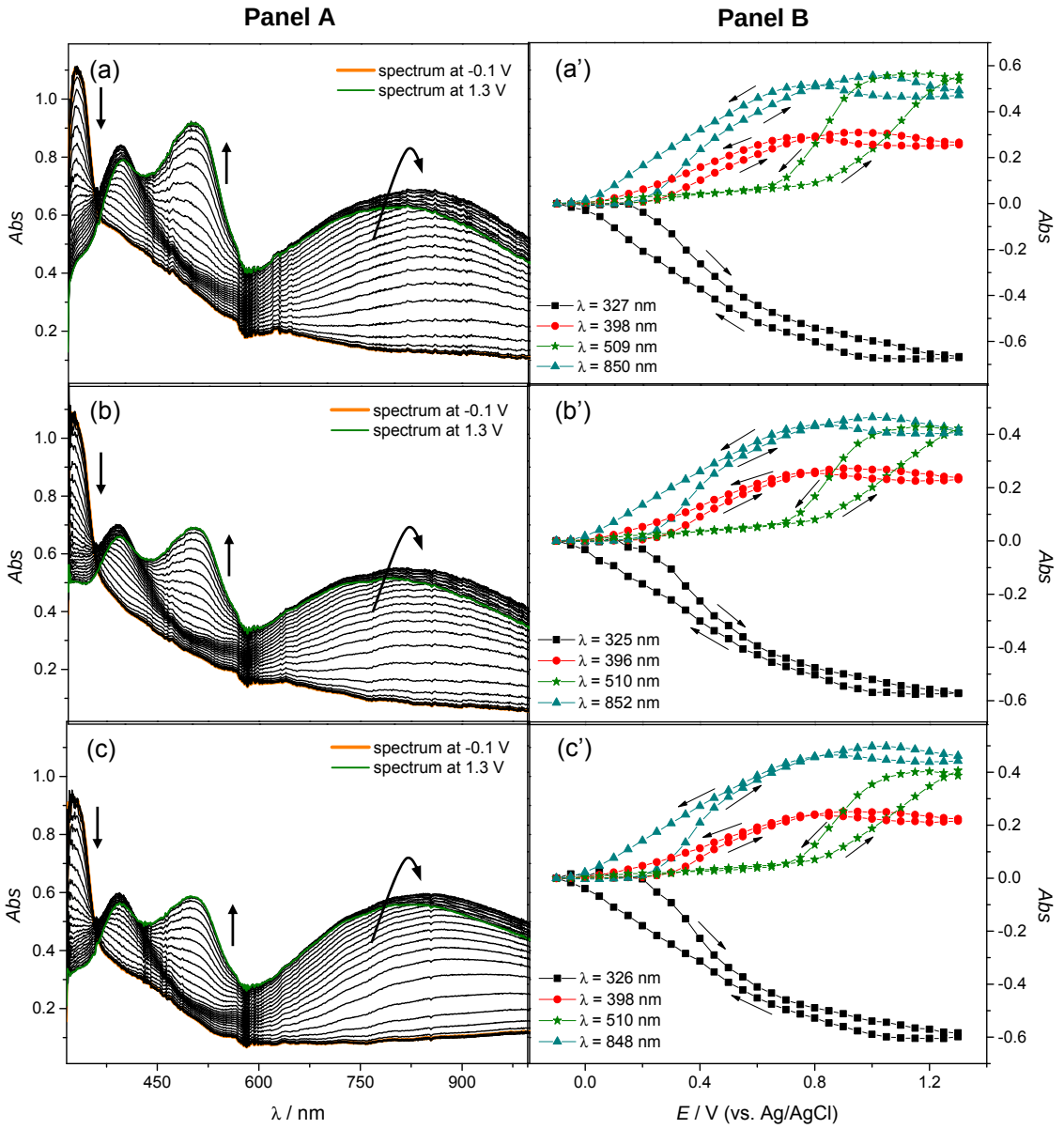

Figure 3.16 Panel A: Absolute UV-Vis spectra of (a) poly[1], (b) WO_3@poly[1]_s and (c) WO_3@poly[1]_r films acquired during films oxidation in 0.1 mol dm^{-3} $LiClO_4$/PC (referenced to the electrolyte spectrum; Γ= 0.06-0.10 μmol cm^{-2}). Panel B: *Abs* vs. *E* plots for the electronic bands identified in absolute UV-Vis spectra, referenced to the spectra at *E* = -0.1 V (arrows indicate scan direction).

The energies of the electronic bands are summarised in Table 3.4, as well as the molar extinction coefficients, ε, estimated using the Equation 2.1, from the slopes of *Abs* vs. *Q* plots (Figure 3.19).

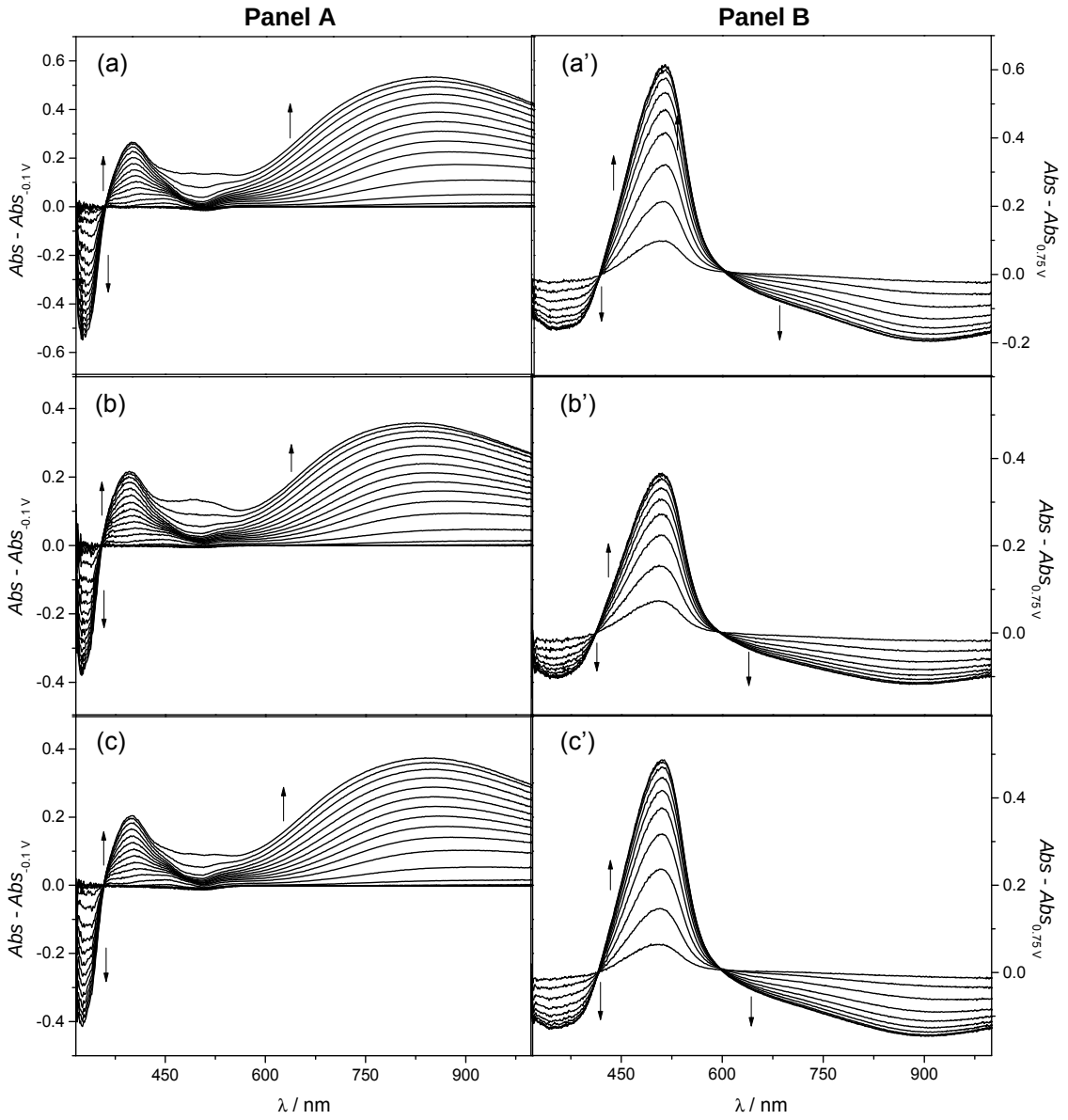

Figure 3.17 UV-Vis spectra of (a and a') poly[1], (b and b') WO_3@ poly[1]_s and (c and c') WO_3@ poly[1]_r acquired during films oxidation in $LiClO_4/CH_3CN$ from -0.1 to 0.75 V, referenced to the spectra of neutral films (Panel A) and from 0.75 to 1.3 V, referenced to the spectra of films at E = 0.75 V (Panel B).

Taking into account the rational of ligand-based film oxidation, supported by the electronic bands ε-values and previously proposed for pristine (Chapter 2) and other similar poly[M(*salen*)] films,[34,35,50] the following band assignment can be made: (i) the bands at λ = 325-327 nm are attributed to the intervalence transition (band gap, E_g = 3.79 eV for pristine film and E_g = 3.81 / 3.82 eV for nanocomposites), (ii) the bands at λ = 396-402 nm (3.09-3.13 eV) and λ = 826-852 nm (1.46-1.50 eV), that appears during the film oxidation, are attributed to transitions from the valence band to the antibonding and bonding polaron levels (or between polaron levels), respectively,

and (iii) the bands at λ = 509-513 nm (2.42-2.44 eV) are assigned to charge transfer (CT) transitions between the metal and the oxidised ligand.

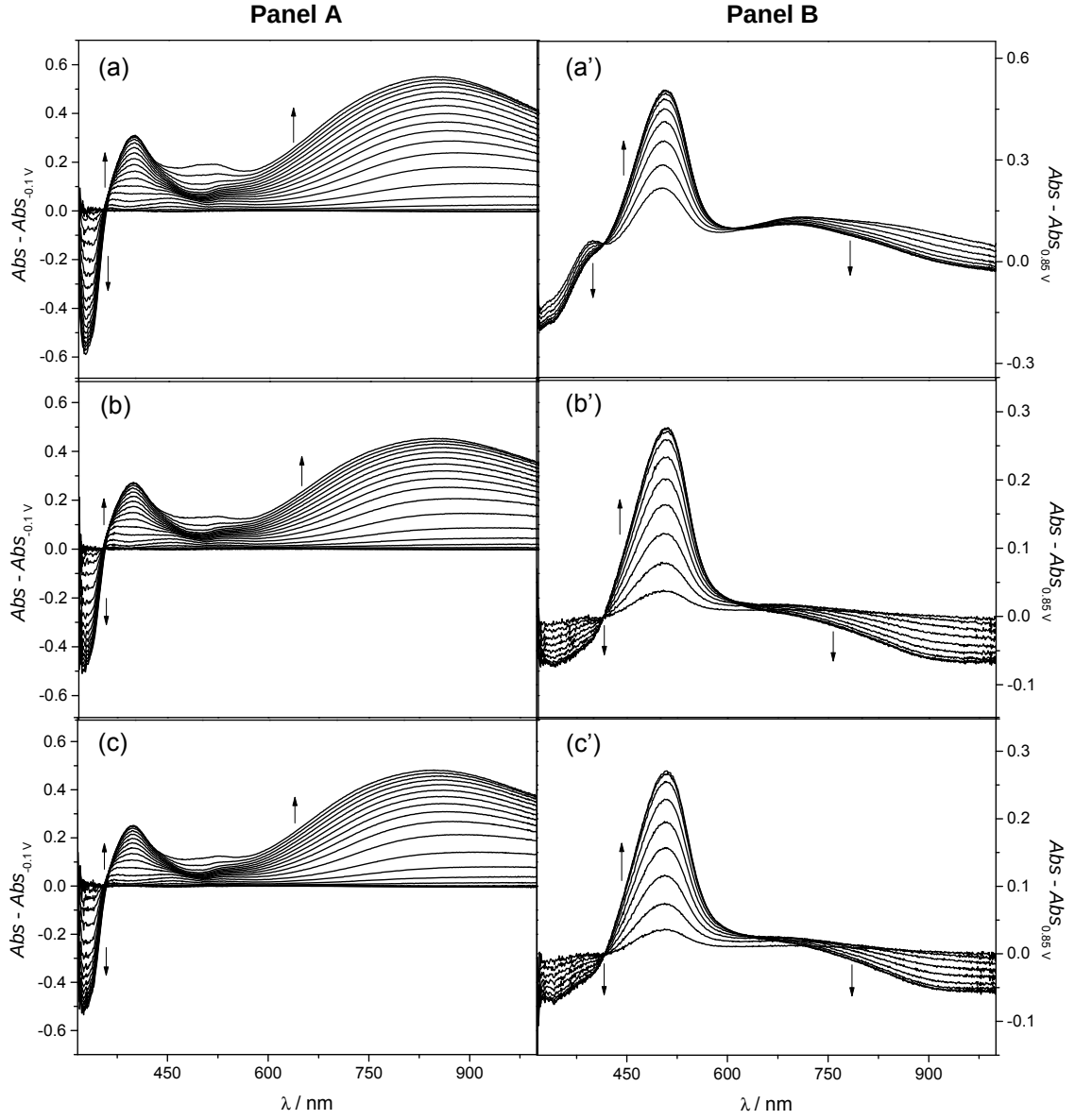

Figure 3.18 UV-Vis spectra of (a and a') poly[1], (b and b') WO_3@ poly[1]_s and (c and c') WO_3@ poly[1]_r acquired during films oxidation in $LiClO_4$/PC from -0.1 to 0.85 V, referenced to the spectra of neutral films (Panel A) and from 0.85 to 1.3 V, referenced to the spectra of films at *E* = 0.85 V (Panel B).

The data summarised in Table 3.4 reveal that the energies of the observed bands in nanocomposites are similar to those of the pristine film in the same supporting electrolyte, showing that the incorporation of WO_3 in poly[1] matrix did not change the metallopolymer electronic structure.

Table 3.4 Wavelengths of the electronic bands and respective energies and molar extinction coefficients (ε) for pristine poly[1] and WO_3@poly[1] nanocomposites.

Film	Supporting Electrolyte	λ_{max} / nm (eV)	ε x 10^{-3} / mol^{-1} dm^3 cm^{-1}
poly[1]	$LiClO_4/CH_3CN$	327 (3.79)	7.24
		402 (3.09)	3.89
		513 (2.42)	**17.27**
		842 (1.47)	6.96
	$LiClO_4$/PC	327 (3.79)	7.21
		398 (3.12)	4.26
		509 (2.44)	**11.35**
		850 (1.46)	6.77
WO_3@poly[1]_s	$LiClO_4/CH_3CN$	325 (3.82)	6.62
		396 (3.13)	3.98
		509 (2.44)	**15.03**
		826 (1.50)	6.40
	$LiClO_4$/PC	325 (3.82)	7.25
		396 (3.13)	4.51
		510 (2.43)	**9.94**
		852 (1.46)	6.53
WO_3@poly[1]_r	$LiClO_4/CH_3CN$	326 (3.81)	6.99
		399 (3.11)	3.85
		511 (2.43)	**15.72**
		840 (1.48)	6.66
	$LiClO_4$/PC	326 (3.81)	7.10
		398 (3.12)	4.11
		510 (2.43)	**9.78**
		848 (1.46)	6.60

The ε-values for the nanocomposite electronic bands are also similar to those of pristine film, except for the bands attributed to CT transitions at λ = 509-513 nm (2.42-2.44 eV) in $LiClO_4/CH_3CN$ and at λ = 509-510 nm (2.43-2.44 eV) in $LiClO_4$/PC. For the nanocomposites, the CT band ε-values decrease ≈ 36.0 % from $LiClO_4/CH_3CN$ to $LiClO_4$/PC electrolytes (ε ≈ 15.4 vs. 9.86 × 10^{-3} cm^{-1} mol^{-1} dm^3) similarly to pristine film and as described in Chapter 2. Beyond that, the main achievement is that the ε-values of these bands are ≈ 11.0 % (in $LiClO_4/CH_3CN$) and ≈ 13.1 % (in $LiClO_4$/PC) lower in nanocomposites than in pristine film: in $LiClO_4/CH_3CN$, for example, ε = 17.27 x 10^{-3} cm^{-1} mol^{-1} dm^3 for poly[1] and decreased to ε = 15.03 and 15.72 x 10^{-3} cm^{-1} mol^{-1} dm^3

for nanocomposites. This decrease of the CT band ε-values for nanocomposite films is also a very good outcome since this CT band is related with the over-oxidation and less stable oxidised states of poly-*salen* film, anticipating an increase in film stability towards over-oxidation due to the incorporation of WO_3 NPs.

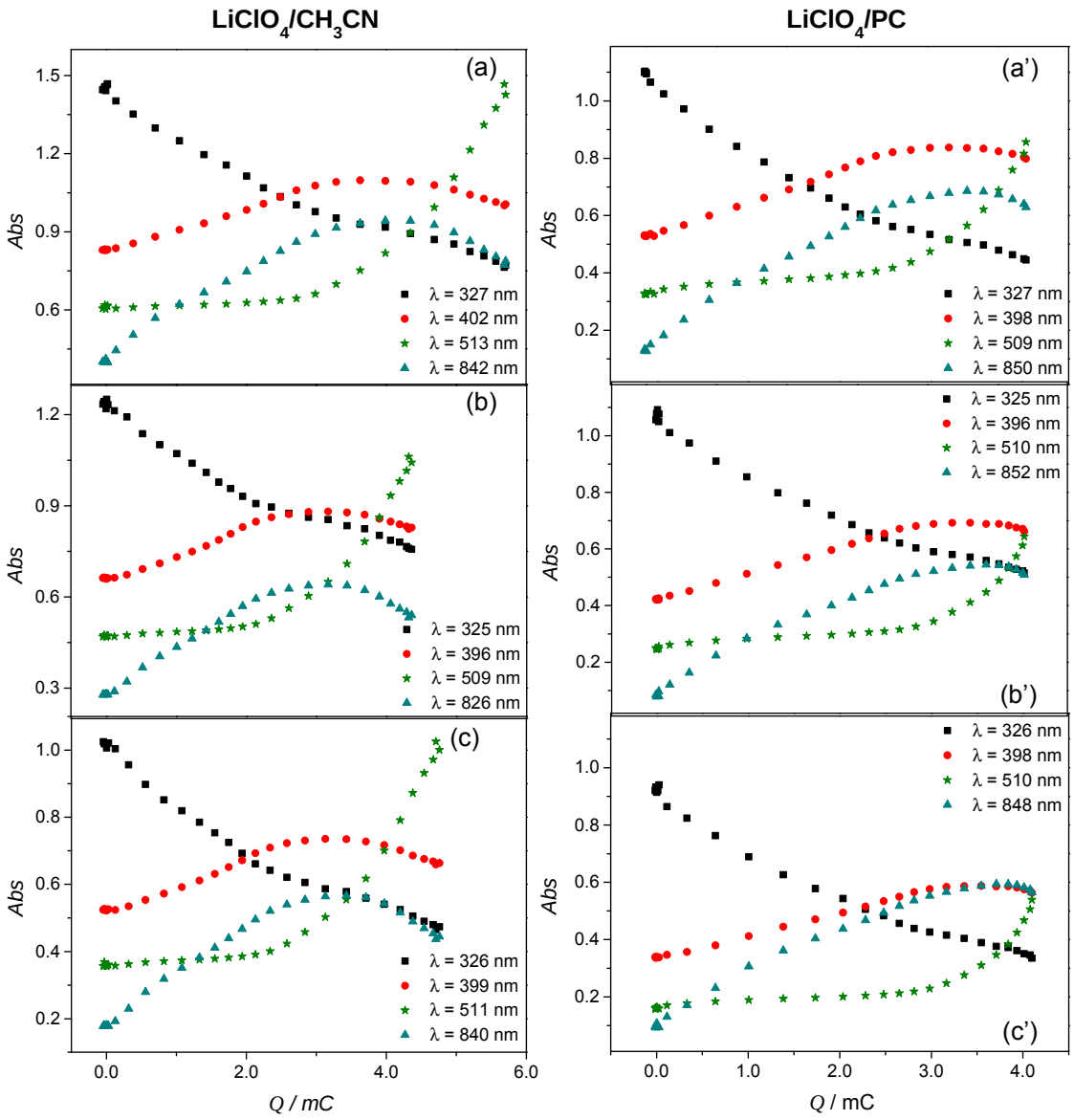

Figure 3.19 Plots of the *Abs* vs. *Q* for selected electronic bands of (a and a') poly[1], (b and b') WO_3@poly[1]_s and (c and c') WO_3@poly[1]_r in 0.1 mol dm^{-3} $LiClO_4/CH_3CN$ and $LiClO_4$/PC (for anodic scan).

3.3.5 Electrochromic properties

The EC parameters - switching times, optical contrasts, changes of the optical densities and colouration efficiencies - of WO_3@poly[1] nanocomposites were determined in order to evaluate the effect of WO_3 incorporation in the EC response of

the material. The studies were performed with nanocomposite films prepared from the two different pre-treatment starting solutions (ultrasound or ultrasound + reflux) and in $LiClO_4/CH_3CN$ and $LiClO_4$/PC supporting electrolytes, to explore the effect of these conditions in the EC properties.

In Figure 3.20 are depicted the chronoabsorptograms obtained for nanocomposites and pristine film in $LiClO_4/CH_3CN$ and $LiClO_4$/PC supporting electrolytes, considering the colour change between yellow (E = 0.0 V) and green (E = 0.7 V), at fixed λ = 750 nm.

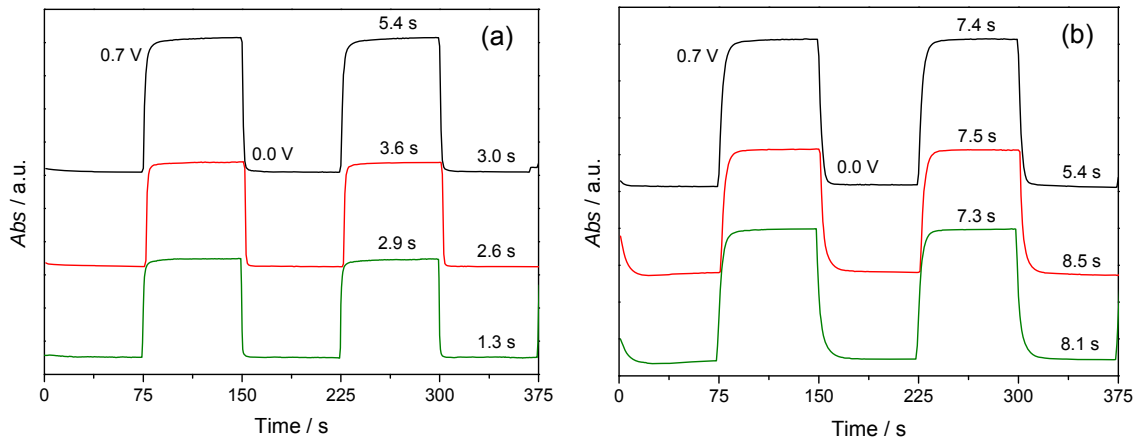

Figure 3.20 Chronoabsorptograms obtained for pristine (—), WO_3@poly[1]_s (—) and WO_3@poly[1]_r (—) films, at the fixed wavelength of λ = 750 nm in (a) $LiClO_4/CH_3CN$ and (b) $LiClO_4$/PC 0.1 mol dm^{-3}, indicating the measured switching times; E = 0.0 V (yellow) or 0.7 V (green), Γ = 0.06-0.10 μmol cm^{-2}.

The measured times ranging from τ = 1.3 and 5.4 s in $LiClO_4/CH_3CN$ and τ = 5.4 and 8.1 s in $LiClO_4$/PC; the higher switching times in $LiClO_4$/PC were already observed for pristine film (Chapter 2). In $LiClO_4/CH_3CN$ medium, the nanocomposites showed a decrease in switching times (faster responses) of 33.3 % for WO_3@poly[1]_s and 46.3 % for WO_3@poly[1]_r, in comparison with pristine film, which shows the advantage of the WO_3 incorporation. In $LiClO_4$/PC, the nanocomposites switching times remain similar or slight increase from those of the pristine film.

In Table 3.5 are summarised the optical contrasts, changes of the optical density, charge requirements and colouration efficiencies, determined from the chronoabsorptograms considering the full optical change. In $LiClO_4/CH_3CN$, the ΔT increased from ΔT = 18.7 % in pristine film to $\Delta T \approx$ 31.0 % in nanocomposites, which corresponds to an improvement of ≈ 40 %, whereas in $LiClO_4$/PC, ΔT of nanocomposites remains similar or slight decrease, in comparison with poly[1] film.

Table 3.5 Optical contrasts (ΔT %), changes of the optical density (ΔOD), charge requirements (Q_d), and colouration efficiencies (η) for pristine poly[1] and WO_3@poly[1] nanocomposite films in $LiClO_4/CH_3CN$ and $LiClO_4$/PC supporting electrolytes, at λ = 750 nm.

Film	Supporting Electrolyte	ΔT %	ΔOD	Q_d / mC cm^{-2}	η / cm^2 C^{-1}
poly[1]	$LiClO_4/CH_3CN$	18.7	0.40	4.50	90.02
	$LiClO_4$/PC	45.5	0.39	4.64	85.04
WO_3@poly[1]_s	$LiClO_4/CH_3CN$	30.8	0.32	2.74	115.19
	$LiClO_4$/PC	39.4	0.33	3.87	85.86
WO_3@poly[1]_r	$LiClO_4/CH_3CN$	31.5	0.30	2.88	103.63
	$LiClO_4$/PC	44.6	0.35	4.33	81.59

Each polymeric film shows similar ΔOD values in both supporting electrolytes. Nonetheless, ΔOD values slightly decrease from ΔOD ≈ 0.40 in pristine film to ΔOD ≈ 0.33 in WO_3@poly[1]_s (decrease of 17.5 %) and ΔOD = 0.30/035 in WO_3@poly[1]_r (decrease of 25.0 % in $LiClO_4/CH_3CN$ and 10.2 % in $LiClO_4$/PC).

Furthermore, in $LiClO_4/CH_3CN$, the colouration efficiencies increase from η = 90.02 cm^2 C^{-1} for pristine film to η = 115.19 cm^2 C^{-1} for WO_3@poly[1]_s (+ 21.7 %) and η = 103.63 cm^2 C^{-1} for WO_3@poly[1]_r (+13.1 %), which indicates a greater power efficiency of the nanocomposite films, explained by the decrease of the charge requirements of the nanocomposite films. In $LiClO_4$/PC, the η-values obtained for nanocomposites films remains similar to the pristine film (range between η = 81.59 - 85.86 cm^2 C^{-1}), with the decrease of charge requirements being less remarkable for nanocomposites in this electrolyte. The enhancement observed in some EC properties for nanocomposites can be explained by the better charge carrier transport due to the organized network structure provided by the WO_3 NPs, which can act as a “freeway” for the charge carriers.[27] The new nanoarchitecture provided by the WO_3 NPs incorporation in poly[1] can also favour the supporting electrolyte movement inside the film structure and, thus allow a faster electrochromic response (in $LiClO_4/CH_3CN$). Moreover, apart from the switching times more favourable for WO_3@poly[1]_r, the remaining EC properties are similar for both nanocomposite films.

The electrochemical stability of the WO_3@poly[1]_r nanocomposite film was evaluated by chronoamperometry during around 10 000 redox cycles in $LiClO_4$/PC 0.1 mol dm^{-3}; this supporting electrolyte was chosen because already showed to be the most favourable for a good stability performance of the pristine film (Chapter 2). The chronoamperograms obtained are depicted in Figure 3.21, along with the results obtained in a similar experiment for pristine poly[1]. The data revealed that the

nanocomposite has a lower electrochemical stability than the pristine film (29.6 % vs. 13.7 % of charge loss).

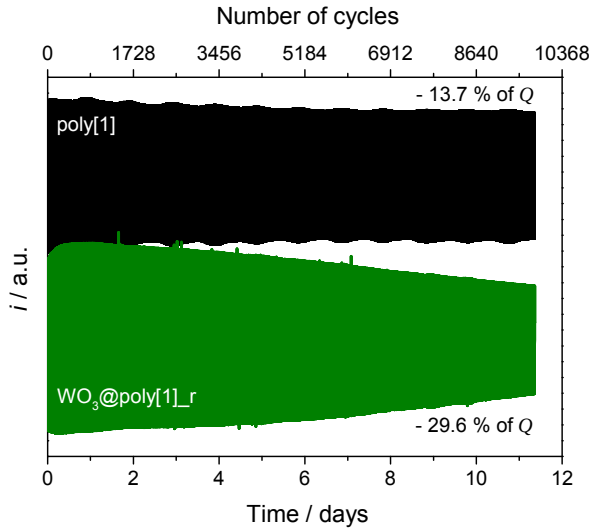

Figure 3.21 Chronoamperograms of poly[1] and WO_3@poly[1]_r in 0.1 mol dm^{-3} $LiClO_4$/PC, applying two potential pulses of 50 s, with potential alternating between 0.0 and 0.7 V.

3.4 Conclusions

The results showed that poly[1] was successfully electropolymerised in the presence of WO_3 NPs, previously prepared and characterised by XRD, XPS and FTIR. These techniques confirmed the preparation of quasi-spherical WO_3 nanoparticles with a monoclinic structure, with higher degree of crystallinity and sizes of ≈ 38 or 35 nm (SEM or TEM, respectively), similar to those estimated by XRD ≈ 37 nm.

The obtained nanocomposite films showed similar electrochemical responses to the pristine film, but with higher electroactive surface coverages, which appoint the advantage of the polymeric nanocomposite assemblage. SEM and XPS confirmed the presence of WO_3 NPs on the poly[1] matrix. Furthermore, the XPS analysis revealed that the redox processes promote the accumulation of large amounts of supporting electrolyte (due to charge compensation processes) in polymeric matrix, although in a lesser extent for nanocomposite film. The data obtained by UV-Vis spectroscopy showed that the electronic bands of nanocomposite films have similar profiles and energies to those of poly[1], confirming the maintenance of the pristine film electronic structure. Nevertheless, the lower ε-values of the CT bands for nanocomposites revealed a higher stability of the composite for over-oxidation processes.

The nanocomposite films showed more favourable EC properties in $LiClO_4/CH_3CN$ than the pristine film, with lower switching times (ranging between

τ = 1.3 and 3.6 s), higher optical contrasts (ΔT = 30.8 / 31.5 %) and better colouration efficiencies (η = 103.63 / 115.19 cm^2 C^{-1}). These results revealed the advantage of the preparation of the nanocomposite in the pursue for a solution to improve the EC properties of the pristine poly[1]. However, in $LiClO_4$/PC there was no significant enhancement of the nanocomposite EC properties when compared to the pristine film, what is a drawback for future technological applications.

References

[1] Pascariu, P.; Airinei, A.; Grigoras, M.; Vacareanu, L.; Iacomi, F. *Appl. Surf. Sci.* **2015**, *352*, 95.

[2] Guo, F. J.; Mi, H. Y.; Zhou, J. P.; Zhao, Z. B.; Qiu, J. S. *Carbon* **2015**, *95*, 323.

[3] Abdulla, S.; Mathew, T. L.; Pullithadathil, B. *Sens. Actuator B-Chem.* **2015**, *221*, 1523.

[4] Rafiqi, F. A.; Majid, K. *Synth. Met.* **2015**, *202*, 147.

[5] Janaky, C.; de Tacconi, N. R.; Chanmanee, W.; Rajeshwar, K. *J. Phys. Chem. C* **2012**, *116*, 4234.

[6] Zhu, J. H.; Wei, S. Y.; Zhang, L.; Mao, Y. B.; Ryu, J.; Mayinakuli, P.; Karki, A. B.; Young, D. P.; Guo, Z. H. *J. Phys. Chem. C* **2010**, *114*, 16335.

[7] Ma, D. Y.; Shi, G. Y.; Wang, H. Z.; Zhang, Q. H.; Li, Y. G. *J. Mater. Chem. A* **2014**, *2*, 13541.

[8] Moon, S. J.; Baranoff, E.; Zakeeruddin, S. M.; Yeh, C. Y.; Diau, E. W. G.; Gratzel, M.; Sivula, K. *Chem. Commun.* **2011**, *47*, 8244.

[9] Heo, J. H.; Im, S. H.; Noh, J. H.; Mandal, T. N.; Lim, C. S.; Chang, J. A.; Lee, Y. H.; Kim, H. J.; Sarkar, A.; Nazeeruddin, M. K.; Gratzel, M.; Seok, S. I. *Nat. Photonics* **2013**, *7*, 487.

[10] Hidalgo, D.; Bocchini, S.; Fontana, M.; Saracco, G.; Hernandez, S. *RSC Adv.* **2015**, *5*, 49429.

[11] Jain, R.; Tiwari, D. C.; Karolia, P. *J. Mol. Liq.* **2014**, *196*, 308.

[12] Chen, L.; Song, Z. X.; Liu, G. C.; Qiu, J. S.; Yu, C.; Qin, J. W.; Ma, L.; Tian, F. Q.; Liu, W. *J. Phys. Chem. Solids* **2013**, *74*, 360.

[13] Tovide, O.; Jaheed, N.; Mohamed, N.; Nxusani, E.; Sunday, C. E.; Tsegaye, A.; Ajayi, R. F.; Njomo, N.; Makelane, H.; Bilibana, M.; Baker, P. G.; Williams, A.; Vilakazi, S.; Tshikhudo, R.; Iwuoha, E. I. *Electrochim. Acta* **2014**, *128*, 138.

[14] Hicks, S. M.; Killard, A. J. *Sens. Actuator B-Chem.* **2014**, *194*, 283.

[15] Su, P. G.; Peng, Y. T. *Sens. Actuator B-Chem.* **2014**, *193*, 637.

[16] Mane, A. T.; Navale, S. T.; Patil, V. B. *Org. Electron.* **2015**, *19*, 15.

[17] Zou, B. X.; Liu, X. X.; Diamond, D.; Lau, K. T. *Electrochim. Acta* **2010**, *55*, 3915.

[18] Zou, B. X.; Liang, Y.; Liu, X. X.; Diamond, D.; Lau, K. T. *J. Power Sources* **2011**, *196*, 4842.

[19] Yang, P. H.; Sun, P.; Chai, Z. S.; Huang, L. H.; Cai, X.; Tan, S. Z.; Song, J. H.; Mai, W. J. *Angew. Chem.-Int. Edit.* **2014**, *53*, 11935.

[20] Sydam, R.; Deepa, M.; Shivaprasad, S. M.; Srivastava, A. K. *Sol. Energy Mater. Sol. Cells* **2015**, *132*, 148.

[21] Wei, H. G.; Yan, X. R.; Wu, S. J.; Luo, Z. P.; Wei, S. Y.; Guo, Z. H. *J. Phys. Chem. C* **2012**, *116*, 25052.

[22] Nwanya, A. C.; Jafta, C. J.; Ejikeme, P. M.; Ugwuoke, P. E.; Reddy, M. V.; Osuji, R. U.; Ozoemena, K. I.; Ezema, F. I. *Electrochim. Acta* **2014**, *128*, 218.

[23] Cai, G. F.; Tu, J. P.; Zhou, D.; Zhang, J. H.; Wang, X. L.; Gu, C. D. *Sol. Energy Mater. Sol. Cells* **2014**, *122*, 51.

[24] Zhang, J.; Tu, J. P.; Zhang, D.; Qiao, Y. Q.; Xia, X. H.; Wang, X. L.; Gu, C. D. *J. Mater. Chem.* **2011**, *21*, 17316.

[25] Zhang, J.; Tu, J. P.; Du, G. H.; Dong, Z. M.; Wu, Y. S.; Chang, L.; Xie, D.; Cai, G. F.; Wang, X. L. *Sol. Energy Mater. Sol. Cells* **2013**, *114*, 31.

[26] Dulgerbaki, C.; Oksuz, A. U. *Electroanal.* **2014**, *26*, 2501.

[27] Janaky, C.; Rajeshwar, K. *Prog. Polym. Sci.* **2015**, *43*, 96.

[28] Pinheiro, C.; Parola, A. J.; Pina, F.; Fonseca, J.; Freire, C. *Sol. Energy Mater. Sol. Cells* **2008**, *92*, 980.

[29] Branco, A.; Pinheiro, C.; Fonseca, J.; Tedim, J.; Carneiro, A.; Parola, A. J.; Freire, C.; Pina, F. *Electrochem. Solid State Lett.* **2010**, *13*, J114.

[30] Janaky, C.; de Tacconi, N. R.; Chanmanee, W.; Rajeshwar, K. *J. Phys. Chem. C* **2012**, *116*, 19145.

[31] Freire, C.; de Castro, B. *J. Chem. Soc.-Dalton Trans.* **1998**, 1491.

[32] Deepa, M.; Sharma, R.; Basu, A.; Agnihotry, S. A. *Electrochim. Acta* **2005**, *50*, 3545.

[33] Sun, X. L.; Cao, H. T.; Liu, Z. M.; Li, J. Z. *Appl. Surf. Sci.* **2009**, *255*, 8629.

[34] Fonseca, J.; Tedim, J.; Biernacki, K.; Magalhaes, A. L.; Gurman, S. J.; Freire, C.; Hillman, A. R. *Electrochim. Acta* **2010**, *55*, 7726.

[35] Tedim, J.; Patricio, S.; Fonseca, J.; Magalhaes, A. L.; Moura, C.; Hillman, A. R.; Freire, C. *Synth. Met.* **2011**, *161*, 680.

[36] Amb, C. M.; Dyer, A. L.; Reynolds, J. R. *Chem. Mat.* **2011**, *23*, 397.

[37] Wu, T. Y.; Liao, J. W.; Chen, C. Y. *Electrochim. Acta* **2014**, *150*, 245.

[38] Dawson, G.; Zhou, W. Z.; Blackley, R. *Phys. Chem. Chem. Phys.* **2011**, *13*, 20923.

[39] Bertus, L. M.; Faure, C.; Danine, A.; Labrugere, C.; Campet, G.; Rougier, A.; Duta, A. *Mater. Chem. Phys.* **2013**, *140*, 49.

[40] Costa, C.; Pinheiro, C.; Henriques, I.; Laia, C. A. T. *ACS Appl. Mater. Interfaces* **2012**, *4*, 1330.

[41] Zou, X. X.; Li, G. D.; Wang, P. P.; Su, J.; Zhao, J.; Zhou, L. J.; Wang, Y. N.; Chen, J. S. *Dalton Trans.* **2012**, *41*, 9773.

[42] Socrates, G. *Infrared and Raman Characteristic Group Frequencies - Tables and Charts*; third ed.; John Wiley & Sons, Ltd.: England, **2004**.

[43] Meng, Z. C.; Fujii, A.; Hashishin, T.; Wada, N.; Sanada, T.; Tamaki, J.; Kojima, K.; Haneoka, H.; Suzuki, T. *J. Mater. Chem. C* **2015**, *3*, 1134.

[44] Cai, Z. X.; Li, H. Y.; Yang, X. N.; Guo, X. *Sens. Actuator B-Chem.* **2015**, *219*, 346.

[45] Zhu, J.; Li, W. Z.; Li, J.; Li, Y. M.; Hu, H. S.; Yang, Y. H. *Electrochim. Acta* **2013**, *112*, 191.

[46] Salmaoui, S.; Sediri, F.; Gharbi, N.; Perruchot, C.; Aeiyach, S.; Rutkowska, I. A.; Kulesza, P. J.; Jouini, M. *Appl. Surf. Sci.* **2011**, *257*, 8223.

[47] Brown, N. M. D.; Hewitt, J. A.; Meenan, B. J. *Surf. Interface Anal.* **1992**, *18*, 187.

[48] Goldman, A. I. *X-Ray Techniques. Characterization of Materials.*; Wiley, **2002**.

[49] Weng, L. T.; Poleunis, C.; Bertrand, P.; Carlier, V.; Sclavons, M.; Franquinet, P.; Legras, R. *J. Adhes. Sci. Technol.* **1995**, *9*, 859.

[50] Vilas-Boas, M.; Freire, C.; de Castro, B.; Christensen, P. A.; Hillman, A. R. *Chem.-Eur. J.* **2001**, *7*, 139.

Chapter 4

Multicolour electrochromic film based in a TiO_2@poly[Ni(*salen*)] nanocomposite with excellent electrochemical stability

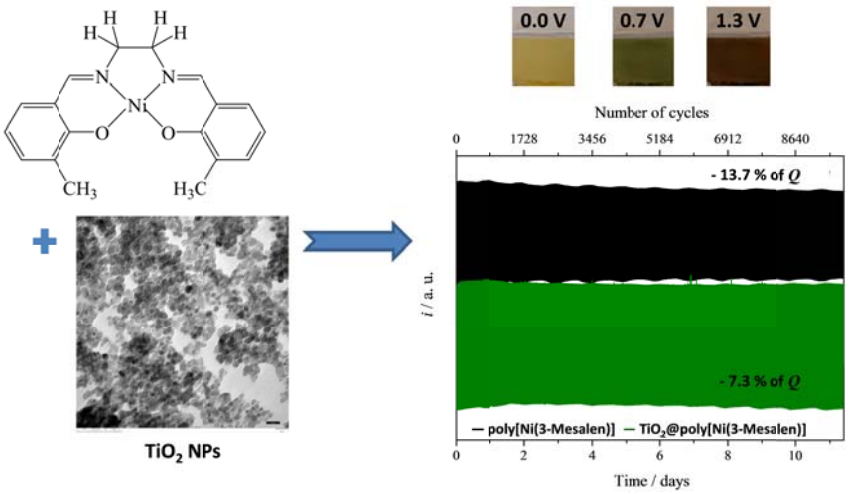

4

Multicolour electrochromic film based in a TiO_2@poly[Ni(*salen*)] nanocomposite with excellent electrochemical stability[1,2,3]

Abstract

This chapter reports the electrochromic properties and performance of a polymeric nanocomposite prepared through the potentiodynamic deposition of the transition metal complex [Ni(3-Mesalen)], designated as [1], in the presence of TiO_2 nanoparticles. The effects of several TiO_2 loadings and of the electropolymerisation scan rate in the electrochemical properties of nanocomposite films (designated as TiO_2@poly[1]) were also evaluated.

The TiO_2 NPs were prepared by sol-gel method and characterised by several techniques that revealed spherical morphology, crystallite size of 9.7 ± 1.1 nm and a composition of anatase (65.5 %) and brookite (34.5 %).

The entrapment of TiO_2 NPs on the poly[1] matrix was confirmed by XPS and SEM/EDS. The nanocomposite films TiO_2@poly[1] showed similar electrochemical responses to the pristine poly[1] film, but with higher electroactive areas and electroactive surface coverages, showing the advantage of nanocomposite preparation. The increase in Γ-values for nanocomposites prepared with 5 and 15 wt.% TiO_2 loading and further decrease for higher loadings (25 wt.%) indicated that there is an optimal loading, from which the electropolymerisation of poly[1] is hampered. The nanocomposite and pristine films showed similar electronic band profiles and energies, indicating that the electronic structure of poly[1] was retained in nanocomposite;

[1] Adapted from: M. Nunes, C. Moura, A. R. Hillman, C. Freire, Multicolour electrochromic film based in a TiO_2@poly[Ni(*salen*)] nanocomposite with excellent electrochemical stability. Submitted.

[2] M. Nunes's contribution to the publication: preparation and characterisation of the TiO_2 nanoparticles, preparation of the TiO_2@poly[1] nanocomposite and pristine poly[1] films, their characterisation, evaluation of the electrochromic properties and manuscript preparation.

[3] The experimental details on the electrochemical/spectroelectrochemical and remaining characterisation techniques are indicated in Appendices A and C, respectively.

nonetheless, lower ε-values were obtained for the CT band of the former film, revealing a superior stability of the nanocomposite for ligand high oxidation states.

The TiO_2@poly[1] nanocomposite showed interesting colour changes, from yellow in reduced state to green and russet in oxidised states, with a superior electrochemical stability, proved by the charge loss of only 7.3 % upon almost 10 000 redox cycles, which represents an electrochemical stability improvement of 46.7 % in comparison to pristine poly[1]; an improvement of 16.7 % in the optical modulation (ΔOD) was also observed for nanocomposite film.

4.1 Introduction

In the last years, the continuous development of new technologies demands novel materials and structures with specific tailored properties.[1] In this context, nanohybridisation of a conducting organic polymer and a metal oxide semiconductor has been recognised as one of the most attractive combinations of organic/inorganic composite structures.[2] The new nanohybrids have the advantages of receiving individual semiconducting functions from the polymer and the metal oxide (p/n junction)[3] and are effective candidates for application in solar cells,[4] electrochemical capacitors,[5,6] lithium batteries,[7] water splitting,[8] sensors[9] and electrochromic devices.[10]

Conducting polymers are a widely studied class of electrochromic materials[11] that show interesting optical properties, due to its multiple redox states with rich colour changes.[12-14] The electrochemical stability and the switching reversibility of the CPs can be enhanced by their combination with organised metal oxide nanostructures, taking advantage of the high surface-to-volume ratio and short diffusion distances for ion/electron transport promoted by the nanomaterial.[15,16] In fact, the synergetic combination of the merits of CPs and metal oxides provides an opportunity to develop new hybrid materials with improved EC properties, in which the colouration change is induced by the CPs redox reactions and the metal oxide has an important role in electronic transport through the metal oxide conduction band.[2,17]

Among the several metal oxides, titanium dioxide (TiO_2) is one of the most investigated wide gap semiconductors, due to its low cost, non-toxicity and good chemical stability.[18,19] The TiO_2 ability to act as electron acceptor and, so, to form electron donor-acceptor pairs when interacting with a p-type CP, raises the possibility that the changes induced by its incorporation go well beyond simply compositional and morphological modifications.[20] In the last years, some examples of TiO_2/CPs hybrids have been reported as new EC materials through the combination of TiO_2 with polyaniline (PANI),[16,20,21] polypyrrole[2] and poly(3,4-ethylenedioxythiophene):

poly(styrene sulfonic acid) (PEDOT:PSS),[22] for instance. In general, the nanocomposites obtained showed faster response times and higher optical contrasts, colouration efficiencies and electrochemical stability.

In this chapter it is described the preparation and characterisation of a hybrid film based in the incorporation of TiO_2 NPs on the matrix of poly[Ni(3-Mesalen)] film, designated as poly[1], and the evaluation of its EC properties. The EC properties of the electroactive metallopolymers poly[M(*salen*)], M ≡ transition metal, have been studied and explore to EC device fabrication;[23,24] in particular, the EC performance of pristine poly[1], described in Chapter 2, showed promising results, with an acceptable electrochemical stability (charge loss of 34.3 % after ≈ 9000 cycles) and interesting colour changes (from yellow in neutral state to green and russet in oxidised states). However, to potentiate its commercial application, the EC properties of poly[1] still need to be improved. Similarly to CPs, this goal can be pursued by the preparation of hybrids with semiconductors. The nanocomposite of poly[1] with WO_3 NPs prepared and discussed in Chapter 3, showed a slight improvement of the EC properties in comparison to the pristine film: lower switching times and higher optical contrasts and colouration efficiencies, but only in $LiClO_4/CH_3CN$ medium. Thus, in this chapter, it is explored the effect of the incorporation of TiO_2 NPs in the EC properties of the host polymeric film. TiO_2 is a n-type semiconductor, such as WO_3, but has a higher band gap (≈ 3.2 eV),[25] similar to that of the pristine film (≈ 3.8 eV). Furthermore, the influence of different TiO_2 NPs loadings in the electrochemical response and in the structural, morphological and optical properties of the TiO_2@poly[1] nanocomposite film was also evaluated.

4.2 Experimental section

4.2.1 Materials and solvents

Titanium (IV) isopropoxide (TTIP, Aldrich, ≥ 97.0 %), $LiClO_4$ (Aldrich, 99 %), isopropanol (VWR, 99.7 %), ethanol absolute (Fisher Chemical, 99.99 %), nitric acid (Panreac, 65 %), and acetonitrile and propylene carbonate (Romil, pro analysis grade) were directly used as received; ultra-pure water (resistivity 18.2 MΩ cm at 25 ºC, Millipore) was used. The complex *N,N'*-bis(3-methylsalicylideneiminate) nickel(II), [Ni(3-Mesalen)], and respective *salen* ligand were prepared by methods described in literature.[26]

4.2.2 TiO_2 NPs preparation and characterisation

The synthesis of TiO_2 NPs was performed by a procedure adapted from literature.[27] A solution of TTIP (5 mL) in isopropanol (15 mL) was added drop by drop to a solution of millipore water (250 mL) at pH 2 (adjusted with HNO_3), under vigorous magnetic stirring. A turbid solution was formed immediately, which was heated up to 65 ºC for 6 h. The obtained product was washed with absolute ethanol and dried for 1 day. Finally, the as-prepared powder was annealed at 300, 400 and 500 ºC for 2 h (60 ºC / hour). According with the annealed temperature, the samples were labeled as TiO_2_300, TiO_2_400 and TiO_2_500, respectively.

The band gap, E_g, of TiO_2 NPs was determined through the Equation (4.1):

$$\alpha = A\,(h\nu - E_g)^{n} / h\nu \qquad (4.1)$$

where α is the absorption coefficient, A is a constant, $h\nu$ is the energy of light and n is a constant (n = 2 for TiO_2, assuming an indirect band gap). At this conditions, the absorption coefficient is proportional to Kubelka-Munk function F(R) and the band gap was extrapolated from the plot $(\alpha h\nu)^{1/2}$ vs. $h\nu$.[28-30]

4.2.3 Films preparation and electrochemical studies

The TiO_2@poly[1] nanocomposite films were prepared by cyclic voltammetry from starting solutions containing 1.0 mmol dm^{-3} [Ni(3-Mesalen)] and 5, 15 or 25 wt.% (TiO_2/$LiClO_4$ wt.%) of TiO_2_400 NPs in 0.1 mol dm^{-3} $LiClO_4$/CH_3CN. The potential of the working electrode (ITO/PET 2.25 cm^2) was cycled between 0.0 and 1.3 V or -0.2 and 1.3 V, at 0.020 or 0.100 V s^{-1}, respectively, during 10 scans. Prior to electrodeposition, the starting solutions were (i) sonicated during 10 minutes or (ii) sonicated during 10 minutes followed by reflux during 3 hours. According with the method used, the films obtained were named TiO_2@poly[1]_s and TiO_2@poly[1]_r, respectively. The pristine poly[1] film was prepared using the same experimental conditions, but in the absence of TiO_2 NPs.

After films deposition, the modified electrodes were rinsed with dry CH_3CN, immersed in a monomer- and TiO_2-free 0.1 mol dm^{-3} $LiClO_4$/CH_3CN solution and cycled (by CV) in the potential range -0.1 at 1.3 V, at 0.020 V s^{-1}, during 5 redox cycles. The electroactive surface coverage, Γ / nmol cm^{-2} (cited in terms of monomeric units) of each film was determined by a coulometric assay,[31,32] using cyclic voltammograms (CVs) obtained in a monomer- and TiO_2-free 0.1 mol dm^{-3} $LiClO_4$/CH_3CN solution at the scan rate of 0.010 V s^{-1}, to ensure complete film redox conversion. The doping level values used for Γ determination were calculated from comparison of coulometric data

for films deposition and cycling, as described in literature,[31,32] and were found to be n = 0.65 and 0.48 for films prepared at 0.020 and 0.100 V s^{-1}, respectively.

The pristine and the nanocomposite film prepared with a TiO_2 loading of 5 wt.%, at 0.020 V s^{-1}, were also characterised by CV in $LiClO_4$/PC 0.1 mol dm^{-3} supporting electrolyte, at 0.010 V s^{-1} during 3 redox cycles, in the typical potential range.

4.2.4 Composition and morphology characterisation

The composition and morphology characterisations of the TiO_2@poly[1]_r nanocomposite were performed by XPS and SEM/EDS, respectively. The films were prepared with 5 wt.% of TiO_2_400 NPs, at 0.020 V s^{-1}, during 10 electrodeposition cycles, and analysed in reduced state (application of E = 0.0 V during 200 s). Films subjected to potential cycling in $LiClO_4$/CH_3CN and in $LiClO_4$/PC 0.1 mol dm^{-3}, using the typical conditions, were also analysed by XPS in order to investigate the influence of successive redox switching in the surface chemical composition. Pristine poly[1] film was prepared in identical conditions and studied for comparison.

The nanocomposite film was analysed by SEM/EDS in two different perspectives: (i) in a cross-section plan and (ii) in an internal structure of polymeric film plan. For (i) the film was subjected to a cut perpendicular to the surface, while in (ii) a part of the film surface was removed (by trapping with a carbon conductive tape), exposing the inside of polymeric film.

4.2.5 Spectroelectrochemical studies

The monitoring of the redox process by *in situ* UV-Vis spectroscopy was performed with films prepared with 3 electrodeposition cycles, at 0.020 V s^{-1}, from a starting solution containing 5 wt.% of TiO_2 NPs (except for pristine film). The films were cycled between -0.1 and 1.3 V at the scan rate of 0.020 V s^{-1}, using $LiClO_4$/PC 0.1 mol dm^{-3} as supporting electrolyte. The UV-Vis spectra were acquired simultaneously, at intervals of 0.5 s, in the wavelengths range of 315 to 1100 nm, during the 4th redox cycle. The molar extinction coefficients, ε / cm^{-1} mol^{-1} dm^3, of all electronic bands were estimated using a combination of the Beer-Lambert and Faraday laws (Equation 2.1).

4.2.6 Electrochromic properties evaluation

The EC properties evaluation was performed for TiO_2@poly[1]_r films, prepared with 5 wt.% of TiO_2 NPs, at 0.020 V s^{-1}, during 10 or 3 (chronoabsorptometric study) electrodeposition cycles. The studies were performed in $LiClO_4$/PC 0.1 mol dm^{-3} supporting electrolyte, considering the colour change yellow ↔ green (that proved to be the most promising for the pristine poly[1], Chapter 2). The electrochemical stability

tests were performed by a double potential step method (chronoamperometry), applying two potential pulses of 50 s by redox cycle, with potential alternating between 0.0 and 0.7 V, for a long period of time (9500 redox cycles, ≈ 11 days). The switching times were determined from the obtained chronoamperograms, considering 90 % of the full switch. The remaining EC parameters were determined through the chronoabsorptograms obtained during the monitoring of the chronoamperometric experiment by UV-Vis spectroscopy; the measurements were performed at the fixed wavelength of λ = 750 nm, acquiring the UV-Vis spectra with intervals of 1 s. The change of the optical density, ΔOD, and the colouration efficiency parameters were estimated through Equation 1.1.

The CIELAB values were determined after subject the polymeric films to the application of a constant potential value - *E* = 0.0, 0.7 or 1.3 V - during 50 s, in $LiClO_4$/PC. The CIELAB system provided a psychometric lightness index L*, which is a chromatic measure in a scale ranging from 0 (black) to 100 (white), and two colour coordinates a*, a green (negative) - red (positive) continuum, and b*, a blue (negative) – yellow (positive) values. The total colour difference (ΔE*) between two different oxidation states of a film was calculated from L*, a* and b* values, using the equation:

$$\Delta E^* = ((\Delta L^*)^2+(\Delta a^*)^2+(\Delta b^*)^2)^{1/2} \quad (4.2)$$

where $\Delta x^* = x^*_{\text{more oxidised state}} - x^*_{\text{less oxidised state}}$ (x* = L*, a* or b*).

4.3 Results and discussion

4.3.1 TiO_2 NPs characterisation

Figure 4.1 shows the XRD patterns of TiO_2 NPs annealed at different temperatures.

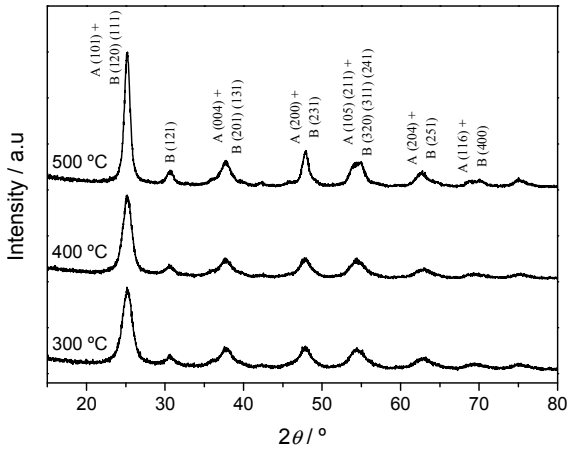

Figure 4.1 XRD patterns of TiO_2 NPs annealed at 300, 400 and 500 ºC (A = anatase, B = brookite).

According to ICSD CIF no. 24276 (anatase, A) and ICSD CIF no. 31122 (brookite, B), the weak diffraction peak at 2θ = 30.52º is indexed to the plane (121) of brookite. The other diffraction peaks, due to their broadness and proximity to the diffraction peaks in anatase (A) and brookite (B) phases, are ascribed to more than one plane: A (101) or B (120)/(111) (2θ = 25.29 º), A (004) or B (201)/(131) (2θ = 37.74 º), A (200) or B (231) (2θ = 47.92 º), A (105)/(211) or B (320)/(311)/(241) (2θ = 54.44 º), A (204) or B (251) (2θ = 62.98 º) and A (116) or B (400) (2θ = 69.36 º). All the TiO_2 samples are composed by two crystallographic structures: anatase and brookite. The Rietveld refinement indicated that the TiO_2 NPs annealed at 300 and 400 ºC (TiO_2_300 and TiO_2_400 samples) are 65.5 % anatase and 34.5 % brookite, whereas the sample annealed at 500 ºC (TiO_2_500 sample) is composed by 67.0 % anatase and 33.0 % brookite. The samples TiO_2_300 and TiO_2_400 have similar grain sizes: 9.32 nm for anatase and 9.00 nm for brookite, but the crystallite sizes increase to 14.25 nm for anatase and 11.57 nm for brookite, for the sample TiO_2_500. These results are in agreement with reported results for similar samples.[33]

The TEM micrographs (representative image for TiO_2_400 sample in Figure 4.2 (a)) show small-size quasi-spherical TiO_2 NPs. The particle size distribution was fitted by a log-normal function (Figure 4.2 (b)), leading to an average particle size of 9.7 nm (± 1.1 nm), which is in agreement with the XRD results.

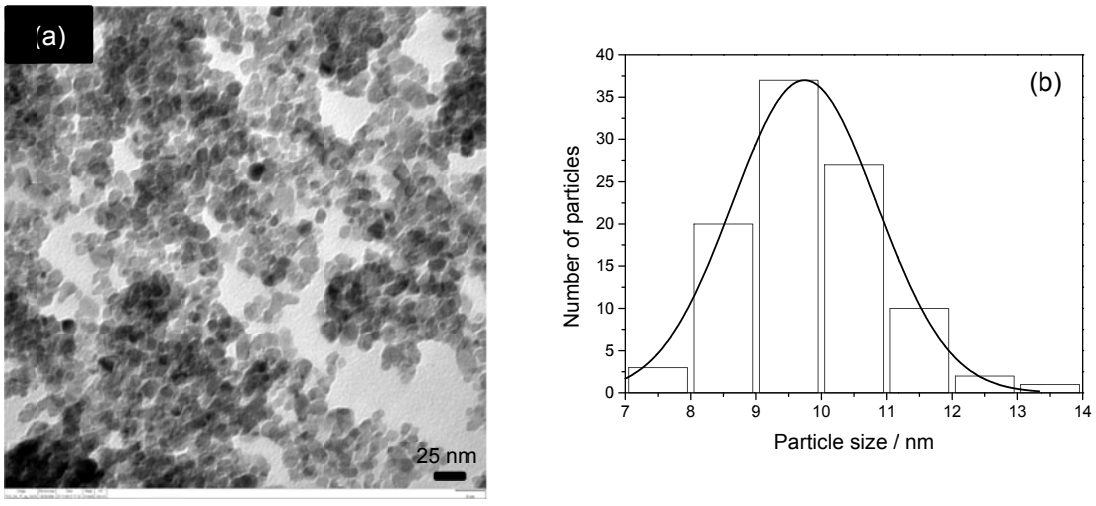

Figure 4.2 (a) TEM micrograph of the TiO_2 NPs; (b) particle size distribution histogram from the analysis of TEM images (the solid line represents the log-normal distribution fit).

XPS characterisation of TiO_2 NPs indicates the presence of Ti, O and N. For the TiO_2_400 sample, the calculated atomic percentages of Ti and O were 24.7 and

74.6 %, respectively, with 0.71 % of nitrogen. The higher value of the obtained O/Ti atomic ratio ($O/Ti_{obtained}$ = 3.0) compared to the theoretical value ($O/Ti_{theoretical}$ =2.0) is explained by the contribution of the O atoms from surface hydroxyl groups.[28] The obtained atomic percentages for TiO_2_300 sample were 28.3, 70.5 and 1.20 % for O, Ti and N, respectively.

The high-resolution XPS spectra of TiO_2_300 and TiO_2_400 samples in Ti2p, O1s and N1s regions are depicted in Figure 4.3.

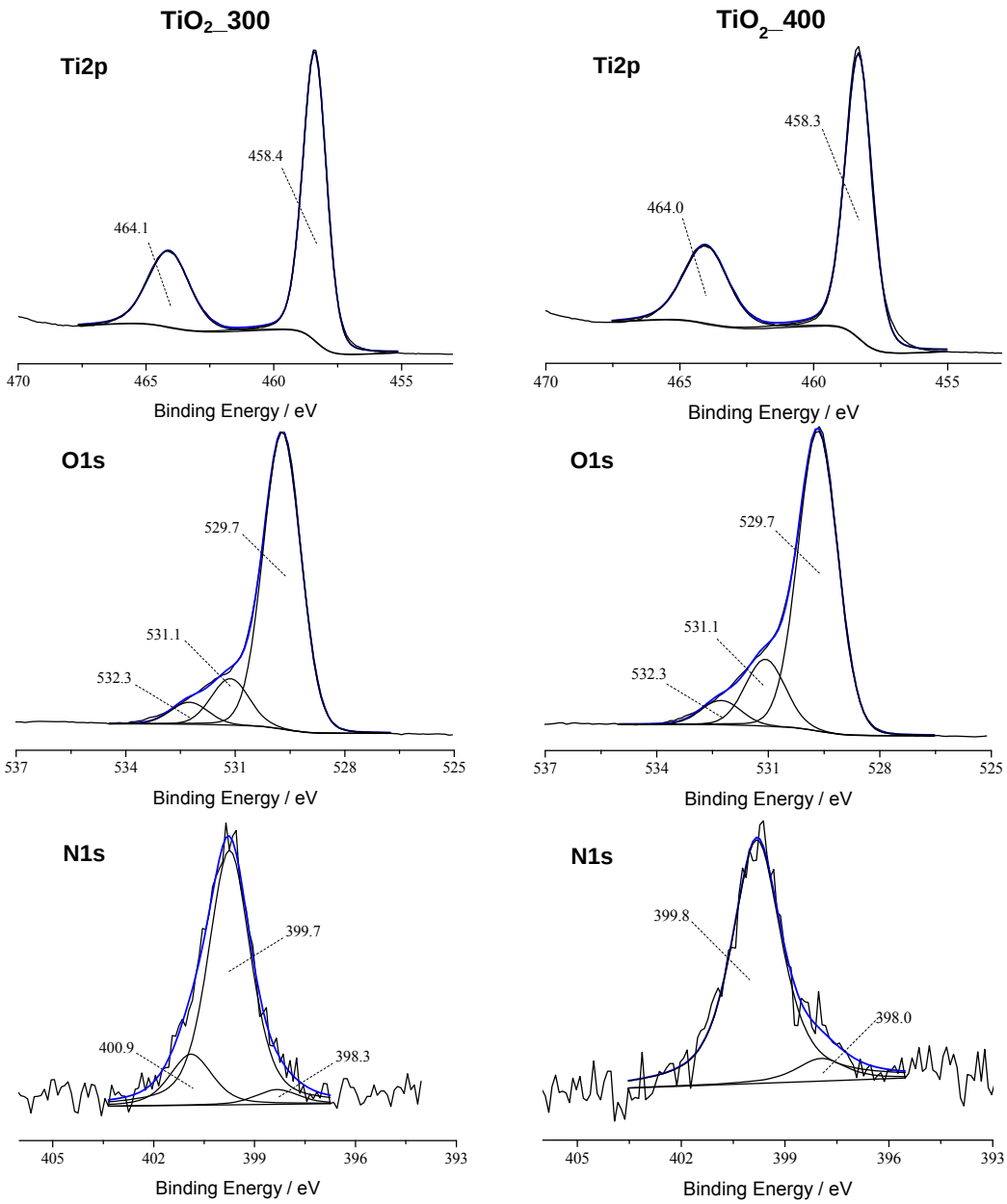

Figure 4.3 High-resolution XPS spectra of TiO_2_300 and TiO_2_400 NPs in Ti2p, O1s and N1s regions, with respective deconvolutions.

For both samples, two peaks are observed, attributed to $Ti2p_{3/2}$ (458.3 eV) and $Ti2p_{1/2}$ (464.0 eV) signals, with a peak separation of 5.70 eV, assignable to $Ti^{(IV)}$ in TiO_2.[34] In the O1s region it is observed a main peak at 529.7 eV due to oxygen bound to $Ti^{(IV)}$, and two minor peaks at 531.1 and 532.3 eV, assigned to oxygen vacancies and surface –OH groups.[28] In the N1s region, the two samples show different XPS spectra. TiO_2_400 spectrum exhibits two peaks at 398.0 and 399.8 eV that can be attributed, respectively, to N-Ti bonds, indicating the substitution of oxygen atoms by nitrogen in TiO_2 lattice, and to N-O-Ti bonds, resultant from the interstitial N-doping. TiO_2_300 spectrum, besides the referred two peaks at 398.3 and 399.7 eV, it shows another peak at 400.9 eV that is tentatively associated with weakly adsorbed N species,[33] since it is removed at higher annealing temperatures (400 ºC). The presence of N is attributed to some nitric acid, added to control the pH of the reaction medium during the TiO_2 NPs synthesis.[35]

FTIR spectra of TiO_2 NPs annealed at the three temperatures are shown in Figure 4.4. All samples present similar spectra, with a strong and broad, almost flat, vibration band in the range 1000 – 400 cm^{-1}, that is attributed to the stretching vibration of Ti-O-Ti bonds;[33] this band profile is also characteristic of TiO_2 nitrogen-doped samples.[36] The vibration band at ≈ 1628 cm^{-1} corresponds to the bending vibration of O-H groups from adsorbed water or from Ti-OH groups. In the FTIR spectrum of TiO_2_300 sample it is observed a vibration band at 1398 cm^{-1} that can be assigned to N adsorbed species,[34,37] and that is not detected in the FTIR spectra of NPs annealed at 400 and 500 ºC, as observed in the N1s high-resolution XPS spectra, corroborating the previous assignment.

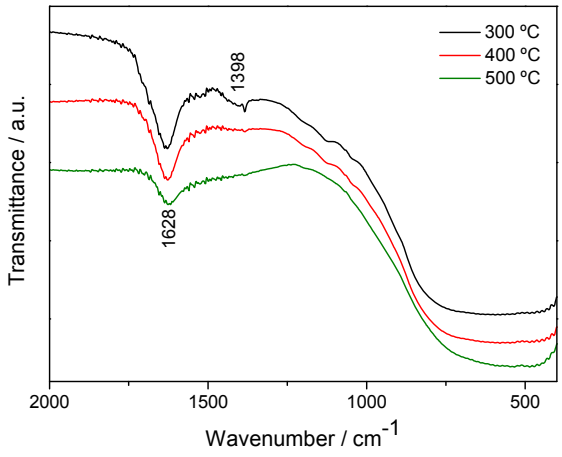

Figure 4.4 FTIR spectra of TiO_2 NPs annealed at different temperatures.

The UV-Vis spectra of TiO_2 NPs are presented in Figure 4.5 (a). All samples present an absorption edge in the range of 300 – 400 cm^{-1}. The band gap, E_g, of TiO_2 NPs was determined through Equation (4.1), from the plots $(\alpha h\nu)^{1/2}$ vs. $h\nu$ (Figure 4.5 (b), (c) and (d)), and it is E_g = 2.61, 2.65 and 2.75 eV for TiO_2_300, TiO_2_400 and TiO_2_500 samples, respectively; these values are lower than that of commercial Degussa P25 (3.0-3.2 eV).[33]

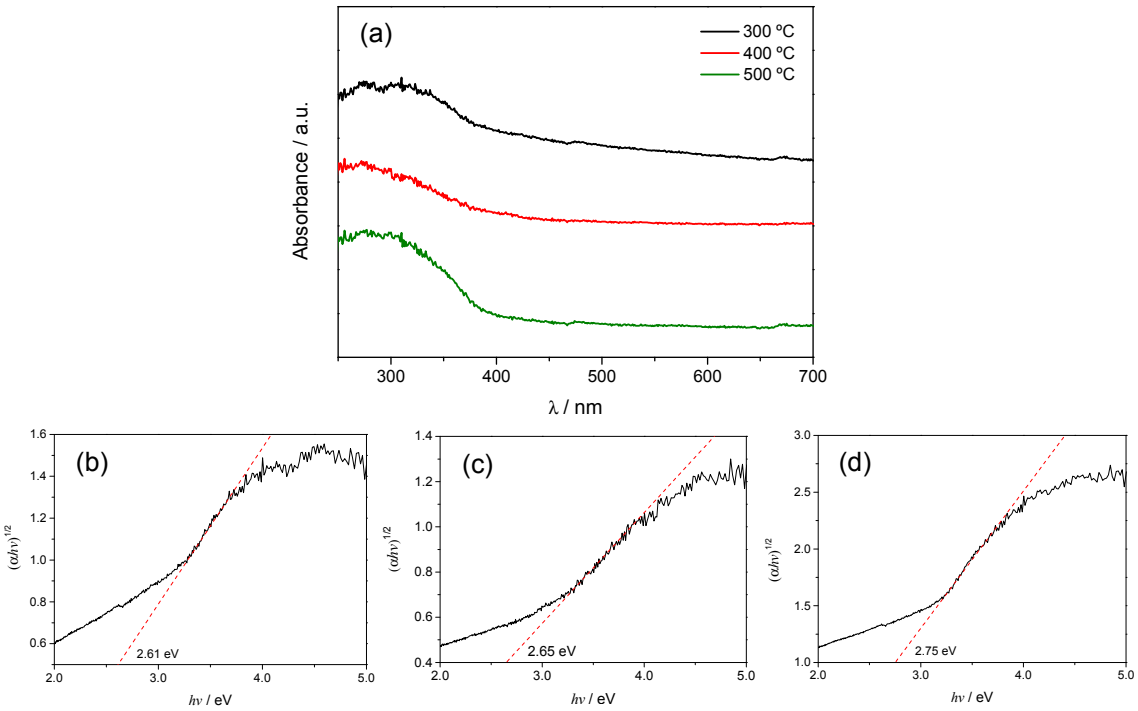

Figure 4.5 (a) UV-Vis absorption spectra for TiO_2 NPs annealed at different temperatures; $(\alpha h\nu)^{1/2}$ = f($h\nu$) plots for TiO_2 NPs annealed at (b) 300, (c) 400 and (d) 500 ºC.

4.3.2 Electrochemical preparation and characterisation of TiO_2@poly[1]

The TiO_2@poly[1] films were potentiodynamically polymerised using starting solutions containing the monomer [Ni(3-Mesalen)] and the TiO_2_400 NPs (NPs with lowest size) in different loadings: 5, 15 and 25 wt.%, using two scan rates - 0.020 or 0.100 V s^{-1}. With the different electropolymerisation conditions we endeavour to optimise not only the quantity of entrapped TiO_2, but also its homogeneity within the polymer supramolecular structure.

In Figure 4.6 (a) and (a') are depicted the CVs obtained during the 10th electropolymerisation cycles of the nanocomposite films (with 5 wt.% of TiO_2 loading) at 0.020 and 0.100 V s^{-1}, along with the equivalent results for poly[1], for comparison. In Figure 4.7 are depicted the CVs obtained during the entire electropolymerisation

process for TiO_2@poly[1]_r at 0.020 and 0.100 V s^{-1}, with 5 wt.% of TiO_2 NPs, as representative example; the peak potentials for all films are summarised in Table 4.1.

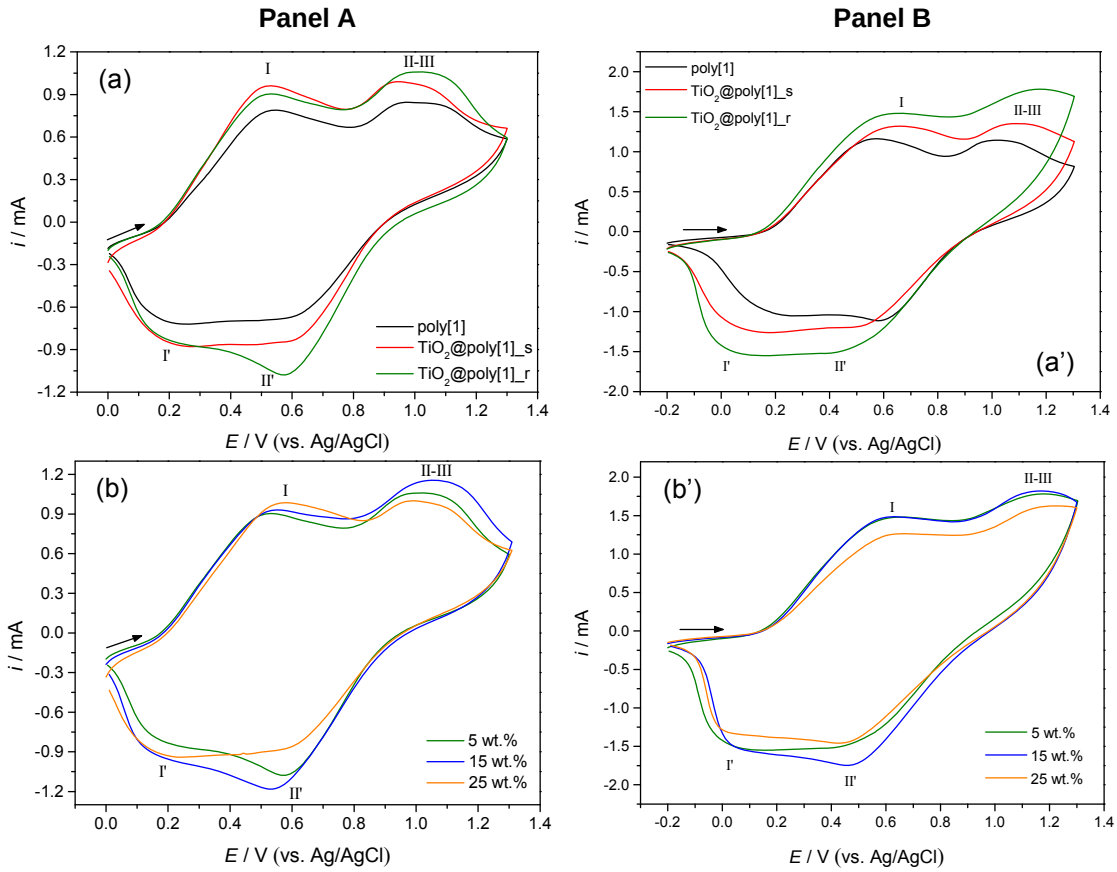

Figure 4.6 CVs obtained during the 10th electrodeposition cycles of (a and a') poly[1], TiO_2@poly[1]_s and TiO_2@poly[1]_r (with 5 wt.% of TiO_2 loading) and (b and b') TiO_2@poly[1]_r with 5, 15 and 25 wt.% of TiO_2 loading, in $LiClO_4/CH_3CN$ 0.1 mol dm^{-3} supporting electrolyte, at 0.020 V s^{-1} (Panel A) and 0.100 V s^{-1} (Panel B).

The voltammetric responses of nanocomposites prepared at 0.020 V s^{-1} are similar to those of the pristine film, and are comparable for films prepared with different loadings of TiO_2 NPs (Figure 4.6 (b)), despite small shifts in anodic and cathodic peaks. An analogous behaviour was observed for films electropolymerised at 0.100 V s^{-1} (Figure 4.6 (a') and (b')), although the films prepared at this scan rate present the anodic voltammetric peaks shift to less negative potential values and the cathodic peaks shift to more negative potentials, in comparison to films prepared at 0.020 V s^{-1}; this effect is more pronounced for the nanocomposites.

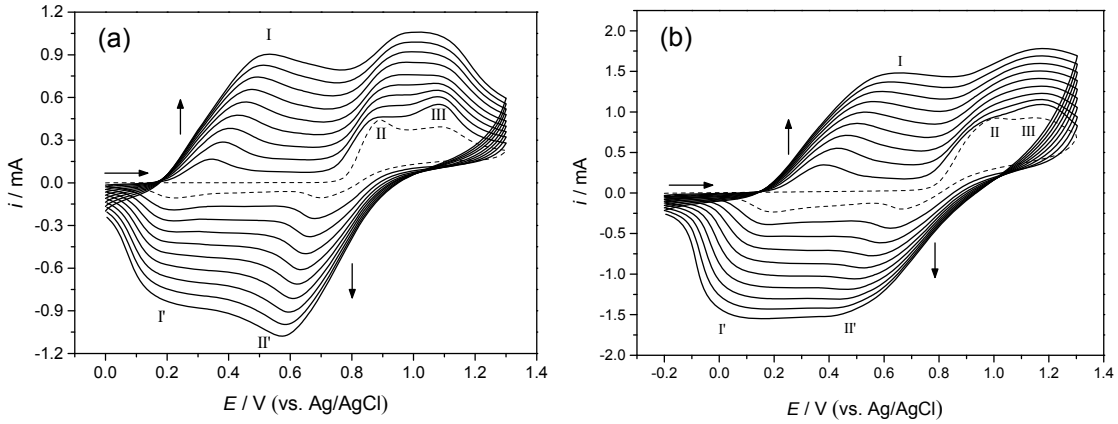

Figure 4.7 CVs of the TiO_2@poly[1]_r electrodeposition at (a) 0.020 V s^{-1} and (b) 0.100 V s^{-1}, using 1.0 mmol dm^{-3} monomer solution containing 5 wt.% of TiO_2 NPs in $LiClO_4/CH_3CN$ 0.1 mol dm^{-3}, during 10 scans.

Table 4.1 Peak potentials in CVs during the 1st, 5th and 10th scans of nanocomposites (with TiO_2 loadings of 5, 15 and 25 wt.%) and pristine poly[1] films electrodepositions, at 0.020 and 0.100 V s^{-1}.

Film	TiO_2 loading	Scan	***E* / V (vs. Ag/AgCl)** (at 0.020 / 0.100 V s^{-1})				
			E_{paI}	E_{paII}	E_{paIII}	$E_{pcI'}$	$E_{pcII'}$
poly[1]	0 %	1st	-/-	0.90/0.96	1.09/1.12	0.21/0.21	0.69/0.70
		5th	0.45/0.47	0.94/0.97	1.08/1.08	0.18/0.18	0.64/0.64
		10th	0.55/0.57	0.98/-	1.06/1.01	0.15/0.15	0.55/0.58
TiO_2@poly[1]_s	5 %	1st	-/-	0.87/0.99	1.06/1.16	0.21/0.19	0.68/0.67
		5th	0.44/0.51	0.92/1.02*	1.04/1.13	0.19/0.13	0.64/0.58
		10th	0.53/0.66	0.95/-	1.03/1.09	0.16/0.09	0.57/0.48
TiO_2@poly[1]_r		1st	-/-	0.89/1.01	1.08/1.14	0.22/0.19	0.70/0.66
		5th	0.43/0.50	0.94/1.06*	1.07/1.17	0.21/0.12	0.64/0.52
		10th	0.53/0.65	-/-	1.00/1.17	0.19/0.06	0.57/0.41
TiO_2@poly[1]_s	15 %	1st	-/-	0.90/1.02	1.10/1.17	0.21/0.18	0.69/0.67
		5th	0.47/0.53	0.95/1.04*	1.06/1.20	0.17/0.08	0.62/0.54
		10th	0.57/0.71	0.98/-	1.06/1.21	0.14/0.00	0.56/0.47
TiO_2@poly[1]_r		1st	-/-	0.90/0.99	1.10/1.15	0.22/0.21	0.69/0.68
		5th	0.44/0.49	0.99/1.06*	1.10/1.16	0.19/0.13	0.61/0.56
		10th	0.55/0.63	-/-	1.06/1.16	0.14/0.06	0.53/0.45
TiO_2@poly[1]_s	25 %	1st	-/-	0.90/0.99	1.10/1.15	0.21/0.20	0.69/0.69
		5th	0.47/0.52	0.96/1.03*	1.07/1.15	0.18/0.13	0.63/0.59
		10th	0.58/0.66	0.99/-	1.07/1.11	0.16/0.04	0.57/0.50
TiO_2@poly[1]_r		1st	-/-	0.93/1.03	1.14/1.18	0.21/0.20	0.69/0.67
		5th	0.47/0.52	1.03/1.06*	1.14/1.21	0.16/0.10	0.57/0.54
		10th	0.62/0.66	-/-	1.13/1.22	0.13/0.02	0.47/0.43

* inflexion

The results indicate that the poly[1] oxidative electropolymerisation mechanism was not changed by the presence of TiO_2, as observed for the nanocomposite with WO_3 (Chapter 3). Thus, the two peaks observed at E_{pa} = 0.87-1.03 V and E_{pa} = 1.06-1.18 V, in the first anodic half-cycle, are attributed to the [Ni(3-Mesalen)] oxidation and subsequent formation of oligomers/polymer in the working electrode surface, while the peaks at E_{pc} = 0.66-0.70 V and E_{pc} = 0.18-0.22 V, observed in reverse scan, correspond to the reduction of the as-formed nanocomposite films. The new anodic peak at E_{pa} = 0.43-0.53 V, in the second and subsequent scans, is assigned to the oxidation of the polymeric films.[31,32]

Furthermore, the CVs of nanocomposites (with 5 and 15 wt.% TiO_2-loading) showed higher current intensities than those of poly[1], which is attributed to a larger electroactive surface area due to the incorporation of the TiO_2 NPs on the poly[1] structure. However, when the TiO_2 loading increase to 25 wt.%, the electrochemical responses exhibit lower current intensities, which can indicate that a higher loading of NPs may decrease the electropolymerisation efficiency.

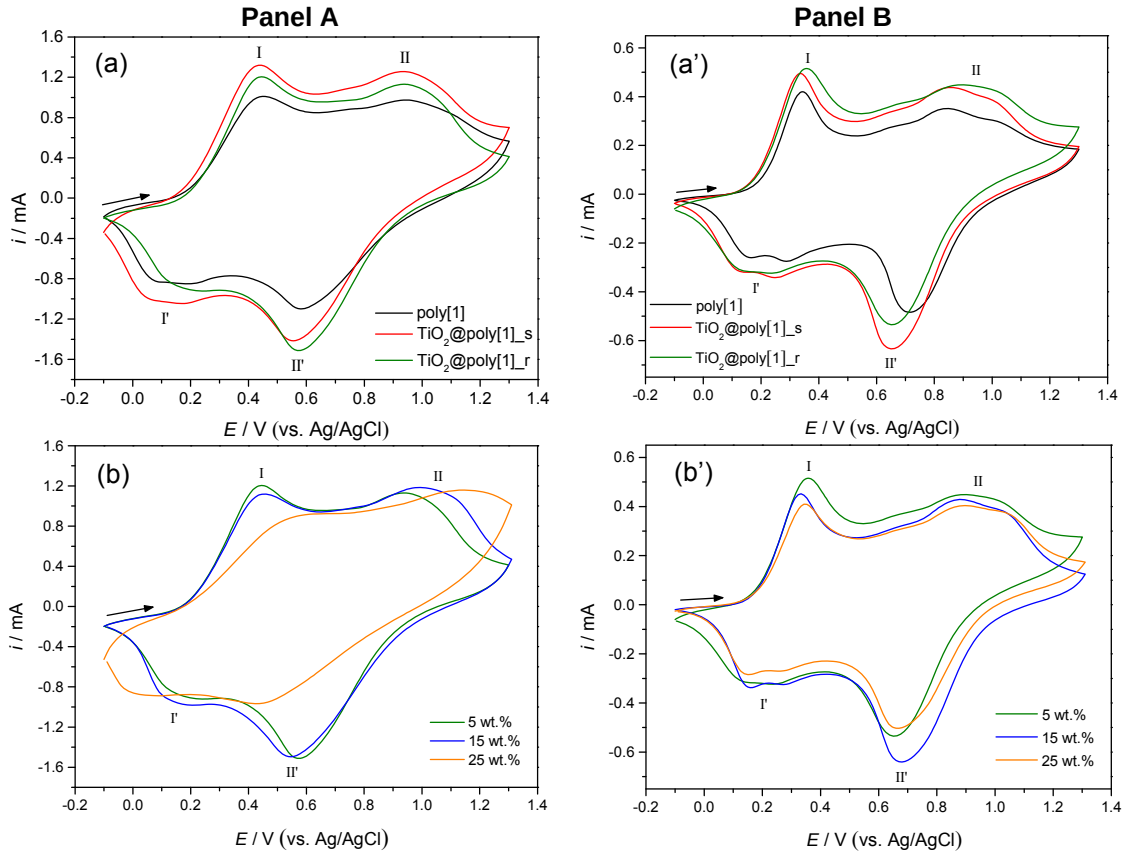

Figure 4.8 CVs obtained during the 5th redox cycles of films electrodeposited at 0.020 V s^{-1} (Panel A) and 0.100 V s^{-1} (Panel B): (a and a') poly[1], TiO_2@poly[1]_s and TiO_2@poly[1]_r (with 5 wt.% of TiO_2 loading) and (b and b') TiO_2@poly[1]_r with 5, 15 and 25 wt.% of TiO_2 loading; supporting electrolyte - $LiClO_4/CH_3CN$ 0.1 mol dm^{-3}, scan rate – 0.020 V s^{-1}.

The voltammetric responses of the TiO_2@poly[1] nanocomposites (prepared at 0.020 and 0.100 V s^{-1}) in $LiClO_4/CH_3CN$, along with the pristine film, are depicted in Figure 4.8 (a) and (a'). The CVs obtained during the entire film conditioning of TiO_2@poly[1]_r films (with 5 wt.% of TiO_2 loading) are depicted in Figure 4.9, as representative examples; in Table 4.2 are summarised the peak potential values.

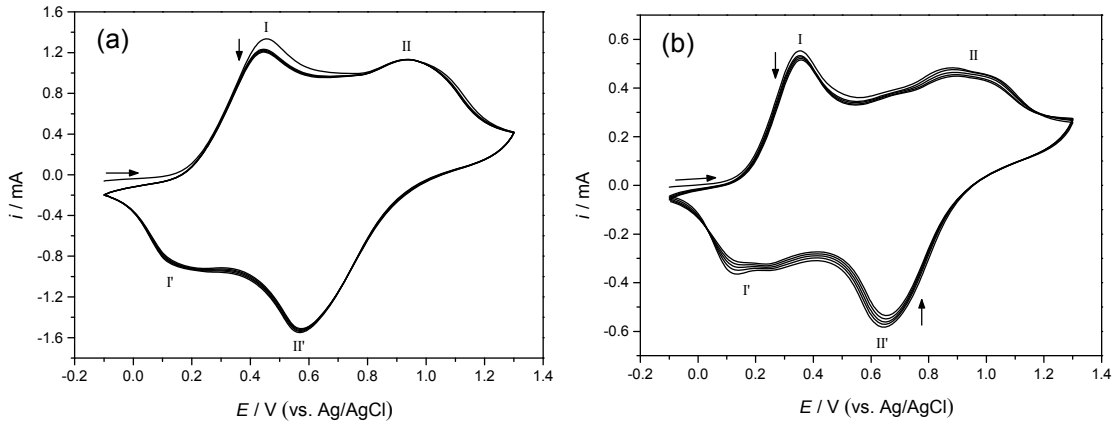

Figure 4.9 CVs obtained during the redox switching of TiO_2@poly[1]_r films electrodeposited at (a) 0.020 V s^{-1} and (b) 0.100 V s^{-1} with a TiO_2 loading of 5 wt.%, in $LiClO_4/CH_3CN$ 0.1 mol dm^{-3}, at 0.020 V s^{-1}.

The voltammetric responses of the nanocomposites are similar to those of poly[1], apart from small shifts of peak potentials. The nanocomposite films prepared with different TiO_2-loadings (Figures 4.8 (b) and (b')) also show similar voltammetric profiles, with the exception of the film electrodeposited at 0.020 V s^{-1} with 25 wt.% TiO_2 loading, whose CV shows the anodic peak strongly shifted to less negative potentials and the cathodic peaks to more negative potentials, revealing a greater resistance of the nanocomposite film.

In Figure 4.10 are plotted the electroactive surface coverage, Γ / nmol cm^{-2}, of films prepared with different TiO_2 loadings and at the two scan rates. The data revealed that the films prepared at 0.020 V s^{-1} have higher Γ than those prepared at 0.100 V s^{-1}, as expected. Moreover, nanocomposite films present higher Γ than the respective pristine film, deposited at the same scan rate, which is in agreement with the higher current intensities observed in nanocomposites CVs and indicates the successful incorporation of the TiO_2 on poly[1] matrix; in the most of cases, Γ-values are higher for TiO_2@poly[1]_r nanocomposites. For films prepared at 0.020 V s^{-1}, Γ increases significantly from poly[1] to nanocomposites deposited with 5 and 15 wt.% of TiO_2 loading, decreasing after for films with 25 wt.%. These results suggest an optimal TiO_2 loading, from which higher loadings may be unfavourable and prevent the deposition of

Ni-*salen* polymer; this behaviour has been also observed for WO_3 films loaded with carbon nanotubes.[38] For films prepared at 0.100 V s^{-1}, the increase of Γ-values from pristine film to nanocomposites and between the nanocomposites (prepared with different TiO_2 loadings) was lower than the observed for films prepared at 0.020 V s^{-1}, which can indicate a lower incorporation of TiO_2 NPs at this scan rate. This observation is supported by the fact that the metal oxides incorporation into the films is limited by their mass transport and, so, favoured by slower polymerisation procedures.[17]

Table 4.2 Peak potentials in CVs during the 1st and 5th scans of redox switching of nanocomposites and pristine poly[1] films, at 0.020 V s^{-1}, in $LiClO_4/CH_3CN$ 0.1 mol dm^{-3}.

Film	TiO_2 loading	Scan	***E* / V (vs. Ag/AgCl)** (films electrodeposited at 0.020 / 0.100 V s^{-1})			
			E_{paI}	E_{paII}	$E_{pcI'}$	$E_{pcII'}$
poly[1]	0 %	1st	0.46/0.34	0.93(1.08*)/ 0.84(1.01*)	0.20(0.10*)/ 0.30(0.16*)	0.58/0.72
		5th	0.45/0.34	0.94/ 0.84(1.01*)	0.19(0.10*)/ 0.29(0.17*)	0.58/0.71
TiO_2@poly[1]_s	5 %	1st	0.44/0.34	0.93(1.07*)/ 0.85(1.00*)	0.19(0.08*)/ 0.26(0.14*)	0.55/0.65
		5th	0.44/0.34	0.93/ 0.86(1.00*)	0.17(0.08*)/ 0.25(0.14*)	0.55/0.65
TiO_2@poly[1]_r		1st	0.45/0.35	0.94(1.07*)/ 0.88(1.02*)	0.24(0.16*)/ 0.13(0.23*)	0.57/0.65
		5th	0.44/0.36	0.94/ 0.89(1.02*)	0.21/ 0.24(0.15*)	0.57/0.65
TiO_2@poly[1]_s	15 %	1st	0.50/0.37	1.01(1.17*)/ 0.91(1.07*)	0.11(0.01*)/ 0.09(0.22*)	0.47/0.57
		5th	0.48/0.37	1.02(1.17*)/ 0.92(1.07*)	0.09(0.02*)/ 0.10(0.21*)	0.48/0.58
TiO_2@poly[1]_r		1st	0.47/0.34	0.99(1.10*)/ 0.87(1.02*)	0.23/ 0.15(0.28*)	0.54/0.67
		5th	0.46/0.33	0.99/ 0.88(1.02*)	0.21/ 0.16(0.27*)	0.54/0.68
TiO_2@poly[1]_s	25 %	1st	0.54/0.38	0.98(1.16)/ 0.91(1.05*)	0.12(0.03)/ 0.11(0.25*)	0.51/0.62
		5th	0.52/0.37	0.98/ 0.90(1.05*)	0.12(0.04*)/ 0.12(0.23*)	0.52/0.62
TiO_2@poly[1]_r		1st	0.65/0.35	1.18/ 0.89(1.04)	0.09/ 0.14(0.28*)	0.42/0.66
		5th	0.65/0.35	1.15/ 0.90(1.04*)	0.10/ 0.15(0.26*)	0.43/0.66

* inflexion

Taking into account the Γ values obtained and the voltammetric profiles, films prepared at 0.020 mV s^{-1} with 5 wt.% of TiO_2 loading were employed to pursue further studies.

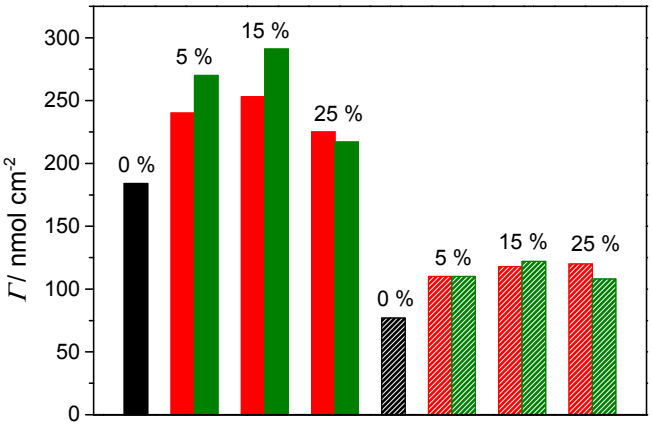

Figure 4.10 Electroactive surface coverage, Γ / nmol cm^{-2}, for films prepared with different TiO_2 loadings, at 0.020 (solid columns) and 0.100 V s^{-1} (dash columns); the black columns correspond to poly[1] and the red and green columns to TiO_2@poly[1]_s and TiO_2@poly[1]_r, respectively.

In Figure 4.11 are shown the CVs obtained during the cycling (3rd scan) of the TiO_2@poly[1]_r film as-prepared and of poly[1] in $LiClO_4$/PC, once this supporting electrolyte promotes the highest electrochemical stability for poly[1] film (Chapter 2); in Table 4.3 are summarised the peak potential values The nanocomposites show similar electrochemical responses to that of pristine film and higher current intensities, similarly to the observed in $LiClO_4/CH_3CN$, although the peaks are less defined in $LiClO_4$/PC.

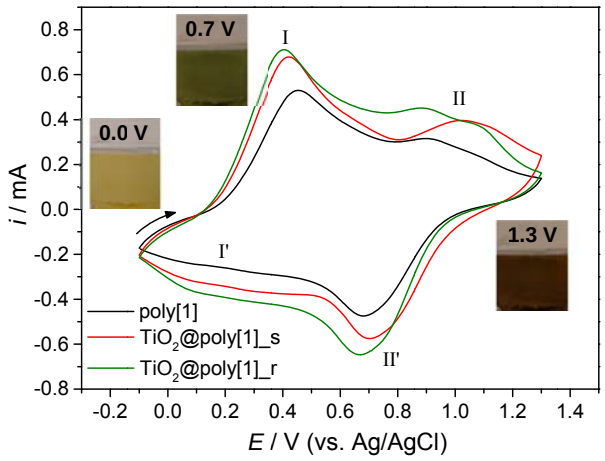

Figure 4.11 CVs obtained during the 3rd redox cycle of the poly[1] and TiO_2@poly[1] (with 5 wt.% of TiO_2 loading, electropolymerised at 0.020 V s^{-1}) in $LiClO_4$/PC 0.1 mol dm^{-3}, at the scan rate of 0.010 V s^{-1}; the insets are photographs of the polymeric film in different oxidation states.

Table 4.3 Peak potentials in CVs during the 1st and 3th scans of redox switching of pristine poly[1] and nanocomposites films with 5 wt.% of TiO_2 loading, at 0.010 V s^{-1}, in $LiClO_4$/PC 0.1 mol dm^{-3} (films prepared at 0.020 V s^{-1}).

Film	Scan	*E* / V (vs. Ag/AgCl)			
		E_{paI}	E_{paII}	$E_{pcI'}$	$E_{pcII'}$
poly[1]	1st	0.39	0.89(1.10*)	0.12(0.29*)	0.68
	3th	0.45	0.89	0.12*	0.68
TiO_2@poly[1]_s	1st	0.36	1.16	0.11(0.27*)	0.69
	3th	0.43	1.00	0.11*(0.27*)	0.70
TiO_2@poly[1]_r	1st	0.36	0.87(1.09*)	0.10(0.29*)	0.67
	3th	0.42	0.88(1.07*)	0.10*(0.29*)	0.68

During redox cycling, the nanocomposites showed the typical electrochromic behaviour of poly[1], exhibiting colour changes between yellow, green and russet according with the applied potential, as depicted in the insets of Figure 4.11.

4.3.3 Morphology and composition

In Figure 4.12 are depicted SEM micrographs of (a) a cross-section plan and (b) inside structure of TiO_2@poly[1]_r nanocomposite.

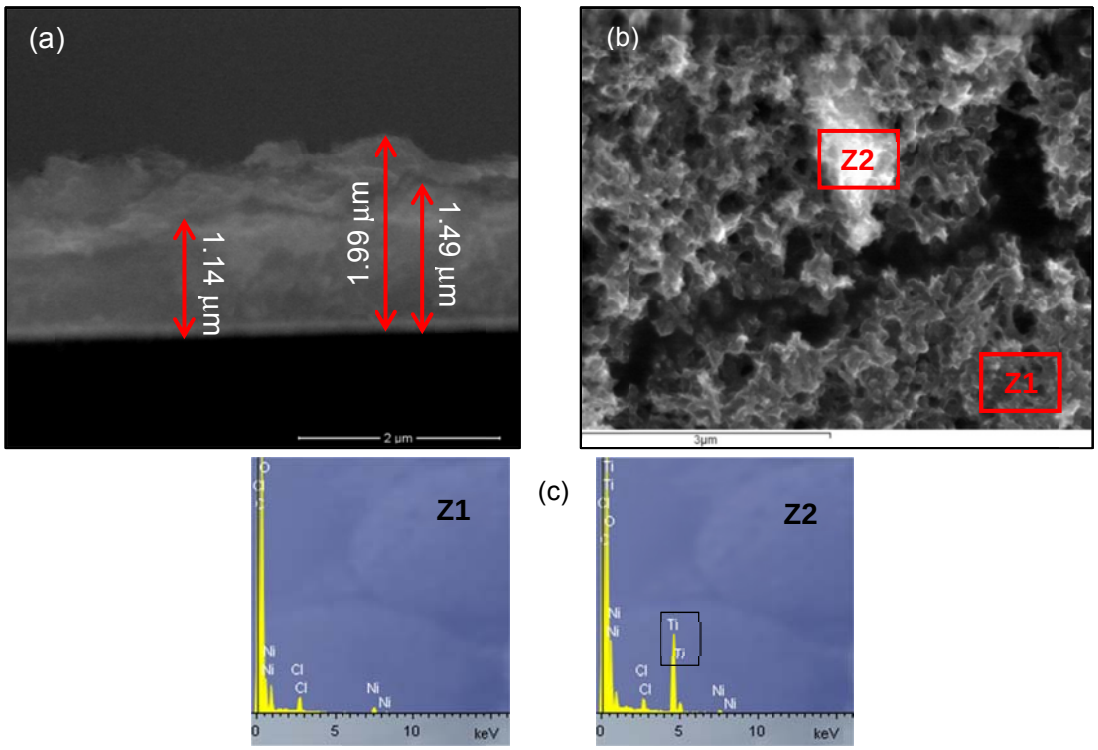

Figure 4.12 Scanning electron micrographs of TiO_2@poly[1]_r nanocomposite film (a) in a cross-section plan and (b) of inside film structure (magnifications of 50000 and 20000 times, respectively); (c) EDS spectra at zones specified in (b).

Both micrographs show the continuous layer with irregular surface, characteristic of the pristine poly[1] (Chapter 2). Through the cross-section micrograph (Figure 4.12 (a)), the thickness of the nanocomposite film was estimated ranging between ≈ 1.00 - 2.00 μm and confirming the irregular film surface. The micrograph of Figure 4.12 (b) is representative of some regions observed in the exposed inside film structure (region Z1), in which were distinguished agglomerates assigned to TiO_2 NPs (region Z2) occluded on poly[1] matrix, on the basis of EDS analyses (Figure 4.12 (c)). These revealed different compositions for regions Z1 and Z2: while in region Z1 the elements characteristic of poly[1] and of ClO_4^- (Ni, O, C and Cl) were detected, in region Z2 there is Ti from the TiO_2 NPs.

The characterisation of TiO_2@poly[1]_r nanocomposite by XPS shows Ni, C, N, O and Cl, from poly[1] and species associated with redox cycling (ClO_4^- and solvent).

The surface atomic percentages determined for all elements and the calculated atomic ratios are summarised in Table 4.4, along with data for poly[1] for comparison (taken from Chapter 3).

Table 4.4 XPS results: surface atomic percentages and calculated atomic ratios of relevant elements for poly[1] pristine film and TiO_2@poly[1]_r nanocomposite, in their reduced states (*E* = 0.0 V).

Sample	Atomic %					Atomic Ratios		
	Ni	C	N	O	Cl	N/Ni	O/Ni	Cl/Ni
poly[1]								
Before redox	3.5	75.5	7.6	12.0	1.3	2.2	3.4	0.4
After redox in CH_3CN	2.5	64.8	6.4	22.4	3.9	2.6	9.0	1.6
After redox in PC	2.7	72.8	6.6	15.9	2.1	2.4	5.9	0.8
TiO_2@poly[1]_r								
Before redox	3.3	76.4	7.6	11.5	1.2	2.3	3.5	0.4
After redox in CH_3CN	2.1	56.6	5.7	29.6	6.0	2.7	14.1	2.9
After redox in PC	2.9	74.3	6.6	14.6	1.6	2.3	5.0	0.6

The atomic ratios of nanocomposite before redox switching are similar to those of pristine poly[1] and the slightly larger ratios in comparison to the theoretical values ($N/Ni_{theoretical}$ = $O/Ni_{theoretical}$ = 2.0 and $Cl/Ni_{theoretical}$ = 0.0) are assigned to the trapping of the TiO_2 NPs and some $LiClO_4/CH_3CN$ on poly[1] matrix, during electropolymerisation.

After redox switching in $LiClO_4/CH_3CN$, the nanocomposite film shows a significant increase in atomic ratios, mainly for Cl/Ni and O/Ni ratios, explained by the successive accumulation of ClO_4^- and solvent on film structure, along the redox cycles. The increase in atomic ratios was larger for TiO_2@poly[1]_r than for poly[1], unlike

what was observed for the nanocomposite between poly[1] and WO_3 NPs (Chapter 3). After redox switching in $LiClO_4$/PC it was also observed an increase in atomic ratios, which was similar for nanocomposite and pristine films.

The high-resolution XPS spectra obtained for both films before and after redox switching in $LiClO_4/CH_3CN$ and $LiClO_4$/PC are shown in Figures from 4.13 to 4.17.

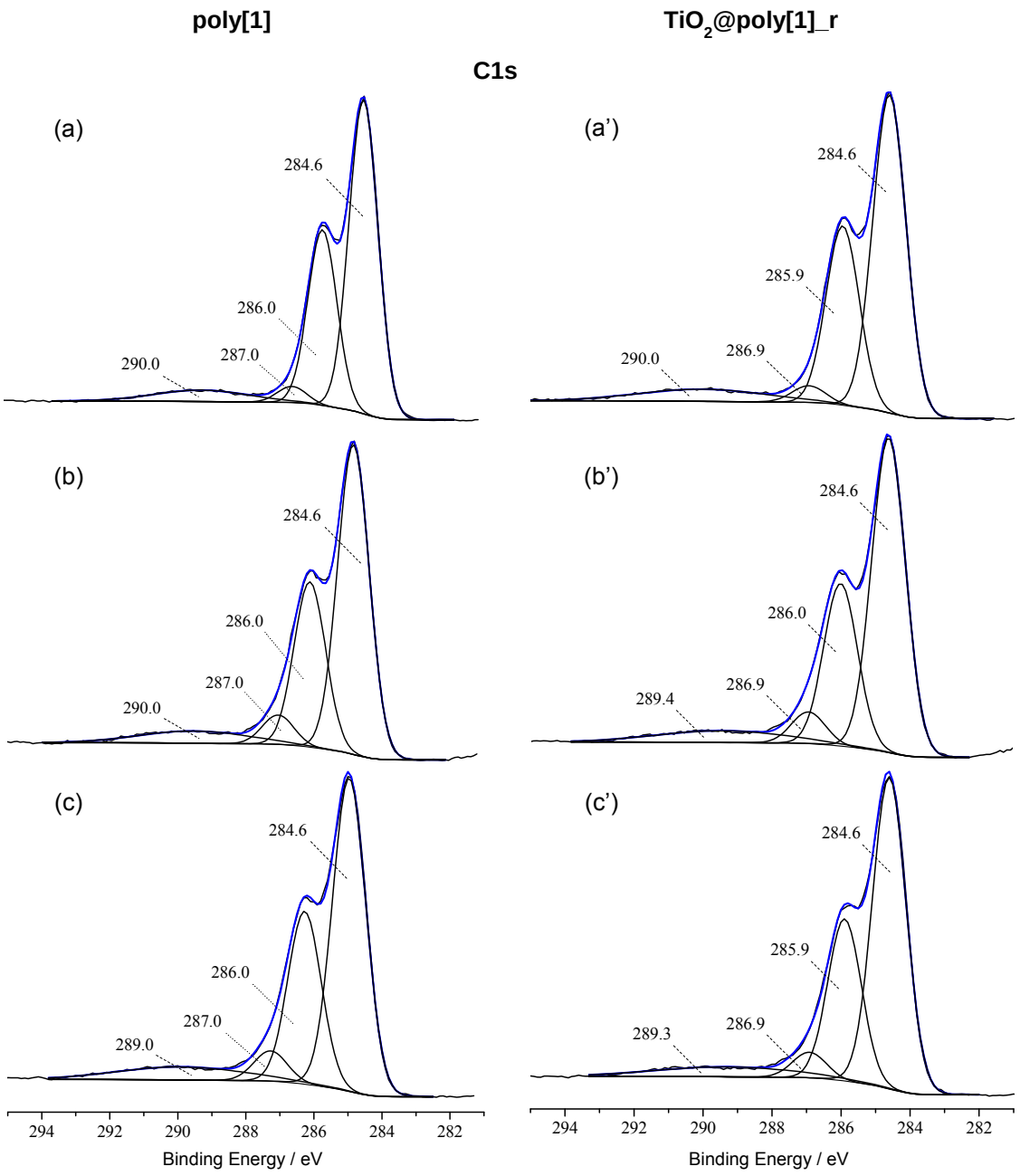

Figure 4.13 High-resolution XPS spectra of pristine poly[1] (taken from Chapter 3) and TiO_2@poly[1]_r in C1s region, with the corresponding deconvolutions, (a and a') before and after redox switching in (b and b') $LiClO_4/CH_3CN$ and (c and c') $LiClO_4$/PC.

The XPS spectra in the C1s region (Figure 4.13) were deconvoluted with four peaks: a main peak at 284.6 eV attributed to aromatic and aliphatic carbons of the *salen* ligand, a peak at 285.9-286.0 eV assigned to carbon bound to oxygen and nitrogen in the *salen* moiety, a peak at 286.9-287.0 eV ascribed to C≡N or to C=O from CH_3CN or PC, respectively, and a peak at 289.3-290.0 eV assigned to a shake-up satellite due to π-π* transitions in the ligand.[31]

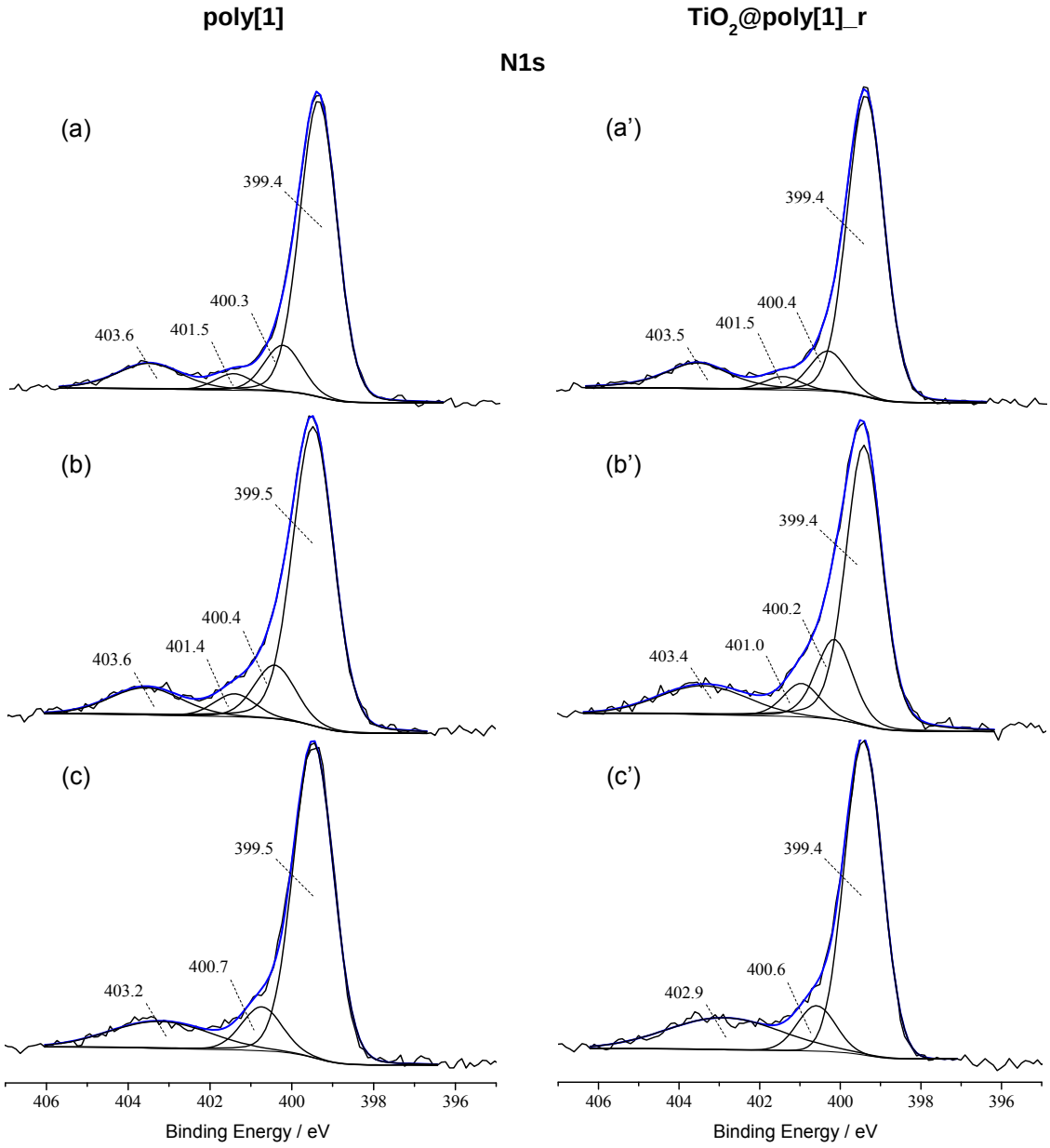

Figure 4.14 High-resolution XPS spectra of pristine poly[1] (taken from Chapter 3) and TiO_2@poly[1]_r in N1s region, with the corresponding deconvolutions, (a and a') before and after redox switching in (b and b') $LiClO_4/CH_3CN$ and (c and c') $LiClO_4$/PC.

The films N1s spectra before and after redox switching in $LiClO_4/CH_3CN$ (Figure 4.14 (a), (a'), (b) and (b')) were deconvoluted with four peaks, at 399.4-399.5 eV, 400.2-400.4 eV, 401.0-401.5 eV and 403.4-403.6 eV attributed, respectively, to the nitrogen atoms of ligand system (N=C and N-C bonds), N≡C of the occluded CH_3CN and to a shake-up phenomenon.[31] In the nanocomposites spectra, the first peak also has the contribution of N-Ti and N-O-Ti bonds from TiO_2 NPs. In the spectra of films after redox cycling in $LiClO_4$/PC (Figure 4.14 (c) and (c')), the peak at 401.0-401.5 eV was not identified, once the solvent was changed for PC, and all others remain similar.

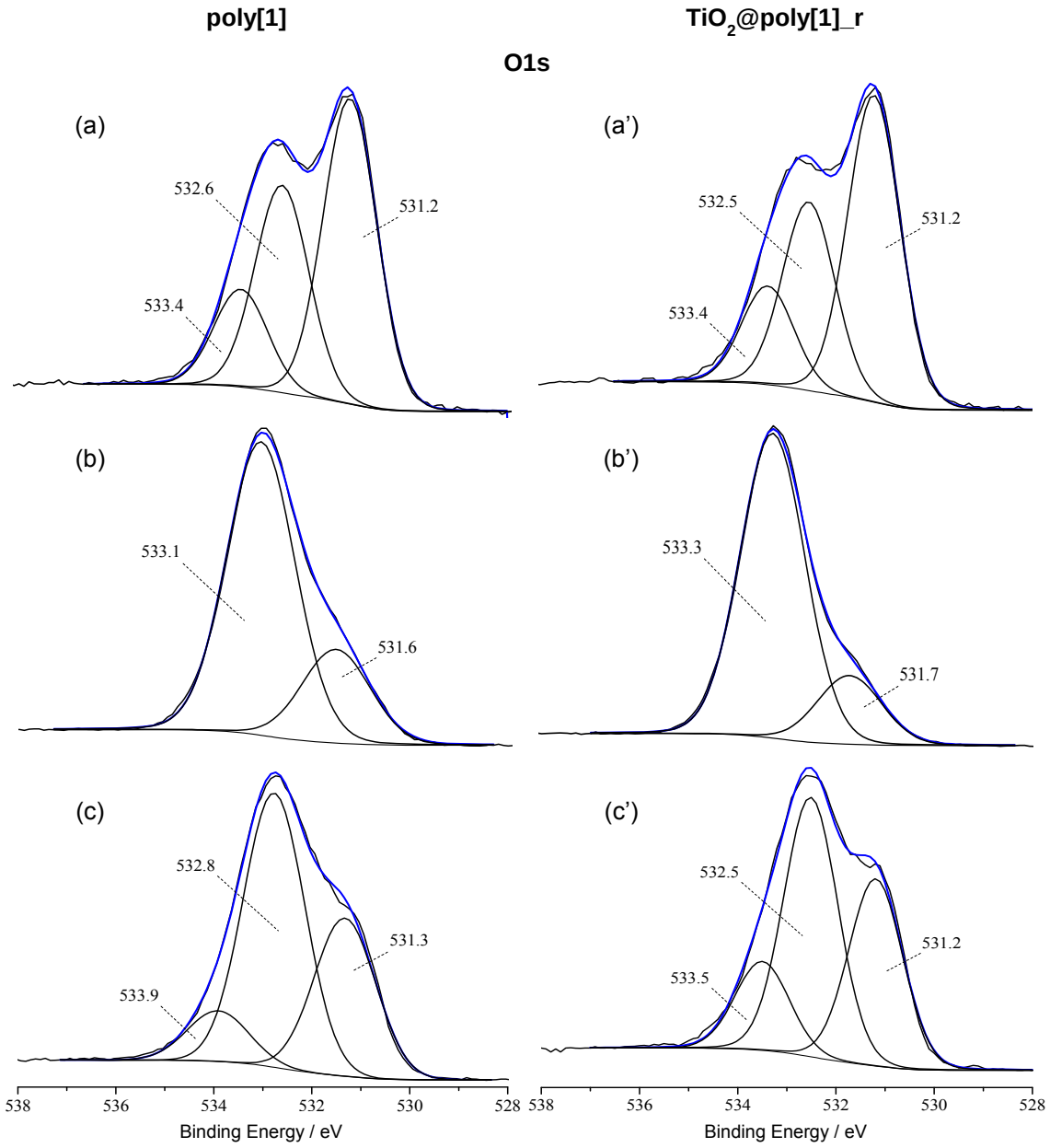

Figure 4.15 High-resolution XPS spectra of pristine poly[1] (taken from Chapter 3) and TiO_2@poly[1]_r in O1s region, with the corresponding deconvolutions, (a and a') before and after redox switching in (b and b') $LiClO_4/CH_3CN$ and (c and c') $LiClO_4$/PC.

The O1s spectrum of nanocomposite before redox switching (Figure 4.15 (a')) was deconvoluted with three peaks at 531.2, 532.5 and 533.4 eV; the former is assigned to the oxygen of the *salen* coordination sphere[31] and to O-Ti bonds, while the last two are ascribed to trapped ClO_4^- with different neighbourhoods and –OH groups from TiO_2 NPs.

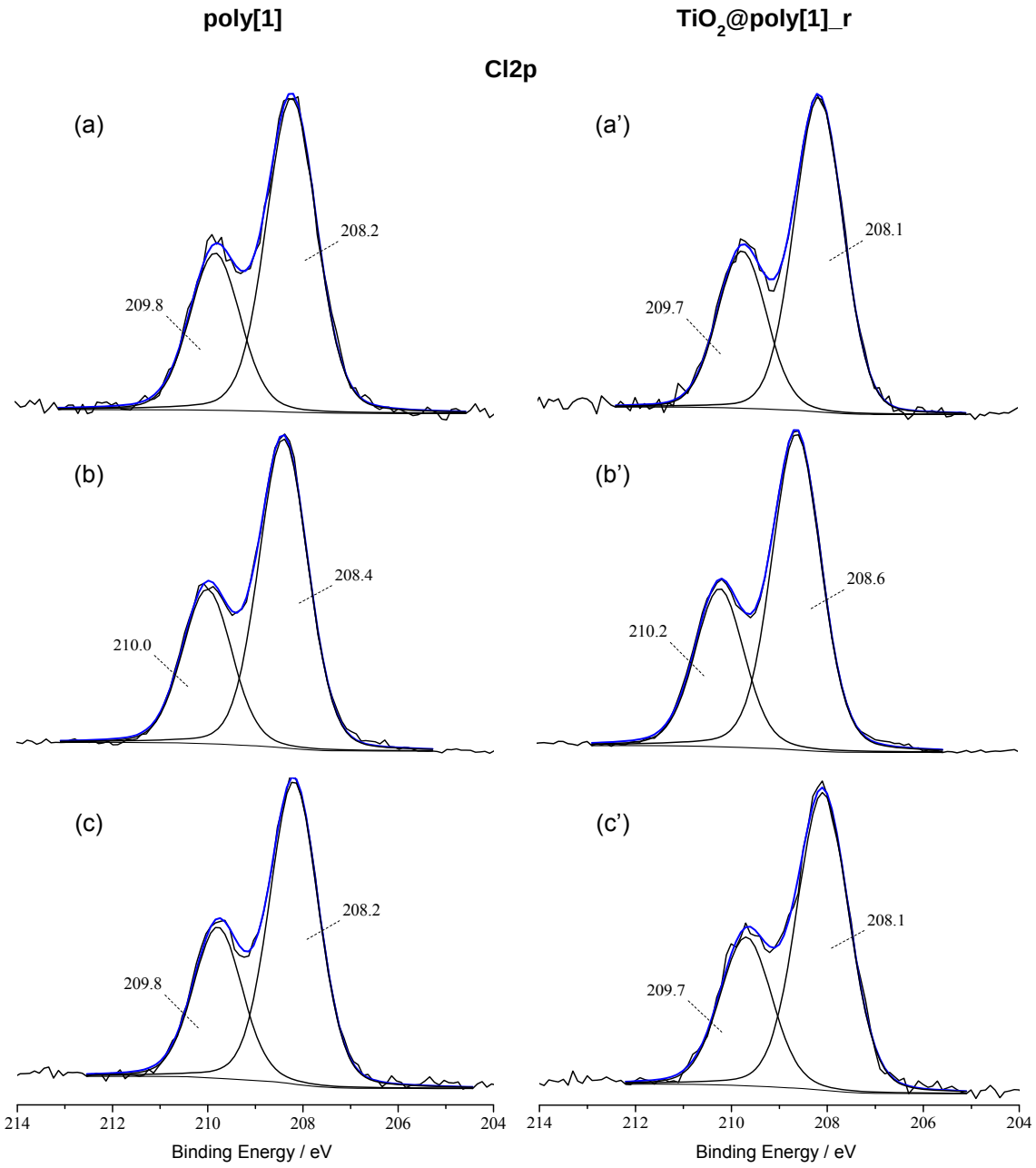

Figure 4.16 High-resolution XPS spectra of pristine poly[1] (taken from Chapter 3) and TiO_2@poly[1]_r in Cl2p region, with the corresponding deconvolutions, (a and a') before and after redox switching in (b and b') $LiClO_4/CH_3CN$ and (c and c') $LiClO_4$/PC.

In the O1s spectrum of nanocomposite after redox switching in $LiClO_4/CH_3CN$ (Figure 4.15 (b')), it is observed a peak at 531.7 eV (O of *salen* coordination sphere and O-Ti), along with a large peak at 533.3 eV ascribed to –OH groups from TiO_2 and to higher amounts of ClO_4^-, trapped in polymeric film as charge compensation anion. For the nanocomposite after redox cycling in $LiClO_4/PC$ (Figure 4.15 (c')), beyond the two peaks at 531.2 and 532.5 eV (similarly to the redox in $LiClO_4/CH_3CN$), it is observed an additional peak at 533.5eV, assigned to O-C bonds in occluded PC (as in Chapter 3).

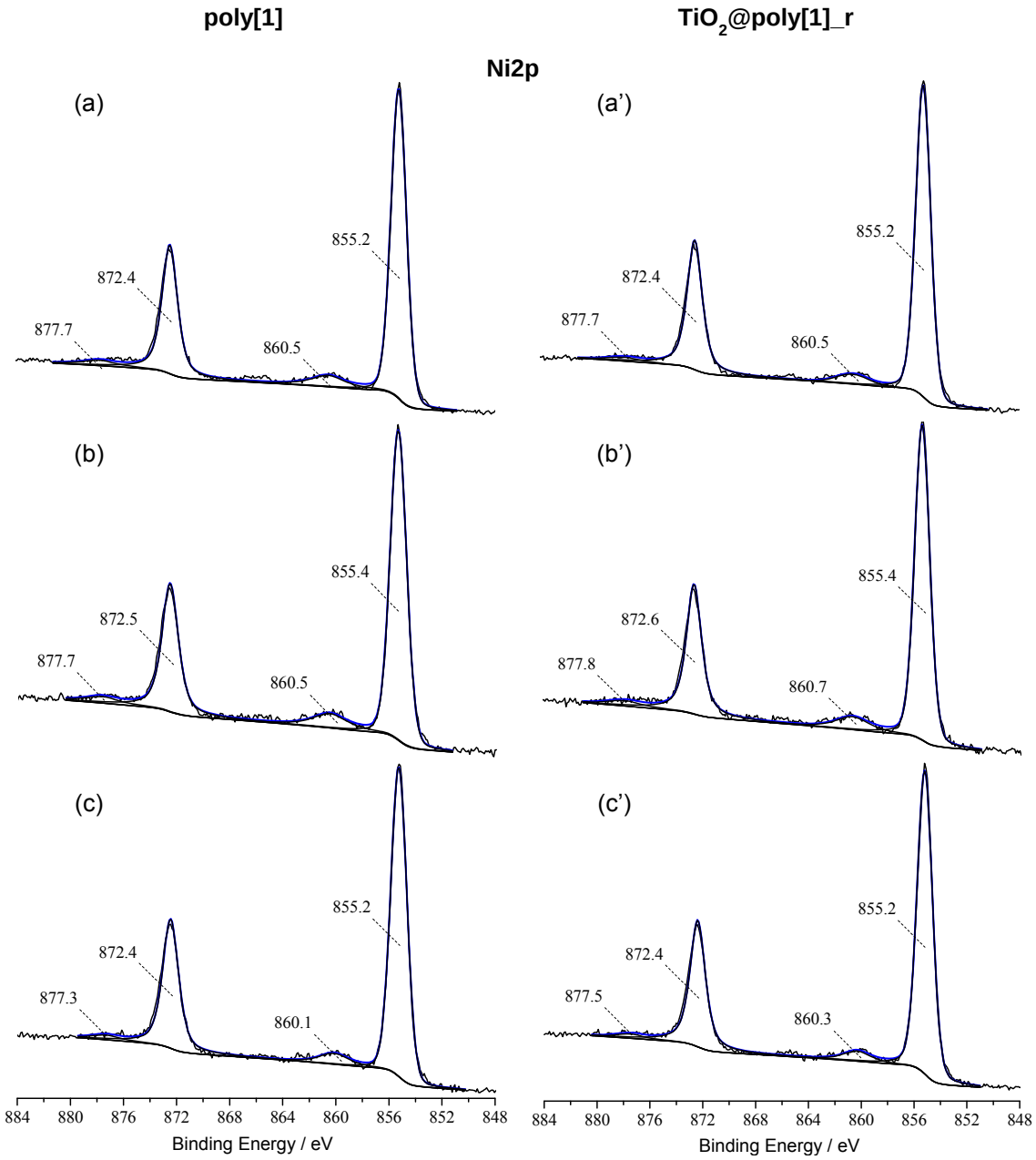

Figure 4.17 High-resolution XPS spectra of pristine poly[1] (taken from Chapter 3) and TiO_2@poly[1]_r in Ni2p region, with the corresponding deconvolutions, (a and a') before and after redox switching in (b and b') $LiClO_4/CH_3CN$ and (c and c') $LiClO_4/PC$.

In the Cl2p spectra (Figure 4.16) two peaks are observed at 208.1-208.6 eV and 209.7-210.2 eV, assigned to Cl $2p_{3/2}$ and Cl $2p_{1/2}$ from ClO_4^- trapped on films.[31]

The Ni2p region (Figure 4.17) shows the characteristic peaks of Ni in a formal +2 oxidation state, which are attributed to $Ni2p_{3/2}$ (855.2-855.4 eV), $Ni2p_{3/2}$ satellite (860.1-860.7 eV), $Ni2p_{1/2}$ (872.4-872.6 eV) and $Ni2p_{1/2}$ satellite (877.3-877.8 eV).[31]

In the typical XPS analyses, Ti was not detected, which can be explained by the low content of TiO_2 NPs in proportion to the high thickness of polymeric film, coupled with the fact that XPS is a surface characterisation technique. Nonetheless, a parallel XPS experiment was performed, by treating the nanocomposite by ionic erosion. The results revealed new peaks in the BE range 455 – 470 eV. The XPS spectrum in this region (Figure 4.18) was deconvoluted with two peaks at 459.9 eV and 465.5 eV, assigned to $Ti2p_{3/2}$ and $Ti2p_{1/2}$, respectively, with Δ = 5.6 eV, which is typical of Ti in TiO_2 matrix[34] and confirm the successful preparation of the TiO_2@poly[1]_r nanocomposite.

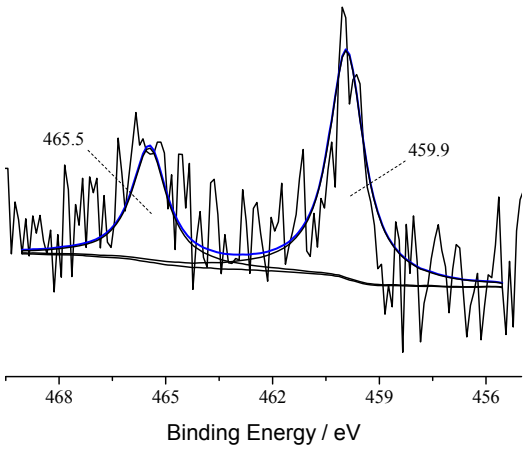

Figure 4.18 High-resolution XPS spectra in Ti2p region for TiO_2@poly[1]_r treated by ionic erosion, with respective deconvolutions.

4.3.4 *In situ* UV-Vis spectroscopy

The absolute UV-Vis spectra acquired during the oxidation of TiO_2@poly[1] nanocomposites (with 5 wt.% of TiO_2 NPs) and pristine poly[1], for comparison, are depicted in Figure 4.19 (a), (b) and (c); the spectra obtained during films reduction show an inverse behaviour and were omitted for simplicity.

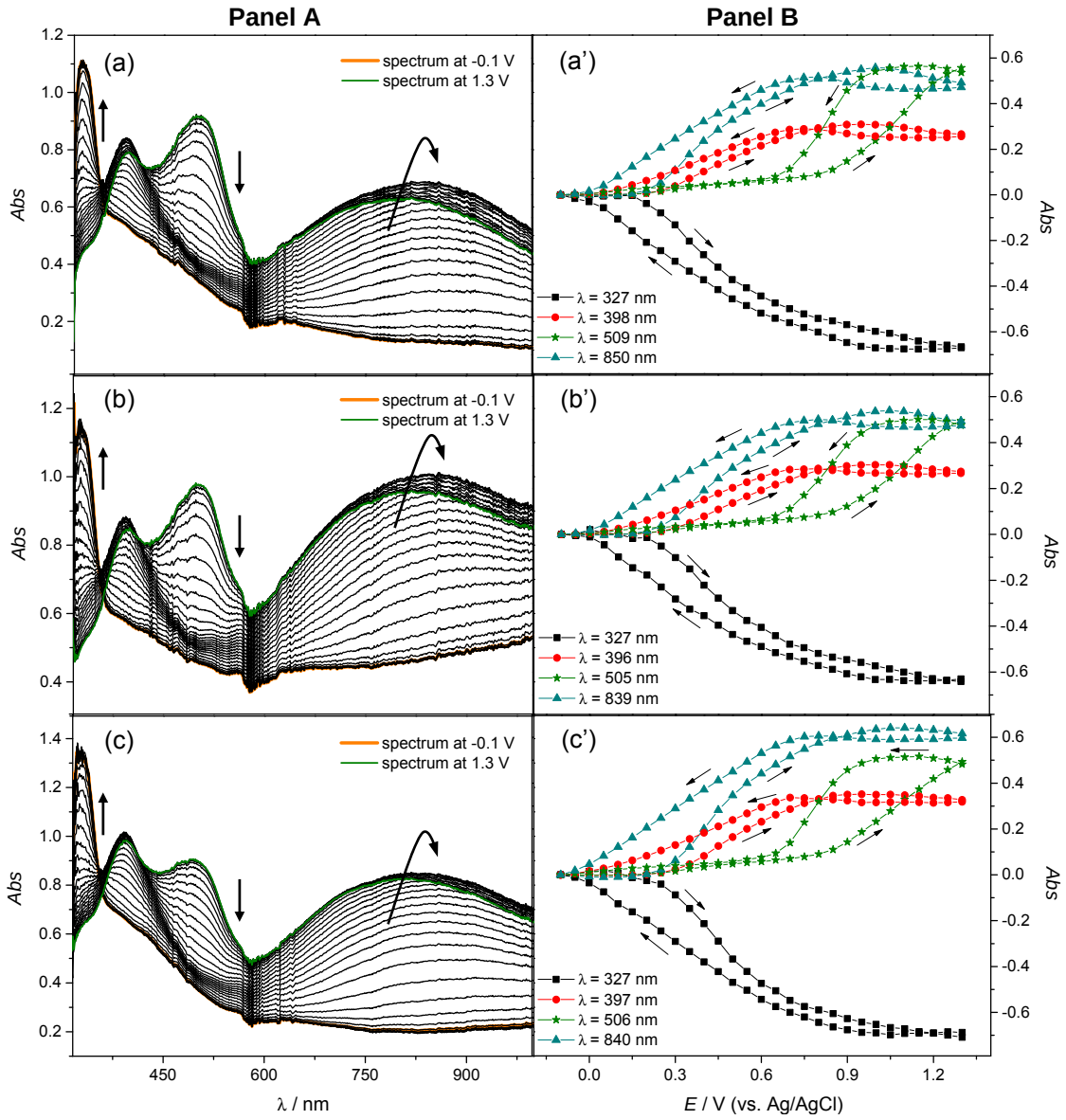

Figure 4.19 Panel A: Absolute UV-Vis spectra of (a) poly[1] (Γ = 95.3 nmol cm^{-2}), (b) TiO_2@poly[1]_s and (c) TiO_2@poly[1]_r (prepared with 5 wt.% of TiO_2 NPs at 0.020 V s^{-1}, Γ = 104.2-107.7 nmol cm^{-2}) acquired during films oxidation in 0.1 mol dm^{-3} $LiClO_4$/PC (referenced to the electrolyte spectrum). Panel B: *Abs* vs. *E* plots for the electronic bands identified in absolute UV-Vis spectra, referenced to the spectra at *E* = -0.1 V (arrows indicate scan direction).

Both nanocomposites spectra show four electronic bands, likewise the spectra of the poly[1] film. In Figure 4.20 are shown the differential spectra, in which responses at selected potentials were used as reference, allowing an easy view of the electronic bands dependence with the potential. These spectra, as well as the absorbance vs. potential (*Abs* vs. *E*) profiles at selected wavelengths (Figure 4.19 (a'), (b') and (c')), indicated that the nanocomposites present three main band profiles, such as the pristine film and similar to other poly[M(*salen*)] films:[31,32] (i) a band at lower wavelengths (λ = 327 nm) whose intensities decrease monotonically with increasing

potential, (ii) two bands at λ = 396-398 nm and at λ = 839-850 nm, whose intensities increase until *E* = 0.8-0.9 V and thereafter decrease until the end of the positive half cycle, and (iii) a band at λ = 505-509 nm, whose intensities increase monotonically with potential from *E* = 0.8-0.9 V until the end of the positive half scan.

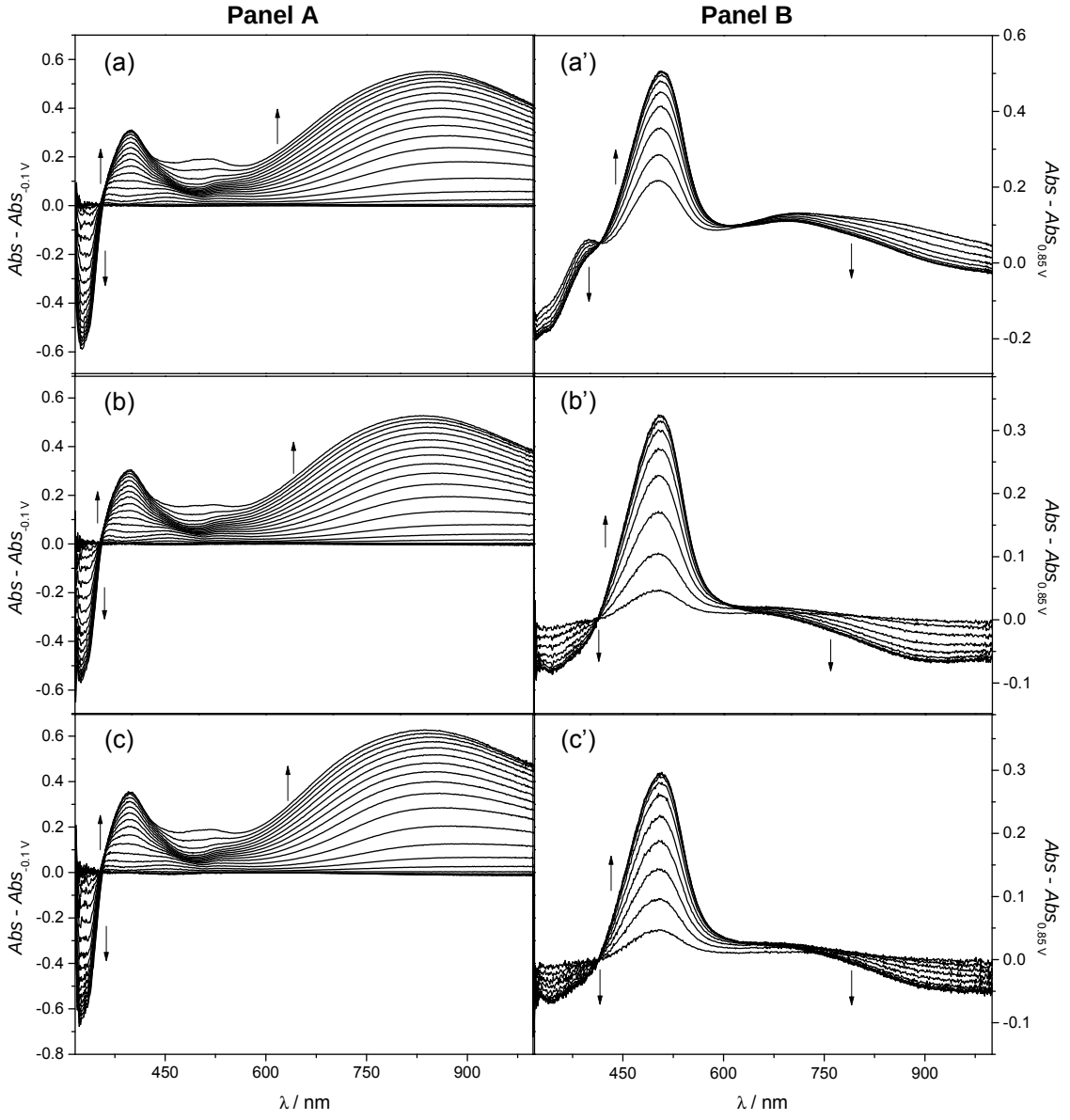

Figure 4.20 UV-Vis spectra of (a and a') poly[1], (b and b') TiO_2@poly[1]_s and (c and c') TiO_2@poly[1]_r acquired during films oxidation in $LiClO_4$/PC from (Panel A) -0.1 to 0.85 V and referenced to the spectra of neutral films and (Panel B) 0.85 to 1.3 V and referenced to the spectra of films at *E* = 0.85 V.

The energies of the electronic bands for all films are summarised in Table 4.5, together with the molar extinction coefficients, ε, estimated using the Equation 2.1, from the slopes of *Abs* vs. Q plots (Figure 4.21).

Table 4.5 Wavelengths of the electronic bands and respective energies and molar extinction coefficients (ε) for poly[1] and TiO_2@poly[1] nanocomposites (prepared with 5 wt.% of TiO_2 NPs at 0.020 V s^{-1}).

Film	λ / nm (eV)	$\varepsilon \times 10^{-3}$ / mol^{-1} dm^3 cm^{-1}
poly[1]	327 (3.80)	6.80
	398 (3.12)	3.78
	509 (2.44)	**12.19**
	850 (1.46)	6.44
TiO_2@poly[1]_s	327 (3.80)	6.81
	396 (3.14)	3.57
	505 (2.46)	**11.75**
	839 (1.48)	6.12
TiO_2@poly[1]_r	327 (3.80)	7.24
	397 (3.13)	3.96
	506 (2.45)	**10.21**
	840 (1.48)	6.68

The ε-values obtained for nanocomposites are typical of electronic transitions between states with large contribution from ligand, which is consistent with the ligand-based film oxidation, as proposed for poly[1] (Chapter 2) and other similar poly[Ni(*salen*)] films.[31,32] Using the polaronic model[31,32] and considering that electronic bands with similar *Abs* vs. *E* profiles are associated with the same charge carriers, the follow band assignment can be made: (i) the band at λ = 327 nm is attributed to the intervalence transition (band gap, E_g = 3.80 eV), (ii) the band at λ = 396-397 nm (3.14-3.13 eV) is assigned to transitions from the valence band to the antibonding polaron level and (iii) the band at λ = 839-840 nm (1.48 eV) corresponds to transitions from the valence band to the bonding polaron level (or between polaron levels). The band at λ = 505-509 nm (2.44-2.46 eV), with their different *Abs* vs. *E* profiles, is attributed to charge transfer (CT) transitions between the metal and the oxidised ligand.[31,32]

Furthermore, the bands observed in spectra of nanocomposites and pristine films have similar energies, which indicate that the electronic structure of poly[1] was not changed by the incorporation of TiO_2 NPs.

The ε-values for the nanocomposites electronic bands are also similar to those of the pristine film, except for the band assigned to CT transitions at λ = 505-506 nm (2.44-2.46 eV). For this band, the ε-value decreases significantly from the pristine to the nanocomposites films. For TiO_2@poly[1]_s nanocomposite, the ε-value decreases 3.6 % (ε = 11.75 x 10^{-3} vs. 12.19 x 10^{-3} mol^{-1} dm^3 cm^{-1}), being more significant -

16.2 % - for TiO_2@poly[1]_r (ε = 10.21 x 10^{-3} vs. 12.19 x 10^{-3} mol^{-1} dm^3 cm^{-1}). Once the CT bands are associated with less stable oxidised states of poly[1], its decrease can point to an increase of nanocomposites stability for over-oxidation due to the TiO_2 incorporation, mainly for TiO_2@poly[1]_r. An identical behaviour was already observed for nanocomposites of poly[1] with WO_3 NPs (Chapter 3). The different results between TiO_2@poly[1] nanocomposites indicate that the preparation method of starting solutions can influence into some extent the electrical properties of the nanocomposite.

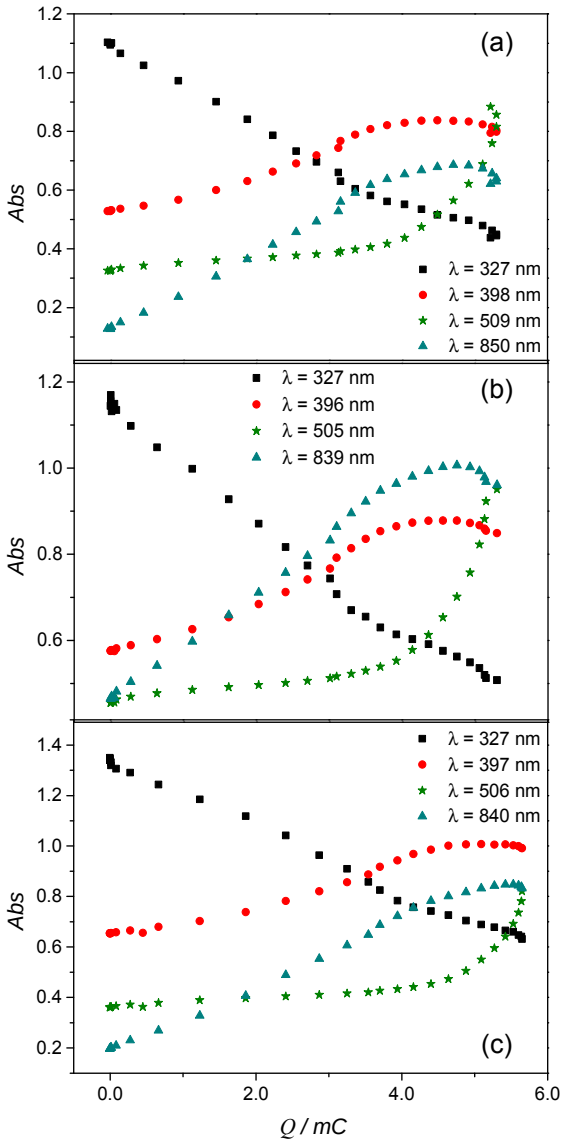

Figure 4.21 Plots of the *Abs* vs. Q for selected electronic bands of (a) poly[1], (b) TiO_2@poly[1]_s and (c) TiO_2@poly[1]_r (c) in 0.1 mol dm^{-3} $LiClO_4$/PC (for anodic scan).

4.3.5 Electrochromic properties

Considering the results obtained in the spectroeletrochemical studies, the investigation of the EC properties was performed with TiO_2@poly[1]_r and pristine film, for comparison.

The electrochemical stability of the nanocomposite film was evaluated by a chronoamperometric study, monitoring the current intensity variations along almost consecutive 10 000 redox cycles of colour change between yellow and green. The chronoamperograms are depicted in Figure 4.22 (a) and show that at the end of 11 days (9504 electrochemical cycles), the nanocomposite film had a charge loss of only 7.3 %, while the pristine film, in the same experimental conditions, lost 13.7 %; this represents an improvement of 46.7 % in the electrochemical stability for the nanocomposite film, which is attributed to an intimate contact (electron donor-acceptor interaction) of the TiO_2 NPs and poly[1] and to the hybrid architecture promoted by the nanomaterial incorporation.[17]

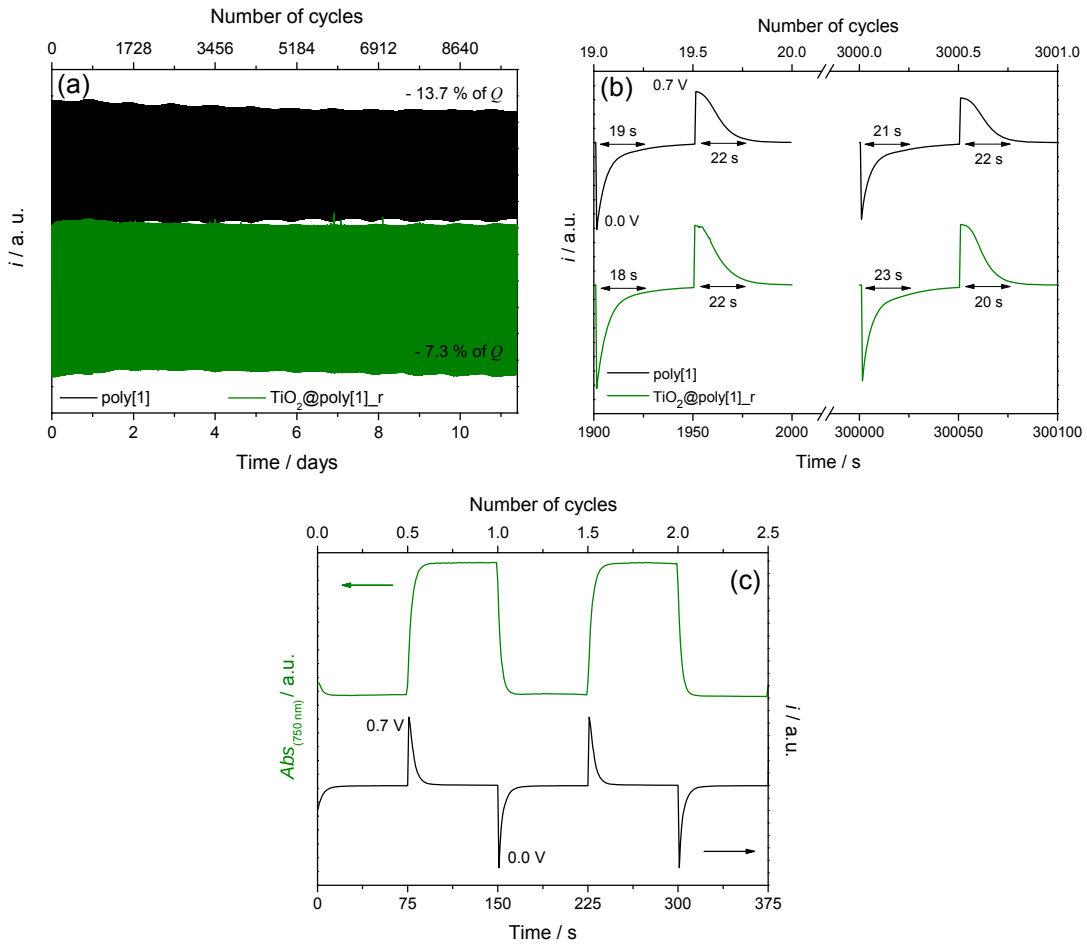

Figure 4.22 (a) Chronoamperograms of pristine and TiO_2@poly[1]_r films in $LiClO_4$/PC 0.1 mol dm^{-3}, applying two potential pulses of 50 s by redox cycle, with potential alternating between 0.0 V (yellow) and 0.7 V (green); (b) expansion of the chronoamperograms, showing the measured switching times at the 19th and 3000th cycles; (c) chronoamperograms/absorptograms obtained for TiO_2@poly[1]_r film, at the fixed wavelength of λ = 750 nm.

The response times (Figure 4.22 (b)) reveal very similar responses between the nanocomposite and the pristine film: during the 19th cycle, the nanocomposite needs τ = 18 s to change colour between green and yellow and τ = 22 s to return to green, while poly[1] needs τ = 19 and 22 s, respectively. These response times remains almost unchanged during several cycles, as demonstrate by the times obtained at the 3000th cycle (τ = 20 - 23 s).

The optical contrast, optical density change and colouration efficiency were evaluated through the monitoring of a similar chronoamperometry by *in situ* UV-Vis spectroscopy, at λ = 750 nm (Figure 4.22 (c)). The values obtained for these parameters and the charge requirements are summarised in Table 4.6.

Table 4.6 EC parameters: optical contrast (ΔT %), change of the optical density (ΔOD), charge requirement (Q_d), and colouration efficiency (η) for pristine poly[1] and TiO_2@poly[1]_r nanocomposite films in $LiClO_4$/PC supporting electrolyte, at λ = 750 nm.

Film	ΔT %	ΔOD	Q_d / mC cm^{-2}	η / cm^2 C^{-1}
poly[1]	46.3	0.40	4.53	87.7
TiO_2@poly[1]_r	43.4	0.48	5.45	87.5

The ΔT values, measured considering the full optical change between yellow and green, slightly decrease from the pristine poly[1] film (ΔT = 46.3 %) to TiO_2@poly[1]_r (ΔT = 43.4 %). The ΔOD values, slightly increase from ΔOD = 0.40 in poly[1] to ΔOD = 0.48 in TiO_2@poly[1]_r, representing an improvement of 16.7 %, what is not expected since ΔT values slightly decreases on going from the pristine film to the nanocomposite; this may result from the conversion of absorbance to transmittance units necessary for the calculations. For the colouration efficiency of the nanocomposite, the obtained value remain similar to the pristine film (η = 87.5 vs. 87.7 cm^2 C^{-1}), once the higher ΔOD value obtained for nanocomposite involved a slight increase in charge requirement in comparison to pristine film (Q_d = 5.45 vs. 4.53 mC cm^{-2}).

In comparison with the EC properties achieved for the nanocomposite between poly[1] and WO_3 NPs (Chapter 3), the incorporation of TiO_2 NPs on poly[1] matrix shows to be more advantageous once, in $LiClO_4$/PC, allowed to obtain nanocomposites with higher ΔOD and an excellent electrochemical stability. The WO_3@poly[1] in $LiClO_4$/PC showed similar ΔOD values and smaller electrochemical stability than the pristine film. In literature, some works also have reported the preparation of

nanocomposites between TiO_2 NPs and PANI[16,20,21] and PEDOT:PSS[22] electroactive polymers, which showed fast and better optical modulation and superior cycling stability than the correspondents pristine CPs.

The EC properties evaluation was complemented by a colorimetric study, considering the importance of the colour for practical applications of EC materials. The CIELAB coordinate values (L*, a* and b*) and colour difference ΔE* between different oxidation states of nanocomposite and pristine films are summarised in Table 4.7.

Table 4.7 CIELAB colour values (L*, a*, b*) and colour difference, ΔE*, between different oxidation states of pristine and nanocomposite films.

Film	*E* / V[a]	L*	a*	b*	*E* range / V	ΔL*	Δa*	Δb*	ΔE*
poly[1]	0.0	63.2	4.8	55.4					
	0.7	31.9	-10.0	18.8	0.0-0.7	-31.3	-14.8	-36.6	50.4
	1.3	22.2	2.2	7.4	0.7-1.3	-9.7	12.2	-11.5	19.4
TiO_2@poly[1]_r	0.0	58.7	6.6	56.2					
	0.7	27.9	-7.1	12.9	0.0-0.7	-30.8	-13.7	-43.3	54.9
	1.3	20.6	0.5	3.2	0.7-1.3	-7.3	7.6	-9.7	14.3

[a] Values at *E* = 1.3 V may be subject to uncertainty (see main text).

The b* vs. a* plot (Figure 4.23) shows that at *E* = 0.0 V, the colour of both films is situated in the yellow-red quadrant, at high b* coordinates, indicating a predominant yellow colour. At *E* = 0.7 V, the coordinates are dislocated to yellow-green quadrant, at low a* values, reflecting a green colour. These results are in agreement with the photographs shown in Figure 4.11. At *E* = 1.3 V, the coordinates are localised in the yellow-red quadrant, at low a* and b* values, reflecting a colour between green and red, but lighter than the real colour observed (russet). This divergence is explained by the low stability of the films at high potential values: after the removal of the electrical stimulus (*E* = 1.3 V), the colour of films decays rapidly from russet to green; however, as the colorimetric study is *ex situ*, some uncertainty is associated with the CIELAB coordinates determined at *E* = 1.3 V.

For the colour change yellow-green, the nanocomposite film showed a slightly greater EC response (ΔE* = 54.9) than the poly[1], which is in agreement with the obtained ΔOD values. For the colour change green-russet, the ΔE* obtained was lower for nanocomposite, but it is need consider the uncertainty of coordinates at *E* = 1.3 V.

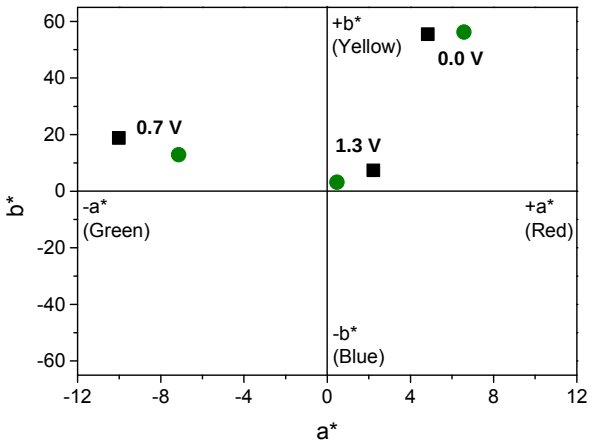

Figure 4.23 Graph of the CIELAB colour values (a*, b*) of pristine (symbol ■) and nanocomposite TiO_2@poly[1]_r (symbol ●) films, at different oxidation states: *E* = 0.0 V (yellow), *E* = 0.7 V (green) and *E* = 1.3 V (russet).

4.4 Conclusions

The results showed that the poly[1] was successfully electropolymerised in the presence of TiO_2 NPs, previously prepared and characterised by XRD, TEM and XPS. The NPs have a spherical shape with 9.7 ± 1.1 nm and are composed by anatase and brookite phases (65.5 vs. 34.5 %).

The CVs of the nanocomposites have similar electrochemical profiles to those of pristine film, but higher electroactive areas and electroactive surface coverages, which appoint the advantage of the polymeric nanocomposites assemble. Moreover, the increase of Γ is most significance for nanocomposite films electropolymerised at 0.020 mV s^{-1} and rise for TiO_2 loadings of 5 and 15 wt.%, decreasing for the loading of 25 wt.%, which indicates an optimal loading from which higher TiO_2 contents can hinder the poly[1] electrodeposition. The incorporation of the TiO_2 NPs on poly[1] matrix was confirmed by SEM and XPS. Furthermore, the XPS data revealed a superior accumulation of supporting electrolyte along the successive redox cycles for the nanocomposite film. The UV-Vis spectra show similar electron band profiles and energies between the pristine and the nanocomposites films, but lower ε-values were determined for the CT band of nanocomposites, indicating higher stability for ligand oxidation.

The TiO_2@poly[1]_r nanocomposite showed an excellent electrochemical stability, with a charge loss of 7.3 % after ≈ 10 000 redox cycles, which represents an improvement of 46.7 % in comparison to pristine film. The ΔOD also showed an increase of 16.7 % for nanocomposite film. These results clearly show the advantage

of the preparation of the nanocomposite in the pursue for a solution to improve the EC properties of the pristine poly[1].

References

[1] Dziewonski, P. M.; Grzeszczuk, M. *Electrochim. Acta* **2010**, *55*, 3336.

[2] Takagi, S.; Makuta, S.; Veamatahau, A.; Otsuka, Y.; Tachibana, Y. *J. Mater. Chem.* **2012**, *22*, 22181.

[3] Janaky, C.; de Tacconi, N. R.; Chanmanee, W.; Rajeshwar, K. *J. Phys. Chem. C* **2012**, *116*, 19145.

[4] Yang, L.; Zhang, J. B.; Shen, Y.; Park, B. W.; Bi, D. Q.; Haggman, L.; Johansson, E. M. J.; Boschloo, G.; Hagfeldt, A.; Vlachopoulos, N.; Snedden, A.; Kloo, L.; Jarboui, A.; Chams, A.; Perruchot, C.; Jouini, M. *J. Phys. Chem. Lett.* **2013**, *4*, 4026.

[5] Sidhu, N. K.; Rastogi, A. C. *Nanoscale Res. Lett.* **2014**, *9*, 16.

[6] Gottam, R.; Srinivasan, P. *J. Appl. Polym. Sci.* **2015**, *132*, 7.

[7] Arjomandi, J.; Mossa, N. K. I.; Jaleh, B. *J. Appl. Polym. Sci.* **2015**, *132*, 11.

[8] Hidalgo, D.; Bocchini, S.; Fontana, M.; Saracco, G.; Hernandez, S. *RSC Adv.* **2015**, *5*, 49429.

[9] Zhu, J.; Liu, X. Q.; Wang, X. H.; Huo, X. H.; Yan, R. *Sens. Actuator B-Chem.* **2015**, *221*, 450.

[10] Cai, G. F.; Tu, J. P.; Zhou, D.; Zhang, J. H.; Wang, X. L.; Gu, C. D. *Sol. Energy Mater. Sol. Cells* **2014**, *122*, 51.

[11] Mortimer, R. J. *Annu. Rev. Mater. Res.* **2011**, *41*, 241.

[12] Beverina, L.; Pagani, G. A.; Sassi, M. *Chem. Commun.* **2014**, *50*, 5413.

[13] Shankar, S.; Lahav, M.; van der Boom, M. E. *J. Am. Chem. Soc.* **2015**, *137*, 4050.

[14] Yassin, A.; Ocafrain, M.; Blanchard, P.; Mallet, R.; Roncali, J. *ChemElectroChem* **2014**, *1*, 1312.

[15] Ma, D. Y.; Shi, G. Y.; Wang, H. Z.; Zhang, Q. H.; Li, Y. G. *J. Mater. Chem. A* **2014**, *2*, 13541.

[16] Xia, X. H.; Chao, D. L.; Qi, X. Y.; Xiong, Q. Q.; Zhang, Y. Q.; Tu, J. P.; Zhang, H.; Fan, H. J. *Nano Lett.* **2013**, *13*, 4562.

[17] Janaky, C.; Rajeshwar, K. *Prog. Polym. Sci.* **2015**, *43*, 96.

[18] Eren, E.; Celik, G.; Uygun, A.; Tabaciarova, J.; Omastova, M. *Synth. Met.* **2012**, *162*, 1451.

[19] Ngaboyamahina, E.; Cachet, H.; Pailleret, A.; Sutter, E. M. M. *Electrochim. Acta* **2014**, *129*, 211.

[20] Cai, G. F.; Tu, J. P.; Zhou, D.; Zhang, J. H.; Xiong, Q. Q.; Zhao, X. Y.; Wang, X. L.; Guts, C. D. *J. Phys. Chem. C* **2013**, *117*, 15967.

[21] Xiong, S. X.; Phua, S. L.; Dunn, B. S.; Ma, J.; Lu, X. H. *Chem. Mat.* **2010**, *22*, 255.

[22] Lu, J. L.; Song, H.; Li, S. N.; Wang, L.; Han, L.; Ling, H.; Lu, X. H. *Thin Solid Films* **2015**, *584*, 353.

[23] Pinheiro, C.; Parola, A. J.; Pina, F.; Fonseca, J.; Freire, C. *Sol. Energy Mater. Sol. Cells* **2008**, *92*, 980.

[24] Branco, A.; Pinheiro, C.; Fonseca, J.; Tedim, J.; Carneiro, A.; Parola, A. J.; Freire, C.; Pina, F. *Electrochem. Solid State Lett.* **2010**, *13*, J114.

[25] Huang, B. R.; Lin, T. C.; Liu, Y. M. *Sol. Energy Mater. Sol. Cells* **2015**, *133*, 32.

[26] Freire, C.; de Castro, B. *J. Chem. Soc.-Dalton Trans.* **1998**, 1491.

[27] Mahshid, S.; Askari, M.; Ghamsari, M. S. *J. Mater. Process. Technol.* **2007**, *189*, 296.

[28] Silva, E.; La Porta, F. A.; Liu, M. S.; Andres, J.; Varela, J. A.; Longo, E. *Dalton Trans.* **2015**, *44*, 3159.

[29] Chen, C. C.; Hu, S. H.; Fu, Y. P. *J. Alloy. Compd.* **2015**, *632*, 326.

[30] Choi, M.; Yong, K. *Nanoscale* **2014**, *6*, 13900.

[31] Fonseca, J.; Tedim, J.; Biernacki, K.; Magalhaes, A. L.; Gurman, S. J.; Freire, C.; Hillman, A. R. *Electrochim. Acta* **2010**, *55*, 7726.

[32] Tedim, J.; Patricio, S.; Fonseca, J.; Magalhaes, A. L.; Moura, C.; Hillman, A. R.; Freire, C. *Synth. Met.* **2011**, *161*, 680.

[33] Lei, X. F.; Xue, X. X.; Yang, H.; Chen, C.; Li, X.; Niu, M. C.; Gao, X. Y.; Yang, Y. T. *Appl. Surf. Sci.* **2015**, *332*, 172.

[34] Cheng, J.; Chen, J.; Lin, W.; Liu, Y.; Kong, Y. *Appl. Surf. Sci.* **2015**, *332*, 573.

[35] Manzo-Robledo, A.; Lopez, A. C.; Caballero, A. A. F.; Cadena, A. A. Z.; Lopez, M.; Vazquez-Cuchillo, O. *Mater. Sci. Semicond. Process* **2015**, *31*, 94.

[36] Jagadale, T. C.; Takale, S. P.; Sonawane, R. S.; Joshi, H. M.; Patil, S. I.; Kale, B. B.; Ogale, S. B. *J. Phys. Chem. C* **2008**, *112*, 14595.

[37] Nolan, N. T.; Synnott, D. W.; Seery, M. K.; Hinder, S. J.; Van Wassenhoven, A.; Pillai, S. C. *J. Hazard. Mater.* **2012**, *211*, 88.

[38] Lin, C. K.; Tseng, S. C.; Cheng, C. H.; Chen, C. Y.; Chen, C. C. *Thin Solid Films* **2011**, *520*, 1375.

Chapter 5

N-doped graphene@poly[Ni(*salen*)] nanocomposite with outstanding electrochromic properties

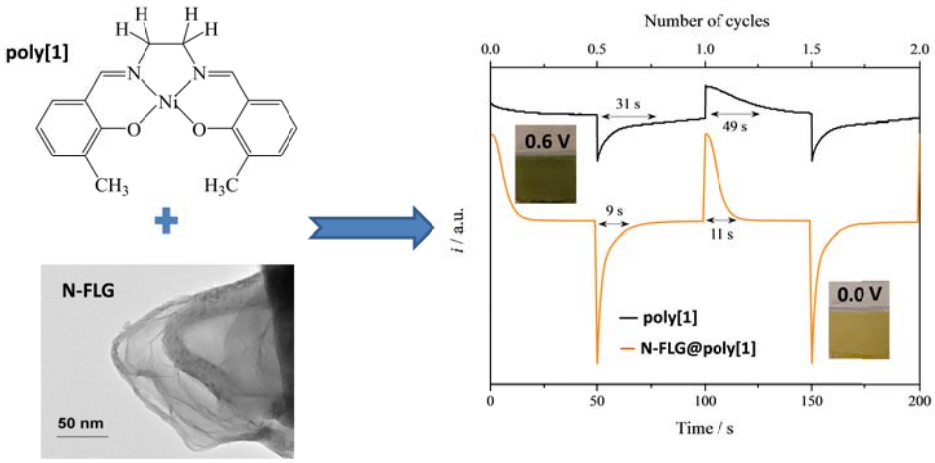

5

N-doped graphene@poly[Ni(*salen*)] nanocomposite with outstanding electrochromic properties[1,2,3]

Abstract

A new nanocomposite was obtained through the incorporation of N-doped few layer graphene (N-FLG) on poly[Ni(3-Mesalen)] electroactive polymer (poly[1]). The nanocomposite, N-FLG@poly[1], prepared by *in situ* electropolymerisation of the metal complex [Ni(3-Mesalen)] in the presence of N-FLG, showed similar electrochemical responses to pristine poly[1], but with more well-defined redox peaks and higher current intensities, in compliance with significantly larger electroactive surface coverage. N-FLG incorporation did not affect the electronic structure of poly[1], but caused significant increase (19 - 26 %) in the molar extinction coefficients of electronic bands assigned to transitions within polymer band gap and a decrease of 12 % in the molar extinction coefficient of the charge transfer band between metal and oxidised ligand (λ = 507 nm), which is a promising advantage once this band is related to ligand over-oxidation.

The N-FLG@poly[1] showed multi-electrochromic behaviour (yellow in reduced state and green / russet in oxidised states) and revealed an excellent improvement on electrochromic performance compared to pristine poly[1], showing an increase of 40 %

[1] Adapted from: M. Nunes, M. Araújo, R. Bacsa, R. V. Ferreira, E. Castillejos, P. Serp, A.R. Hillman and C. Freire, N-doped graphene@poly[Ni(*salen*)] nanocomposite with outstanding electrochromic properties. Submitted.

[2] M. Nunes's contribution to the publication: characterisation of the N-FLG by XPS, preparation and characterisation of the N-FLG@poly[1] nanocomposite and pristine poly[1] films, evaluation of the electrochromic properties and manuscript preparation.

[3] The experimental details on the electrochemical/spectroelectrochemical and remaining characterisation techniques are indicated in Appendices A and C, respectively.

in electrochemical stability, with a loss of only 2.7 % in charge after 10 000 colour switching cycles. Furthermore, the switching times decreased significantly to τ = 9 and 11 s (71/77 %) and the optical contrast and colouration efficiency have remarkable improvements, rising to ΔT = 35.9 % (increase of 38 %) and to η = 108.95 cm^2 C^{-1} (increase of 12 %), respectively. The conductive and electrochromic performance improvements are attributed to the alternative conducting pathways and to the morphologic modifications induced by the N-FLG incorporation within the electroactive polymer.

5.1 Introduction

Nowadays, the improvement of the electrochemical stability and the electrochromic contrast and the reduction of the switching times remain priority demands for successful application of conducting polymers as electrochromic materials.[1] In order to achieve these goals, composites of CPs with nanostructures have been prepared;[2-4] these new materials, generally known as polymeric nanocomposites (PNCs), are functional hybrid materials that typically comprise a nanometric filler, and show considerable improved properties due to the synergic effects of both counterparts.[5-7]

Due to its conjugated structure, excellent electron-transport properties and versatile chemistry, graphene (GF) has emerged as one of the most attractive carbon nanomaterials to be combined with CPs. With a two-dimensional (2D) sp^2-hybridised carbon structure in a single-atom-thick sheet, graphene shows interesting physicochemical properties, such as a large theoretical specific surface area, high carrier mobility at room temperature, good thermal conductivity, high Young's modulus and good optical transmittance.[8-10] Several graphene/PNCs have been prepared to optimise the properties and performances of polymers for several applications, such as in supercapacitors,[11-13] fuel[14,15] and solar[16] cells, sensors,[17,18] lithium-ion batteries[19] and in anticorrosion coatings.[20] For EC applications, some graphene/CPs nanocomposites with enhanced EC properties have also been reported, combining polyaniline and pyrrole-derivatives with graphene,[21,22] sulfonated-graphene,[23] graphene oxide[24] or reduced graphene oxide,[1] as counterparts. Ma *et al.*[25] reported the preparation of an electrochromic polySchiff base functionalised with reduced graphene oxide.

More recently, the chemical doping of graphene with heteroatoms (nitrogen, boron and sulphur) has emerged as an important approach to tailor the electrical, morphological and chemical properties of pristine graphene. Nitrogen is the most commonly used dopant, mainly due to its similar atomic radius to carbon, which

prevents significant lattice mismatch.[26,27] The main differences between nitrogen-doped graphene (N-GF) and pristine graphene are (i) the spin density and charge distribution on the carbon atoms (influenced by the neighbour nitrogen dopants) and (ii) the open band gap, making of N-GF a n-type semiconductor,[28] which is very useful for nanoelectronic applications. In the electrochromism field, the application of N-GF/TiO_2 nanocomposite, as an efficient electrode material to improve the EC properties of polythiophene-derivative EC polymer was reported.[29]

In this chapter it is described the preparation of a novel PNC made from poly[Ni(3-Mesalen)] electroactive film, designated hereafter as poly[1], and nitrogen-doped few layer graphene (N-FLG), and the evaluation of its EC performance. The pristine poly[Ni(3-Mesalen)], as described in Chapter 2, showed promising EC properties, with good electrochemical stability and interesting colour changes (yellow, green and russet). The preparation of a nanocomposite between poly[Ni(3-Mesalen)] and graphene flakes[30] allowed to improve in some extent the EC properties, leading to more favourable switching times and better optical contrast and colouration efficiencies relatively to pristine poly[1]. The novel PNC, N-FLG@poly[1], prepared by *in situ* electropolymerisation of poly[1] in the presence of N-FLG allowed the resulting nanocomposite to surpass the conductive and electrochromic properties of both pristine poly[1] and nanocomposite with graphene flakes, indicating that N-doping of few layer graphene had a unique beneficial effect. To the best of our knowledge, this is the first study on PNCs from the group of Metal-*salen* type electroactive metallopolymers and nitrogen-doped graphene.

5.2 Experimental section

5.2.1 Materials and solvents

The complex *N,N'*-bis(3-methylsalicylideneiminate) nickel(II), [Ni(3-Mesalen)] and respective *salen* ligand were prepared as described in literature.[31] Acetonitrile and propylene carbonate (Romil, pro analysis grade) and $LiClO_4$ (Aldrich, 99 %) were used as received.

N-FLG was prepared by chemical vapour deposition (CVD) from a mixture of ethylene and ammonia gases (Air Liquid, France) at 650 ºC in a vertical fluidised bed reactor using a cobalt ferrite spinel catalyst, the preparation of which is reported elsewhere.[32]

5.2.2 N-FLG preparation and characterisation

N-FLG were prepared by fluidised bed chemical vapour deposition process, by the decomposition of a mixture of ethylene and ammonia (90:10) in the presence of a

ternary oxide powder catalyst at 650°C.[32] The N-FLG powder was recovered after washing with 35 % HCl at 25°C. The nitrogen content was determined by XPS; the structure of the as-prepared N-FLG was confirmed by TEM and Raman spectroscopy.

5.2.3 Films preparation and electrochemical studies

The N-FLG@poly[1] nanocomposite films were prepared by cyclic voltammetry from the corresponding monomer solution, 1.0 mmol dm^{-3} [Ni(3-Mesalen)] complex in 0.1 mol dm^{-3} $LiClO_4/CH_3CN$, containing 0.5 wt.% of N-FLG/[Ni(3-Mesalen)]. The potential of the working electrode (ITO/PET 3.00 cm^2) was cycled between -0.2 and 1.3 V, at the scan rate of 0.100 V s^{-1}, during 30 scans; other conditions will be mentioned on the text. Prior to electrodeposition, the starting solution was refluxed for 3 hours, followed by sonication for 10 min, to ensure an optimum dispersion of the N-FLG powder and to promote some type of interaction between the monomer and N-FLG (e.g. adsorption of monomer on N-FLG). Pristine poly[1] films were prepared using the same experimental conditions but without N-FLG in the deposition solution.

After film deposition, the modified electrodes were rinsed with dry CH_3CN, immersed in a monomer- and N-FLG-free 0.1 mol dm^{-3} $LiClO_4$/PC solution and cycled (by CV) in the potential range of -0.2 to 1.3 V, at 0.010 V s^{-1}.

The electroactive surface coverage, Γ / nmol cm^{-2} (cited in terms of monomeric units), of each film was determined by a coulometric assay,[33,34] using cyclic voltammograms obtained in a monomer-free 0.1 mol dm^{-3} $LiClO_4/CH_3CN$ solution at the scan rate of 0.010 V s^{-1}, to ensure complete film redox conversion. The Γ variation with the number of electrodeposition cycles was studied for films prepared with 1 - 50 cycles. The doping level value used for the determination of Γ was calculated from the comparison of coulometric data for films deposition and cycling, as described in literature,[33,34] and the value of n = 0.65 was used.

5.2.4 Composition and morphology characterisation

The composition and morphology of the nanocomposite films were characterised by XPS and SEM/EDS, respectively, by the analysis of films in the reduced state (E = -0.2 V, after cycling the potential between -0.2 and 1.3 V at 0.010 V s^{-1}, during 2 scans, in $LiClO_4/CH_3CN$). Exceptionally, in the preparation of nanocomposite for SEM/EDS analysis, the percentage of N-FLG used in the deposition solution was increased to 25 wt.%, in order to make the N-FLG flakes easily observable in the polymeric matrix.

5.2.5 Spectroelectrochemical studies

In the monitoring of the films redox switching by *in situ* UV-Vis spectroscopy, the potential was cycled between -0.2 and 1.3 V, at the scan rate of 0.020 V s^{-1}, using $LiClO_4$/PC 0.1 mol dm^{-3} as the supporting electrolyte. The UV-Vis spectra were acquired simultaneously over 0.5 s intervals, in the wavelength range of 315 – 1100 nm. The molar extinction coefficients, ε / cm^{-1} mol^{-1} dm^3, of all electronic bands were calculated using the combination of the Beer-Lambert and Faraday laws (Equation 2.1).

5.2.6 Electrochromic properties evaluation

The evaluation of the EC parameters was performed in $LiClO_4$/PC 0.1 mol dm^{-3} supporting electrolyte, considering the colour change yellow ↔ green (see Chapter 2).

The electrochemical stability tests were carried out by double potential step method (chronoamperometry), applying two potential pulses of 50 s by redox cycle, with potential alternating between E = 0.0 and 0.6 V, for the period of time of 9815 redox cycles (≈ 12 days). The switching times were determined from the obtained chronoamperograms considering 85 % of the full optical change.[35]

The remaining EC parameters were determined by *in situ* monitoring of the chronoamperometry using UV-Vis spectroscopy (chronoabsorptometry); the simultaneous chronoabsorptometric measurements were performed at the fixed wavelength of λ = 820 nm, acquiring the UV-Vis spectra at intervals of 1 s, during 4 redox cycles. The change of the optical density and the colouration efficiency parameters were estimated through Equation 1.1.

All the EC parameters were also evaluated for pristine poly[1] film under the same conditions, for comparison.

5.3 Results and discussion

5.3.1 N-FLG characterisation

Figure 5.1 shows the TEM images of (a) purified N-FLG and (b) an enlarged view of the edge of a flake. The microscopy images show the presence of uniform flakes of around 200 nm. The edges of the flakes showed increased exfoliation and appeared more transparent. An enlarged view of the edge shows curving indicating that the edges are doped preferentially, when compared to the centre. This result is consistent with the results obtained for graphene films doped with nitrogen or hydrogen.[36]

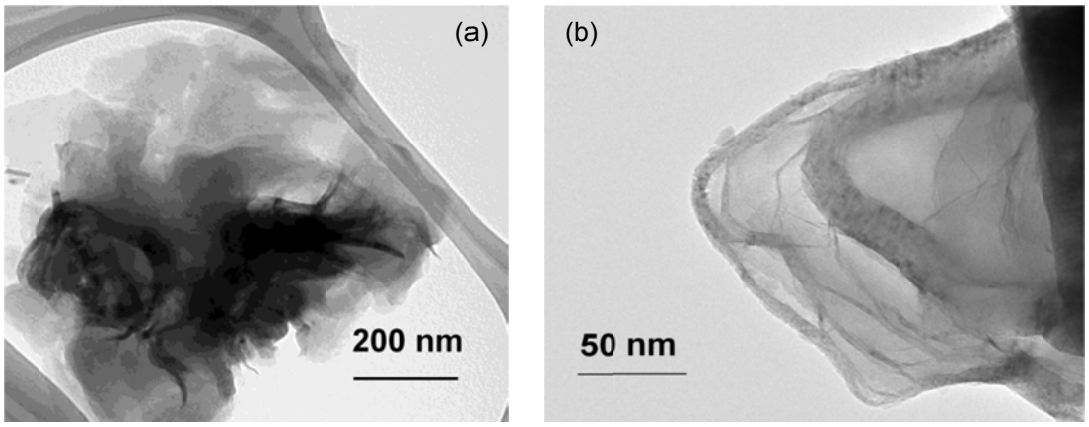

Figure 5.1 TEM micrographs of (a) purified N-FLG and (b) an enlarged view of the edge of a flake.

The nitrogen content of N-FLG was determined by XPS. The deconvoluted high-resolution spectra of the identified elements are presented in Figure 5.2.

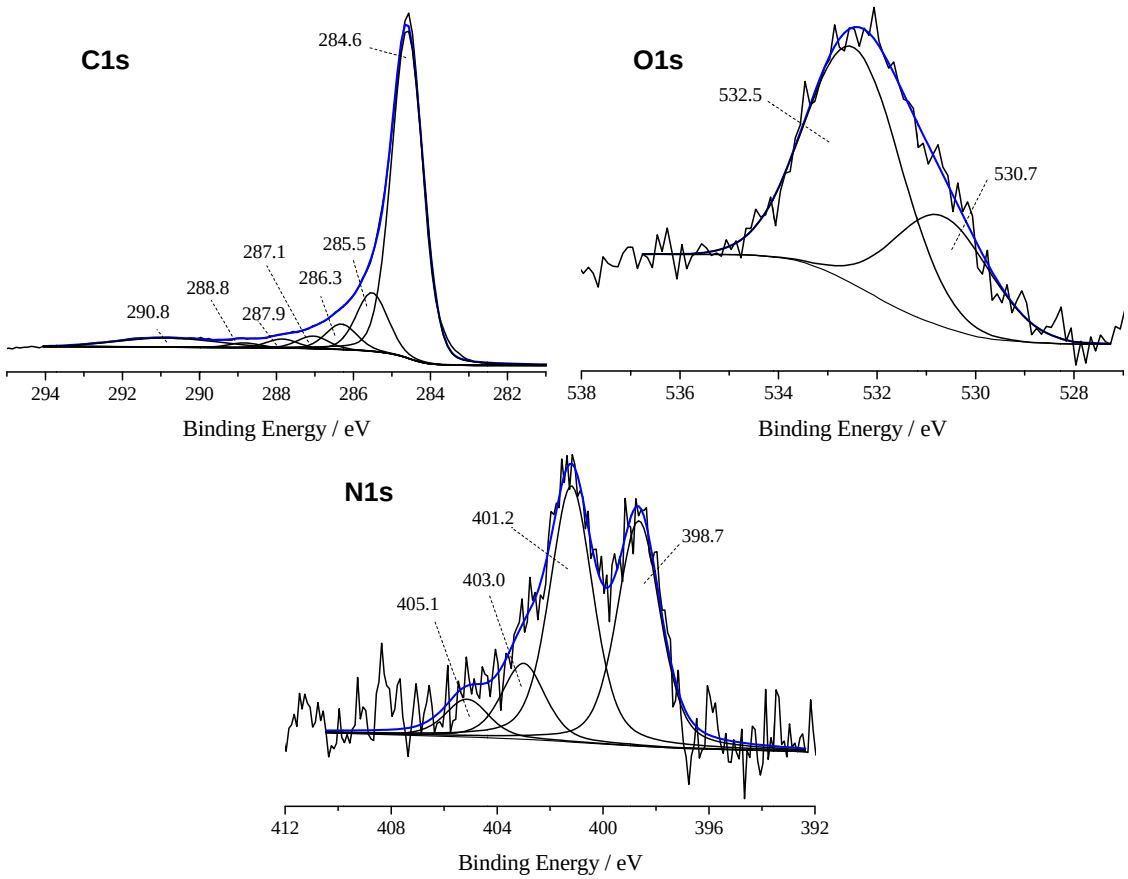

Figure 5.2 High-resolution XPS spectra of N-FLG in the C1s, N1s and O1s regions, with the corresponding deconvolutions.

The C1s spectrum was fitted with seven peaks: a main peak at 284.6 eV assigned to the graphitic structure (sp^2), a peak at 285.5 eV attributed to C-C single bonds of defects on graphene structure (sp^3) and C=N double bond (resulting of the nitrogen-doping), a peak at 286.3 eV related to C-O single bonds in alcohols and ethers, a peak at 287.1 eV due to C-N single bonds, two peaks at 287.9 and 288.8 eV assigned, respectively, to carbon-oxygen double bonds in ketones and quinones (C=O) and in carboxylic acids and esters (-COO) and a peak at 290.8 eV attributed to the characteristic shake-up satellite for the π-π^*transition.[37,38]

The O1s spectrum was fitted with two peaks at 530.7 and 532.5 eV, which can be ascribed to O=C double bond from ketone and quinone moieties and to O-C single bond from ether and phenol groups, respectively. These peaks have also the contribution of the carboxylic acid and esters groups and of the O-N bond (from nitrogen-doping).[37,39]

The N1s spectrum was fitted into four components: at 398.7 eV (pyridinic-N), 401.2 eV (pyrrolic-N), 403.0 eV (quaternary-N) and 405.1 eV (pyridinic-N-oxide).[28,38]

The total atomic content of each element on N-FLG sample was found to be 95.6 at.% of C, 2.1 at.% of N and 2.2 at.% of O. From the 2.1 at.% of N, pyrrolic-N and pyridinic-N constitute the major components, 43.0 and 37.8 at.%, respectively, followed by quaternary-N 12.7 at.% and pyridinic-N-oxide 6.4 at.%.

The effect of doping on the structure of the FLG was further confirmed from Raman spectra. Figure 5.3 shows the Raman spectra of doped and undoped FLG.

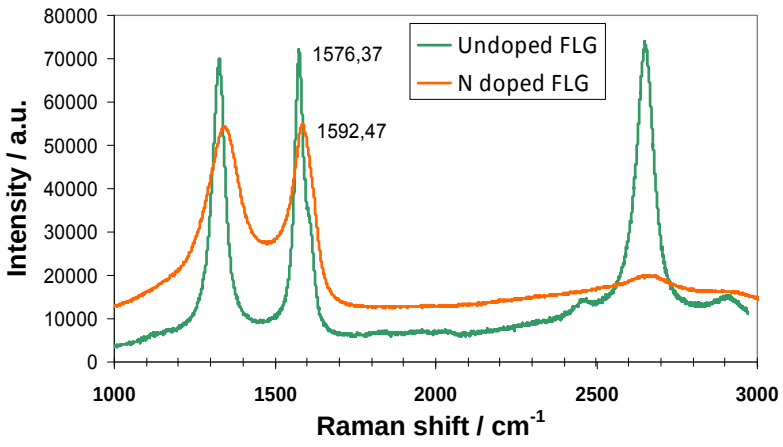

Figure 5.3 Raman spectra of the undoped and N-doped FLG.

For the undoped FLG, the spectrum is highly uniform over the entire flake. The undoped FLG shows a narrow G band confirming the presence of a well crystallised

sp^2 carbon network. The D and D_0 bands are relatively high that could be the result of defects at edges of smaller flakes, the small area of flakes giving rise to a large number of edges.[32] The Raman spectrum of N-FLG is significantly changed showing the combined effect of both nitrogen and oxygen doping on the electronic structure. The blue shift in the G band frequency and the attenuation of the 2D band indicate doping of the graphene lattice.[40] However, spectra of FLG containing oxygen functional groups produced by acid treatment did not show a G band shift. Hence, it appears that the change in the G band frequency is a direct consequence of the substitution of nitrogen in the graphene lattice.

5.3.2 Electrochemical preparation and characterisation of N-FLG@poly[1]

The CVs obtained during the 1st, 10th and 30th electrodeposition cycles of the N-FLG@poly[1] film are depicted in Figure 5.4 (a), along with the same electrodeposition cycles for pristine poly[1], for comparison. The CVs obtained in the complete films electrodepositions are showed in Figure 5.5 and the potential peak values are summarised in Table 5.1.

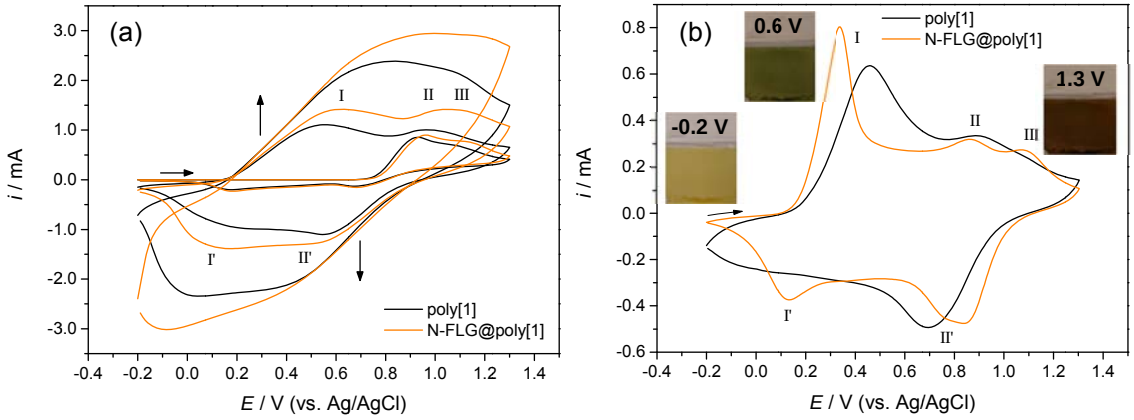

Figure 5.4 CVs obtained during (a) the 1st, 10th and 30th scans of the electrodeposition and (b) the 3rd scan of the redox switching in $LiClO_4$/PC 0.1 mol dm^{-3} of N-FLG@poly[1] (Γ= 296 nmol cm^{-2}) and poly[1] (Γ= 180 nmol cm^{-2}) films; insets in (b) are films photographs in different oxidation states.

The CVs of the nanocomposite electrodeposition have similar electrochemical profiles to those of the pristine poly[1] film, despite a small shift of the anodic peaks for less negative potentials and of the cathodic peaks for more negative potentials. These results indicate that the presence of N-FLG did not change the oxidative electropolymerisation mechanism of poly[1]. Consequently, the two peaks observed in the first anodic half-cycle, at E_{pa} = 0.96 and 1.13 V are attributed to the [Ni(3-Mesalen)]

monomer oxidation and subsequent formation of oligomers/polymer on the working electrode surface, while in reverse scan, the peaks at E_{pc} =0.68 and 0.18 V correspond to the reduction of the as-formed nanocomposite film. The anodic peak around E_{pa} = 0.49 V, which appears in the second and subsequent scans, is attributed to the oxidation of the as-formed polymeric film.[41]

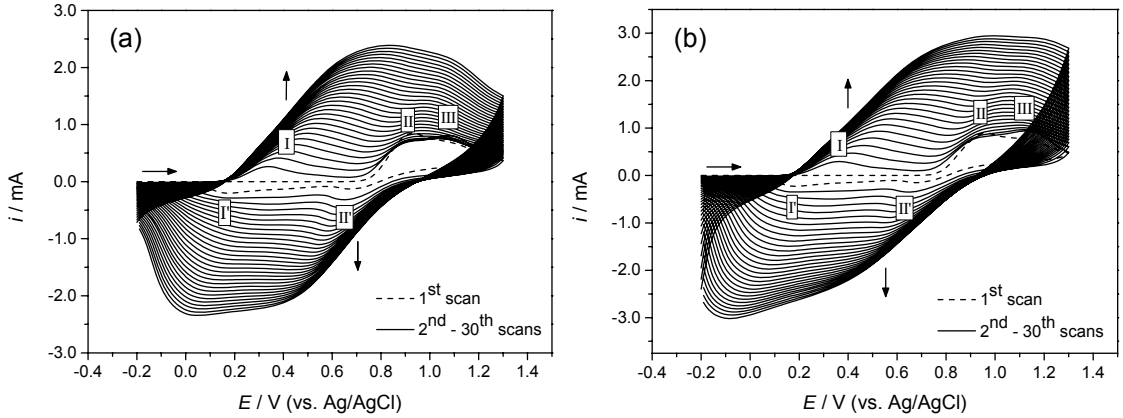

Figure 5.5 CVs of the films electrodeposition, using 1.0 mmol dm^{-3} solution of [Ni(3-Mesalen)] complex in $LiClO_4/CH_3CN$ 0.1 mol dm^{-3}, at 0.100 V s^{-1} during 30 scans: (a) poly[1] and (b) N-FLG@poly[1] (containing 0.5 wt.% of N-FLG).

Moreover, the CVs of nanocomposite show higher current intensities when compared to those of the pristine film, which become more significant with the increasing number of electrodeposition cycles. This is attributed to the larger electroactive surface area of the as-prepared nanocomposite film, resulting from the incorporation of the N-FLG in the polymeric matrix.

Table 5.1 Peak potentials observed in CVs during 1st, 5th, 10th and 20th scans of nanocomposite and pristine poly[1] films electrodepositions.

Film	Scan	*E* / V (vs. Ag/AgCl)				
		E_{paI}	E_{paII}	E_{paIII}	$E_{pcI'}$	$E_{pcII'}$
poly[1]	1st	-	0.93	1.10	0.17	0.68
	5th	0.45	0.95	1.06	0.16	0.61
	10th	0.56	-	0.97	0.16	0.54
	20th	0.72	-	1.00	0.09	0.47
N-FLG@poly[1]	1st	-	0.96	1.13	0.18	0.68
	5th	0.49	0.99	1.10	0.17	0.58
	10th	0.62	-	1.05	0.15	0.53
	20th	0.84	-	1.08	0.02	0.45

The CV obtained during the cycling (3rd scan) of the as-prepared N-FLG@poly[1] film in $LiClO_4$/PC 0.1 mol dm^{-3}, along with the CV of the pristine film, is depicted in Figure 5.4 (b). In Figure 5.6 are depicted the CVs upon films conditioning and Table 5.2 summarises the peak potential values.

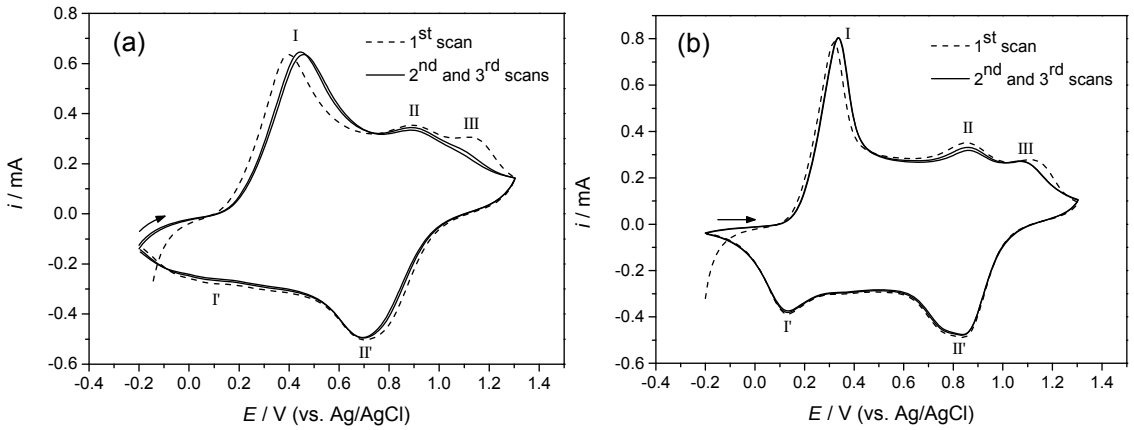

Figure 5.6 CVs of the redox switching in $LiClO_4$/PC 0.1 mol dm^{-3}, at 0.010 V s^{-1} during 3 scans: (a) poly[1] and (b) N-FLG@poly[1].

The nanocomposite and pristine films have similar electrochemical responses although, in the former, the anodic and cathodic peaks are more well-defined and appear at less and more positive potentials, respectively. These observations suggest that N-FLG@poly[1] film is more easily oxidised (and reduced) than the pristine film, which is attributed to the presence of N-FLG, presumably arising from its high electrical conductivity;[26] thus, N-FLG is enhancing the electrical transport throughout the polymeric matrix, facilitating the polymer redox processes, which combined with the N-FLG high surface area, affords higher current intensities.

Table 5.2 Peak potentials observed in CVs during 1st and 3rd scans of nanocomposite and pristine poly[1] film redox switching in $LiClO_4$/PC 0.1 mol dm^{-3}.

Film	Scan	*E* / V (vs. Ag/AgCl)				
		E_{paI}	E_{paII}	E_{paIII}	$E_{pcI'}$	$E_{pcII'}$
poly[1]	1st	0.39	0.89	1.13	0.11*	0.70
	3rd	0.46	0.88	-	-	0.69
N-FLG@poly[1]	1st	0.32	0.85	1.11	0.13	0.84(0.78*)
	3rd	0.33	0.86	1.07	0.13	0.83 (0.77*)

* inflexion

In Figure 5.7 are shown the electroactive surface coverage (Γ) profiles for nanocomposite and pristine films, with increasing number of the electropolymerisation cycles.

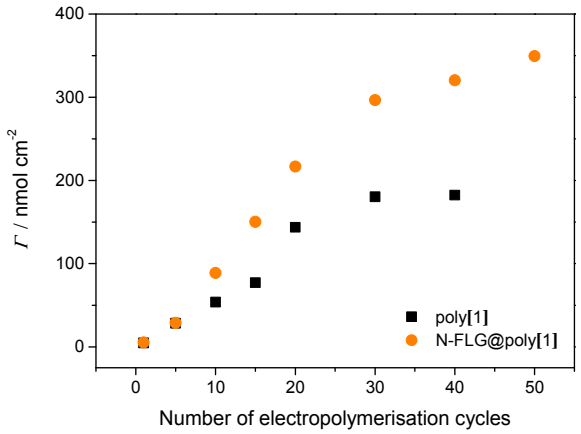

Figure 5.7 Plot of the electroactive surface coverage, Γ, with the number of electropolymerisation cycles for N-FLG@poly[1] and pristine films.

For thin films (prepared with 1 or 5 electropolymerisation cycles), the N-FLG@poly[1] and the pristine poly[1] show similar Γ values, with Γ increasing linearly with the number of deposition cycles. However, as the number of cycles increases further than ≈ 10 electropolymerisation cycles, N-FLG@poly[1] shows higher Γ values than the pristine film. This behaviour is similar to that observed for poly[1] doped with pristine graphene;[30] nevertheless, the Γ increase is even more pronounced with N-FLG. Moreover, these results are in agreement with the higher current intensities observed for the nanocomposite, as mentioned above, and provide an indirect indication of the successful incorporation of the N-FLG on poly[1] matrix. For films prepared in the typical conditions employed in this work (at 0.100 V s^{-1} during 30 scans), Γ = 180 nmol cm^{-2} for pristine poly[1] and Γ = 296 nmol cm^{-2} for N-FLG@poly[1].

The visual inspection of the N-FLG@poly[1] film during its redox switching allowed to observe that the nanocomposite has similar EC behaviour as the pristine poly[1] (Chapter 2). In the inset in Figure 5.4 (b), photographs of the nanocomposite film in different oxidation states are presented, showing yellow (E = -0.2 V), green (E = 0.6 V) and russet (reddish-brown) (E = 1.3 V) colours at the different applied potentials.

5.3.3 Composition and morphology

The surface composition of N-FLG@poly[1] film in the reduced state (*E* = -0.2 V) was obtained by XPS, which revealed the presence of C, Ni, N, O and Cl elements, as expected. The deconvoluted high-resolution XPS spectra for nanocomposite and pristine films, for comparison, are shown in Figures 5.8 and 5.9.

Once the two components of the nanocomposite film (N-FLG and poly[1]) are composed by the same chemical elements, XPS does not provide direct evidences that could be attributed to each component individually. However, the comparison between the two deconvoluted XPS spectra and the atomic ratios of the nanocomposite vs. to those of pristine film provide valuable information.

The C1s spectrum of N-FLG@poly[1] was deconvoluted into four components: a peak at 284.6 eV attributed to aromatic and aliphatic carbons of the *salen* moiety and to the structure of N-FLG, a peak at 285.9 eV associated with the C-O and C-N bonds of the *salen* coordination sphere and with the C-O single bonds in N-FLG, a peak with lower intensity at 286.9 eV assigned to C≡N from CH_3CN entrapped on the film and to C-N bonds of the N-FLG, and a peak at 289.3 eV related to the shake-up satellite of π-π* transitions due to the aromatic carbons of *salen* and N-FLG and that also has the contribution of C=O and –COO bonds of N-FLG.[33,38]

The N1s spectrum of the nanocomposite was deconvoluted into four peaks at 399.4, 400.4, 401.3 and 403.4 eV. The first peaks are attributed to the nitrogen bonds of the ligand system and to pyridinic-N of the N-FLG, the peak at 401.3 eV is assigned to the N≡C bound of occluded CH_3CN and to pyrrolic-N of the N-FLG and the peak at 403.4 eV is associated to a shake-up phenomenon due to *salen* ligand and to quaternary-N and pyridinic-N-oxide of the N-FLG.[28,33,38]

The deconvoluted O1s spectrum of the nanocomposite exhibits two peaks: one at 531.5 eV assigned to oxygen belonging to the coordination sphere of *salen* ligand and O=C bonds from N-FLG, and other at 533.1 eV attributed to the presence of ClO_4^- (from supporting electrolyte) occluded on polymeric films and to O-C bonds from N-FLG.[33]

The Ni2p spectrum of the nanocomposite shows the characteristic peaks due to Ni coordinated to *salen* ligand in a formal +2 oxidation, which are assigned to: $Ni2p_{3/2}$ (855.3 eV), $Ni2p_{3/2}$ satellite (860.6 eV), $Ni2p_{1/2}$ (872.5 eV) and $Ni2p_{1/2}$ satellite (877.8 eV). The presence of peaks in the high resolution Cl2p region at 208.4 eV ($Cl2p_{3/2}$) and 210.0 eV ($Cl2p_{1/2}$) are consistent with the presence of ClO_4^- from supporting electrolyte on nanocomposite film.[33]

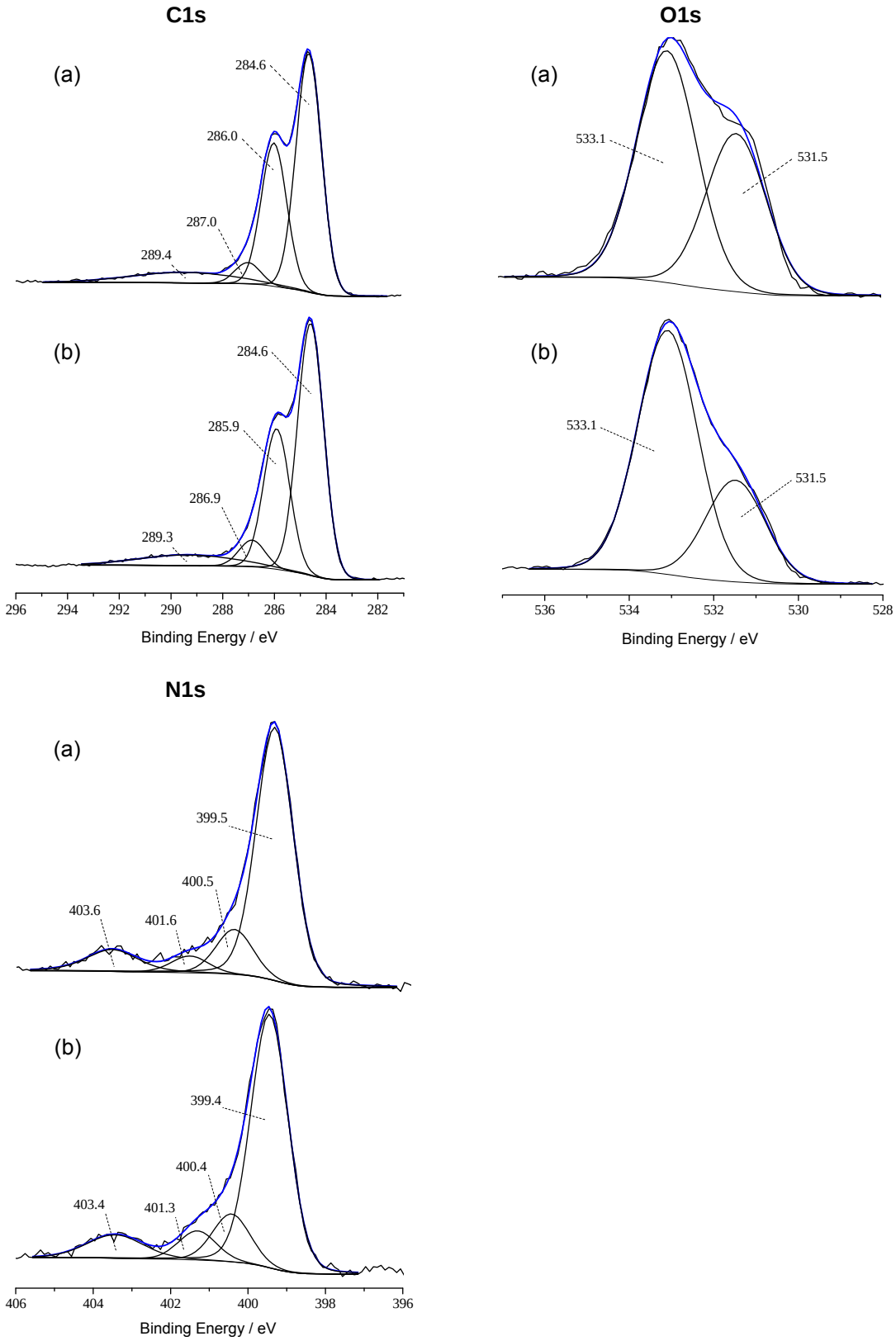

Figure 5.8 High-resolution XPS spectra in C1s, O1s and N1s regions, with the corresponding deconvolutions: (a) pristine poly[1] and (b) N-FLG@poly[1] films.

The deconvoluted XPS spectra of the pristine poly[1] show the typical peaks of the Ni-*salen* polymer, as described in Chapters 3 and 4 for poly[1] and elsewhere for similar films.[33] The C1s spectrum was deconvoluted into four components: a peak at 284.6 eV attributed to aromatic and aliphatic carbons of *salen* ligand, a peak at 286.0 eV associated with C-O and C-N bonds of the *salen* moiety, a peak at 287.0 eV assigned to C≡N from CH_3CN and a peak at 289.4 eV related to the shake-up satellite of the π-π*transitions.[33] The N1s spectrum was deconvoluted into four peaks at 399.5, 400.5, 401.6 and 403.6 eV attributed to the nitrogen bonds of the ligand system, to the N≡C bound of occluded CH_3CN and to a shake-up phenomenon, respectively.[33] The deconvoluted O1s spectrum shows two peaks: one at 531.5 eV assigned to oxygen belonging to the coordination sphere of *salen* ligand, and other at 533.1 eV attributed to the presence of occluded ClO_4^-.[33] The peaks observed in the Ni2p spectrum are assigned to the $Ni2p_{3/2}$ (855.3 eV), $Ni2p_{3/2}$ satellite (860.6 eV), $Ni2p_{1/2}$ (872.5 eV) and $Ni2p_{1/2}$ satellite (877.8 eV), while the observed in Cl2p spectrum are attributed to $Cl2p_{3/2}$ (208.3 eV) and $Cl2p_{1/2}$ (209.9 eV) from ClO_4^-.[33]

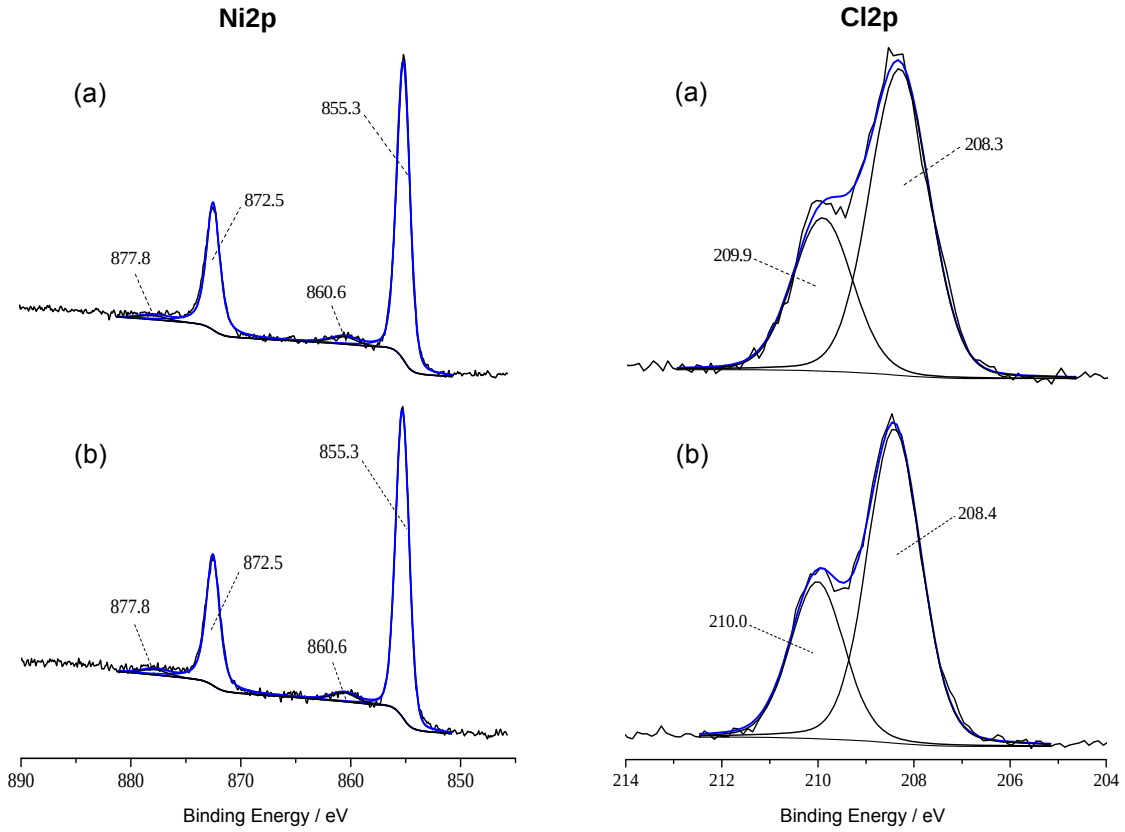

Figure 5.9 High-resolution XPS spectra in Ni2p and Cl2p regions, with the corresponding deconvolutions: (a) pristine poly[1] and (b) N-FLG@poly[1] films.

Surface atomic percentages obtained for the nanocomposite and pristine films are summarised in Table 5.3, as well as the calculated atomic ratios.

Table 5.3 Surface atomic percentages obtained by XPS and calculated atomic ratios of relevant elements for poly[1] and N-FLG@poly[1] nanocomposite films, in reduced states (*E* = -0.2 V).

Films	Atomic %					Atomic Ratios		
	Ni	C	N	O	Cl	N/Ni	O/Ni	Cl/Ni
poly[1]	3.1	70.8	6.7	16.9	2.5	2.2	5.4	0.8
N-FLG@poly[1]	2.6	67.3	6.4	20.5	3.3	2.5	7.9	1.3

The atomic ratio N/Ni calculated for N-FLG@poly[1] is higher than of the expected value considering the [Ni(3-Mesalen)] chemical structure ($N/Ni_{theoretical}$ = 2.0), which is explained by the trapping of CH_3CN on nanocomposite matrix (associated with the peak at 401.3 eV in N 1s nanocomposite spectrum) and by the presence of N-FLG; in fact, for the nanocomposite, the N/Ni atomic ratio is 12 % larger than that observed for poly[1].

The O/Ni and Cl/Ni atomic ratios are also above the expected values ($O/Ni_{theoretical}$ = 2.0), but their increase in a proportion ca. 1:4 (Cl:O) confirms that this is due to the trapping of ClO_4^- on the polymeric film, as typically observed for other analogous systems.[33] In the nanocomposite, the O/Ni and Cl/Ni atomic ratios are ca. 32 / 38 % larger than in pristine film, which clearly indicates a higher amount of occluded ClO_4^-.

Figure 5.10 shows a SEM micrograph of the N-FLG@poly[1] film with the corresponding EDS spectrum at a selected region, identified as Z1.

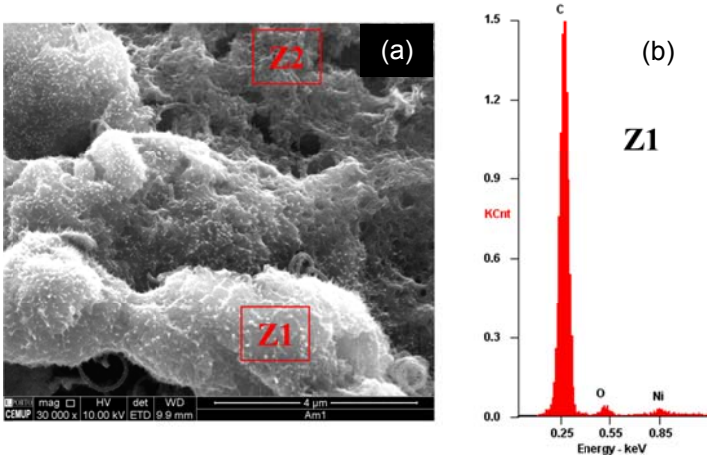

Figure 5.10 (a) Scanning electron micrograph and (**b**) EDS spectrum at a specified zone of N-FLG@ poly[1] film.

It is possible identify a continuous layer with an irregular surface (Z2 region) characteristic of the metal *salen*-type pristine films (Chapter 2), which is blended with N-FLG fragments in certain regions (Z1). The micrograph shows that the poly[1] matrix extents over the N-FLG fragments and, thus, N-FLG is in fact occluded on poly[1] and not just resting on the surface of the film. The nature of the fragment was confirmed by EDS analysis in Z1 region (Figure 5.10 (b)). The elements predominantly detected were carbon and oxygen, which are characteristics of graphene flakes. It was also detected nickel in a low amount and the absence of other elements typically observed in poly[1], such as chloride, confirms that the fragment is predominantly a carbon-based material. These results also demonstrate the successful preparation of the N-FLG@poly[1] nanocomposite.

5.3.4 *In situ* UV-Vis spectroscopy

In Figures 5.11 (a) are depicted the absolute UV-Vis spectra acquired during the oxidation of the N-FLG@poly[1] nanocomposite film; for comparison, the equivalent spectra for pristine poly[1] are depicted in Figure 5.12 (a). The spectra obtained during films reduction showed an inverse behaviour and were omitted for simplicity.

The N-FLG@poly[1] spectra are very similar to the spectra of the pristine film and both show four electronic bands. The electronic bands profile with the applied potential is most readily appreciated in the differential spectra, depicted using the responses at selected potentials as reference potentials (Figures 5.11 (b) and (c) for nanocomposite and Figures 5.12 (b) and (c) for poly[1]) and by the representation of the absorbance *vs.* potential (*Abs vs. E*) profiles, at the wavelength of detected bands (Figures 5.11 (d) and 5.12 (d)). These representations reveal that the nanocomposite and pristine films have similar electronic band behaviours, allowing to identify three main band profiles, characteristics of several metal *salen*-type films[33,34,42] and of the pristine poly[1] film (Chapter 2).

The energy of the electronic bands for both films are summarised in Table 5.4; the molar extinction coefficients, ε, were estimated using the Equation 2.1, from the slopes of *Abs* vs. Q plots (Figure 5.13).

Taking into account the assertion of ligand-based film oxidation, supported by the ε-values and proposed for the pristine (Chapter 2) and other similar poly[M(*salen*)] films,[33,34,42] the polaronic model previously employed in the assignment of the electronic bands of metal *salen*-type films,[33,34,42] can be used for band assignment: (i) the band at λ = 332-335 nm is attributed to the intervalence transition and corresponds to the band gap (E_g = 3.74 and 3.70 eV for pristine and nanocomposite

films, respectively), (ii) the bands at λ = 401-404 nm (3.09-3.07 eV) and λ = 818-826 nm (1.52-1.50 eV), that appear during the film oxidation, are attributed to transitions within the band gap, from the valence band to the antibonding and bonding polaron levels, respectively, and (iii) the band at λ = 507-509 nm (2.45-2.44 eV) is assigned to charge transfer (CT) transition between the metal and the oxidised ligand.

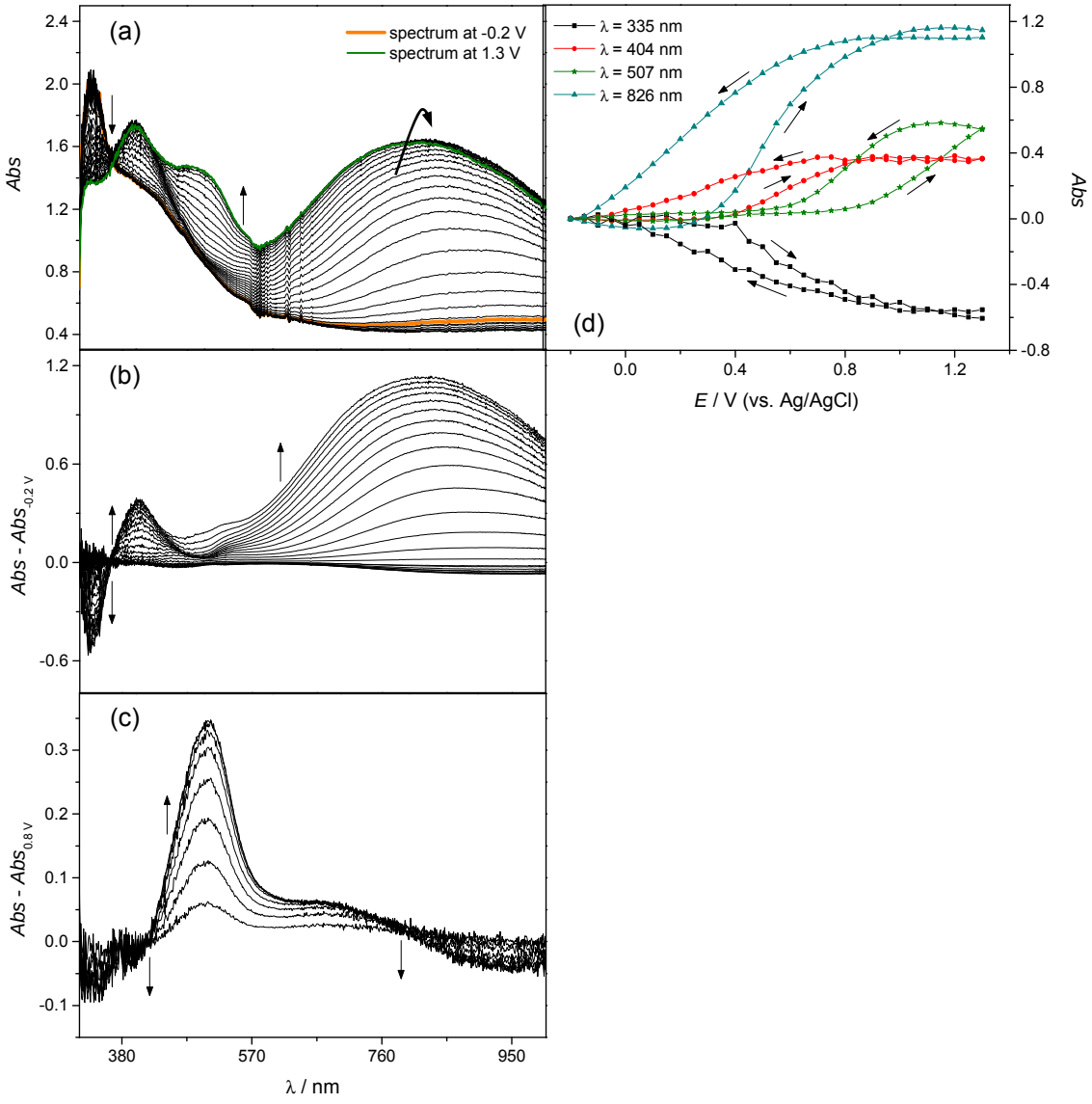

Figure 5.11 UV-Vis spectra of N-FLG@poly[1] acquired during film oxidation in 0.1 mol dm^{-3} $LiClO_4$/PC: (a) absolute spectra, referenced to the electrolyte spectrum, and differential spectra (b) from -0.2 to 0.8 V, referenced to the spectrum of neutral film and (c) from 0.8 to 1.3 V, referenced to the spectrum of film at *E* = 0.8 V; (d) *Abs* vs. *E* plots of the electronic bands identified in absolute UV-Vis spectra, referenced to spectrum at *E* = -0.2 V (arrows indicate scan direction).

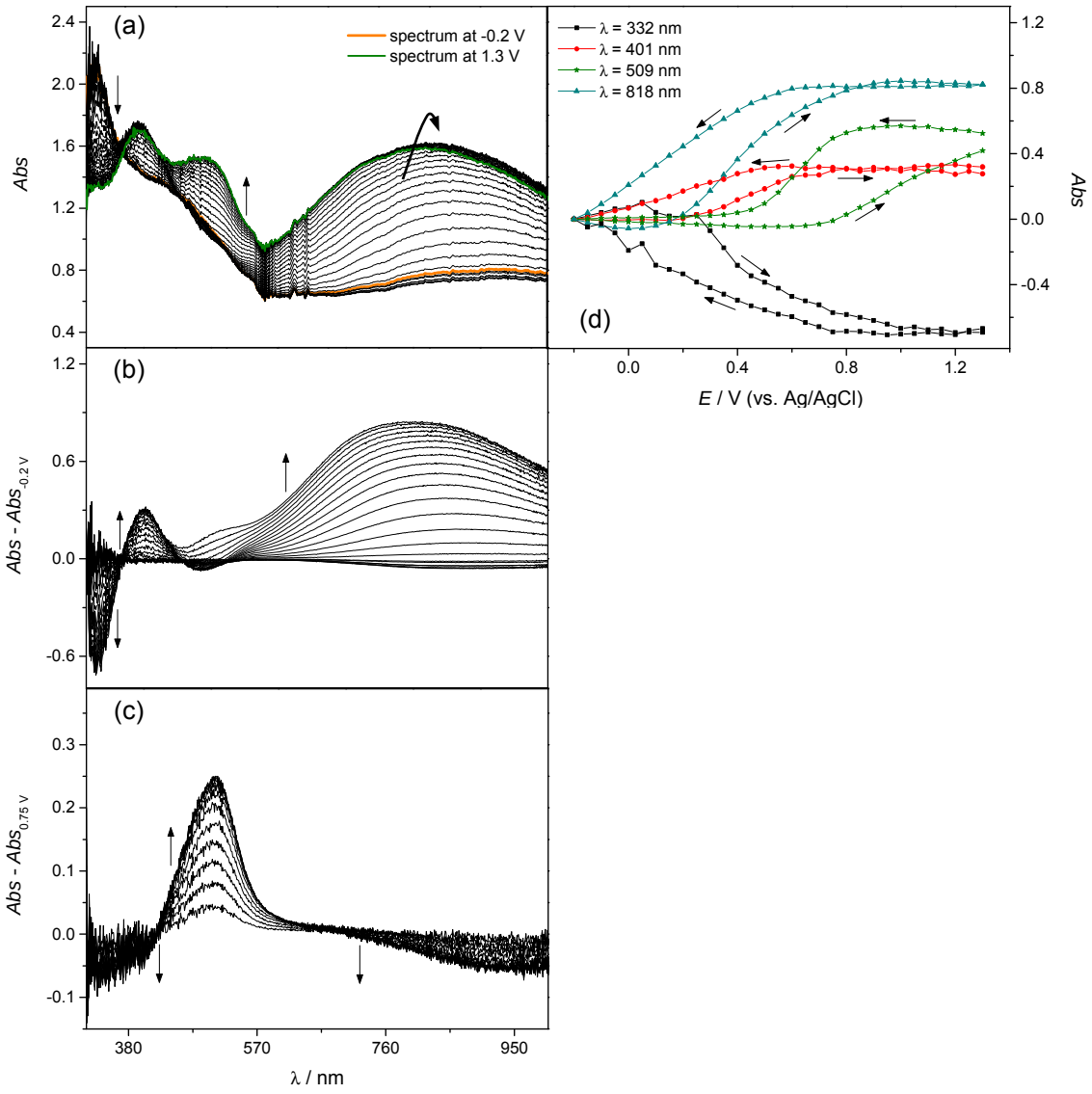

Figure 5.12 UV-Vis spectra of poly[1] acquired during film oxidation in 0.1 mol dm^{-3} $LiClO_4$/PC: (a) absolute spectra, referenced to the electrolyte spectrum, and differential spectra (b) from -0.2 to 0.75 V, referenced to the spectrum of neutral polymer and (c) from 0.75 to 1.3 V, referenced to the spectrum of polymer at *E*=0.75 V; (d) *Abs* vs. *E* plots of the electronic bands identified in absolute UV-Vis spectra, referenced to spectrum at -0.2 V (arrows indicate scan direction).

The data summarised in Table 5.4 reveal that the energies of the observed bands in nanocomposite are very similar to those of the pristine film, showing that the incorporation of the N-FLG in poly[1] matrix did not change the metallopolymer electronic structure. However, the ε-values for the nanocomposite electronic bands are different from those of the pristine film. The nanocomposite electronic bands assigned to transitions within the band gap, at λ = 401-404 nm and λ = 818-826 nm showed, respectively, 19 % and 26 % increase (from $\varepsilon = 2.16 \times 10^3$ / 5.26×10^3 cm^{-1} mol^{-1} dm^3 for pristine to $\varepsilon = 2.66 \times 10^3$ / 7.11×10^3 cm^{-1} mol^{-1} dm^3 for nanocomposite films), whereas, for the CT band at λ = 507-509 nm, the ε–value diminished 12 % (from

$\varepsilon = 8.80$ x 10^3 cm^{-1} mol^{-1} dm^3 in pristine film to $\varepsilon = 7.11$ x 10^3 cm^{-1} mol^{-1} dm^3 in nanocomposite).

Table 5.4 Electronic bands energy and molar extinction coefficients (ε) for pristine poly[1] and N-FLG@poly[1] films.

Film	λ / nm (eV)	$\varepsilon \times 10^{-3}$ / cm^{-1} mol^{-1} dm^3
poly[1]	332 (3.74)	3.86
	401(3.09)	2.16
	509 (2.44)	8.80
	818 (1.52)	5.26
N-FLG@poly[1]	335 (3.70)	3.17
	404 (3.07)	2.66
	507 (2.45)	7.78
	826 (1.50)	7.11

Since the electronic bands associated to transitions within the band gap are associated with charge carriers within the film, the increase in the molar extinction coefficients is in line with the previous conclusions that the incorporation of N-FLG in the poly-*salen* matrix is providing alternative conductive pathways and improved the overall charge transport.[1] On the other hand, the decrease of the CT band ε-value is also a very good outcome since this CT band is related with the ligand over-oxidation and less stable oxidised states of poly-*salen* film, anticipating an increase of the film stability towards over-oxidation.

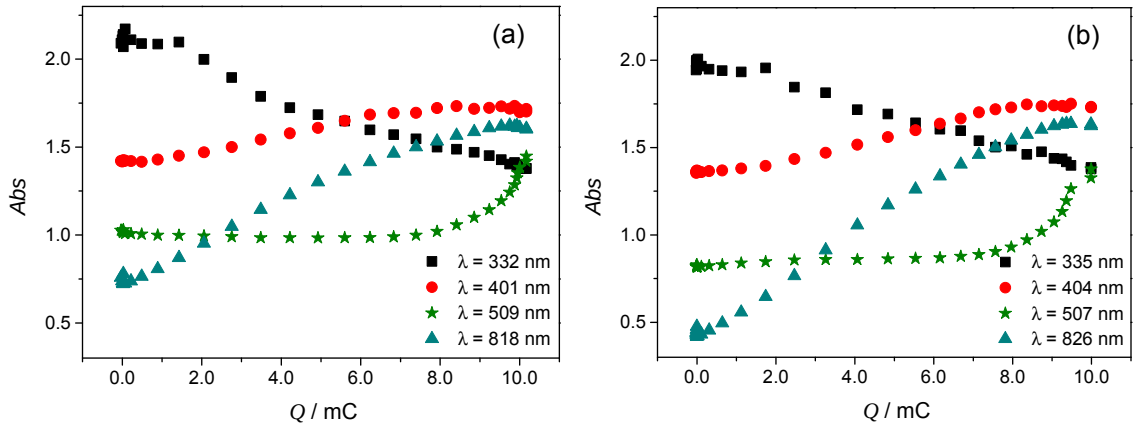

Figure 5.13 Plots of the *Abs* vs. *Q* for selected electronic bands in 0.1 mol dm^{-3} $LiClO_4$/PC (for anodic scan) of: (a) poly[1] and (b) N-FLG@poly[1].

5.3.5 Electrochromic properties

The EC parameters of N-FLG@poly[1] nanocomposite were determined in order to evaluate the effect of the N-FLG incorporation in the EC response of the material. This characterisation was performed for the colour change yellow ↔ green and using $LiClO_4$/PC as supporting electrolyte, since these conditions were observed to be the most favourable for an optimised EC performance of the pristine film (Chapter 2).

The electrochemical stability of the N-FLG@poly[1] film was evaluated by chronoamperometry, monitoring the current intensity decay along consecutive 10 000 redox cycles, the equivalent of ≈ 12 days, after which the colour change was still visually perceptible.

The chronoamperograms, Figure 5.14 (a), show that, at the end of the experiment, the nanocomposite film only lost 2.7 % of charge, while the pristine poly[1] film lost 9.3 % of charge, clearly showing the highest electrochemical stability (in 71.0 %) of the nanocomposite film. These observations are supported by very similar CVs profiles (peak potentials and current intensities) obtained for N-FLG@poly[1] film before and after the chronoamperometric study, Figure 5.15.

In Figure 5.14 (b) the chronoamperograms obtained during the first cycles for N-FLG@poly[1] and poly[1] are overlapped, with indication of their respective switching times, τ. The nanocomposite film shows much faster switching times, τ = 11 and 9 s, which correspond to an improvement of 77 / 71 % relatively to the pristine poly[1] film that needed τ = 49 s to change colour from yellow to green and τ = 31 s to reverse the change. The best switching times of the nanocomposite are attributed to the N-FLG incorporation into the poly-*salen* matrix, which not only provides alternative conductive pathways, but also reduces the packaging of the polymer, creating a more porous structure that facilitates the mobility of the charge compensation ions, crucial for the polymer redox process.[24] The asymmetry in the switching times observed for both polymer films with respect to the switching direction is justified by differences in conductivity of the EC polymer, electric field strength, film solvation and mobile ion diffusion rates within the film, depending on the switching direction.[43]

The optical contrast ΔT %, optical density changes ΔOD and colouration efficiencies η of the N-FLG@poly[1] nanocomposite (and of the pristine film for comparison) were evaluated by chronoabsorptometry (λ = 820 nm). The chronoamperograms/absorptograms are shown in Figure 5.14 (c) and the calculated data are summarised in Table 5.5.

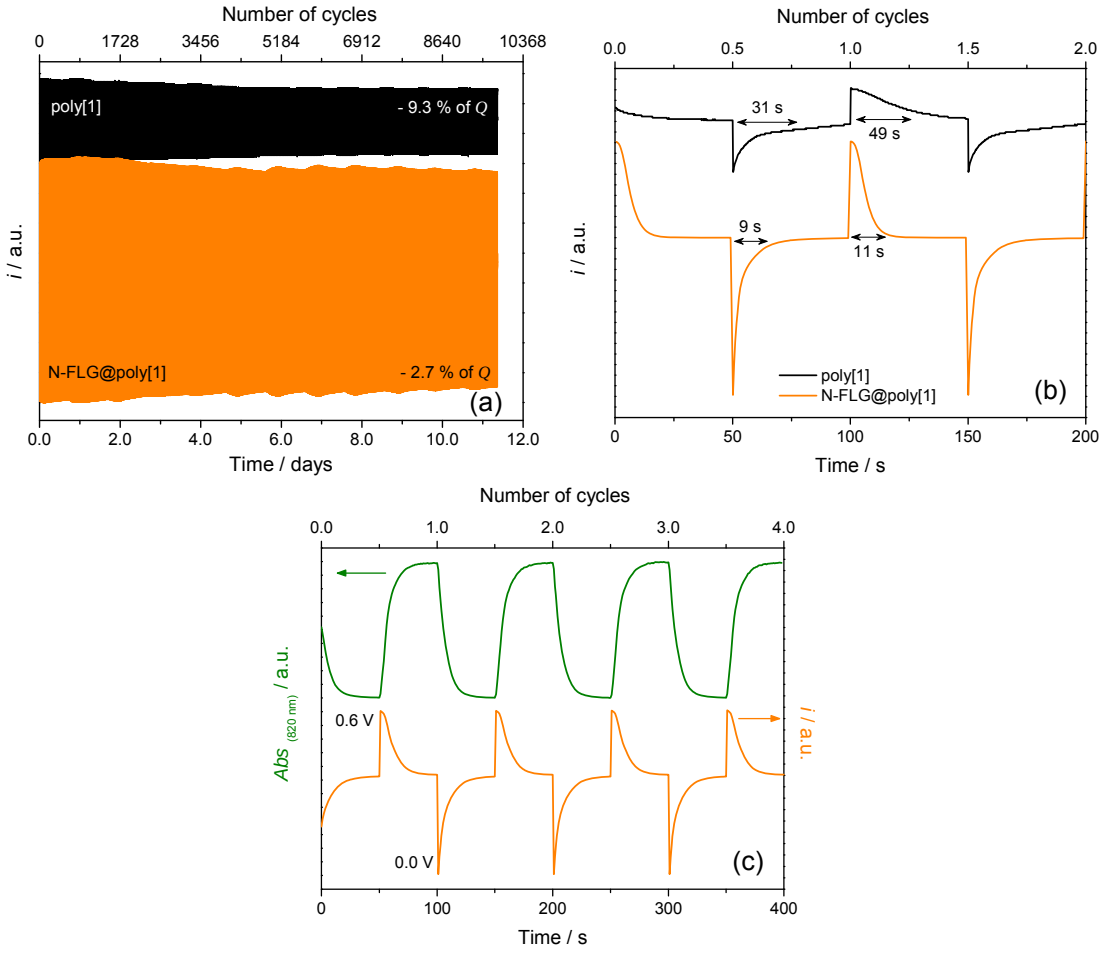

Figure 5.14 (a) Chronoamperograms of N-FLG@poly[1] and poly[1] films in $LiClO_4$/PC 0.1 mol dm^{-3}, applying two potential pulses of 50 s by redox cycle, with potential alternating between E = 0.0 V (yellow) and E = 0.6 V (green); (b) expansion of the chronoamperograms, showing the measured switching times; (c) chronoamperograms/absorptograms obtained for N-FLG@poly[1] film during 4 redox cycles, at the fixed wavelength of λ = 820 nm.

The ΔT value increased from ΔT = 22.1 % in pristine poly[1] to 35.9 % in nanocomposite film (38 % improvement) and the ΔOD values, from ΔOD = 0.86 in pristine film to ΔOD = 0.99 for nanocomposite film (13 % improvement).

Similarly, N-FLG@poly[1] film exhibited higher colouration efficiency than for pristine film, η = 108.95 cm^2 C^{-1} vs. η = 95.44 cm^2 C^{-1}. For the nanocomposite film, the slight increase in charge requirement, in comparison to the pristine film (Q_d = 9.11 vs. 9.06 mC cm^{-2}) is compensated by the higher ΔOD value, resulting effectively in an enhancement of η value of 12 %.

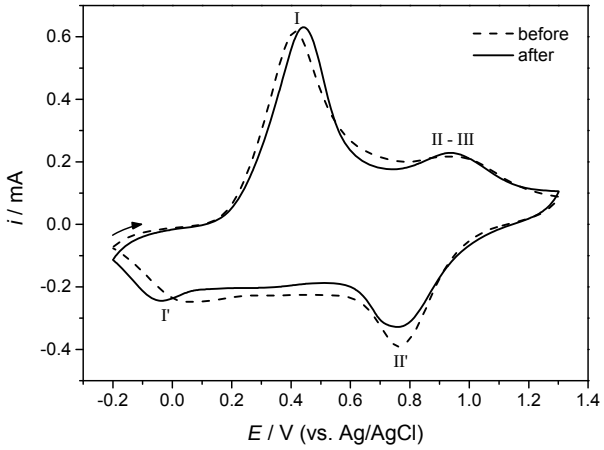

Figure 5.15 CVs of the N-FLG@poly[1] redox switching before and after the chronoamperometric study in $LiClO_4$/PC 0.1 mol dm^{-3} (E = 0.0 and 0.6 V with pulses of 50 s).

The improvement in all the EC parameters is explained by the increase in electrical conductivity promoted by the N-FLG incorporation and by the creation of alternative conducting pathways that allow a uniform current distribution and improve the overall charge transport behaviour, in compliance with a larger electroactive surface coverage of the nanocomposite, as result of the incorporation of the N-FLG.[1]

Table 5.5 EC parameters: optical contrasts (ΔT %), changes of the optical density (ΔOD), charge requirements (Q_d) and colouration efficiencies (η) for pristine poly[1] and N-FLG@poly[1] nanocomposite in $LiClO_4$/PC supporting electrolyte, at λ = 820 nm.

Film	ΔT%	ΔOD	Q_d / mC cm^{-2}	η / cm^2 C^{-1}
poly[1]	22.1	0.86	9.06	95.44
N-FLG@poly[1]	35.9	0.99	9.11	108.95

5.4 Conclusions

The new N-FLG@poly[1] nanocomposite was successful prepared by *in situ* electropolymerisation, using CV. The electrochemical characterisation of the nanocomposite film revealed similar electrochemical profiles to that of pristine poly[1] film, but better defined peaks and higher current intensities were observed, which are associated with higher electroactive surface coverages. UV-Vis spectroscopy revealed that the incorporation of N-FLG did not change the electronic structure of poly[1] film, as for all the other nanomaterials used in Chapters 3 and 4, but influences the molar extinction coefficients of the bands assigned to transitions within the band gap (at λ = 404 and 826 nm, increase of 19 and 26 %), i.e. that are associated with the charge

carriers, as consequence of the alternative conducting pathways provide by the nanomaterial. In the nanocomposite the molar extinction coefficients of the CT band decrease in 12 %, which also is a very good outcome once this band is associated with over-oxidation processes.

The as-prepared N-FLG@poly[1] nanocomposite showed excellent enhancement of all EC properties, intrinsic of the pristine electroactive film. The incorporation of the N-FLG increased the electrochemical stability by 71.0 %, recording only 2.7 % of charge loss after ≈ 10 000 cycles (≈ 12 days). Simultaneously, the switching times diminished significantly from τ = 31 / 49 s for the pristine film to τ = 9 / 11 s in the nanocomposite, which correspond to a decrease of 77 / 71 %. The optical contrast and colouration efficiency also have an amazing improvement, rising from ΔT = 22.1 to 35.9 % (+ 38 %) and from η = 95.44 to 108.95 $cm^2\ C^{-1}$ (+ 12 %), respectively, from the pristine poly[1] to the nanocomposite film.

Furthermore, the preparation of the nanocomposite using N-doped graphene allowed to surpass the EC performance of the graphene@poly[1] nanocomposite film,[30] as it was the purpose of this report. This is explained by the extraordinary properties provided by the N-doping of graphene, namely the better conductivity given by the n-type semiconductor ability of the N-doped graphene.

The obtained results showed undoubtedly the advantage of the N-FLG@poly[1] nanocomposite preparation and of the N-doping of graphene, as promising approaches to enhance the EC properties of the pristine Ni-*salen* film.

References

[1] Reddy, B. N.; Deepa, M.; Joshi, A. G.; Srivastava, A. K. *J. Phys. Chem. C* **2011**, *115*, 18354.

[2] Wei, H. G.; Zhu, J. H.; Wu, S. J.; Wei, S. Y.; Guo, Z. H. *Polymer* **2013**, *54*, 1820.

[3] Xiong, S. X.; Wei, J.; Jia, P. T.; Yang, L. P.; Ma, J.; Lu, X. H. *ACS Appl. Mater. Interfaces* **2011**, *3*, 782.

[4] Wei, H. G.; Yan, X. R.; Wu, S. J.; Luo, Z. P.; Wei, S. Y.; Guo, Z. H. *J. Phys. Chem. C* **2012**, *116*, 25052.

[5] Kuilla, T.; Bhadra, S.; Yao, D. H.; Kim, N. H.; Bose, S.; Lee, J. H. *Prog. Polym. Sci.* **2010**, *35*, 1350.

[6] Qi, X. Y.; Tan, C. L.; Wei, J.; Zhang, H. *Nanoscale* **2013**, *5*, 1440.

[7] Potts, J. R.; Dreyer, D. R.; Bielawski, C. W.; Ruoff, R. S. *Polymer* **2011**, *52*, 5.

[8] Wang, L.; Lu, X. P.; Lei, S. B.; Song, Y. H. *J. Mater. Chem. A* **2014**, *2*, 4491.

[9] Lee, T.; Min, S. H.; Gu, M.; Jung, Y. K.; Lee, W.; Lee, J. U.; Seong, D. G.; Kim, B. S. *Chem. Mat.* **2015**, *27*, 3785.

[10] Wei, D.; Kivioja, J. *Nanoscale* **2013**, *5*, 10108.

[11] Liu, Y.; Wang, H. H.; Zhou, J.; Bian, L. Y.; Zhu, E. W.; Hai, J. F.; Tang, J.; Tang, W. H. *Electrochim. Acta* **2013**, *112*, 44.

[12] Zhou, S. P.; Zhang, H. M.; Zhao, Q.; Wang, X. H.; Li, J.; Wang, F. S. *Carbon* **2013**, *52*, 440.

[13] Chu, C. Y.; Tsai, J. T.; Sun, C. L. *Int. J. Hydrog. Energy* **2012**, *37*, 13880.

[14] Zhao, C.; Gai, P. P.; Liu, C. H.; Wang, X.; Xu, H.; Zhang, J. R.; Zhu, J. J. *J. Mater. Chem. A* **2013**, *1*, 12587.

[15] Hou, J. X.; Liu, Z. L.; Zhang, P. Y. *J. Power Sources* **2013**, *224*, 139.

[16] Wang, G. Q.; Xing, W.; Zhuo, S. P. *Electrochim. Acta* **2012**, *66*, 151.

[17] Bo, Y.; Yang, H. Y.; Hu, Y.; Yao, T. M.; Huang, S. S. *Electrochim. Acta* **2011**, *56*, 2676.

[18] Dong, Y. P.; Zhang, J.; Ding, Y.; Chu, X. F.; Chen, J. *Electrochim. Acta* **2013**, *91*, 240.

[19] Song, Z. P.; Xu, T.; Gordin, M. L.; Jiang, Y. B.; Bae, I. T.; Xiao, Q. F.; Zhan, H.; Liu, J.; Wang, D. H. *Nano Lett.* **2012**, *12*, 2205.

[20] Chang, C. H.; Huang, T. C.; Peng, C. W.; Yeh, T. C.; Lu, H. I.; Hung, W. I.; Weng, C. J.; Yang, T. I.; Yeh, J. M. *Carbon* **2012**, *50*, 5044.

[21] Saxena, A. P.; Deepa, M.; Joshi, A. G.; Bhandari, S.; Srivastava, A. K. *ACS Appl. Mater. Interfaces* **2011**, *3*, 1115.

[22] Sheng, K. X.; Bai, H.; Sun, Y. Q.; Li, C.; Shi, G. Q. *Polymer* **2011**, *52*, 5567.

[23] Lu, J. L.; Liu, W. S.; Ling, H.; Kong, J. H.; Ding, G. Q.; Zhou, D.; Lu, X. H. *RSC Adv.* **2012**, *2*, 10537.

[24] Xiong, S. X.; Li, Z. F.; Gong, M.; Wang, X. Q.; Fu, J. L.; Shi, Y. J.; Wu, B. H.; Chu, J. *Electrochim. Acta* **2014**, *138*, 101.

[25] Ma, L. N.; Zhao, P.; Wu, W. J.; Niu, H. J.; Cai, J. W.; Lian, Y. F.; Bai, X. D.; Wang, W. *Polym. Chem.* **2013**, *4*, 4746.

[26] Wood, K. N.; O'Hayre, R.; Pylypenko, S. *Energy Environ. Sci.* **2014**, *7*, 1212.

[27] Wang, H. B.; Xie, M. S.; Thia, L.; Fisher, A.; Wang, X. *J. Phys. Chem. Lett.* **2014**, *5*, 119.

[28] Wang, H. B.; Maiyalagan, T.; Wang, X. *ACS Catal.* **2012**, *2*, 781.

[29] Yang, C. H.; Chen, S. M.; Wang, T. L.; Shieh, Y. T. *Electrochim. Acta* **2014**, *123*, 268.

[30] Araújo, M. *unpublished work*.

[31] Freire, C.; de Castro, B. *J. Chem. Soc.-Dalton Trans.* **1998**, 1491.

[32] Bacsa, R. R.; Camean, I.; Ramos, A.; Garcia, A. B.; Tishkova, V.; Bacsa, W. S.; Gallagher, J. R.; Miller, J. T.; Navas, H.; Jourdain, V.; Girleanu, M.; Ersen, O.; Serp, P. *Carbon* **2015**, *89*, 350.

[33] Fonseca, J.; Tedim, J.; Biernacki, K.; Magalhaes, A. L.; Gurman, S. J.; Freire, C.; Hillman, A. R. *Electrochim. Acta* **2010**, *55*, 7726.

[34] Tedim, J.; Patricio, S.; Fonseca, J.; Magalhaes, A. L.; Moura, C.; Hillman, A. R.; Freire, C. *Synth. Met.* **2011**, *161*, 680.

[35] Beaujuge, P. M.; Reynolds, J. R. *Chem. Rev.* **2010**, *110*, 268.

[36] Ju, M. J.; Jeon, I. Y.; Kim, J. C.; Lim, K.; Choi, H. J.; Jung, S. M.; Choi, I. T.; Eom, Y. K.; Kwon, Y. J.; Ko, J.; Lee, J. J.; Kim, H. K.; Baek, J. B. *Adv. Mater.* **2014**, *26*, 3055.

[37] Fernandes, D. M.; Freire, C. *ChemElectroChem* **2015**, *2*, 269.

[38] Ratso, S.; Kruusenberg, I.; Vikkisk, M.; Joost, U.; Shulga, E.; Kink, I.; Kallio, T.; Tammeveski, K. *Carbon* **2014**, *73*, 361.

[39] Lipinska, M. E.; Rebelo, S. L. H.; Pereira, M. F. R.; Gomes, J.; Freire, C.; Figueiredo, J. L. *Carbon* **2012**, *50*, 3280.

[40] Beams, R.; Cancado, L. G.; Novotny, L. *J. Phys.-Condes. Matter* **2015**, *27*, 26.

[41] Tedim, J.; Goncalves, F.; Pereira, M. F. R.; Figueiredo, J. L.; Moura, C.; Freire, C.; Hillman, A. R. *Electrochim. Acta* **2008**, *53*, 6722.

[42] Vilas-Boas, M.; Freire, C.; de Castro, B.; Christensen, P. A.; Hillman, A. R. *Chem.-Eur. J.* **2001**, *7*, 139.

[43] Amb, C. M.; Dyer, A. L.; Reynolds, J. R. *Chem. Mat.* **2011**, *23*, 397.

In the land of energy-conversion…

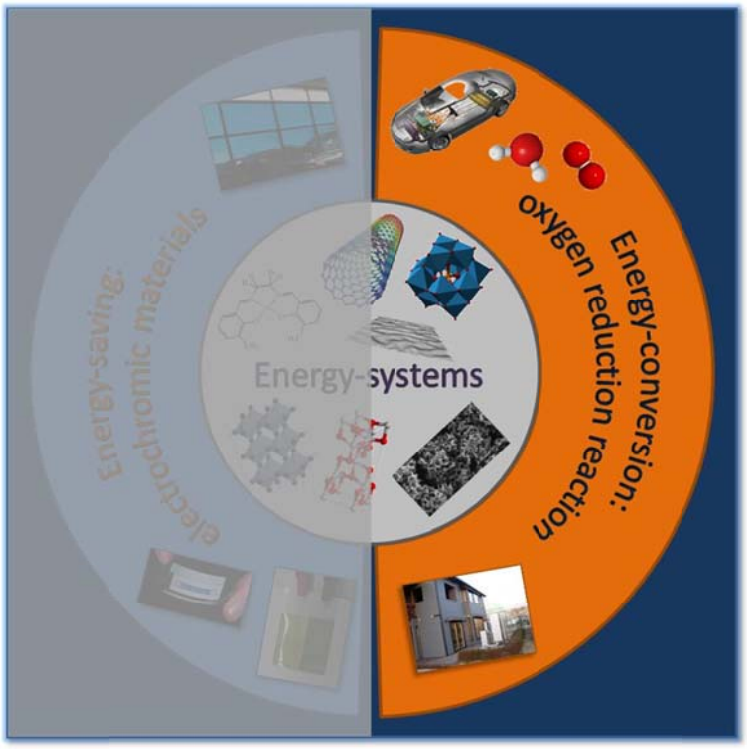

Chapter 6

Sucrose-derived activated carbons: electron transfer properties and application as oxygen reduction electrocatalysts

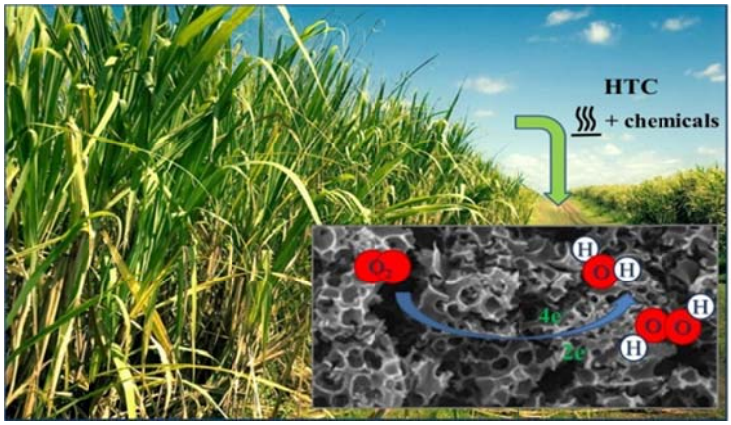

6

Sucrose-derived activated carbons: electron transfer properties and application as oxygen reduction electrocatalysts[1,2,3]

Abstract

Two sustainable sucrose-based activated carbons (ACs), denominated SC800 and SH800, are applied as ORR electrocatalysts. In alkaline medium the ACs showed similar onset potentials at E_{onset} ≈ -0.20 V vs. Ag/AgCl, which are 0.06 V more negative than that observed for 20 wt% Pt/C used as reference. Higher diffusion-limiting current densities ($j_{L(-1.0\ V,\ 1600\ rpm)}$ = -3.44 mA cm^{-2}) were obtained for SH800 electrocatalyst, in contrast to SC800 ($j_{L(-1.0\ V,\ 1600\ rpm)}$ = -3.04 mA cm^{-2}); these differences can be related with their different textural properties. Both ACs were neither selective to 2- or 4-electron ORR processes. SH800 and SC800 showed very similar Tafel plots with two different slopes, with SH800 showing in both low and high current densities the lowest values 53 / 171 mV dec^{-1} vs. 68 / 217 mV dec^{-1}. Furthermore, the ACs presented excellent tolerance to methanol, with SH800 electrocatalyst also showing greater long-term electrochemical stability than Pt/C electrocatalyst which are very important advantages. The ACs-based electrocatalysts also showed ORR catalytic activity in acidic medium, which makes them promising candidates for applications with acidic electrolytes (e.g. proton exchange fuel cells). In this case, E_{onset} = 0.06 V vs. Ag/AgCl for SC800 and E_{onset} = -0.01 V vs. Ag/AgCl for SH800, and the diffusion-limiting current densities are very similar for both ACs (j_L = -2.59/-2.76 mA cm^{-2} at -1.3 V vs. Ag/AgCl, at 1600 rpm). SH800 and SC800 Tafel plots also showed two different slopes, but with

[1] Adapted from: M. Nunes, I. M. Rocha, D. M. Fernandes, A. S. Mestre, C. N. Moura, A. P. Carvalho, M. F. R. Pereira, C. Freire, Sucrose-derived activated carbons: electron transfer properties and application as oxygen reduction electrocatalysts, *RSC Adv.* **2015**, *5*, 102919. DOI: 10.1039/c5ra20874b. Reproduced by permission of The Royal Society of Chemistry.

[2] M. Nunes's contribution to the publication: characterisation of activated carbons by XPS, electrochemical characterisation, evaluation of the ORR electrocatalytic activity and manuscript preparation.

[3] The experimental details on the electrochemical / electrocatalytic and remaining characterisation techniques are indicated in Appendices B and C, respectively.

higher values in both low and high current density regions, when compared with those obtained in alkaline medium; still SH800 continues to show the lowest slopes.

6.1 Introduction

Carbon-based materials, with their versatile properties, appeared as ideal metal-free ORR electrocatalysts and have attracted a great attention.[1,2] In particular, the activated carbons have been applied with this purpose mainly due to their high surface areas and well developed pore structures,[3] which increase the number of active sites exposed to the electrolyte and promote the ORR electrocatalytic activity.[4,5,6] Unfortunately, a great number of commercial carbons are prepared from coal, a non-renewable raw material.[7] In this context, biomass emerged as a class of ideal starting materials for the green synthesis of carbon materials, once it is earth-abundant, readily available, cheap and environmental friendly.[8,9] The hydrothermal carbonization of biomass, via dehydration reactions in aqueous medium under mild conditions,[10] allows its conversion into valuable materials with fine tuning chemical structure and morphology.[6] The use of hydrothermal carbonization followed by activation was recently evaluated,[11] allowing to prepare superactivated carbons. The materials obtained are carbon- and oxygen-rich, due to the nature of biomass precursors,[7] which can constitute an advantage, since the ORR electrocatalytic activity and H_2O/H_2O_2 selectivity, could be influenced by the oxygen-containing groups.[12]

Numerous studies have been published, reporting the application in ORR of carbon-based materials (undoped and doped) derived from several biomass sources, such as carbohydrates / polysaccharides (e.g. glucose[10,13-15] and chitin[16,17]), proteins from silk,[18,19] egg[20] and blood,[21] animal wastes,[22,23] plants,[5,6,8,24,25] fungus[9] and marine algae.[4,26] Some of these materials showed excellent ORR performance (assigned though E_{onset} and j_L values), with catalytic activities competitive with the Pt/C electrocatalyst, but greater stability and tolerance to methanol poisoning is still a prior demand.[4,6,26] Nevertheless, these results constitute a tremendous advantage and encourage further studies with this type of biomass-derived materials.

In this chapter is described the application of two sustainable activated carbons prepared from a sucrose-derived hydrochar,[11,27] denoted by SC800 and SH800, as ORR electrocatalysts. Their ORR electrocatalytic activities are explored in alkaline and acidic media using cyclic and linear sweep voltammetry, and their stabilities and tolerances to methanol poisoning effects in alkaline medium are also evaluated by chronoamperometry and cyclic voltammetry, respectively. Complementary characterisation included ACs surface chemical composition by X-ray photoelectron

spectroscopy and electron transfer properties of the ACs-based modified electrodes in the presence of selected redox probes, $[Fe(CN)_6]^{3-/4-}$, $[Ru(NH_3)_6]^{3+/2+}$ and $Eu^{3+/2+}$. Dependency between the electron transfer properties and materials C/O ratios with multiple concurrent effects, has already been observed in studies involving graphite oxides,[28] graphene-type materials[29,30] and carbon quantum dots,[31] evaluating the electrochemical response of materials in the presence of selected redox probes.

To the best of our knowledge, this is the first time that it is explored the application of ACs metal-free ORR electrocatalysts derived from sucrose. Di Noto *et. al*[32-34] already presented ORR electrocatalysts whose preparation included the use of sucrose, but the resulting materials included metallic nanoparticles (Pt, Ni and Rh) deposited in carbon nitrides.

6.2 Experimental section

6.2.1 Reagents and solvents

All reagents used in activated carbons preparation, namely sucrose (Analar Normapur, > 90 %), potassium carbonate (K_2CO_3, Aldrich, 99 %) and potassium hydroxide (KOH, Panreac, 85 %) were used as received. Potassium chloride (KCl, Merck, ≥ 99.5 %), potassium hexacianoferrate (III) ($K_3[Fe(CN)_6]$, Merck, ≥ 99 %), aminoruthenium (III) chloride ($[Ru(NH_3)_6]Cl_3$, Aldrich, 98.0 %), europium (III) chloride hexahydrate ($EuCl_3.6H_2O$, Aldrich, 99.9 %), potassium hydroxide (KOH, Riedel-de-Häen), sodium sulfate (Na_2SO_4, Prolabo, 99.5 %), sulfuric acid (H_2SO_4, Merck, 95-97 %), Nafion (Aldrich, 5 wt% solution in lower aliphatic alcohols and water), ethanol (Panreac, 99.8 %) and methanol (Fisher Scientific, > 99.99 %) were used as received. The 20 wt% Pt/C standard catalyst was prepared by incipient wetness impregnation method. The active metal precursor, $H_2PtCl_6.6H_2O$, dissolved in water, was slowly added to the carbon support, Printex80. During 24 hours, the sample was dried in an oven at 373 K. The dried sample was annealed at T = 523 K, during 1 h under N_2 and reduced during 3 h under H_2.

6.2.2 Preparation of materials

The sucrose-derived activated carbons were prepared by a hydrothermal carbonization of sucrose solution followed by a chemical activation, as described in literature.[27] Briefly, 15 mL of a 1.5 mol dm^{-3} sucrose aqueous solution was introduced in a Teflon-line stainless steel autoclave during 5 h at 190 ºC. The obtained powder (hydrochar S) was washed with distilled water and acetone and dried (60 ºC). For chemical activation, 1 g of hydrochar was impregnated under stirring on a solution with

4 g of K_2CO_3 or KOH during 2 h and then dried. Activation was performed at 800 ºC in a horizontal furnace (Thermolyne, model 21100) for 1 h under a N_2 flow of 5 cm^3 s^{-1} (10 ºC min^{-1}). After cooling, the materials were thoroughly washed with distilled water until pH 7 was reached, dried overnight at 100 ºC and stored. The materials are labelled as S (hydrochar) followed by H or C for KOH or K_2CO_3, respectively, resulting in designations SH800 and SC800, and were characterized by N_2 and CO_2 adsorption isotherms and XPS.

6.2.3 Evaluation of the ORR electrocatalytic activity

The ORR performance of each electrocatalyst was evaluated by cyclic voltammetry and linear sweep voltammetry (LSV). The modified-electrodes were prepared by the following procedure: 1 mg of SH800 or 20 wt% Pt/C catalysts or 2 mg of SC800 were dispersed ultrasonically in 1 mL of a Nafion/ethanol (1:9 v/v) mixture for 30 min. Then, a 3 μL drop of the select dispersion was deposited in the glassy carbon rotating disk electrode (RDE) surface and dried under an air flux, yielding an electrocatalyst loading of 99.05 μg cm^{-2}. Prior to modification, the electrode was conditioned by a polishing/cleaning procedure, using diamond pastes of 6, 3 and 1 μm (MetaDi II, Buehler) and aluminium oxide of particle size 0.3 μm (Buehler), on a microcloth polishing pad (BAS Bioanalytical Systems Inc.). To finish, the electrode was rinsed and sonicated for 10 min in ultra-pure water.

The electrochemical tests were accomplished in N_2- or O_2-saturated (purged for 30 min before the measurements) 0.1 mol dm^{-3} KOH or H_2SO_4/Na_2SO_4 buffer solution with pH= 2.5 (prepared by mixing appropriate amounts of a 0.2 mol dm^{-3} H_2SO_4 solution with a 0.5 mol dm^{-3} Na_2SO_4 solution). CV experiments were conducted at the scan rate of 0.005 V s^{-1} and the LSV at 0.005 V s^{-1} for different rotation speeds from 400 to 3000 rpm; chronoamperometry measurements were performed at E = -0.6 V vs. Ag/AgCl and 1600 rpm during 20 000 s. The methanol-tolerance evaluation was performed by CV at 0.010 V s^{-1}. The ORR current was obtained by subtracting the current measured in N_2-saturated electrolytes from the current measured in O_2-saturated electrolytes.

The onset potential (E_{onset}) was calculated as described in literature.[35] In order to facilitate the comparison with the literature, the E_{onset} values determined vs. Ag/AgCl were converted to the reversible hydrogen electrode (RHE) scale according to the Nernst equation:

$$E_{RHE} = E_{Ag/AgCl} + 0.059\ pH + E^{o}_{Ag/AgCl} \quad (6.1)$$

where E_{RHE} is the converted potential vs. RHE, $E°_{Ag/AgCl}$ = 0.1976 at 25 ºC and $E_{Ag/AgCl}$ is the experimentally measured potential against Ag/AgCl reference.[36]

LSV data was analysed though Koutecky-Levich (K-L) plot, Equations (1.2) and (1.3). In 0.1 mol dm^{-3} KOH medium C_{O_2}= 1.15x10^{-3} mol dm^{-3}, υ = 0.008977 cm^2 s^{-1} and D_{O_2}=1.95x10^{-5} cm^2 s^{-1},[37] while in H_2SO_4/Na_2SO_4 buffer medium C_{O_2}=1.26x10^{-3} mol dm^{-3}, υ = 0.01 cm^2 s^{-1} and D_{O_2}= 1.77x10^{-5} cm^2 s^{-1}.[38] The Tafel plots (E_{RHE} vs. log i_k) for oxygen reduction kinetics were obtained after the measured currents in LSV were corrected for diffusion to give the kinetic currents. The mass transport correction was made using the diffusion-limiting current density j_L, calculated by combination of Equations (1.2) and (1.3), since it could not be obtained directly from the LSV. The obtained current density j_k was multiplied by the geometric area of the GCE disk (A = 0.07067 cm^2) yielding i_k, which was normalised for the total deposited mass of ACs for SC800 and SH800 electrocatalysts; in the case of Pt/C, i_k was normalised on Pt mass existing in the deposited Pt/C mass.[39]

6.2.4 Electrochemical characterisation of the modified electrodes

To prepare the modified electrodes, the activated carbons (SC800 or SH800, 1 mg) were dispersed in N,N'-dimethylformamide (DMF, 1 mL) and sonicated for 20 min. Then, a 3 µL drop of the selected material dispersion was deposited onto the GCE surface, followed by solvent evaporation under an air flux. Prior to modification, the GCE electrode was conditioned as described above.

CV of the redox probes $K_3[Fe(CN)_6]$, $[Ru(NH_3)_6]Cl_3$ or $EuCl_3.6H_2O$ were performed using solutions 1.0 x 10^{-3} mol dm^{-3} in KCl 1.0 mol dm^{-3}. All solutions were prepared using ultra-pure water (resistivity 18.2 MΩ cm at 25°C, Millipore). According with the electrochemical probe used, the potential was cycled between 0.75 and -0.25 V, 0.20 and -0.50 V or -0.10 and -1.00 V, at several scan rates from 0.010 to 0.500 V s^{-1}. Each experiment was repeated until obtain concordant results.

The electroactive surface areas were determined using the Randles-Sevcik equation, Equation (6.2), assuming that the electrode process is controlled by diffusion:

$$i_{pc} = 2.69 \times 10^5 \, n^{3/2} \, A \, D_x^{1/2} \, C \, \nu^{1/2} \qquad (6.2)$$

where n is the number of electrons involved in the process (1 in this case), A is the electrode surface area (cm^2), D_x the diffusion coefficient (6.30 x 10^{-6} cm^2 s^{-1} for $[Fe(CN)_6]^{3-/4-}$,[40] 6.20 x 10^{-6} cm^2 s^{-1} for $[Ru(NH_3)_6]^{3+/2+}$ [41] and 6.50 x 10^{-6} cm^2 s^{-1} for $Eu^{3+/2+}$ [42]), C the concentration of the specie (mol cm^{-3}), ν is the scan rate (V s^{-1}) and i_{pc} the intensity of the cathodic peak current (A).[43]

The heterogeneous electron transfer (HET) rates were evaluated by Nicholson's method, that relates the ΔE_p to a dimensionless charge transfer parameter Ψ and, consequently, to k_{HET} (HET rate constant), through Equation (6.3)[44,45]

$$\Psi = \frac{k_{HET}}{(\pi D_x \frac{nFv}{RT})^{1/2}} \quad (6.3)$$

where R is the gas constant, F is Faraday's constant, T is the temperature (25 ºC) and the remaining symbols have the significance described above. The Ψ values were estimated from ΔE_p, according with the tabulated values by Nicholson.[44]

6.3 Results and discussion

6.3.1 Activated carbons characterisation

The N_2 adsorption-desorption isotherms (Figure 6.1(a)) of the sucrose-derived activated carbons belong to type I in the IUPAC classification,[46] being characteristic of materials with a well-developed micropore network. Carbon SH800, obtained by KOH activation, presents the more developed microporous structure and the rounder off knee of its N_2 isotherm is indicative of the presence of larger micropores (supermicropores). This sample presents a sponge-like morphology.[27] Sample SC800, activated with K_2CO_3, has lower N_2 adsorption capacity and the isotherm presents a sharper knee revealing the existence of narrower micropores, but retains the spherical morphology of the hydrochar.[27]

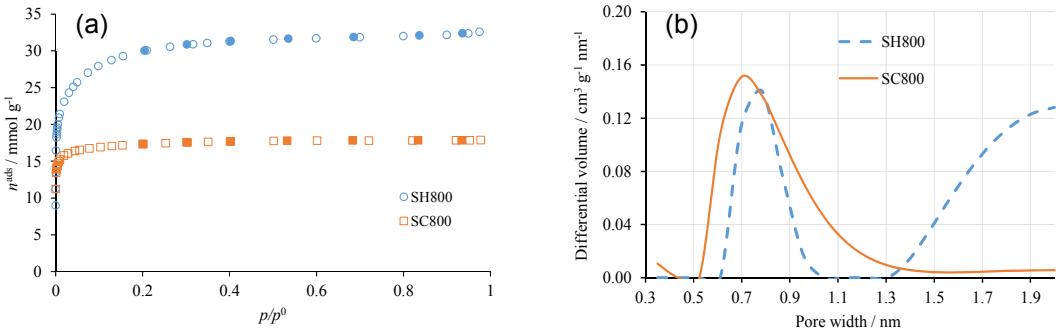

Figure 6.1 (a) N_2 adsorption–desorption isotherms at -196 ºC, closed symbols are the desorption points; (b) micropore size distributions of the activated carbons (adapted from Ref. [27]).

The textural parameters of the materials (Table 6.1) are in accordance with the analysis of the shape of the curves. The apparent surface area of carbon SH800

attains more than 2400 m^2 g^{-1} while for carbon SC800 is 1375 m^2 g^{-1}, and the total microporous volume of SH800 is almost the double of that presented by SC800 (1.08 vs. 0.62 cm^3 g^{-1}). As expected from the configuration of the N_2 isotherms, the data from the α_s method reveal that the micropore network of carbon SH800 is composed exclusively by larger micropores (supermicropores – widths between 0.7 and 2 nm), while carbon SC800 presents similar amounts of ultra (widths < 0.7 nm) and supermicropores.

Further characterisation of the sucrose-derived activated carbons by micropore size distributions (Figure 6.1(b)), assessed by fitting CO_2 adsorption data at 0 ºC to the method described by Pinto *et al.*,[47] corroborates the assumptions made above. Carbon SH800 has a bimodal micropore size distribution with pores mainly in the supermicropore region and a very large amount of pores with widths between 1.3 and 2 nm, whereas sample SC800 presents a monomodal distribution centered at ≈ 0.7 nm and negligible volume of pores with widths > 1.5 nm.

Table 6.1 Textural properties of the sucrose-derived activated carbons (adapted from Ref. [27]).

Sample	A_{BET} (m^2 g^{-1})	V_{total} [a] (cm^3 g^{-1})	V_{meso} [b] (cm^3 g^{-1})	α_s Method[c,d,e]		
				$V_{\alpha\ total}$ (cm^3 g^{-1})	$V_{\alpha\ ultra}$ (cm^3 g^{-1})	$V_{\alpha\ super}$ (cm^3 g^{-1})
SH800	2431	1.14	0.06	1.08	0.00	1.08
SC800	1375	0.63	0.01	0.62	0.35	0.27

[a] evaluated at p/p^0 = 0.975 in the N_2 adsorption isotherms at -196 ºC.

[b] difference between V_{total} and $V_{\alpha\ total}$.

[c] $V_{\alpha\ total}$ – obtained by back extrapolation of the high relative pressure region (α_s < 1).

[d] $V_{\alpha\ ultra}$ – intercept of the linear range defined the region $p/p^0 \geq 0.02$ (ϕ < 0.7 nm).

[e] $V_{\alpha\ super}$ – difference between $V_{\alpha\ total}$ and $V_{\alpha\ ultra}$ (0.7 nm < ϕ < 2 nm).

The SH800 and SC800 sucrose-derived activated carbons were further characterized by XPS; the obtained survey spectra for both materials are depicted in Figure 6.2 (a) and (a'). In the survey spectra, both activated carbons do not show any peak due to any catalytic active metal; besides C and O, the spectra show residual traces of Al2p, Si2p and K2p. Consequently, the ORR electrocatalytic activity described below for both SC800 and SH800 activated carbons relates to metal-free electrocatalysts. The deconvoluted high-resolution XPS spectra of SC800 in C1s and O1s regions are showed in Figure 6.2 (b) and (c), with the indication of the binding energies, and the equivalent spectra for SH800 are depicted in Figure 6.2 (b') and (c').

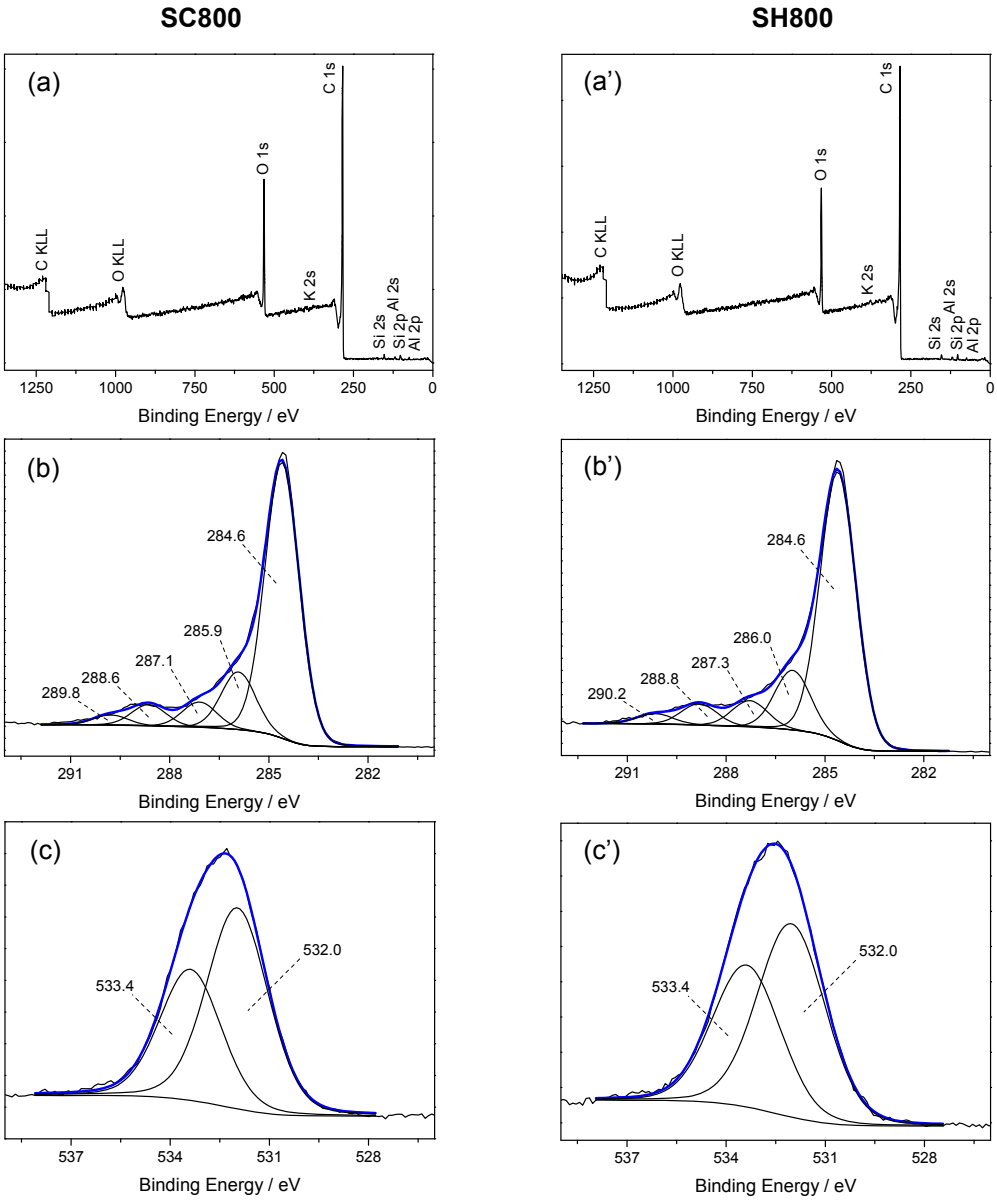

Figure 6.2 High-resolution XPS spectra for SC800 (left) and SH800 (right) activated carbons: (a) and (a') survey spectra and deconvoluted spectra in (b) and (b') C1s region and (c) and (c') O1s region.

For both samples, the C1s high-resolution spectra were deconvoluted with five peaks: a main peak at 284.6 eV assigned to graphitic carbon (sp^2), a peak at 285.9 / 286.0 eV attributed to sp^3 hybridised carbon, a peak at 287.1 / 287.3 eV assigned to C-O, a peak at 288.6 / 288.8 eV related to C=O and a peak at 289.8 / 290.2 eV ascribed to –COO bonds.[48] The O1s spectra were fitted with two peaks, at 532.0 and 533.4 eV, assigned to C=O and C-O environments, respectively.[3,49]

The surface atomic percentages of each element in both materials are summarised in Table 6.2. The results showed that both materials have very similar C% ≈ 82 (≈ 65 mmol g^{-1}) and O% ≈ 18 (≈ 14 mmol g^{-1}), indicating that they are surface

enriched in oxygen-containing groups. For SC800, C% is similar to the compositional data provided by the elemental analysis previously published (81.2 wt% of C, 67.6 mmol g^{-1})[11] while, for SH800, the C% obtained by XPS is higher than the reported by elemental analysis (74.5 wt%, 62.0 mmol g^{-1}),[11] suggesting for the latter material inhomogeneity between the carbon and oxygen bulk and surface compositions.

Table 6.2 XPS atomic percentages for SC800 and SH800.

Sample	**Atomic %** (mmol g^{-1})[a]	
	C 1s	**O 1s**
SC800	82.3 (64.8)	17.7 (13.9)
SH800	82.8 (65.2)	17.2 (13.5)

[a] Calculated through: mass C (or O) / mass of sample (calculated from the XPS data) = at.% C 1s (or O 1s) / [(at.% C 1s x atomic mass C) + (at.% O 1s x atomic mass O)].

6.3.2 Electrocatalytic activity for ORR

LSV measurements with rotating disk electrode (RDE) were performed to investigate the ORR performances of the prepared activated carbons electrocatalysts. The ORR activities were tested in alkaline (0.1 mol dm^{-3} KOH) and acidic (H_2SO_4/Na_2SO_4 buffer solution, pH 2.5) media. For comparison, the standard 20 wt% Pt/C was also measured in ORR. The results obtained in alkaline medium are depicted in Figure 6.3.

Figure 6.3 (a) presents the CVs obtained for SC800 and SH800 modified electrodes in N_2- and O_2- saturated solutions. In N_2-saturated solution no electrochemical processes are observed, while in O_2-saturated solution all materials exhibited an irreversible electrochemical process indicative of their electrocatalytic activity for ORR. The SC800 modified electrode showed two cathodic peaks, at E_{pc} = -0.26 and E_{pc} = -0.44 V vs. Ag/AgCl (0.70 and 0.52 V vs. E_{RHE}, respectively), and the SH800 showed only one defined cathodic peak, at E_{pc} = -0.28 V vs. Ag/AgCl (0.68 V vs. E_{RHE}).

Figure 6.3 (b) shows the ORR polarisation plots of the prepared catalysts, the 20 wt% Pt/C and the bare GCE. The RDE voltammograms for the ORR on individual bare GCE and SC800, SH800 and Pt/C modified electrodes, at rotation rates from 400 to 3000 rpm, are depicted in Figure 6.4. Both activated carbons-based electrocatalysts showed similar onset potentials (E_{onset} = -0.19 and -0.20 V vs. Ag/AgCl (0.77 and 0.76 V vs. E_{RHE}) for SC800 and SH800, respectively), but higher diffusion-limiting current densities ($j_{L(-1.0\ V,\ 1600\ rpm)}$ = -3.44 mA cm^{-2}) were obtained for SH800

electrocatalyst, in contrast to SC800 ($j_{L(-1.0\ V,\ 1600\ rpm)}$ = -3.04 mA cm^{-2}). These differences can be related to the distinct morphologies, surface area and micropore size distributions of the two materials. The material SH800 revealed a higher specific surface area, A_{BET}, around 2500 m^2 g^{-1}, presenting larger micropores and widths between 0.7 and 2 nm (Table 6.1), and sponge-like morphologies; on the other hand, SC800 showed a spherical shape, with A_{BET} ≈ 1400 m^2 g^{-1} and narrow micropores with pore width < 0.7 nm.[11]

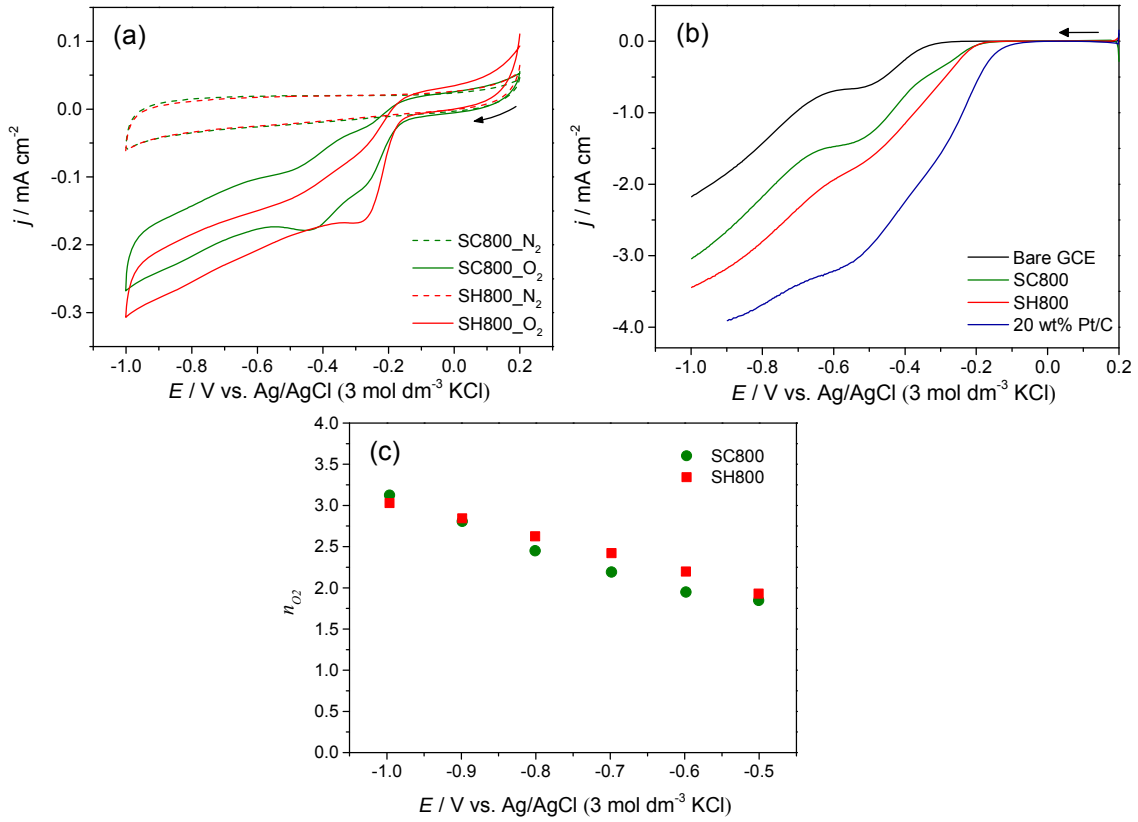

Figure 6.3. ORR results in KOH 0.1 mol dm^{-3}: (a) CVs of the as-prepared catalysts in N_2- and O_2-saturated solutions at 0.005 V s^{-1}, (b) LSV using RDE in O_2-saturated solution at 1600 rpm and 0.005 V s^{-1} and (c) number of electrons transferred per O_2 molecule (n_{O_2}) at several potential values.

Several works[4-6] have reported that high surface areas and large pore structures are favourable conditions for ORR, since it would favour mass transport of the electrolyte, allowing for a higher catalytic current density, assuming mass transfer limited currents. In this context, the better performance (higher current densities) exhibited by SH800 is a consequence of its larger pores that enable the electrolyte solution to flow into/out of the catalyst more easily.

The results indicated a superior ORR performance of the activated carbons modified electrodes in comparison to the bare GCE (E_{onset} = -0.33 V vs. Ag/AgCl (0.63 V vs. E_{RHE}), $j_{L(-1.0\ V,\ 1600\ rpm)}$ = -2.18 mA cm^{-2}), with onset potential at less negative values and higher current densities, which demonstrates the advantage of the electrode modification. On the other hand, the results obtained with activated carbons are near to those obtained with 20 wt% Pt/C (E_{onset} = -0.14 V vs. Ag/AgCl (0.82 V vs. E_{RHE}), $j_{L(-0.9\ V,\ 1600\ rpm)}$ = -3.91 mA cm^{-2}), with a difference of ΔE_{onset} = 0.06 V between the onset potentials of Pt/C and ACs-based modified electrodes.

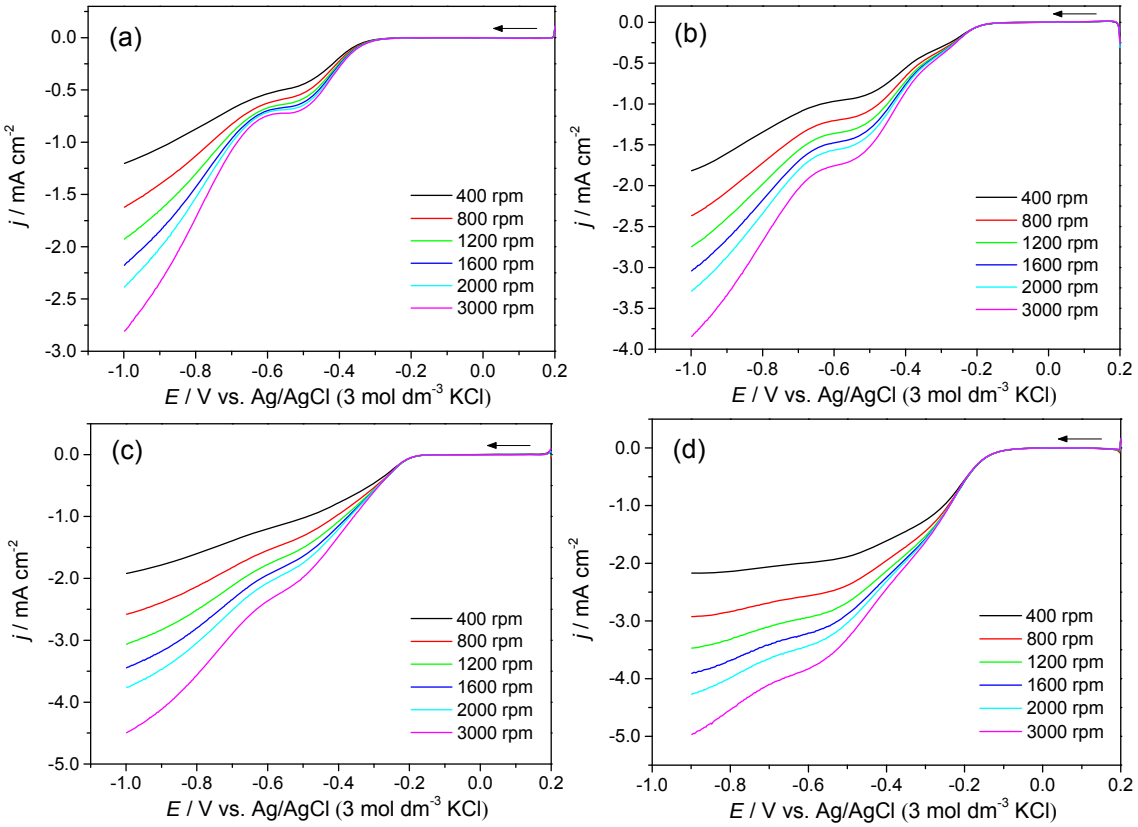

Figure 6.4 ORR polarisation plots of (a) bare GCE, (b) SC800 and (c) SH800 modified electrodes and (d) 20 wt% Pt/C at several rotation rates and 0.005 V s^{-1}, in 0.1 mol dm^{-3} KOH electrolytes.

In the context of other biomass-based carbon materials (usually, highly porous materials) for ORR,[4,5,13-15] the majority refers to heteroatom doped materials (N and S), with the undoped analogues being equivalent to those prepared in this work. The E_{onset} values obtained for SH800 and SC800 (-0.20 V vs. Ag/AgCl) compare well or are less negative to those obtained for undoped and N-doped glucose-derived carbon aerogels (E_{onset} = -0.10, -0.20, -0.30 V vs. Ag/AgCl) when they are used as electrocatalysts in alkaline medium.[5,13-15]

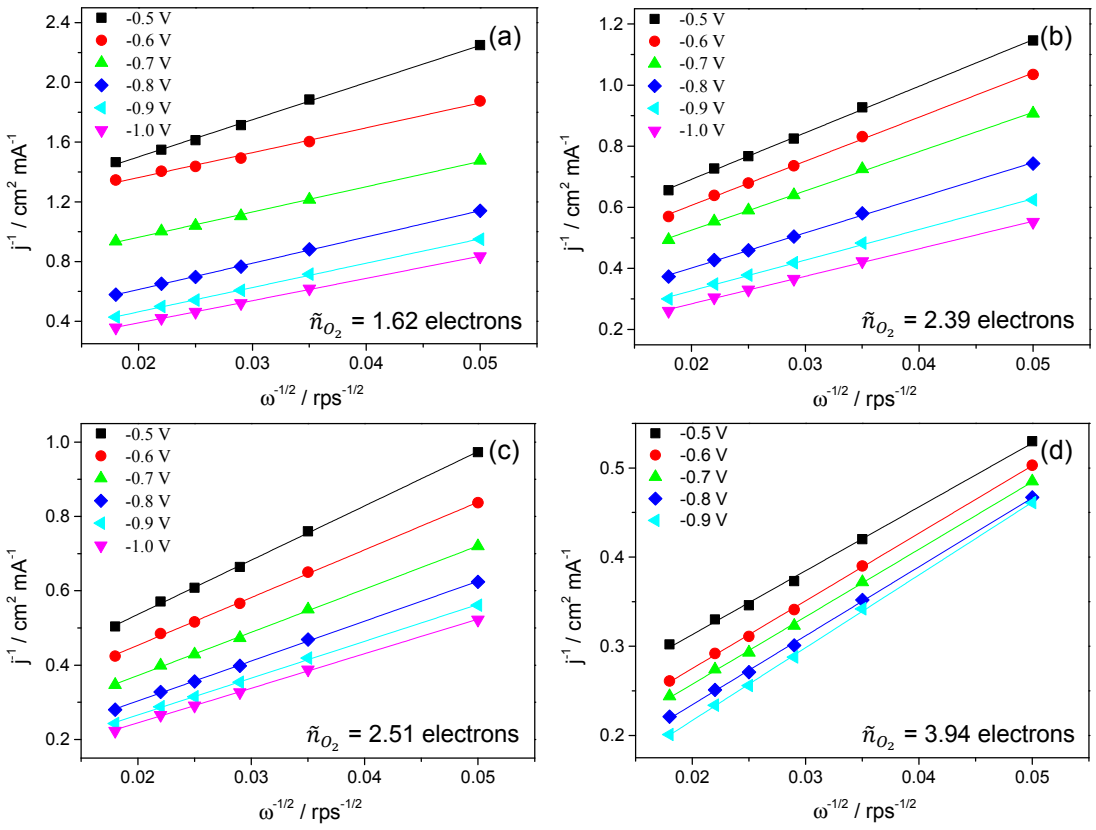

Figure 6.5 Koutecky-Levich (K-L) plots of (a) bare GCE, (b) SC800 and (c) SH800 modified electrodes and (d) 20 wt% Pt/C obtained from data in Figure 6.4.

The ORR kinetic parameters were analysed by the Koutecky-Levich (K-L) plots (j^{-1} vs. $\omega^{-1/2}$) at various potentials, using the RDE voltammograms. The slopes of their linear fit lines were used to estimate the number of electrons transferred per oxygen molecule (n_{O_2}), although it is recognised that the high surface areas and high degree of porosity may interfere in the transport properties of the active species (O_2 and reaction intermediates) in the electrolyte. From the corresponding K-L plots (in the range -0.5 to -1.0 V vs. Ag/AgCl), Figure 6.5, it can be seen that the data exhibited good linearity, although the different straight lines exhibited different slopes, anticipating a variation in the n_{O_2} values with potential. From Figure 6.3 (c) it is possible to verify that the estimated number of electrons transferred is very similar between the SC800 and SH800 catalysts, increasing as the potential become more negative, revealing that the electrocatalysts are not selective for either the 2 (indirect reduction through peroxide pathway) or 4 electron processes (direct O_2 reduction): at *E* = -0.5 V vs. Ag/AgCl, the electrocatalysts are involved in a n_{O_2} = 1.85-1.93 electrons process, shifting to n_{O_2} = 3.03-3.12 electrons at *E* = -1.0 V vs. Ag/AgCl. These values are bigger than that displayed by GCE (n_{O_2} = 1.70 electrons, at *E* = -1.0 V vs. Ag/AgCl), being closer to the

$\tilde{n}_{O_2}$= 3.94 electrons estimated for 20 wt% Pt/C, for which a 4 electron process is observed. The obtained n_{O_2} values and its dependence with potential are also very similar to what is observed when glucose-derived carbon materials are used as ORR electrocatalysts in alkaline medium.[13-15]

Further information on ORR kinetics and mechanism can be obtained from the Tafel plots for both ACs and Pt/C, Figure 6.6. Both ACs showed very similar Tafel plots with two different slopes with similar values: 53 /68 mV dec^{-1} in low current density region and 171 / 217 mV dec^{-1} in high current density region, for SH800 and SC800, respectively. As expected, the highest performance electrocatalyst SH800 showed lower slopes. The Pt/C electrocatalyst showed a different Tafel plot with different slope values (85 / 192 mV dec^{-1}), suggesting a different mechanism in which Pt is the active site.[50]

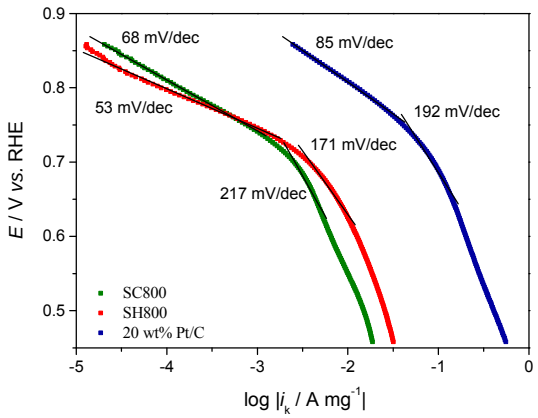

Figure 6.6 ORR Tafel plots for SC800 and SH800 activated carbons and 20 wt% Pt/C, obtained from LSV data in Figure 6.3 (b); current intensities normalised to the mass of each electrocatalyst deposited on electrode (see experimental section).

The ORR mechanism in undoped carbon materials that present oxygen groups is still a matter of debate and only few papers address the topic, for pyrolytic graphite, CNTs and graphene oxide.[1] The identified oxygen containing groups with ORR activity are the so-called quinone-like groups, that are capable of O_2 adsorbing and efficiently mediate the first 2e$^-$ reduction of O_2 to HO_2^- and subsequent reduction of the intermediates to HO^-.[51-53] The ACs-based electrocatalysts have very similar oxygen contents and although XPS is not able to discrimination the oxygen-type groups and respective quantities, the similarity of the Tafel slopes and profiles suggests that the different electrocatalytic activities may be not directly related to the type of oxygen

groups, but to the different textural properties, namely the higher surface area and larger microporous of SH800 comparative to SC800.

An important parameter in fuel-cells where methanol is used as fuel, as in direct methanol fuel-cells, is the tolerance of the catalyst to fuel molecules, that may pass across the membrane from the anode to the cathode and to poison the catalyst.[6,26] The platinum-based electrocatalysts have the disadvantage of selectivity to methanol oxidation, which completely subdues the ORR and reduces the current output.[4] Therefore, methanol tolerance tests were performed by cyclic voltammetry, with SC800, SH800 modified electrodes and standard Pt/C for comparison. The CVs obtained in O_2-saturated 0.1 mol dm^{-3} KOH solutions, in the presence and absence of methanol (1.0 mol dm^{-3}), for SC800, SH800 and 20 wt% Pt/C modified electrodes are depicted in Figures 6.7 (a), (b) and (c), respectively. In the presence of methanol, the Pt/C electrocatalyst showed an anodic peak at E_{pa} = -0.17 V vs. Ag/AgCl attributed to methanol oxidation, that overlaps the ORR and reflects the low tolerance of Pt to methanol, as expected. On the contrary, there were no significant changes in the electrochemical response of SC800 and SH800 electrocatalysts after the introduction of methanol, demonstrating their high selectivity for oxygen reduction against the electro-oxidation of methanol and, consequently, the excellent tolerance towards crossover methanol effect. These results make SC800 and SH800 materials promising electrocatalysts to be applied in fuel cells, especially in direct methanol fuel cells.

Another important parameter is the stability / durability of the ORR electrocatalysts. Thus, the long-term stabilities of the SC800, SH800 and Pt/C electrocatalysts were evaluated by chronoamperometric measurements at E = -0.60 V vs. Ag/AgCl in O_2-saturated 0.1 mol dm^{-3} KOH solution at 1600 rpm, and the results are present in Figure 6.7 (d). After 20 000 s, the 20 wt% Pt/C chronoamperogram showed a current decay to 68.0 %. At the end of the same period of time, the SC800 current declined to 53.9 %, while the SH800 showed a current decay only to 72.9 %. These data revealed that the activated carbons have different electrochemical stabilities, with the SH800 being the most stable ORR electrocatalyst. These differences can be related to the combination of distinct morphologies, surface areas and porosity: the SH800 electrocatalyst showing higher surface area and larger pores,[11] will have higher number of active sites (quinone-like groups) that will be easily accessed by the O_2/HO_2^-/electrolyte, leading to higher durability. Furthermore, SH800 also showed to be more stable than the standard Pt/C catalyst, which is a promisor result. This could be a consequence of the migration and aggregation of Pt particles caused by continuous potential variation, contrasting to the higher stability of carbon materials structure.

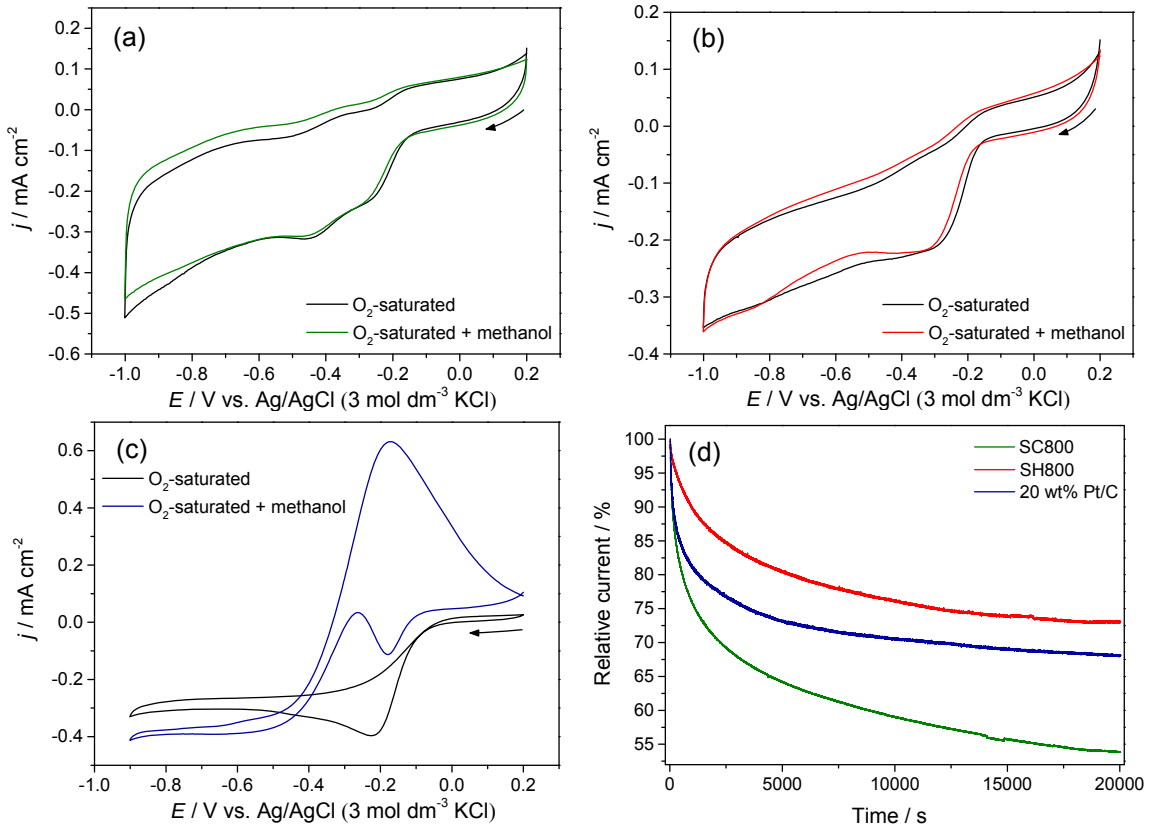

Figure 6.7 CVs for ORR in O_2-saturated 0.1 mol dm^{-3} KOH with and without methanol (1.0 mol dm^{-3}) for (a) SC800, (b) SH800 and (c) 20 wt% Pt/C; (d) relative *j*-t chronoamperometric responses of catalysts at *E* = -0.60 V and 1600 rpm, in O_2-saturated 0.1 mol dm^{-3} KOH solution.

Figure 6.8 shows the results obtained in acidic medium (H_2SO_4/Na_2SO_4 buffer solution, pH 2.5). The CVs obtained in N_2- and O_2-saturated solutions are depicted in Figure 6.8 (a). The activated carbon-based electrocatalysts showed ORR electrocatalytic activity also in acidic medium, exhibiting cathodic peaks at E_{pc} = -0.16 V and E_{pc} = -0.11 V vs. Ag/AgCl (0.18 V and 0.24 V vs. E_{RHE}), for SC800 and SH800, respectively. This is a key result because usually carbon materials are known to be inactive or present lower ORR activity in acidic media.[6] The ORR catalytic activity in acidic medium is also very important for proton exchange fuel cells which required acid electrolytes.[54]

Interestingly, other electrochemical processes (at *E* = -0.72 / 0.28 V for SC800 and *E* = -0.73 / 0.06 or 0.20 V for SH800 vs. Ag/AgCl) were also observed in both N_2- and O_2-saturated solutions, which can be related to other redox processes inherent of the activated carbon materials in acidic medium and not directly related to ORR.

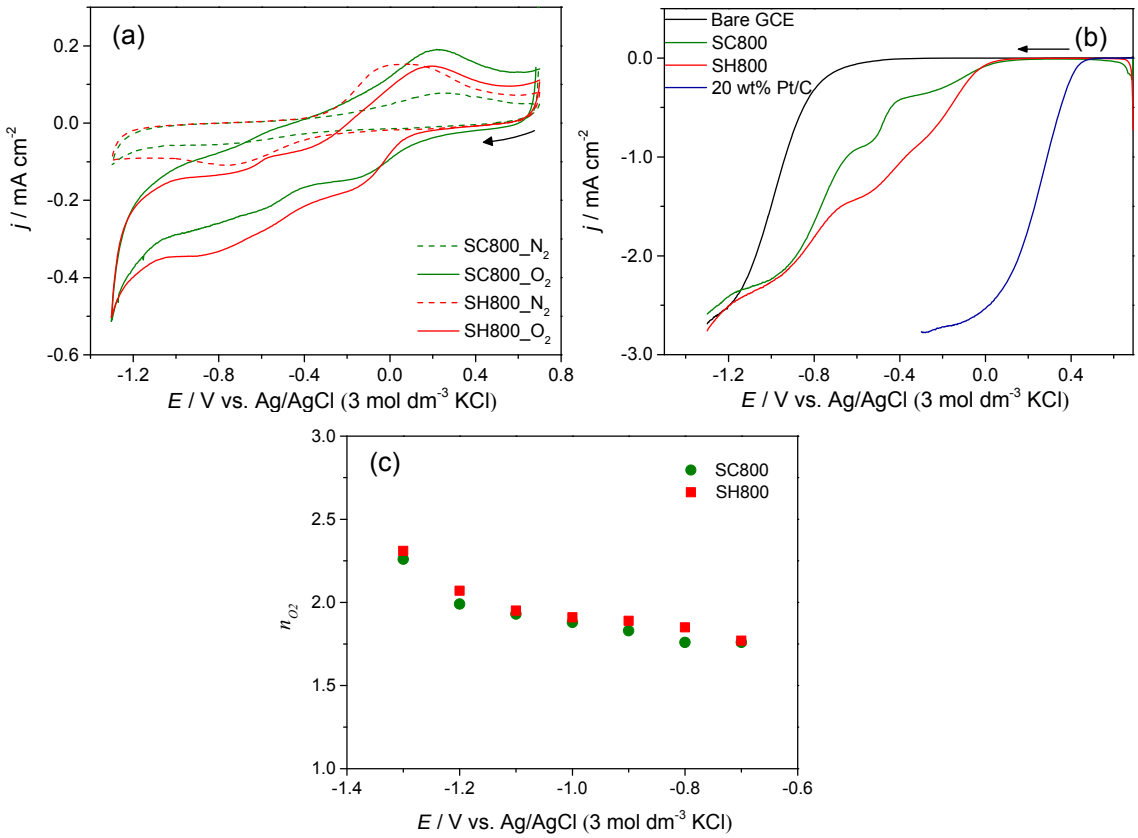

Figure 6.8 ORR results in H_2SO_4/Na_2SO_4 (pH 2.5): (a) CVs of the as-prepared catalysts in N_2- and O_2-saturated solutions at 0.005 V s^{-1}, (b) LSV using RDE in O_2-saturated solution at 1600 rpm and 0.005 V s^{-1} and (c) number of electrons transferred per O_2 molecule (n_{O_2}) at several potential values.

The ORR polarisation plots for all materials are depicted in Figure 6.8 (b) and the individual RDE voltammograms can be observed in Figure 6.9. Similarly to the results obtained in alkaline medium, also in acidic medium, the electrodes modified with SC800 and SH800 showed higher ORR performance than the bare GCE, exhibiting onset potentials at more positive values (E_{onset} = 0.06 V vs. Ag/AgCl (0.41 V vs. E_{RHE}) for SC800 and E_{onset} = -0.01 V vs. Ag/AgCl (0.34 V vs. E_{RHE}) for SH800). These onset potential values are considerably more negative than those obtained with the Pt/C modified electrode (E_{onset} = 0.41 V vs. Ag/AgCl (0.76 V vs. E_{RHE})), resulting in a ΔE_{onset} = 0.35-0.42 V. The declining of the carbon materials performance in acidic medium, when compared with Pt/C, can be associated to some active sites deactivation, for example protonation of oxygen ORR active groups which become inactive and non-accessible for O_2 adsorption.[35]

Furthermore, all modified electrodes displayed identical ORR diffusion-limiting current densities (j_L = -2.68, -2.59 and -2.76 mA cm^{-2} for bare GCE, SC800 and SH800,

respectively (at *E* = -1.3 V vs. Ag/AgCl), and j_L = -2.78 for 20 wt% Pt/C (at *E* = -0.3 V vs. Ag/AgCl), at 1600 rpm.

In comparison with other biomass-based carbon materials (N- and S-doped) reported as ORR electrocatalysts,[5,13] the E_{onset} values obtained for SC800 and SH800 (0.06 and -0.01 V vs. Ag/AgCl, respectively) are less positive than those obtained for N-doped glucose-based carbons materials (0.20 - 0.50 V vs. Ag/AgCl).

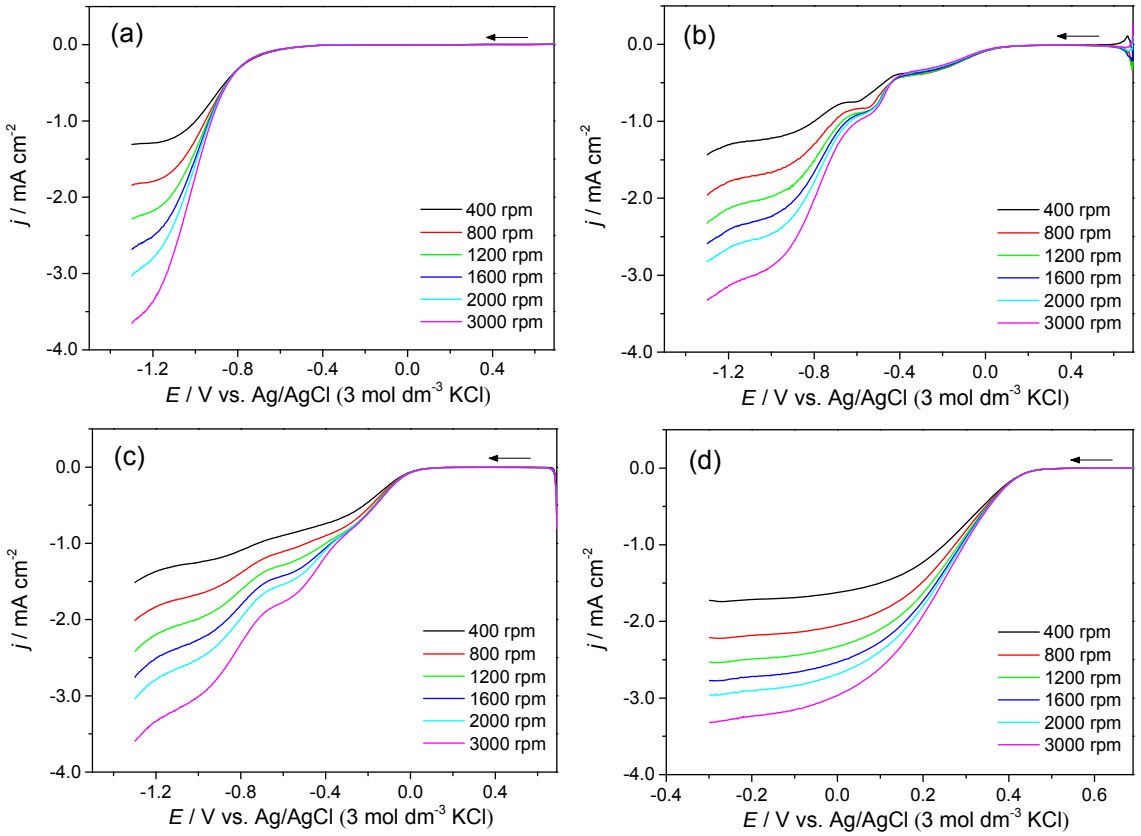

Figure 6.9 ORR polarisation plots of (a) bare GCE, (b) SC800 and (c) SH800 modified electrodes and (d) 20 wt% Pt/C at several rotation rates and 0.005 V s^{-1}, in H_2SO_4/Na_2SO_4 (pH 2.5).

K-L plots are presented in Figure 6.10 and the number of electrons transferred per O_2 molecule and its variation according with the applied potential can be observed in Figure 6.8 (c) for all electrocatalysts. The SC800 and SH800 electrocatalysts continue to present similar n_{O_2} values, but with some variation with the applied potential: at *E* = -1.3 V, n_{O_2} = 2.26 for SC800, n_{O_2} = 2.31 for SH800 and n_{O_2} = 1.80 for the bare GCE. At this experimental conditions, Pt/C electrocatalyst presented n_{O_2} = 3.27 (at -0.3 V).

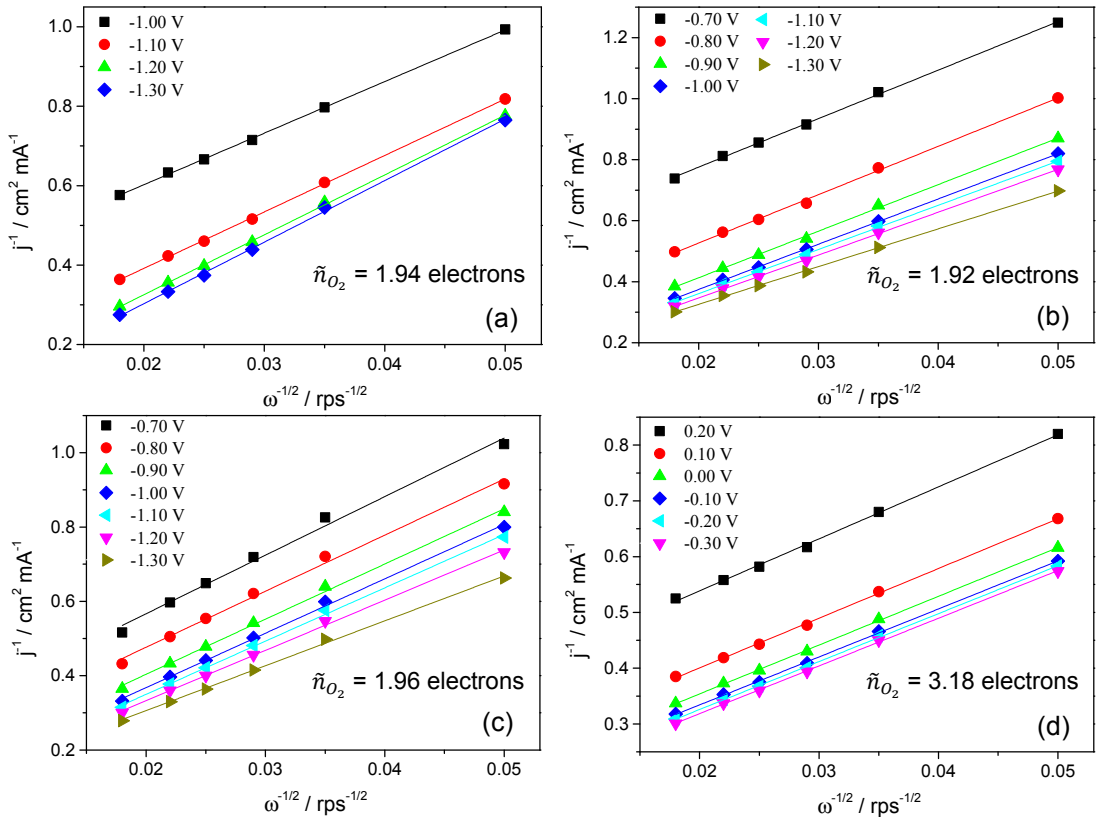

Figure 6.10 Koutecky-Levich (K-L) plots of (a) bare GCE, (b) SC800 and (c) SH800 modified electrodes and (d) 20 wt% Pt/C obtained from data in Figure 6.9.

Tafel plots for ACs, depicted in Figure 6.11, also presented two different slopes: 227 / 1001 mV dec^{-1} for SC800 and 145 / 561 mV dec^{-1} for SH800, in low and high current density regions, respectively.

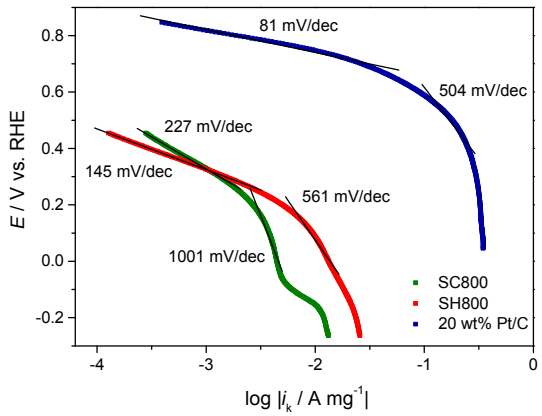

Figure 6.11 ORR Tafel plots for SC800 and SH800 activated carbons and 20 wt% Pt/C, obtained from LSV data in Figure 6.8 (b); current intensities normalised to the mass of each electrocatalyst deposited on electrode (see experimental section).

Globally, the results suggest lower electrocatalytic activity and different ORR mechanisms compared to the equivalent data in alkaline medium; nevertheless SH800 still showed the lowest slopes and consequently highest ORR performance. Moreover, Pt/C electrocatalyst showed lower Tafel slopes (81 / 504 mV dec^{-1}) than for ACs, indicating highest catalytic activity.[50]

6.3.3 Electrochemical characterisation of the modified electrodes

Further electrochemical characterisation was performed to the SC800- and SH800-modified electrodes, in order to evaluate other possible applications.

The CVs of SC800 and SH800 activated carbon-modified electrodes and bare GCE, in KCl 1.0 mol dm^{-3}, are compared in Figure 6.12 (a).

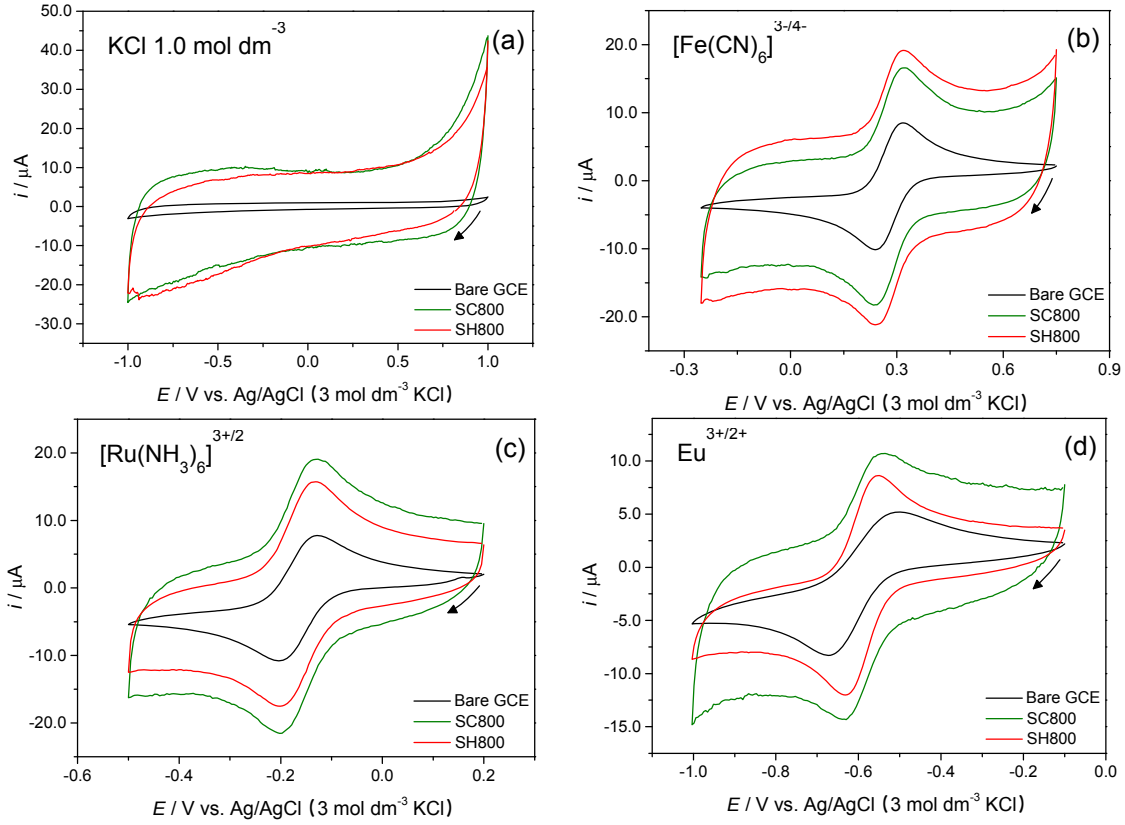

Figure 6.12 CVs of bare GCE and SC800 and SH800 modified electrodes, at the scan rate of 0.05 V s^{-1} in (a) KCl 1.0 mol dm^{-3} supporting electrolyte and in the presence of 1.0x10^{-3} mol dm^{-3} redox probe in KCl 1.0 mol dm^{-3}: (b) $K_3[Fe(CN)_6]$; (c) $[Ru(NH_3)_6]Cl_3$ and (d) $EuCl_3.6H_2O$.

Rectangular voltammograms are observed for both activated carbons, suggesting a capacitive behaviour for these materials;[26,55] this was proved by the linear plots of current intensities (measured at E = 0.0 V) as a function of scan rates (from ν = 0.5 to

0.06 V s^{-1}) (*i vs.* ν) for both materials, as depicted in Figure 6.13. Both ACs show high capacitive values of similar magnitudes, although SC800 exhibited a higher value, 233.2 μF, compared to 143.3 μF for SH800.

The electrochemical properties of activated carbons were explored in the presence of the redox probes $[Fe(CN)_6]^{3-/4-}$, $[Ru(NH_3)_6]^{3+/2+}$ and $Eu^{3+/2+}$, Figures 6.12 (b), (c) and (d), respectively.

The CVs for $[Ru(NH_3)_6]^{3+/2+}$ using the SC800 and SH800 modified electrodes, Figure 6.12 (c), showed one pair of redox peaks at E_{pc} = -0.20 V / E_{pa} = -0.13 V vs. Ag/AgCl that are assigned to Ru^{3+}/Ru^{2+} electronic transfer; furthermore, the CVs profiles are very similar to that observed when using bare GCE, indicating that the redox probe does not interact significantly with the modified electrodes. The anodic to cathodic peak-to-peak separations (ΔE_p) obtained for both modified electrodes are very similar (ΔE_p = 0.072 V for SC800 and ΔE_p = 0.071 V for SH800 vs. Ag/AgCl), which are in agreement with the insensitivity of the $[Ru(NH_3)_6]^{3+/2+}$ probe to surface defects and oxygen-containing groups.[30]

With the $[Fe(CN)_6]^{3-/4-}$ redox probe (Figure 6.12 (b)), the CVs profiles for both SC800 and SH800 modified electrodes are also similar to the bare GCE, with a cathodic peak at E_{pc} ≈ 0.24 V and an anodic peak at E_{pa} ≈ 0.32 V (Fe^{3+}/Fe^{2+} electron transfer), and with ΔE_p = 0.083 and 0.080 V vs. Ag/AgCl for SC800 and SH800, respectively. The similarity between peak potentials and ΔE_p values for the modified and bare electrodes are also indicative of a non-significant interaction between the redox probe and the modified electrodes surface.

The CV of $Eu^{3+/2+}$ probe using the bare GCE, Figure 6.12 (d), showed the electrochemical process associated with Eu^{3+}/Eu^{2+} electron transfer, with E_{pc} = -0.67 V and E_{pa} = -0.50 V and ΔE_p = 0.172 V vs. Ag/AgCl. In the CVs of activated carbons-modified electrodes it is also possible to observe the redox processe due to Eu^{3+}/Eu^{2+}, but the peak potentials are shifted: E_{pc} values are shifted to less negative potentials whereas the E_{pa} values are shifted to more negative potentials (E_{pc} = -0.64 V / E_{pa} = -0.54 V for SC800 and E_{pc} = -0.63 V / E_{pa} = -0.55 V for SH800 vs. Ag/AgCl). These variations are reflected in a decrease in ΔE_p values, compared to the GCE: ΔE_p = 0.097 V for SC800 and ΔE_p = 0.080 V for SH800 vs. Ag/AgCl. These results indicate a different interaction of the redox probe with each modified electrode through the oxygen groups, since the probe can, in this case, bind directly to the carbon-oxygen groups.[30] Thus, in the CV of redox probe using bare GCE the electrochemical process due to Eu^{3+}/Eu^{2+} is dominated by the europium species in solution. On the other hand, in CVs of the redox probe using the activated carbons-modified electrodes, the

observed electrochemical process due to Eu^{3+}/Eu^{2+} may also has contributions from the europium species attached to the oxygen groups in carbon materials. Although the activated carbons showed similar surface oxygen content (O% from XPS), the material SH800 has a higher bulk oxygen content associated with a higher surface area and well developed porosity. In this context, the lower ΔE_p value compared to SC800-modified electrode is compatible with a higher % of adsorbed Eu^{3+}/Eu^{2+} due to the highest bulk oxygen content.

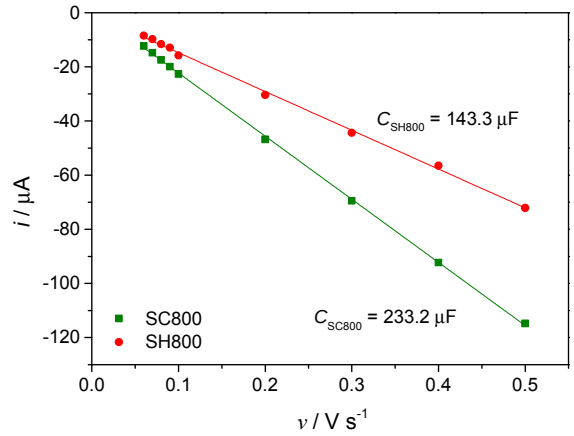

Figure 6.13 Plots of *i* vs. v for SC800 and SH800, with indication of the respective slope / capacity, *C*, values.

In the experimental timescale employed (scan rates in the range 0.01 to 0.5 V s^{-1}) both E_{pc} and E_{pa} varied less than 0.010 V for $[Fe(CN)_6]^{3-/4-}$, 0.010 V (SC800) and 0.005 V (SH800) for $[Ru(NH_3)_6]^{3+/2+}$ and 0.030 V (SC800) and 0.009 (SH800) for $Eu^{2+}/^{3+}$ vs. Ag/AgCl. Figure 6.14 shows the plots of log i_p versus log v for bare GCE and SC800 and SH800 modified electrodes. All plots have slopes around 0.50, indicating predominantly diffusion-controlled processes.[43] In addition, the ratios i_{pa}/i_{pc} are close to one in all cases (see Table 6.3).

The electroactive surface areas of bare GCE and SC800 and SH800 modified electrodes were determined from CVs of 1 x 10^{-3} mol dm^{-3} $K_3[Fe(CN)_6]$, $[Ru(NH_3)_6]Cl_3$ and $EuCl_3.6H_2O$ in KCl 1.0 mol dm^{-3} (Figures 6.15 and 6.16), using the Equation (6.2); the A values are summarised in Table 6.4.

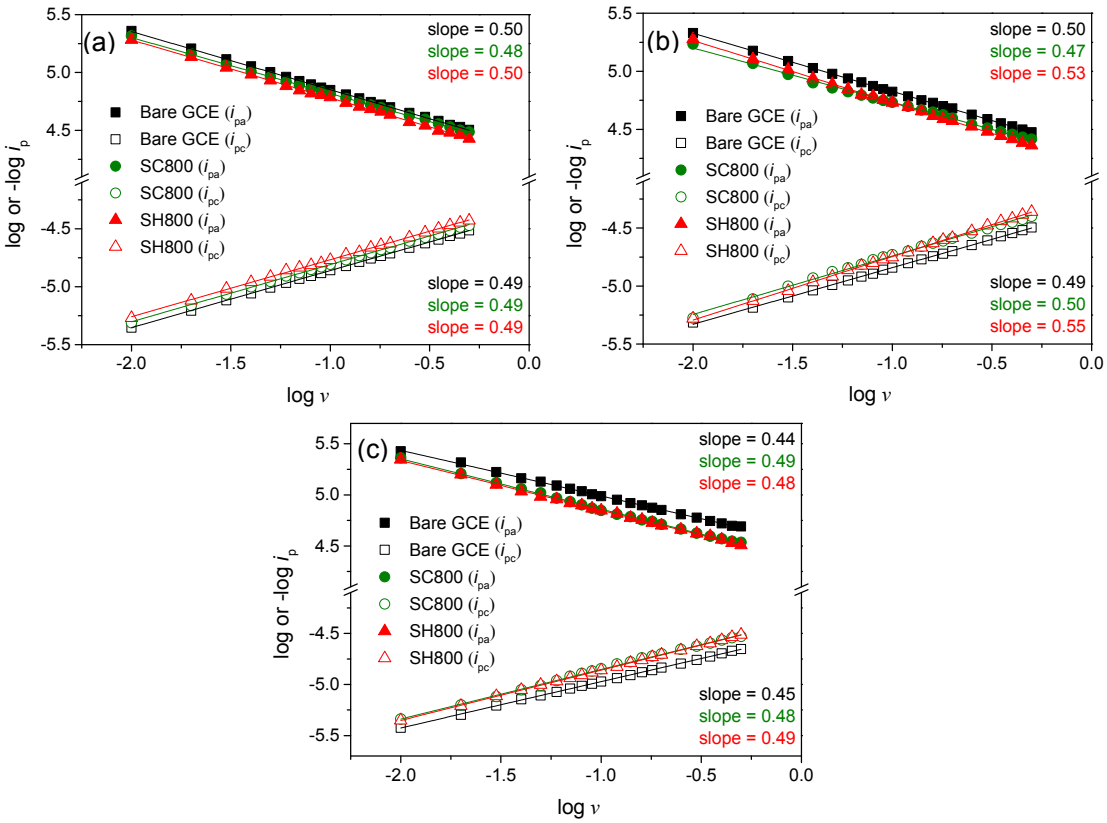

Figure 6.14 Plots of log i_{pc} and i_{pa} vs. log v of bare GCE, SC800 and SH800 modified electrodes in: (a) $[Fe(CN)_6]^{3-/4-}$, (b) $[Ru(NH_3)_6]^{3+/2+}$ and (c) $Eu^{2+}/^{3+}$ solutions 1.0x10^{-3} mol dm^{-3} in KCl 1.0 mol dm^{-3}; log values were obtained using i_{pc} and i_{pa} in A and v in V s^{-1}.

For all probes, the electroactive areas determined for SC800 and SH800 are larger than for bare electrode, indicating that the modification with these materials provides a more conductive pathway for the electron transfer of tested probes.

Table 6.3 ΔE_p and i_{pa}/i_{pc} ratios determined from Figures 6.15 and 6.16.

Sample	$[Fe(CN)_6]^{3-/4-}$		$Ru(NH_3)_6]^{3+/2+}$		$Eu^{2+}/^{3+}$	
	ΔE_p	i_{pa}/i_{pc}	ΔE_p	i_{pa}/i_{pc}	ΔE_p	i_{pa}/i_{pc}
Bare GCE	0.081[a,b]	1.02 (± 0.01)	0.076[a,b]	1.04 (± 0.02)	0.133[a] 0.284[b]	0.96 (± 0.01)
SC800	0.071[a] 0.090[b]	0.96 (± 0.07)	0.071[a] 0.076[b]	1.01 (± 0.04)	0.075[a] 0.128[b]	0.98 (± 0.01)
SH800	0.066[a] 0.081[b]	0.97 (± 0.02)	0.071[a,b]	1.03 (± 0.02)	0.076[a] 0.085[b]	1.02 (± 0.01)

[a] at 0.01 V s^{-1}

[b] at 0.5 V s^{-1}

The areas determined using the $[Fe(CN)_6]^{3-/4-}$ and $[Ru(NH_3)_6]^{3+/2+}$ probes are very similar for each modified electrode and, even, identical between the SC800 and SH800 materials. With the $Eu^{2+}/^{3+}$ probe, the areas determined for activated carbon materials remain very similar between them, but are smaller than the areas calculated with the other two probes.

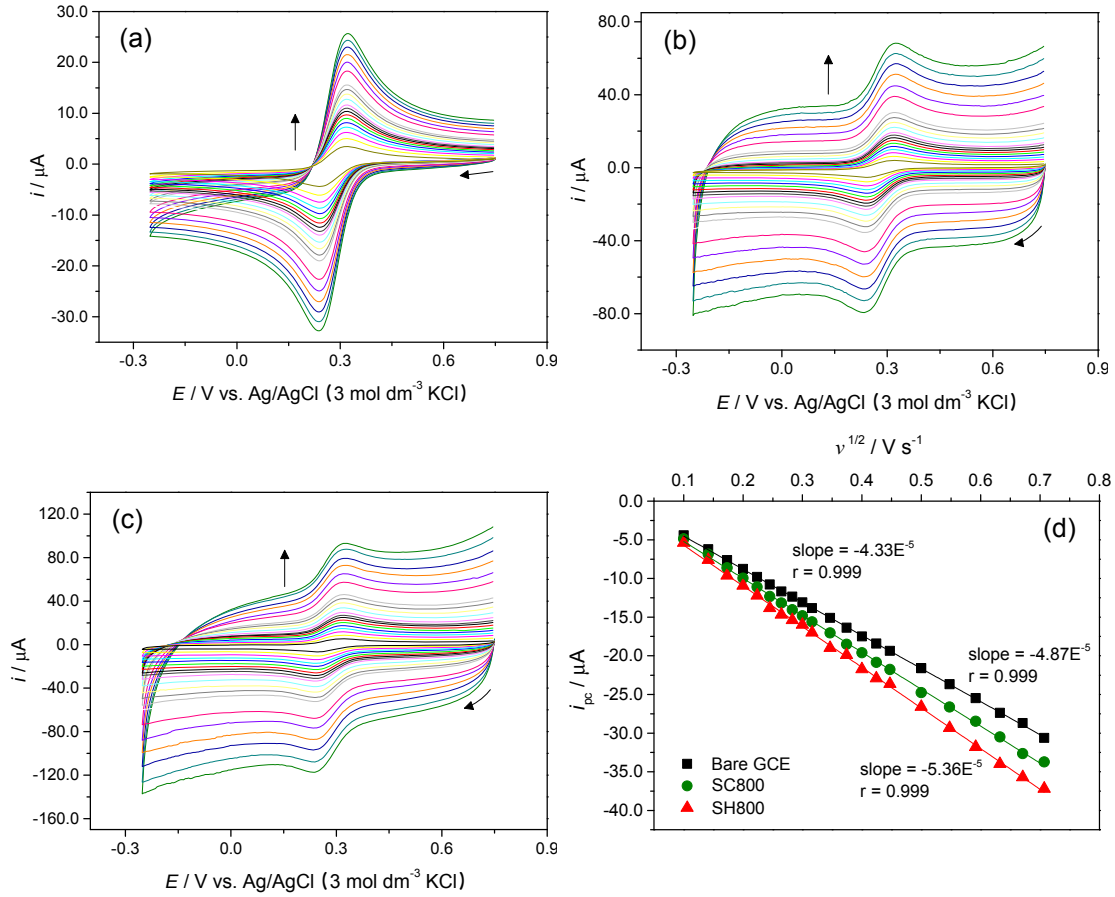

Figure 6.15 CVs of $[Fe(CN)_6]^{3-/4-}$ (1.0 mmol dm^{-3} in KCl 1.0 mol dm^{-3}) at (a) bare GCE, (b) SC800 and (c) SH800 modified electrodes at several scan rates (0.010 – 0.500 V s^{-1}) and (d) respective plots of i_{pa} vs. v$^{1/2}$.

The HET rate constants, k_{HET}, were determined through Equation (6.3) for SC800 and SH800 modified electrodes for all redox probes solutions. The higher k_{HET} values were obtained for $[Ru(NH_3)_6]^{3+/2+}$, k_{HET} = 1.23 x 10^{-2} cm^2 s^{-1}, for both modified electrodes, reflecting the lowest ΔE_p values. For $[Fe(CN)_6]^{3-/4-}$, k_{HET} are similar for both modified electrodes, k_{HET} = 6.20 x 10^{-3} and 6.82 x 10^{-3} cm^2 s^{-1} for SC800 and SH800 modified electrodes, respectively. In the case of $Eu^{2+}/^{3+}$ probe, the SC800 modified electrode showed a k_{HET} = 4.72 x 10^{-3} cm^2 s^{-1}, which is different from that of SH800 (k_{HET} = 6.30 x 10^{-3} cm^2 s^{-1}).

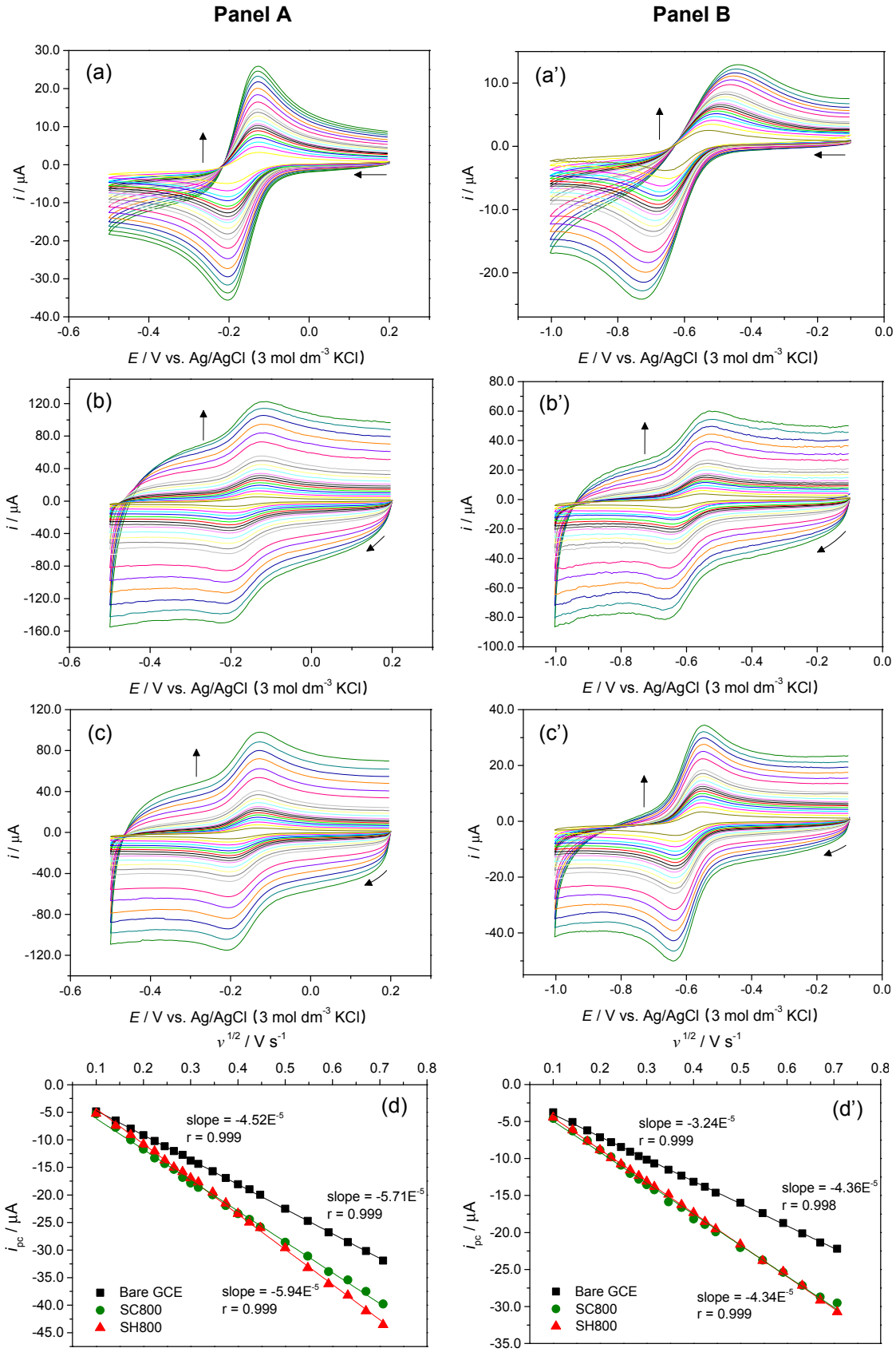

Figure 6.16 CVs of $Ru(NH_3)_6]^{3+/2+}$ (Panel I) and $Eu^{3+/2+}$ (Panel II) (1.0 mmol dm^{-3} in KCl 1.0 mol dm^{-3}) at (a) and (a') bare GCE, (b) and (b') SC800 and (c) and (c') SH800 modified electrodes at several scan rates (0.010 – 0.500 V s^{-1}) and (d) and (d') respective plots of i_{pa} vs. $v^{1/2}$.

Table 6.4 Electroactive surface areas (A / cm^2) determined using the Randles-Sevcik equation.

Sample	$[Fe(CN)_6]^{3-/4-}$	$Ru(NH_3)_6]^{3+/2+}$	$Eu^{2+}/^{3+}$
GCE	0.0679 (± 0.0017)	0.0678 (± 0.0004)	0.0447 (± 0.0015)
SC800	0.0776 (± 0.0054)	0.0848 (± 0.0009)	0.0597 (± 0.0010)
SH800	0.0807 (± 0.0013)	0.0840 (± 0.0047)	0.0601 (± 0.0022)

6.4 Conclusions

The SC800 and SH800 activated carbons derived from sucrose were characterised by XPS, revealing that both have similar surface C% and O%, although SH800 showed higher oxygen bulk contents. The ACs showed different textural properties: SH800 revealed a higher specific surface area (A_{BET} ≈ 2500 m^2 g^{-1}), larger micropores (widths between 0.7 and 2 nm) and sponge-like morphology, whereas SC800 showed spherical shape, A_{BET} ≈ 1400 m^2 g^{-1} and narrow micropores with pore width < 0.7 nm.

Both activated carbons showed ORR electrocatalytic activity in alkaline medium, with similar onset potentials (E_{onset} ≈ -0.20 V vs. Ag/AgCl) but higher current densities were obtained for SH800, which was explained by its more well-developed porosity and higher surface area. Both electrocatalysts revealed excellent tolerance to methanol, with SH800 presenting inclusive, greater long-term electrochemical stability than the state-of-the-art Pt/C electrocatalyst. The sucrose-derived activated carbons also showed ORR catalytic activity in acidic medium, although with modest ORR performances, but making them promising for applications in proton exchange fuel cells.

All of these results, allied with the fact of both electrocatalysts are made from a renewable biomass, highlight the potential of these porous activated carbons (mainly SH800, due to its superior stability in alkaline medium) towards electrocatalysis for energy conversion. Moreover, although the 4-electrons mechanism (selectivity to H_2O) is known to be favourable for ORR in order to have higher efficiencies, a process with H_2O_2 selectivity (2-electrons mechanism), can also be useful for the co-generation of hydrogen peroxide and electricity under the same electrochemical reaction conditions; consequently, the sustainable approach used offers a versatile protocol for carbon-based electrocatalysts application.

References

[1] Wang, D. W.; Su, D. S. *Energy Environ. Sci.* **2014**, *7*, 576.

[2] Trogadas, P.; Fuller, T. F.; Strasser, P. *Carbon* **2014**, *75*, 5.

[3] Chen, Y.; Zhai, S. R.; Liu, N.; Song, Y.; An, Q. D.; Song, X. W. *Bioresour. Technol.* **2013**, *144*, 401.

[4] Song, M. Y.; Park, H. Y.; Yang, D. S.; Bhattacharjya, D.; Yu, J. S. *ChemSusChem* **2014**, *7*, 1755.

[5] Li, J. P.; Wang, S. G.; Ren, Y. Q.; Ren, Z. H.; Qiu, Y. J.; Yu, J. *Electrochim. Acta* **2014**, *149*, 56.

[6] Chen, P.; Wang, L. K.; Wang, G.; Gao, M. R.; Ge, J.; Yuan, W. J.; Shen, Y. H.; Xie, A. J.; Yu, S. H. *Energy Environ. Sci.* **2014**, *7*, 4095.

[7] Si, W. J.; Zhou, J.; Zhang, S. M.; Li, S. J.; Xing, W.; Zhuo, S. P. *Electrochim. Acta* **2013**, *107*, 397.

[8] Zhang, H. M.; Wang, Y.; Wang, D.; Li, Y. B.; Liu, X. L.; Liu, P. R.; Yang, H. G.; An, T. C.; Tang, Z. Y.; Zhao, H. J. *Small* **2014**, *10*, 3371.

[9] Gao, S. Y.; Fan, H.; Zhang, S. X. *J. Mater. Chem. A* **2014**, *2*, 18263.

[10] Jung, A.; Han, S.; Kim, T.; Cho, W. J.; Lee, K. H. *Carbon* **2013**, *60*, 307.

[11] Mestre, A. S.; Tyszko, E.; Andrade, M. A.; Galhetas, M.; Freire, C.; Carvalho, A. P. *RSC Adv.* **2015**, *5*, 19696.

[12] Zhang, H. J.; Li, H. L.; Deng, C. C.; Zhao, B.; Yang, J. H. *ECS Electrochem. Lett.* **2015**, *4*, 5.

[13] Wohlgemuth, S. A.; White, R. J.; Willinger, M. G.; Titirici, M. M.; Antonietti, M. *Green Chem.* **2012**, *14*, 1515.

[14] Brun, N.; Wohlgemuth, S. A.; Osiceanu, P.; Titirici, M. M. *Green Chem.* **2013**, *15*, 2514.

[15] Wohlgemuth, S. A.; Fellinger, T. P.; Jaker, P.; Antonietti, M. *J. Mater. Chem. A* **2013**, *1*, 4002.

[16] Rybarczyk, M. K.; Lieder, M.; Jablonska, M. *RSC Adv.* **2015**, *5*, 44969.

[17] Yuan, H. R.; Deng, L. F.; Cai, X. X.; Zhou, S. G.; Chen, Y.; Yuan, Y. *RSC Adv.* **2015**, *5*, 56121.

[18] Iwazaki, T.; Obinata, R.; Sugimoto, W.; Takasu, Y. *Electrochem. Commun.* **2009**, *11*, 376.

[19] Iwazaki, T.; Yang, H. S.; Obinata, R.; Sugimoto, W.; Takasu, Y. *J. Power Sources* **2010**, *195*, 5840.

[20] Wang, K. L.; Wang, H.; Ji, S.; Feng, H. Q.; Linkov, V.; Wang, R. F. *RSC Adv.* **2013**, *3*, 12039.

[21] Guo, C. Z.; Liao, W. L.; Li, Z. B.; Chen, C. G. *Carbon* **2015**, *85*, 279.

[22] Zhang, J.; Wu, S. Y.; Chen, X.; Cheng, K.; Pan, M.; Mu, S. C. *RSC Adv.* **2014**, *4*, 32811.

[23] Zhang, Z.; Li, H.; Yang, Y. X.; Key, J. L.; Ji, S.; Ma, Y. Y.; Wang, H.; Wang, R. F. *RSC Adv.* **2015**, *5*, 27112.

[24] Zhang, H. M.; Chen, J. Y.; Li, Y. B.; Liu, P. R.; Wang, Y.; An, T. C.; Zhao, H. J. *Electrochim. Acta* **2015**, *165*, 7.

[25] Liu, X. J.; Zhou, Y. C.; Zhou, W. J.; Li, L. G.; Huang, S. B.; Chen, S. W. *Nanoscale* **2015**, *7*, 6136.

[26] Liu, F. F.; Peng, H. L.; You, C. H.; Fu, Z. Y.; Huang, P. Y.; Song, H. Y.; Liao, S. J. *Electrochim. Acta* **2014**, *138*, 353.

[27] Mestre, A. S.; Freire, C.; Pires, J.; Carvalho, A. P.; Pinto, M. L. *J. Mater. Chem. A* **2014**, *2*, 15337.

[28] Wong, C. H. A.; Sofer, Z.; Pumera, M. *Chem.-Eur. J.* **2015**, *21*, 8435.

[29] Moo, J. G. S.; Ambrosi, A.; Bonanni, A.; Pumera, M. *Chem.-Asian J.* **2012**, *7*, 759.

[30] Tan, S. M.; Ambrosi, A.; Chua, C. K.; Pumera, M. *J. Mater. Chem. A* **2014**, *2*, 10668.

[31] Lim, C. S.; Hola, K.; Ambrosi, A.; Zboril, R.; Pumera, M. *Electrochem. Commun.* **2015**, *52*, 75.

[32] Di Noto, V.; Negro, E.; Gliubizzi, R.; Gross, S.; Maccato, C.; Pace, G. *J. Electrochem. Soc.* **2007**, *154*, B745.

[33] Di Noto, V.; Negro, E.; Vezzu, K.; Toniolo, L.; Pace, G. *Electrochim. Acta* **2011**, *57*, 257.

[34] Di Noto, V.; Negro, E.; Polizzi, S.; Vezzu, K.; Toniolo, L.; Cavinato, G. *Int. J. Hydrog. Energy* **2014**, *39*, 2812.

[35] Daems, N.; Sheng, X.; Vankelecom, I. F. J.; Pescarmona, P. P. *J. Mater. Chem. A* **2014**, *2*, 4085.

[36] Hoang, S.; Guo, S. W.; Hahn, N. T.; Bard, A. J.; Mullins, C. B. *Nano Lett.* **2012**, *12*, 26.

[37] Tuci, G.; Zafferoni, C.; Rossin, A.; Milella, A.; Luconi, L.; Innocenti, M.; Phuoc, L. T.; Cuong, D. V.; Cuong, P. H.; Giambastian, G. *Chem. Mat.* **2014**, *26*, 3460.

[38] Mani, A.; Birss, V. I. *J. Electroanal. Chem.* **2012**, *687*, 102.

[39] Negro, E.; Vezzu, K.; Bertasi, F.; Schiavuta, P.; Toniolo, L.; Polizzi, S.; Di Noto, V. *ChemElectroChem* **2014**, *1*, 1359.

[40] Fernandes, D. M.; Costa, M.; Pereira, C.; Bachiller-Baeza, B.; Rodriguez-Ramos, I.; Guerrero-Ruiz, A.; Freire, C. *J. Colloid Interface Sci.* **2014**, *432*, 207.

[41] Keeley, G. P.; O'Neill, A.; McEvoy, N.; Peltekis, N.; Coleman, J. N.; Duesberg, G. S. *J. Mater. Chem.* **2010**, *20*, 7864.

[42] Henstridge, M. C.; Laborda, E.; Wang, Y. J.; Suwatchara, D.; Rees, N.; Molina, A.; Martinez-Ortiz, F.; Compton, R. G. *J. Electroanal. Chem.* **2012**, *672*, 45.

[43] Bard, A. J.; Faulkner, L. R. *Electrochemical Methods, Fundamentals and Applications*, **2001**.

[44] Nicholson, R. S. *Anal. Chem.* **1965**, *37*, 1351.

[45] Ambrosi, A.; Pumera, M. *Chem.-Eur. J.* **2013**, *19*, 4748.

[46] Thommes, M.; Kaneko, K.; Neimark, A. V.; Olivier, J. P.; Rodriguez-Reinoso, F.; Roquerol, J.; Sing, K. S. W. *Pure Appl. Chem.* **2015**, *87*, 1051.

[47] Pinto, M. L.; Mestre, A. S.; Carvalho, A. P.; Pires, J. *Ind. Eng. Chem. Res.* **2010**, *49*, 4726.

[48] Wu, X. L.; Chen, L. L.; Xin, S.; Yin, Y. X.; Guo, Y. G.; Kong, Q. S.; Xia, Y. Z. *ChemSusChem* **2010**, *3*, 703.

[49] Lipinska, M. E.; Rebelo, S. L. H.; Pereira, M. F. R.; Gomes, J.; Freire, C.; Figueiredo, J. L. *Carbon* **2012**, *50*, 3280.

[50] Zhang, Y. J.; Fugane, K.; Mori, T.; Niu, L.; Ye, J. H. *J. Mater. Chem.* **2012**, *22*, 6575.

[51] Deng, D. H.; Yu, L.; Pan, X. L.; Wang, S.; Chen, X. Q.; Hu, P.; Sun, L. X.; Bao, X. H. *Chem. Commun.* **2011**, *47*, 10016.

[52] Wang, S.; Dong, S. M.; Wang, J.; Zhang, L. X.; Han, P. X.; Zhang, C. J.; Wang, X. G.; Zhang, K. J.; Lan, Z. G.; Cui, G. L. *J. Mater. Chem.* **2012**, *22*, 21051.

[53] Zhang, M. N.; Yan, Y. M.; Gong, K. P.; Mao, L. Q.; Guo, Z. X.; Chen, Y. *Langmuir* **2004**, *20*, 8781.

[54] Lu, G. L.; Yang, H. S.; Zhu, Y. L.; Huggins, T.; Ren, Z. J.; Liu, Z. N.; Zhang, W. *J. Mater. Chem. A* **2015**, *3*, 4954.

[55] Ambrosi, A.; Poh, H. L.; Wang, L.; Sofer, Z.; Pumera, M. *ChemSusChem* **2014**, *7*, 1102.

Chapter 7

Phosphomolybdate@carbon-based nanocomposites as electrocatalysts for oxygen reduction

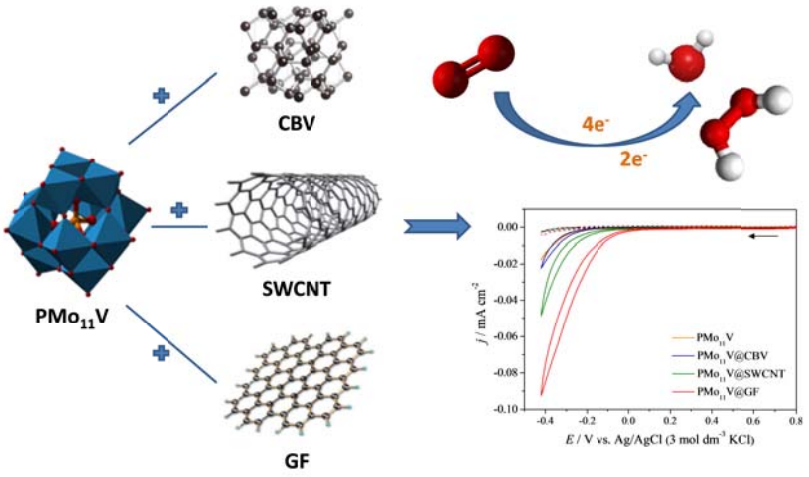

7

Phosphomolybdate@carbon-based nanocomposites as electrocatalysts for oxygen reduction[1,2,3]

Abstract

In this chapter it is described the application of several nanocomposites, prepared by the incorporation of a vanadium-substituted phosphomolybdate $[PMo_{11}VO_{40}]^{4-}$ ($PMo_{11}V$) into the carbon materials carbon black Vulcan (CBV), single-walled carbon nanotubes (SWCNT) and graphene (GF)), as ORR electrocatalysts. The nanocomposites, denominated as $PMo_{11}V$@CBV, $PMo_{11}V$@SWCNT and $PMo_{11}V$@GF, show electrocatalytic activity for the ORR, with a strong dependency between the electrocatalytic ORR performance and the carbon-based material employed. Among the materials studied, the $PMo_{11}V$@GF nanocomposite exhibits the most promising performance, having the less negative onset potential (E_{onset} = -0.16 V vs. Ag/AgCl), which is explained by the excellent electronic properties of GF. An ORR process based in a 2-electron mechanism is assumed for all modified electrodes.

The $PMo_{11}V$- and the nanocomposite-modified electrodes also are effective for the reduction of hydrogen peroxide, with $PMo_{11}V$@GF displaying the most promising electrocatalytic performance.

The successful preparation of the nanocomposites is confirmed by X-ray photoelectron spectroscopy and Fourier transformed infrared spectroscopy techniques. The electrochemical characterisation of all modified electrodes is also reported.

---

[1] Adapted from: M. Nunes, D. M. Fernandes, I. M. Rocha, M. F. R. Pereira, I.-M. Mbomekalle, P. de Oliveira, C. Freire, Phosphomolybdate@carbon-based nanocomposites as electrocatalysts for oxygen reduction. Submitted.

[2] M. Nunes's contribution to the publication: preparation and characterisation of the $PMo_{11}V$@CBV composite, electrochemical characterisations and evaluation of the ORR electrocatalytic activities of all composites and manuscript preparation.

[3] The experimental details on the electrochemical / electrocatalytic and remaining characterisation techniques are indicated in Appendices B and C, respectively.

7.1 Introduction

Carbon-based materials have been applied as ORR electrocatalysts as metal-free electrocatalysts themselves and also as catalyst supports in functional composites. As catalyst supports, carbon black (CB) is the most commonly used due to its low cost, being employed in the preparation of composites with conducting polymers,[1,2] Pt-based alloys[3] and non-noble metals.[4] CNTs and GF supports, although more expensive than CB, normally result in an improved catalyst performance. An electrocatalyst with high ORR activity based on the dispersion of silver nanoparticles on multi-walled carbon nanotubes (MWCNTs) was reported by Cheng *et al.*,[5] and several GF-based composites have also been prepared[6] through the immobilisation of metals (e.g. Pt),[7] metal oxides[8] and metallic complexes.[9] Normally, GF-based composites have an enhanced ORR activity in comparison with the other carbon-based allotropes, mainly due to presence of peculiar graphitic sites that result in a large number of ORR active sites.[10]

The ability of POMs to mediate electron, proton and oxygen atom transfer reactions, makes them particularly interesting as ORR catalysts. In this regard, the ORR electrocatalytic activity of several POMs has been evaluated both in their pristine form[11,12] and as co-catalysts. Mbomekalle and co-workers published several works reporting the application of several pristine POMs (Cu(II)-[11] and Mn(II)-[12] substituted polyoxoanions) as ORR electrocatalysts and promising results were obtained, with significant positive shifts in potentials of oxygen reduction. As co-catalysts, the combination of POMs with a porphyrin[13] and Au,[14] Pd[15] and Pt[16,17] nanoparticles (NPs) was described, resulting in enhanced ORR performances.

Therefore, the incorporation of POMs on carbon materials may be a good approach to obtain functional composites with an enhanced ORR catalytic activity, as result of the improvement of the POM redox properties and of the synergetic influence of the POM and the carbon material on the properties of the nanocomposite. Some POM/carbon material composites have been prepared for applications as chemical sensors,[18] in lithium batteries,[19] as supercapacitors[20] and for water oxidation,[21] but their application for the ORR has still been little explored. Nevertheless, recently was reported the preparation of polyoxotungstates/graphene multilayer films[22] and a polyoxometalate/carbon black nanocomposite[23] with good ORR activity, selectivity towards the 4-electron pathway and better tolerance to methanol crossover and superior durability than the state-of-the-art 20 wt% Pt/C electrocatalyst. Additionally, the preparation of several nanocomposites between Ag NPs and CNTs,[24] GF[25] and reduced graphene oxide,[26] using POMs as reducing agents and bridging molecules

was also reported; the as-prepared nanohybrids showed higher ORR electrocatalytic activities than the non-POM functionalised forms. All these results encourage further studies on this matter.

In this chapter is described the preparation of different nanocomposites, $PMo_{11}V$@carbon material, by the immobilisation of the tetrabutylammonium salt of vanadium-substituted phosphomolybdate $[PMo_{11}VO_{40}]^{4-}$ ($PMo_{11}V$) into some carbon-based materials – carbon black (Vulcan XC72) (CBV), SWCNT and GF. The ORR catalytic activities of the pristine $PMo_{11}V$ and of the several composites were evaluated, in order to study the influence of the carbon support on the global electrocatalytic performance of the nanocomposite. The H_2O_2 reduction reaction was also evaluated using these catalysts.

7.2 Experimental section

7.2.1 Reagents and solvents

The reagents used in the preparation of the polyoxometalate, namely sodium phosphate monobasic dehydrate (Sigma-Aldrich, > 99 %), ammonium metavanadate (Sigma-Aldrich, > 99 %), sodium molybdate (Sigma-Aldrich, > 98 %) and tetra-n-butylammonium bromide (Merck, > 99 %) were used as received. Hydrochloric acid (Merck, 37 %), lithium sulfate monohydrate (Merck, suprapur 99.99 %), sulfuric acid (Merck, 95-97 %), toluene (Aldrich, 99.8 %), acetonitrile (Panreac, 99 %), N,N'-dimethylformamide (DMF, Fisher Scientific, 99.97 %), Nafion (Aldrich, 5 wt% solution in lower aliphatic alcohols and water), H_2O_2 (Aldrich, 30 % in H_2O), carbon black (Vulcan XC72, CAS no. 1333-86-4), SWCNT (Nanoledge, Batch nº P0329 A) and GF (Graphene Technologies, Lot GTX-7/6-10.4.13) were used as received. The 20 wt% Pt/C standard catalyst was prepared by incipient wetness impregnation method. The active metal precursor, $H_2PtCl_6.6H_2O$, dissolved in water, was slowly added to the carbon support, Printex80. The sample was dried in an oven at 373 K for 24 hours. The dried sample was annealed at T = 523 K for 1 h under N_2 and reduced during 3 h under H_2.

7.2.2 Preparation of materials

The tetrabutylammonium (TBA) salt of vanadium phosphomolybdate $[PMo_{11}VO_{40}]^{4-}$ ($PMo_{11}V$) was prepared as in Ref. [27], using a reported procedure.[28]

The $PMo_{11}V$ – carbon black (CBV) composite was prepared through the immobilization of the $PMo_{11}V$ into CBV, using a procedure adapted from a previous report.[27] Briefly, an acetonitrile solution (2.5 mL) of the $PMo_{11}V$ (20 mg) was added to a

toluene dispersion (20 mL) of the CBV (20 mg). The resulting yellowish suspension was vigorously stirred at room temperature for 30 min and then left to rest until it became colourless and a black precipitate formed (suggesting that all of the POM was grafted onto the CBV surface). The excess of solvent was removed and the precipitate was dried in an oven. The nanocomposite obtained was designated as $PMo_{11}V$@CBV and was characterised by XPS and FTIR. The other nanocomposites, $PMo_{11}V$@SWCNT and $PMo_{11}V$@GF, had already been prepared and characterised, as reported in Ref. [27].

7.2.3 Electrochemical characterisation

The electrolyte solutions used in the electrochemical characterisation of the materials were prepared using ultra-pure water (resistivity 18.2 MΩ cm at 25 ºC, Millipore Integral 5). H_2SO_4/Li_2SO_4 buffer solutions with pH values from 1.0 to 3.5 were prepared by mixing appropriate amounts of 0.5 mol dm^{-3} H_2SO_4 and 0.2 mol dm^{-3} $Li_2SO_4.H_2O$ solutions. The studies at several scan rates (from 0.050 to 0.500 V s^{-1}) were performed with a H_2SO_4/Li_2SO_4 buffer solution with a pH of 2.5 in the potential range from 0.8 to ≈ -0.51 V (adjusted according with the sample). The electrochemical potentials were converted from SCE to Ag/AgCl (3 mol dm^{-3} KCl) using the correction factor 0.032 V.[29]

The dispersions used to prepare the modified electrodes were obtained by dissolving $PMo_{11}V$ (1 mg) in acetonitrile (1 mL) or by dispersing $PMo_{11}V$@carbon nanocomposites (1 mg) in DMF (3 mL) with sonication for 10 min.

Prior to modification, the GCE electrode was conditioned by a polishing/cleaning procedure as described elsewhere,[30] which finished with rinsing and sonicating in ethanol (3 min) and ultra-pure water (3 min). The electrode modification consisted in depositing a 3 µL drop of the selected material dispersion onto the GCE surface and the solvent was allowed to evaporate at room temperature.

The electrochemical surface coverages, Γ / nmol cm^{-2}, of the modified electrodes were calculated by the Equation (7.1):[27]

$$\Gamma = (4i_pRT)/(n^2F^2vA) \quad (7.1)$$

where i_p is the peak current (amperes), R is the gas constant, T is the temperature (298 K), n is the number of electrons transferred (2 in this case), F is the Faraday's constant, v is the scan rate (V s^{-1}) and A is the geometric area of the electrode (0.07067 cm^2).

7.2.4 Evaluation of the ORR electrocatalytic activity

The ORR electrocatalytic capability of the materials was, in a first step, evaluated by cyclic voltammetry, at the scan rate of 0.002 V s^{-1}.

In a second stage, the ORR performance of each catalyst was systematically evaluated by CV and linear sweep voltammetry measurements. The electrochemical tests were accomplished in a N_2- or O_2-saturated pH 2.5 H_2SO_4/Li_2SO_4 buffer solution (bubbled for 30 min before the measurements). The modified electrodes were prepared by the deposit of a 3 μL drop of the select dispersion prepared as described above (for Pt/C, 1 mg of 20 wt% Pt/C was dispersed ultrasonically in 3 mL of DMF) on the glassy carbon rotating disk electrode (RDE) surface and dried under an air flux. Then, a 3 μL drop of Nafion (0.5 % in Millipore water) was deposited to protect the sample, which was also dried under an air flux. The obtained electrocatalyst loadings were 14.15 μg cm^{-2} for $PMo_{11}V$, 28.30 μg cm^{-2} for $PMo_{11}V$@CBV, $PMo_{11}V$@SWCNT and $PMo_{11}V$@GF nanocomposites and 70.75 μg cm^{-2} for 20 wt% Pt/C. Prior to modification, the electrode was conditioned by a polishing/cleaning procedure, using diamond pastes of 6, 3 and 1 μm (MetaDi II, Buehler) and aluminium oxide of particle size 0.3 μm (Buehler), on a microcloth polishing pad (BAS Bioanalytical Systems Inc.). Then, the electrode was rinsed and sonicated for 10 min in ultra-pure water. CV experiments were conducted at a scan rate of 0.005 V s^{-1} and LSV experiments at 0.005 V s^{-1} for rotation speeds ranging from 400 to 3000 rpm. The ORR current was obtained by subtracting the current measured in N_2-saturated electrolyte from the current measured in O_2-saturated electrolyte.

The onset potential (E_{onset}) was calculated as described in literature.[31] LSV data was analysed though Koutecky-Levich (K-L) plot, Equations (1.2) and (1.3). Based on the data applying to H_2SO_4/Na_2SO_4 electrolytes,[32] it is assumed for H_2SO_4/Li_2SO_4 buffer medium that C_{O_2}= 1.26x10^{-3} mol dm^{-3}, ν = 0.01 cm^2 s^{-1} and D_{O_2}= 1.77x10^{-5} cm^2 s^{-1}.

The Tafel plots (E vs. log i_k) for oxygen reduction kinetics were obtained after the measured currents in LSV were corrected for diffusion to give the kinetic currents. The mass transport correction was made using the diffusion-limiting current density j_L, calculated by combination of Equations (1.2) and (1.3), since it could not be obtained directly from the LSV. The obtained current density j_k was multiplied by the geometric area of the GCE disk (A = 0.07067 cm^2) yielding i_k, which was normalised for the total deposited mass of $PMo_{11}V$ and nanocomposites electrocatalysts; in the case of Pt/C, i_k was normalised to the Pt mass existing in the amount of Pt/C deposited.[33,34]

7.2.5 Hydrogen peroxide reduction

The electrocatalytic activity of the materials for H_2O_2 reduction was evaluated by cyclic voltammetry, in N_2-saturated pH 2.5 H_2SO_4/Li_2SO_4 buffer solution at 0.050 V s^{-1} using H_2O_2 concentrations of 0.038 and 0.15 mol dm^{-3}.

7.3 Results and discussion

7.3.1 Compositional characterisation of materials

The pristine CBV, used as a reference, and the $PMo_{11}V$@CBV nanocomposite were characterised by XPS and the deconvoluted high-resolution spectra are depicted in Figures 7.1 and 7.2, respectively. The XPS characterisation of $PMo_{11}V$@SWCNT and $PMo_{11}V$@GF and of the respective free carbon materials (SWCNT and GF) was already performed previously.[27]

The C1s high-resolution spectra of the CBV and $PMo_{11}V$@CBV nanocomposite (Figures 7.1 (a) and 7.2 (a)) were deconvoluted with seven peaks: a main peak at 284.6 eV assigned to graphitic carbon (sp^2), a peak at 285.4-285.6 eV attributed to sp^3 hybridised carbon, a peak at 286.3-286.5 eV assigned to C-O, a peak at 287.1-287.5 eV related to C=O, a peak at 288.1-288.6 eV ascribed to –COO groups and a peak at approximately 290.2-290.5 eV characteristic of shake-up satellite of the π-π* transitions;[35,36] a peak at lower binding energies (283.8-283.9 eV) is also observed that may be assigned to a C-Si bond, since Si is detected as a contaminant at very low levels in the CBV matrix.[37]

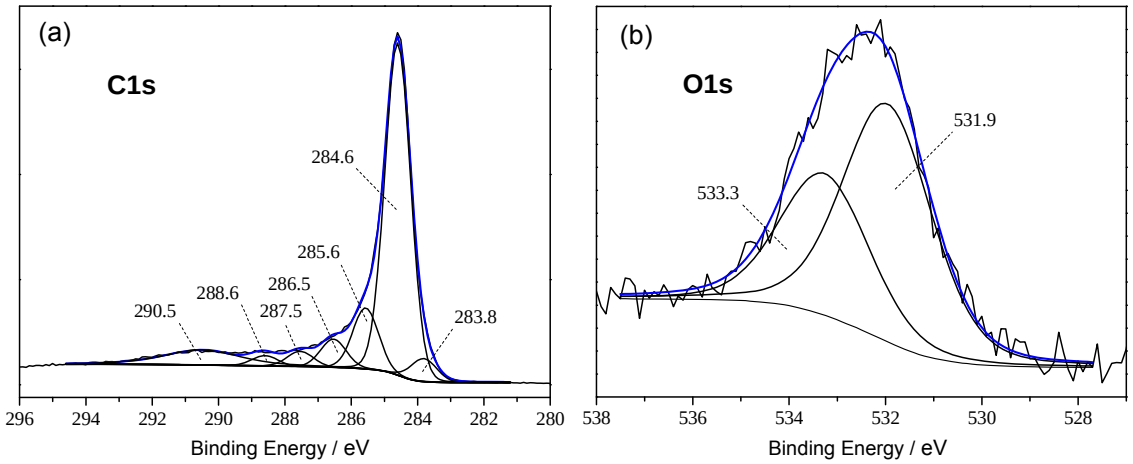

Figure 7.1 High-resolution XPS spectra for CBV in (a) C1s and (b) O1s regions.

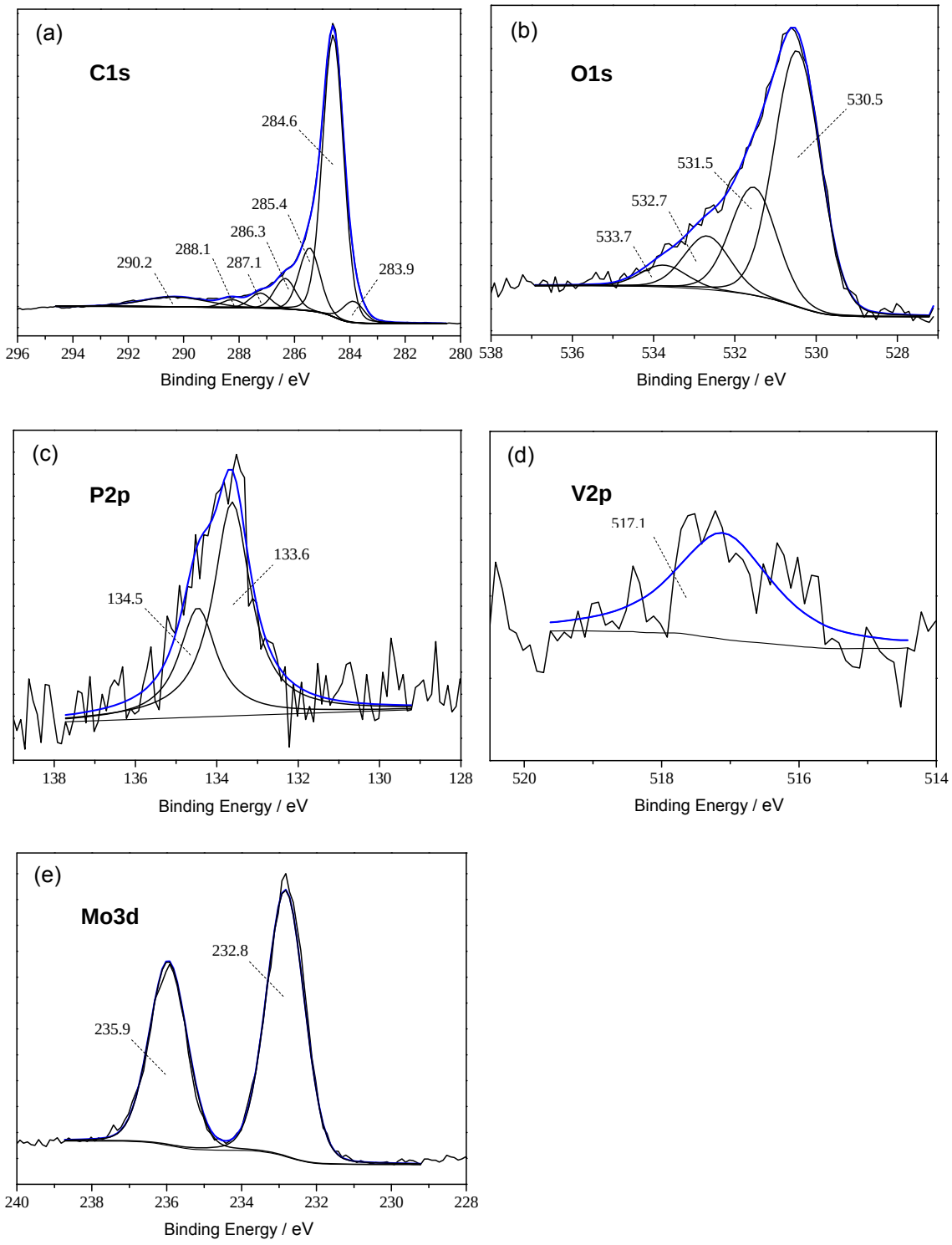

Figure 7.2 High-resolution XPS spectra for $PMo_{11}V$@CBV in (a) C1s, (b) O1s, (c) P2p, (d) V2p and (e) Mo3d regions.

The O1s spectrum of CBV (Figure 7.1 (b)) was fitted with two peaks at 531.9 and 533.3 eV ascribed to O=C (ketone and quinone moieties) and C-O (ether and phenol groups) bonds; both peaks have the contribution of oxygen atoms from carboxylic and esters groups.[36] On the other hand, the O1s spectrum of $PMo_{11}V$@CBV

nanocomposite (Figure 7.2 (b)) was deconvoluted with four peaks at 530.5, 531.5, 532.7 and 533.7 eV; the last two peaks are assigned to CBV, as described above, while the first peak can be attributed to the O-Mo bond and the peak at 531.5 eV to the O-P bond.[27]

For the remaining elements detected in the nanocomposite, in the P2p region (Figure 7.2 (c)) two peaks are observed at 133.6 and 134.5 eV, being attributed to $P2p_{1/2}$ and $P2p_{3/2}$, respectively,[27] in the V2p region (Figure 7.2 (d)) one peak attributed to $V2p_{3/2}$ (517.1 eV) is identified,[27] and the Mo3d spectrum (Figure 7.2 (e)) was fitted with two peaks at 232.8 and 235.9 eV attributed to $Mo3d_{5/2}$ and $Mo3d_{3/2}$, respectively, due to Mo^{6+} in the POM structure.[27]

The XPS surface atomic percentages of the elements detected in the $PMo_{11}V$@CBV nanocomposite and free CBV are summarised in Table 7.1; in the same table are also reported the atomic percentages for $PMo_{11}V$@SWCNT, $PMo_{11}V$@GF and free SWCNT and GF, taken from Ref. [27]. As observed for other nanocomposites, the detection of the elements from each component, CBV (C and O) and $PMo_{11}V$ (O, P, V, Mo and N), confirms the successful preparation of the $PMo_{11}V$@CBV nanocomposite. Furthermore, the surface atomic percentage values suggest a lower amount of $PMo_{11}V$ immobilised in CBV than in other carbon materials (SWCNT and GF) (as revealed by the Mo3d atomic %).

Table 7.1 XPS atomic percentages.

Sample	Atomic %					
	C1s	**O1s**	**P2p**	**V2p**	**Mo3d**	**N1s**
CBV	98.8	1.2	-	-	-	-
$PMo_{11}V$@CBV	93.1	4.7	0.1	0.1	0.8	1.0
SWCNT[a]	99.3	0.7	-	-	-	-
$PMo_{11}V$@SWCNT[a]	95.2	2.2	0.1	0.1	1.8	0.6
GF[a]	98.8	1.2	-	-	-	-
$PMo_{11}V$@GF[a]	96.0	2.3	0.1	0.1	1.2	1.1

[a] Taken from Ref. [27].

The FTIR spectra of pristine CBV and $PMo_{11}V$@CBV nanocomposite are depicted in Figure 7.3. The spectrum of CBV shows very weak and poorly resolved vibrational bands, with absorptions at 1591 cm^{-1} due to C=C stretching vibrations, and at 1251 cm^{-1}, attributed to the stretching of C-O bonds from the oxygen-containing groups on the carbon surface.[38] The FTIR spectrum of $PMo_{11}V$@CBV, besides the

characteristic adsorptions of CBV at 1585 and 1250 cm^{-1}, also shows the typical vibration bands of the polyoxomolybdate: the two bands in the interval 1075-1055 cm^{-1} are assigned to the splitting of the P-O stretching vibration, the band at 948 cm^{-1} is attributed to the Mo-O_d vibration (O terminal) and the bands at 873 and 804 cm^{-1} are due to the Mo-O_b-Mo (octahedral corner-sharing) and the Mo-O_c-Mo (octahedral edge-sharing) bonds, respectively.[28,39] Additionally, the bands observed at 2957-2872 cm^{-1} (C-H stretching vibration) and 1479 cm^{-1} (C-H bending vibration) are characteristic of TBA cations.[27]

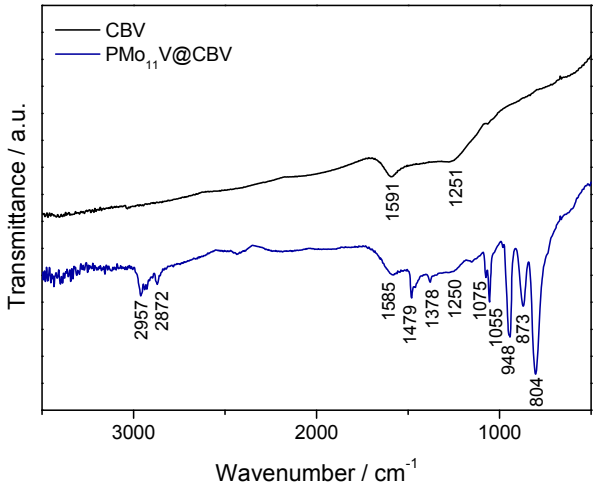

Figure 7.3 Infrared spectra in the range 3500 – 500 cm^{-1} for CBV and $PMo_{11}V$@CBV.

7.3.2 Electrochemical characterisation

The electrochemical behaviour of the free $PMo_{11}V$- and the nanocomposites-($PMo_{11}V$@CBV, $PMo_{11}V$@SWCNT and $PMo_{11}V$@GF) modified electrodes was studied in pH 2.5 H_2SO_4/Li_2SO_4 buffer solution. The cyclic voltammograms obtained at several scan rates, from 0.050 to 0.500 V s^{-1}, are depicted in Figure 7.4 and the voltammetric data are summarised in Table 7.2.

In the potential range explored (from E ≈ 0.8 to ≈ -0.5 V), the $PMo_{11}V$-modified electrode (Figure 7.4 (a)) shows five redox processes at $E_{pc\ V1}$ = 0.308 V, $E_{pc\ Mo1}$ = 0.107 V, $E_{pc\ Mo2}$ = -0.002 V, $E_{pc\ Mo3}$ = -0.222 V and $E_{pc\ Mo4}$ = -0.382 V. The waves Mo_1 to Mo_4 are attributed to molybdenum redox processes ($Mo^{VI} \rightarrow Mo^{V}$) and the waves V_1 are assigned to vanadium redox process ($V^{V} \rightarrow V^{IV}$).[27] The nanocomposite-modified electrodes (Figure 7.4 (b), (c) and (d)) also show five redox processes, as expected of $PMo_{11}V$ (V_1, Mo_1 to Mo_4): 0.304 ≥ E_{pcV1} ≥ 0.316 V, 0.047 ≥ E_{pcMo1} ≥ 0.087 V, -0.034 ≥ E_{pcMo2} ≥ 0.000 V, -0.242 ≥ E_{pcMo3} ≥ -0.212 V and -0.398 ≥ E_{pcMo4} ≥ -0.388 V, assigned to an one-electron redox process of vanadium and four

two-redox processes of molybdenum. In comparison with the $PMo_{11}V$-modified electrode, the peaks observed in the CVs of the nanocomposites exhibited higher current intensities, mainly for $PMo_{11}V$@SWCNT and $PMo_{11}V$@GF, which may be associated with faster electron-transfer kinetics in nanocomposite-modified electrodes due to the favourable electronic properties of carbon matrixes.[27] Furthermore, the peaks observed in the CVs of $PMo_{11}V$@CBV and $PMo_{11}V$@SWCNT are much better resolved than those observed for pristine $PMo_{11}V$; for $PMo_{11}V$@GF the peaks are not so well defined due to the higher capacitive currents detected for this nanocomposite.

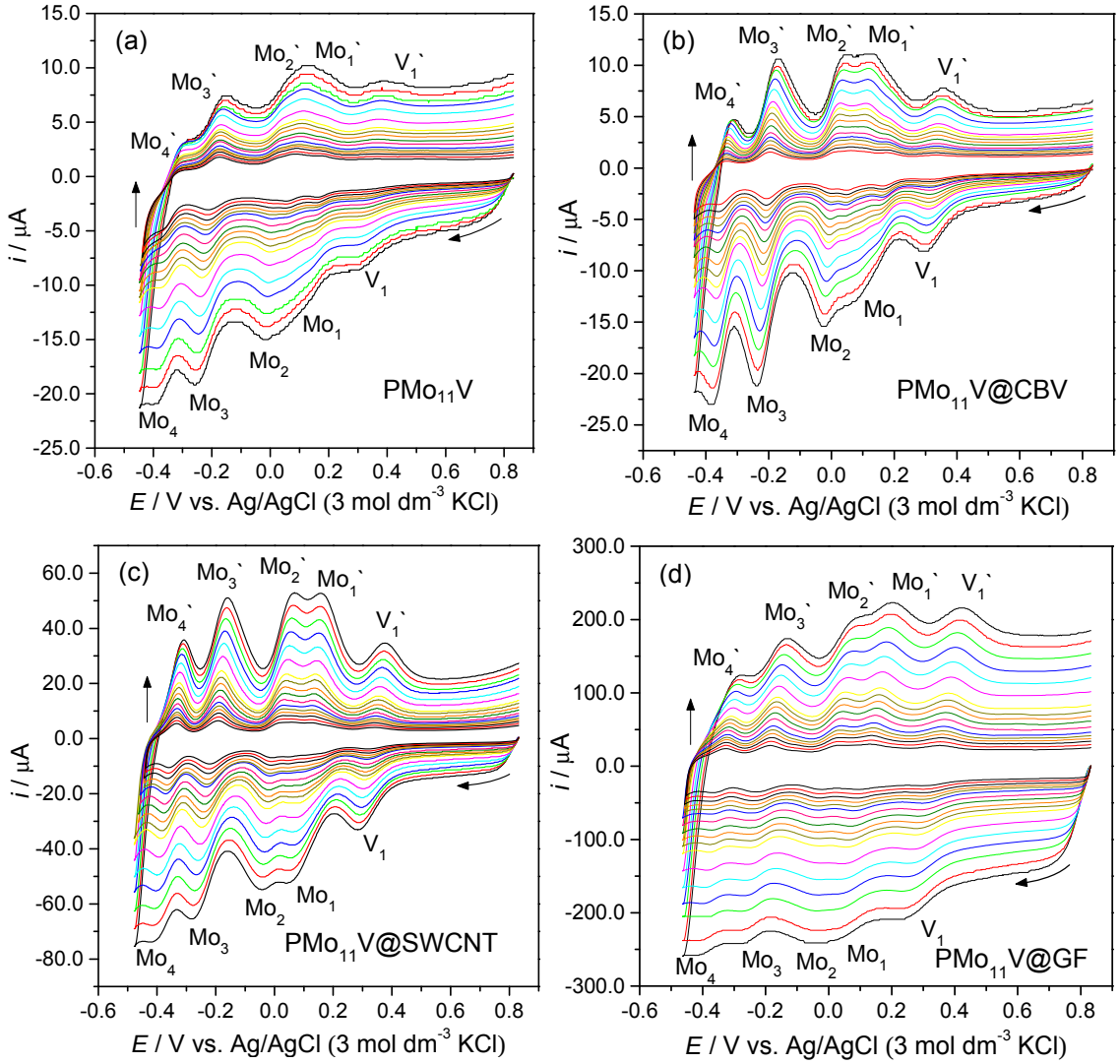

Figure 7.4 CVs of $PMo_{11}V$- and nanocomposites-modified electrodes in pH 2.5 H_2SO_4/Li_2SO_4 buffer solution at scan rates ranging from 0.050 to 0.500 V s^{-1}.

Table 7.2 CV data for free $PMo_{11}V$ and $PMo_{11}V$-based nanocomposites in pH 2.5 H_2SO_4/Li_2SO_4 buffer solution at 0.1 V s^{-1} (potential values in V vs. Ag/AgCl).

Sample	Peak[a]	E_{pc}	E_{pa}	$\lvert\Delta E_p\rvert$	$E_{1/2}$[b]	i_{pa}/i_{pc}
$PMo_{11}V$	V_1[c]	0.308	0.374	0.066	0.341	-
	Mo_2	0.002	0.118	0.116	0.060	1.06
	Mo_3	-0.222	-0.170	0.052	-0.196	0.99
$PMo_{11}V$@CBV	V_1	0.316	0.332	0.016	0.324	0.72
	Mo_2	0.000	0.022	0.022	0.011	0.96
	Mo_3	-0.212	-0.194	0.018	-0.203	0.81
$PMo_{11}V$@SWCNTs	V_1	0.316	0.342	0.026	0.329	0.89
	Mo_2	-0.018	0.030	0.048	0.006	1.08
	Mo_3	-0.230	-0.188	0.042	-0.209	1.10
$PMo_{11}V$@GF	V_1	0.304	0.368	0.064	0.336	1.08
	Mo_2[c]	-0.034	0.046	0.080	0.006	-
	Mo_3[c]	-0.242	-0.174	0.068	-0.208	-

[a] Peaks Mo_1 and Mo_4 were omitted due to the dificulty of establishing a proper baseline, which made i_p measurements difficult.

[b] $E_{1/2} = E^{o'} = 0.5(E_{pa}+E_{pc})$

[c] Some uncertainty in establishing the baseline, whereby the i_{pa}/i_{pc} values are not considered.

On the experimental timescale employed (scan rates in the range 0.050 to 0.500 V s^{-1}), both cathodic (E_{pc}) and anodic (E_{pa}) peak potentials varied less than 0.046 V for $PMo_{11}V$, 0.036 V for $PMo_{11}V$@CBV, 0.054 V for $PMo_{11}V$@SWCNT and 0.068 V for $PMo_{11}V$@GF. In Figure 7.5 are depicted the plots of log i_p vs. log ν for peaks V_1 and Mo_2 of all modified electrodes. For $PMo_{11}V$-, $PMo_{11}V$@CBV- and $PMo_{11}V$@SWCNT-modified electrodes, both cathodic and anodic peaks are directly proportional to the scan rate (slopes between 0.72 and 1.14, with r^2 = 0.971 - 0.998), indicative of surface-confined processes;[27] however, for $PMo_{11}V$@GF, the slopes are between 0.59 and 0.82, with r^2 = 0.961 - 0.995. This might be the result of a less accurate peak current measurement due to the high capacitive currents that render more difficult the establishment of a proper baseline. In addition, the anodic/cathodic peak-to-peak separations (ΔE_p) are comprised between 0.016 and 0.116 V and the ratios i_{pa}/i_{pc} are close to unity.

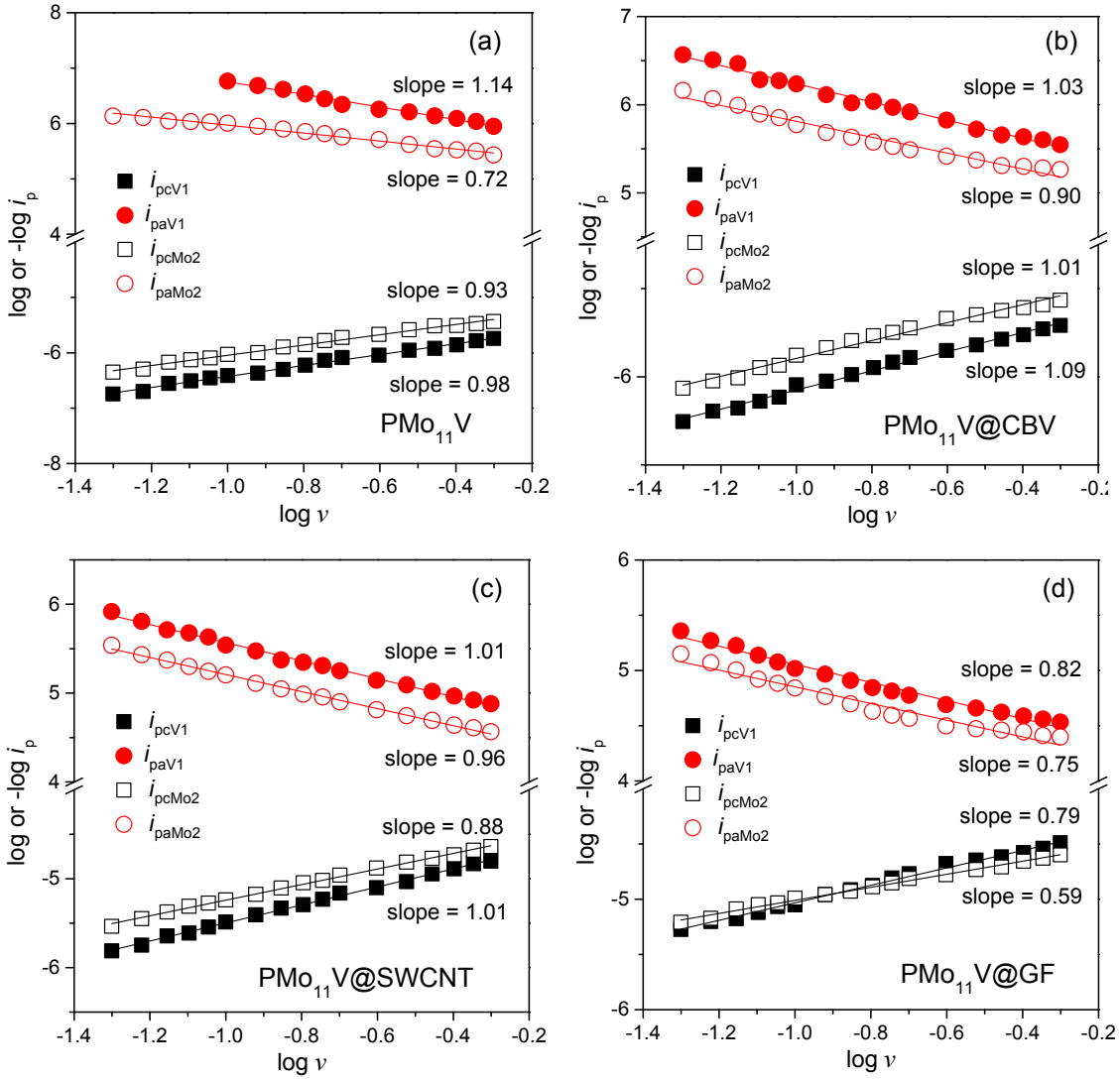

Figure 7.5 Plots of log i_{pc} and i_{pa} vs. log v for (a) $PMo_{11}V$, (b) $PMo_{11}V$@CBV, (c) $PMo_{11}V$@SWCNT and (d) $PMo_{11}V$@GF; log values were obtained using i_{pc} and i_{pa} in A and v in V s^{-1}.

The electrochemical surface coverages, Γ / nmol cm^{-2}, of all modified electrodes were calculated from CV data using the Mo_2 reduction process, according to the Equation (7.1) and the obtained values are summarised in Table 7.3. The Γ values obtained for the nanocomposite-modified electrodes are significantly higher than that obtained for $PMo_{11}V$ (Γ = 0.0329 nmol cm^{-2}), in particular for the $PMo_{11}V$@SWCNT (Γ = 0.2043 nmol cm^{-2}) and the $PMo_{11}V$@GF (Γ = 0.3152 nmol cm^{-2}) nanocomposites. The results indicate that the carbon materials, mainly the nanostructured SWCNT and GF, allow the immobilisation of a larger quantity of the electroactive $PMo_{11}V$ on the electrode surface and simultaneously improve the electrochemical responses, clearly revealing the advantage of the electrode modification with $PMo_{11}V$/carbon-based materials nanocomposites.

Table 7.3 Electrochemical surface coverages, Γ / nmol cm^{-2}, of $PMo_{11}V$- and nanocomposites-modified electrodes.

Sample	Γ / nmol cm^{-2}
$PMo_{11}V$	0.0329
$PMo_{11}V$@CBV	0.0617
$PMo_{11}V$@SWCNT	0.2043
$PMo_{11}V$@GF	0.3152

The influence of the pH of the supporting electrolyte solution on the electrochemical response of $PMo_{11}V$- and nanocomposite-modified electrodes was also studied. In Figure 7.6 (a) and (b) are depicted the CVs obtained at 0.050 V s^{-1}, in H_2SO_4/Li_2SO_4 buffer solution (pH between 1.0 and 3.5), for $PMo_{11}V$ and $PMo_{11}V$@CBV.

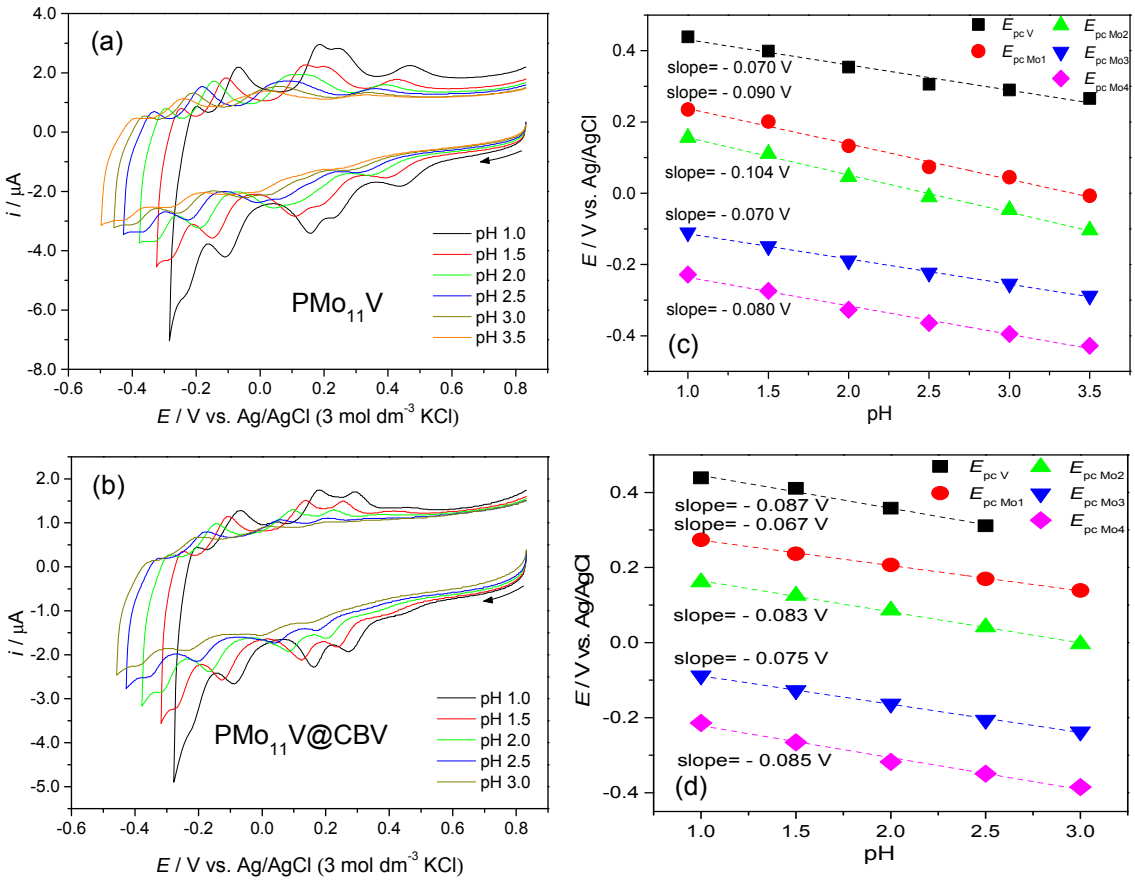

Figure 7.6 CVs of (a) $PMo_{11}V$ and (b) $PMo_{11}V$@CBV in H_2SO_4/Li_2SO_4 buffer solutions with pH values from 1.0 to 3.5 (or 3.0) at 0.050 V s^{-1}; plots of E_{pc} vs. pH for (c) $PMo_{11}V$ and (d) $PMo_{11}V$@CBV.

Note that for $PMo_{11}V$@CBV the maximum electrolyte solution pH used was pH 3.0, because upon increasing the pH the peaks become less defined and it becomes difficult to determine accurately the peak potentials. The CVs obtained reveal that when the pH increases, the peak potentials shift to more negative potentials while the current intensities gradually decrease. A similar behaviour was already observed for several silicotungstates,[40] the decrease of current being explained by the increase of the amount of Li^+ in the buffer solution (in place of H^+) as the pH increase, which leads to a slower penetration of bulkier cations into the active centres.

In Figure 7.6 (c) and (d) are depicted the plots of E_{pc} vs. pH for the several redox processes (V_1 and Mo_1 to Mo_4) observed with both modified electrodes. The dependence of E_p on the pH corresponds to straight lines having slopes between -0.104 and -0.070 V/pH for $PMo_{11}V$ and between -0.087 and -0.067 V/pH for $PMo_{11}V$@CBV, which indicates that the redox mechanism of these electrochemical processes involves protons. In the experimental conditions used and assuming a Nernstian behaviour, the V-based reduction at the $PMo_{11}V$ corresponds to a one-electron/one proton process while at the $PMo_{11}V$@CBV the one electron reduction shall be accompanied by addition of one to two protons. Additionally, for both compounds, the two-electron Mo-based reductions are accompanied by addition of two to three proton.[41] The pH dependence of these electrochemical processes is related to the high negative charge of the polyanion at these reduced states.

7.3.3 ORR electrocatalytic activity

The ORR electrocatalytic activities of the prepared $PMo_{11}V$ polyoxometalate and $PMo_{11}V$@carbon-based nanocomposites ($PMo_{11}V$@CBV, $PMo_{11}V$@SWCNT and $PMo_{11}V$@GF) were evaluated in pH 2.5 H_2SO_4/Li_2SO_4 buffer solution. Figure 7.7 (a) presents the CVs obtained for all modified electrodes in the potential range E = -0.42 to 0.80 V. In N_2-saturated solution no electrochemical process is observed other than the features of $PMo_{11}V$ (discussed in the previous section, not observable on the graph scale shown here), while in O_2-saturated solution all materials exhibit an irreversible electrochemical process, indicative of their electrocatalytic activity for the ORR. The cathodic peak corresponding to this process in the case of the $PMo_{11}V$@GF nanocomposite starts to appear at $E_{pc} \approx 0.06$ V, while for the other materials the onset occurs at more negative potential values ($E_{pc} \approx$ -0.07, -0.14 and -0.20 V for $PMo_{11}V$@SWCNT, $PMo_{11}V$@CBV and free-$PMo_{11}V$, respectively). The reduction peak current density is also higher in absolute values for $PMo_{11}V$@GF (-0.093 mA cm^{-2}), decreasing in the order |-0.049| > |-0.022| > |-0.018| mA cm^{-2} for $PMo_{11}V$@SWCNT, $PMo_{11}V$@CBV and $PMo_{11}V$, respectively. These results suggest that the

nanocomposites exhibit better ORR electrocatalytic activity than the free-$PMo_{11}V$ and that their performances depend on the carbon material employed.

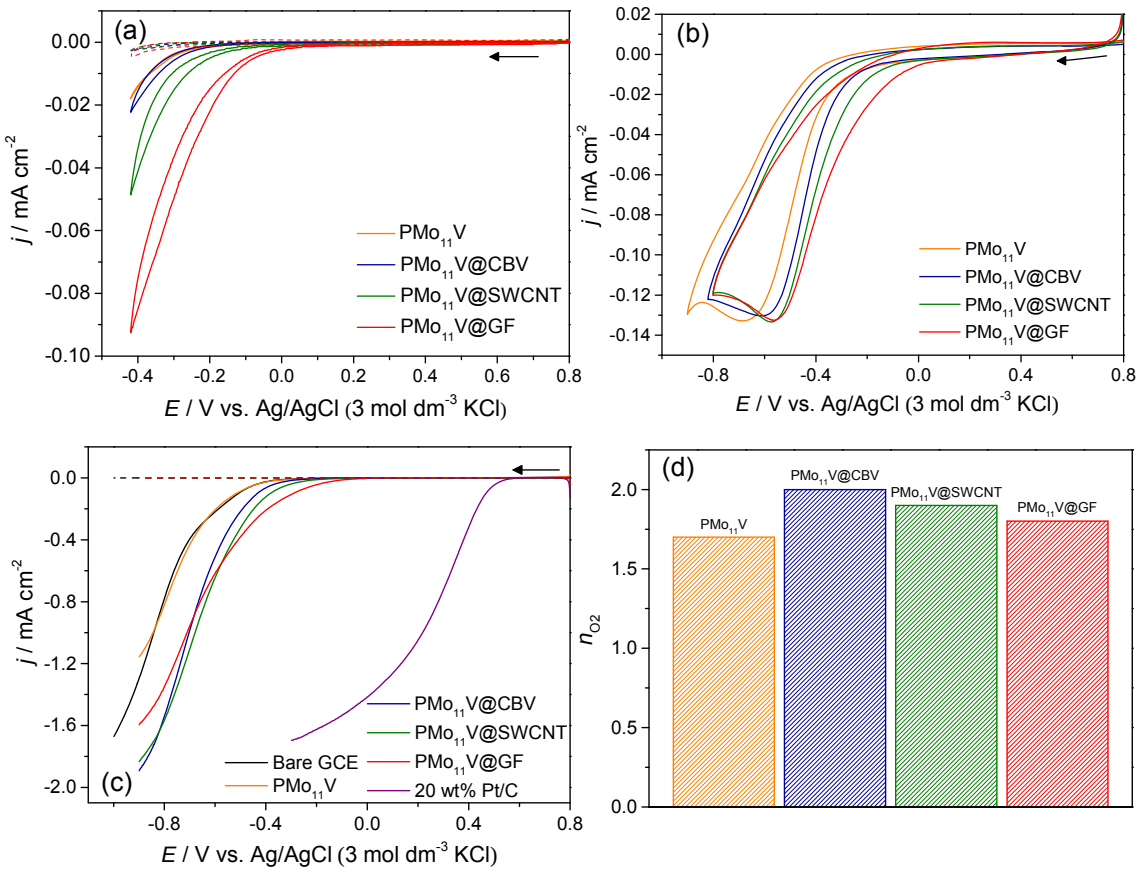

Figure 7.7 ORR results in pH 2.5 H_2SO_4/Li_2SO_4 buffer solution: (a) CVs of the as-prepared catalysts in N_2- (dash lines) and O_2- (full lines) saturated solutions, between -0.42 and 0.80 V at 0.002 V s^{-1}, (b) CVs of the as-prepared catalysts in O_2-saturated solution between -0.90 / -0.80 and 0.8 V at 0.005 V s^{-1} and (c) LSV using RDE in N_2- (dash lines) and O_2- (full lines) saturated solutions at 1600 rpm and 0.005 V s^{-1} (d) number of electrons transferred per O_2 molecules (n_{O_2}) at -0.90 V.

Hereafter, the ORR electrocatalytic activity of the prepared materials was investigated in more detail, applying LSV measurements with the rotating disk electrode (RDE). In Figure 7.7 (b) are depicted the CVs of all modified electrodes in the conditions of the LSV studies (potential range from E = -0.90/-0.80 to 0.80 V) in O_2-saturated solution; these CVs include the entire peak of the oxygen reduction process, while the CVs of Figure 7.7 (a) concern just the beginning of the ORR process. Each modified electrode shows one wave peaking at E_{pc} = -0.68 V for $PMo_{11}V$, E_{pc} = -0.61 V for $PMo_{11}V$@CBV, E_{pc} = -0.57 V for $PMo_{11}V$@SWCNT and E_{pc} = -0.55 V for $PMo_{11}V$@GF, confirming that the nanocomposite with graphene is the one exhibiting

the less negative potential for the ORR peak. Moreover, considering the entire ORR process, all modified electrodes give rise to similar current densities.

Figure 7.7 (c) shows the ORR polarisation plots of the prepared electrocatalysts and of the 20 wt% Pt/C and bare GCE, for comparison, at 1600 rpm. The RDE voltammograms for the ORR obtained with individual bare GCE and $PMo_{11}V$-, $PMo_{11}V$@CBV-, $PMo_{11}V$@SWCNT-, $PMo_{11}V$@GF- and Pt/C-modified electrodes, at rotation rates ranging from 400 to 3000 rpm, are depicted in Figure 7.8. The prepared electrocatalysts showed different onset potentials: for free-$PMo_{11}V$, E_{onset} = -0.42 V, shifting to E_{onset} = -0.37 V for $PMo_{11}V$@CBV, E_{onset} = -0.32 V for $PMo_{11}V$@SWCNT and E_{onset} = -0.16 V for $PMo_{11}V$@GF. These results are in agreement with voltammetric data and showed a strong influence of the supported carbon materials on the E_{onset} values: the E_{onset} shifts positively as the crystallinity of the carbon materials increases. The better results obtained with SWCNT and GF may be explained by the high conductivity of these carbon materials that improves the charge transfer between the modified layer and the GCE electrode and also promotes a beneficial synergistic effect with $PMo_{11}V$.[25,42] Their high surface area and the presence of peculiar graphitic edge sites can also result in a large number of ORR active sites, favouring the ORR performance.[10] The diffusion-limiting current densities also are slightly different, being $j_{L(-0.90\ V,\ 1600\ rpm)}$ = -1.16 and -1.60 mA cm^{-2} for $PMo_{11}V$ and $PMo_{11}V$@GF, respectively, and increasing to $j_{L(-0.90\ V,\ 1600\ rpm)}$ = -1.83 and -1.89 mA cm^{-2} for $PMo_{11}V$@SWCNT and $PMo_{11}V$@CBV, respectively.

In comparison with bare GCE (E_{onset} = -0.42 V), the E_{onset} value determined for free $PMo_{11}V$ remains the same, but less negative E_{onset} values are found with nanocomposite-modified electrodes, the latter revealing a superior ORR electrocatalytic performance and demonstrating the advantage of the electrode modification with these nanocomposites. The current density ($j_{L(-0.90\ V,\ 1600\ rpm)}$ = -1.66 mA cm^{-2}) of bare GCE is similar to that of the nanocomposites, although the current densities of $PMo_{11}V$@CBV and $PMo_{11}V$@SWCNT are slightly higher. Furthermore, the onset potential values of the modified electrodes with the prepared materials are considerably more negative than that obtained with 20 wt% Pt/C (E_{onset} = 0.51 V), the smallest difference between the onset potential of Pt/C and the nanocomposite with the less negative E_{onset} ($PMo_{11}V$@GF) being ΔE_{onset} = 0.67 V; the current densities remain very similar ($j_{L(-0.30\ V,\ 1600\ rpm)}$ = -1.69 mA cm^{-2} for Pt/C).

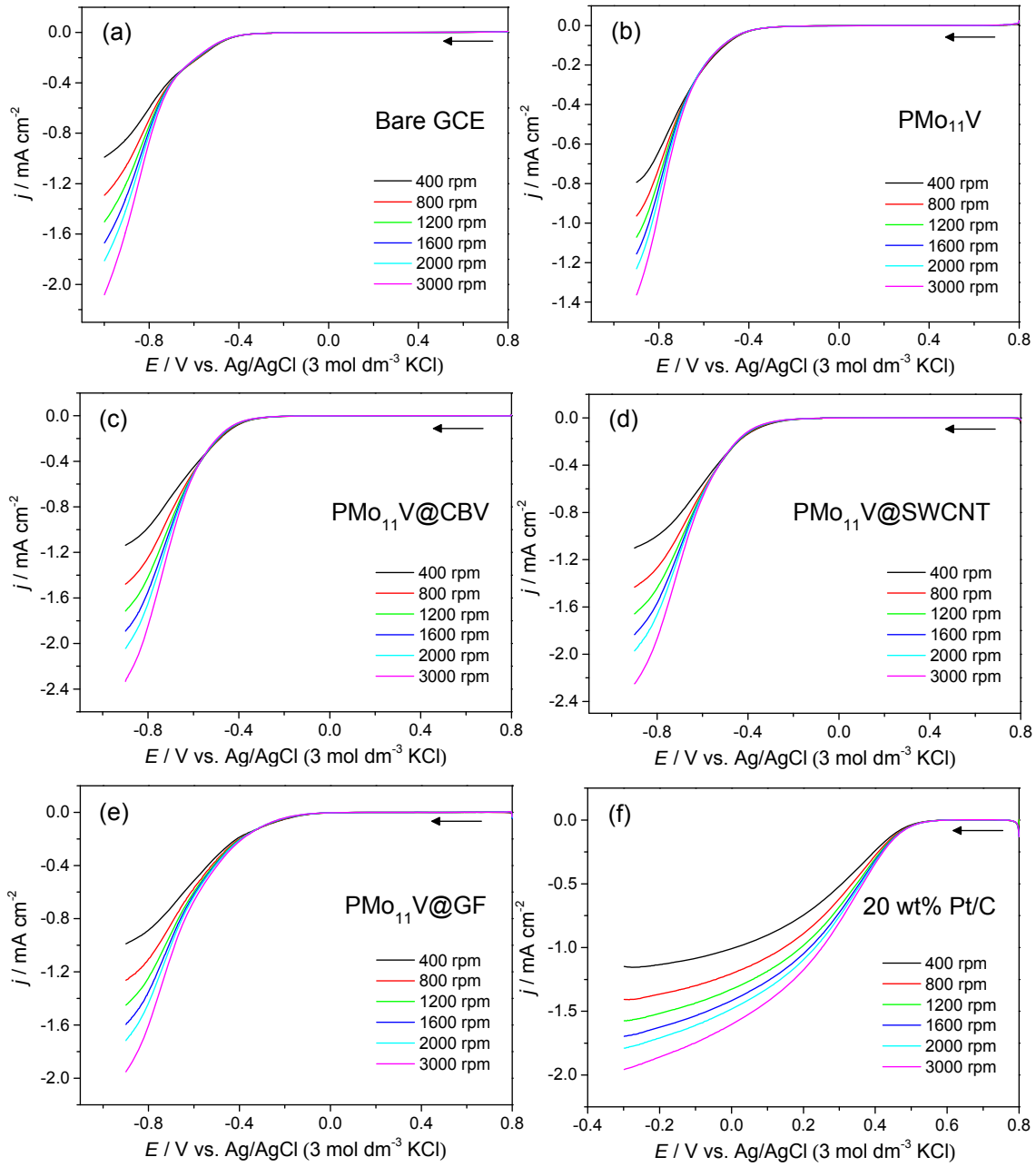

Figure 7.8 ORR polarisation plots of (a) bare GCE, (b) $PMo_{11}V$-, (c) $PMo_{11}V$@CBV-, (d) $PMo_{11}V$@SWCNT-, (e) $PMo_{11}V$@GF- and (f) 20 wt% Pt/C- modified electrodes at several rotation rates and 0.005 V s^{-1}, in pH 2.5 H_2SO_4/Li_2SO_4 buffer solution.

The ORR kinetic parameters were analysed by the Koutecky-Levich (K-L) plots (j^{-1} vs. $\omega^{-1/2}$) at various potentials, using the LSV voltammograms. The slopes of their straight line fits were used to calculate the number of electrons transferred per oxygen molecules (n_{O_2}). From the corresponding K-L plots it can be seen that the data exhibit good linearity (see Figure 7.9).

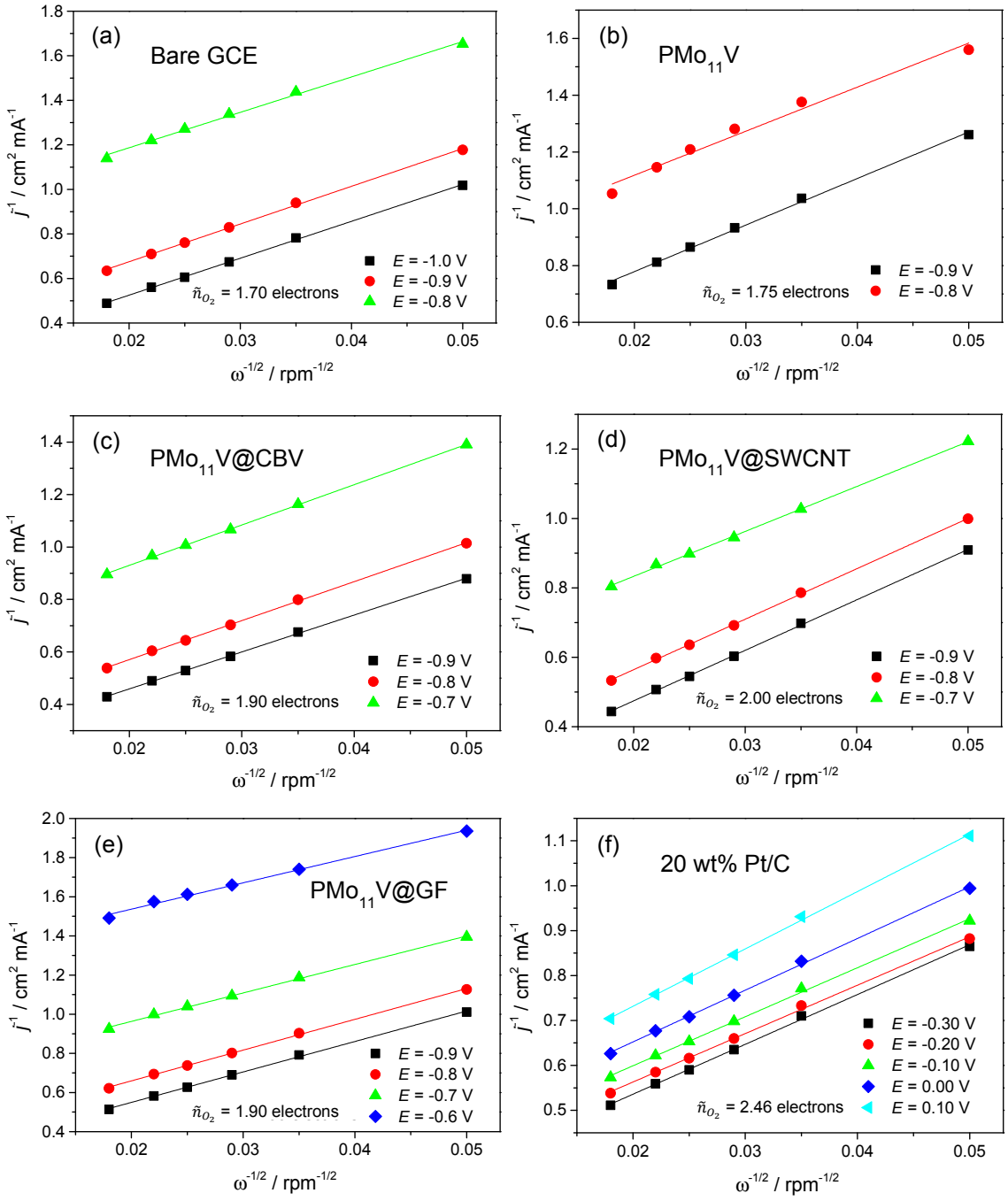

Figure 7.9 Koutecky-Levich (K-L) plots of (a) bare GCE, (b) $PMo_{11}V$, (c) $PMo_{11}V$@CBV, (d) $PMo_{11}V$@SWCNT, (e) $PMo_{11}V$@GF and (f) 20 wt% Pt/C modified electrodes obtained from data in Figure 7.8.

Figure 7.7 (d) shows that the estimated number of electrons transferred at *E* = -0.90 V is very similar for the different prepared materials, with n_{O_2} = 1.7 for $PMo_{11}V$, n_{O_2} = 1.8 for $PMo_{11}V$@GF, n_{O_2} = 1.9 for $PMo_{11}V$@SWCNT and n_{O_2} = 2.0 electrons for $PMo_{11}V$@CBV, although slightly higher values are estimated for the nanocomposites than for the free POM. In the present experimental conditions, the n_{O_2} estimated values obtained with the modified electrodes are larger than that calculated

for bare GCE ($\tilde{n}_{O_2}$= 1.7 electrons), but smaller than the one pertaining to 20 wt% Pt/C ($\tilde{n}_{O_2}$= 2.5 electrons). The n_{O_2} values obtained with prepared materials are similar to the one reported for a polyoxotungstate@graphene nanocomposite at less negative potential values,[22] revealing that the ORR occurs via a two-electron reduction pathway, with formation of H_2O_2. This mechanism is also typically observed for pristine carbon materials (without doping).[43]

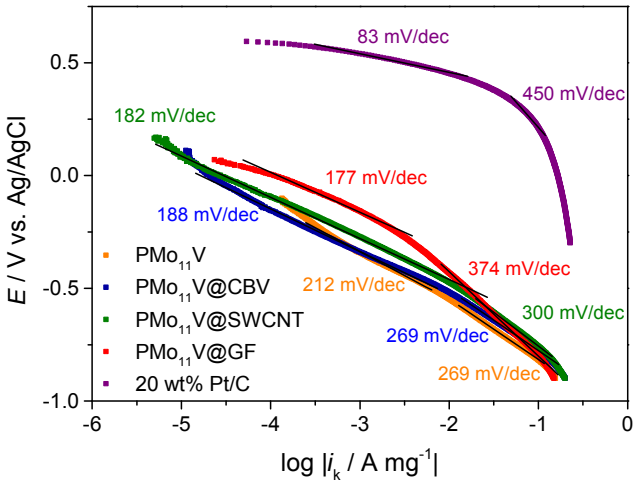

Figure 7.10 ORR Tafel plots for $PMo_{11}V$, $PMo_{11}V$@CBV, $PMo_{11}V$@SWCNT, $PMo_{11}V$@GF and 20 wt% Pt/C, obtained from LSV data in Figure 7.7 (c); current intensities normalised to the mass of each electrocatalyst deposited on electrode (see experimental section).

Tafel plots obtained with electrodes modified with the prepared materials and with Pt/C (Figure 7.10) were also used to gather information on the ORR kinetics and mechanism. The $PMo_{11}V$-modified electrode shows a Tafel plot with two different slopes: 212 mV dec^{-1} in the low current density region and 269 mV dec^{-1} in high current density region. The nanocomposites also show two different slopes, with similar values in the low current density region: 188, 182 and 177 mV dec^{-1} for $PMo_{11}V$@CBV, $PMo_{11}V$@SWCNT and $PMo_{11}V$@GF, respectively. The smaller slopes in comparison with $PMo_{11}V$ reveal a better ORR performance of the nanocomposites, $PMo_{11}V$@GF being the most promising one. In the high current density region, the slopes differ more: 269, 300 and 374 mV dec^{-1} for $PMo_{11}V$@CBV, $PMo_{11}V$@SWCNT and $PMo_{11}V$@GF, respectively. The Pt/C electrocatalyst showed a Tafel plot with different slopes (83 and 450 mV dec^{-1}), suggesting a different mechanism in which Pt is the active site.

7.3.4 Hydrogen peroxide reduction

The $PMo_{11}V$- and nanocomposite-modified electrodes were tested for the electroreduction of H_2O_2. In Figure 7.11 (a) are depicted the CVs obtained with a $PMo_{11}V$@GF-modified electrode, as an example, in N_2-saturated pH 2.5 H_2SO_4/Li_2SO_4 buffer solution, without H_2O_2 and with a H_2O_2 concentration of 0.038 and 0.15 mol dm^{-3}. In the CV obtained in the absence of H_2O_2, no redox peak is observed; however, in the presence of H_2O_2 there is a wave peaking at E_{pc} ≈ -0.40 V, whose current intensity increases with the concentration of H_2O_2, indicative of the electrocatalytic activity of the nanocomposite towards the reduction of hydrogen peroxide. A similar behaviour is observed with the other prepared materials. The CVs obtained for all materials in the presence of 0.15 mol dm^{-3} of H_2O_2 are shown in Figure 7.11 (b) and the results confirm that the electrocatalytic reduction of H_2O_2 occurs with all modified electrodes. The $PMo_{11}V$@GF nanocomposite exhibits the best performance, with the process starting at the least negative potential (E ≈ 0.1 V) and giving rise to a greater current intensity (i = -10 μA) than the remaining tested materials.

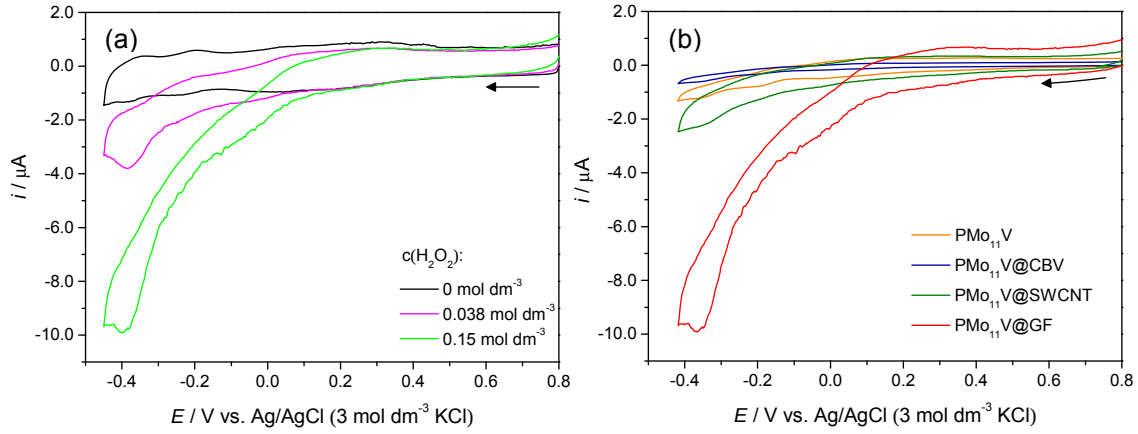

Figure 7.11 CVs of (a) $PMo_{11}V$@GF with different concentrations of H_2O_2 (0, 0.038 and 0.15 mol dm^{-3}) and of (b) free $PMo_{11}V$- and nanocomposite-modified electrodes with 0.15 mol dm^{-3} H_2O_2, in N_2-saturated pH 2.5 H_2SO_4/Li_2SO_4 buffer solution at 0.050 V s^{-1}.

Hydrogen peroxide is an oxidant widely used in food and pharmaceutical proceedings as sterilizing agent and released from several industrial processes, whereby its food content and environmental presence needs to be strictly controlled.[44] Thus, the use of these modified electrodes as H_2O_2 electrochemical sensors may be of great interest and needs to be investigated in more detail in the near future.

7.4 Conclusions

The characterisation of prepared $PMo_{11}V$@carbon material nanocomposites by XPS and FTIR confirms the immobilisation of the $PMo_{11}V$ structure on carbon matrixes. The CVs of $PMo_{11}V$- and nanocomposite-modified electrodes in pH 2.5 H_2SO_4/Li_2SO_4 buffer solution show five pairs of redox waves, attributed to vanadium and molybdenum redox processes of the POM counterpart. In general, higher current densities and better peak resolution are achieved in the CVs of the nanocomposites, which are associated with the favourable electronic properties of carbon-based materials; the results, in association with the superior electrochemical surface coverages determined for nanocomposites, show the advantage of the electrode modification with the prepared nanocomposites.

All the studied materials (free $PMo_{11}V$ and nanocomposites) show electrocatalytic activity for the ORR, with a strong dependency between the electrocatalytic ORR performance and the carbon material employed as support. The onset potentials shift to less negative values in the order $PMo_{11}V$ < $PMo_{11}V$@CBV < $PMo_{11}V$@SWCNT < $PMo_{11}V$@GF; for $PMo_{11}V$@GF, the most promising material, it was measured an E_{onset} = -0.16 V vs. Ag/AgCl. The diffusion-limiting current densities obtained are similar for all studied materials and the analysis of Koutecky-Levich plots reveals that the ORR process occurs through a two-electron process for all modified electrodes.

The materials also have an electrocatalytic activity towards the reduction of H_2O_2, particularly $PMo_{11}V$@GF whose behaviour reveals its potentiality to be explored for H_2O_2 sensing.

References

[1] Wu, G.; Li, L.; Li, J. H.; Xu, B. Q. *Carbon* **2005**, *43*, 2579.

[2] Yuan, Y.; Zhou, S. G.; Zhuang, L. *J. Power Sources* **2010**, *195*, 3490.

[3] Kadirgan, F.; Kannan, A. M.; Atilan, T.; Beyhan, S.; Ozenler, S. S.; Suzer, S.; Yorur, A. *Int. J. Hydrog. Energy* **2009**, *34*, 9450.

[4] Charreteur, F.; Jaouen, F.; Ruggeri, S.; Dodelet, J. P. *Electrochim. Acta* **2008**, *53*, 2925.

[5] Cheng, Y. H.; Li, W. Y.; Fan, X. Z.; Liu, J. G.; Xu, W. G.; Yan, C. W. *Electrochim. Acta* **2013**, *111*, 635.

[6] Zhu, C. Z.; Dong, S. J. *Nanoscale* **2013**, *5*, 1753.

[7] Jafri, R. I.; Rajalakshmi, N.; Ramaprabhu, S. *J. Mater. Chem.* **2010**, *20*, 7114.

[8] Liang, Y. Y.; Li, Y. G.; Wang, H. L.; Zhou, J. G.; Wang, J.; Regier, T.; Dai, H. J. *Nat. Mater.* **2011**, *10*, 780.

[9] Jiang, Y. Y.; Lu, Y. Z.; Wang, X. D.; Bao, Y.; Chen, W.; Niu, L. *Nanoscale* **2014**, *6*, 15066.

[10] Zheng, Y.; Jiao, Y.; Jaroniec, M.; Jin, Y. G.; Qiao, S. Z. *Small* **2012**, *8*, 3550.

[11] Mbomekalle, I. M.; Bian, F.; Tebba, H.; Muller, A.; Weinstock, I. A. *J. Clust. Sci.* **2006**, *17*, 333.

[12] Ammam, M.; Keita, B.; Nadjo, L.; Mbomekalle, I. M.; Ritorto, M. D.; Anderson, T. M.; Neiwert, W. A.; Hill, C. L.; Fransaer, J. *Electroanal.* **2011**, *23*, 1427.

[13] Nagai, M.; Sanpei, H.; Shirakura, M. *J. Mater. Chem.* **2012**, *22*, 9222.

[14] Xin, J. H.; Lindenmuth, T.; Shannon, C. *Electrochim. Acta* **2011**, *56*, 8884.

[15] Sankarraj, A. V.; Ramakrishnan, S.; Shannon, C. *Langmuir* **2008**, *24*, 632.

[16] Chojak, M.; Kolary-Zurowska, A.; Wlodarczyk, R.; Miecznikowski, K.; Karnicka, K.; Palys, B.; Marassi, R.; Kulesza, P. J. *Electrochim. Acta* **2007**, *52*, 5574.

[17] Hsu-Yao, T.; Browne, K. P.; Honesty, N.; Tong, Y. J. *Phys. Chem. Chem. Phys.* **2011**, *13*, 7433.

[18] Zhang, H.; Xie, A. J.; Shen, Y. H.; Qiu, L. G.; Tian, X. Y. *Phys. Chem. Chem. Phys.* **2012**, *14*, 12757.

[19] Chen, W.; Huang, L. J.; Hu, J.; Li, T. F.; Jia, F. F.; Song, Y. F. *Phys. Chem. Chem. Phys.* **2014**, *16*, 19668.

[20] Yang, M.; Choi, B. G.; Jung, S. C.; Han, Y. K.; Huh, Y. S.; Lee, S. B. *Adv. Funct. Mater.* **2014**, *24*, 7301.

[21] Guo, S. X.; Liu, Y. P.; Lee, C. Y.; Bond, A. M.; Zhang, J.; Geletiib, Y. V.; Hill, C. L. *Energy Environ. Sci.* **2013**, *6*, 2654.

[22] Jiang, M.; Zhu, D. D.; Cai, J. J.; Zhang, H. Y.; Zhao, X. B. *J. Phys. Chem. C* **2014**, *118*, 14371.

[23] Rousseau, G.; Zhang, S. S.; Oms, O.; Dolbecq, A.; Marrot, J.; Liu, R. J.; Shang, X. K.; Zhang, G. J.; Keita, B.; Mialane, P. *Chem.-Eur. J.* **2015**, *21*, 12153.

[24] Liu, R. J.; Li, S. W.; Yu, X. L.; Zhang, G. J.; Ma, Y.; Yao, J. N. *J. Mater. Chem.* **2011**, *21*, 14917.

[25] Liu, R. J.; Yu, X. L.; Zhang, G. J.; Zhang, S. J.; Cao, H. B.; Dolbecq, A.; Mialane, P.; Keita, B.; Zhi, L. J. *J. Mater. Chem. A* **2013**, *1*, 11961.

[26] Liu, R. J.; Xian, Z. W.; Zhang, S. S.; Chen, C. H.; Yang, Z. H.; Li, H.; Zheng, W. Q.; Zhang, G. J.; Cao, H. B. *RSC Adv.* **2015**, *5*, 74447.

[27] Fernandes, D. M.; Freire, C. *ChemElectroChem* **2015**, *2*, 269.

[28] Himeno, S.; Ishio, N. *J. Electroanal. Chem.* **1998**, *451*, 203.

[29] Friis, E. P.; Andersen, J. E. T.; Madsen, L. L.; Bonander, N.; Moller, P.; Ulstrup, J. *Electrochim. Acta* **1997**, *42*, 2889.

[30] Vila, N.; Aparicio, P. A.; Secheresse, F.; Poblet, J. M.; Lopez, X.; Mbomekalle, I. M. *Inorg. Chem.* **2012**, *51*, 6129.

[31] Daems, N.; Sheng, X.; Vankelecom, I. F. J.; Pescarmona, P. P. *J. Mater. Chem. A* **2014**, *2*, 4085.

[32] Mani, A.; Birss, V. I. *J. Electroanal. Chem.* **2012**, *687*, 102.

[33] Nunes, M.; Rocha, I. M.; Fernandes, D. M.; Mestre, A. S.; Moura, C. N.; Carvalho, A. P.; Pereira, M. F. R.; Freire, C. *RSC Adv.* **2015**, *5*, 102919.

[34] Negro, E.; Vezzu, K.; Bertasi, F.; Schiavuta, P.; Toniolo, L.; Polizzi, S.; Di Noto, V. *ChemElectroChem* **2014**, *1*, 1359.

[35] Assumpcao, M.; De Souza, R. F. B.; Rascio, D. C.; Silva, J. C. M.; Calegaro, M. L.; Gaubeur, I.; Paixao, T.; Hammer, P.; Lanza, M. R. V.; Santos, M. C. *Carbon* **2011**, *49*, 2842.

[36] Lipinska, M. E.; Rebelo, S. L. H.; Pereira, M. F. R.; Gomes, J.; Freire, C.; Figueiredo, J. L. *Carbon* **2012**, *50*, 3280.

[37] Contarini, S.; Howlett, S. P.; Rizzo, C.; Deangelis, B. A. *Appl. Surf. Sci.* **1991**, *51*, 177.

[38] Yang, F. F.; Ma, L.; Gan, M. Y.; Zhang, J.; Yan, J.; Huang, H.; Yu, L.; Li, Y. J.; Ge, C. Q.; Hu, H. F. *Synth. Met.* **2015**, *205*, 23.

[39] Gaunt, A. J.; May, I.; Sarsfield, M. J.; Collison, D.; Helliwell, M.; Denniss, I. S. *Dalton Trans.* **2003**, 2767.

[40] Fernandes, D. M.; Brett, C. M. A.; Cavaleiro, A. M. V. *J. Electroanal. Chem.* **2011**, *660*, 50.

[41] Fernandes, D. M.; Simoes, S. M. N.; Carapuca, H. M.; Cavaleiro, A. M. V. *Electrochim. Acta* **2008**, *53*, 6580.

[42] Trogadas, P.; Fuller, T. F.; Strasser, P. *Carbon* **2014**, *75*, 5.

[43] Wang, D. W.; Su, D. S. *Energy Environ. Sci.* **2014**, *7*, 576.

[44] Ji, Y. C.; Huang, L. J.; Hu, J.; Streb, C.; Song, Y. F. *Energy Environ. Sci.* **2015**, *8*, 776.

Chapter 8

Conclusions and future perspectives

8

Conclusions and future perspectives

The final chapter of the thesis provides a general overview of the main conclusions and summarises the most important achievements. Moreover, new perspectives for future work are proposed.

8.1 Conclusions

The work described in the thesis focused on the development of novel efficient systems for application in energy saving and conversion technologies.

From the point of view of energy saving, the results obtained in Chapter 2, showed the successful electropolymerisation of poly[1] and poly[2] metallo-polymers on flexible substrates of ITO/PET. Poly[1] exhibited similar electrochemical responses in $LiClO_4/CH_3CN$ and $LiClO_4$/PC electrolytes. The XPS characterisation revealed a larger incorporation of ClO_4^- and solvent on oxidised films, although in a lesser extent in $LiClO_4$/PC. The electronic spectra of both films showed a strong dependency of band profiles with the applied potential, which is similar in both supporting electrolytes; the observed electronic bands were attributed, according to the polaronic model, to transitions between new electronic states created within the band gap of the polymer and to charge transfer (CT) transitions between the metal and the oxidised ligand. The electronic bands ε-values also remain similar in both supporting electrolytes, except for the ε-value of the bands assigned to charge transfer transition that decreases from $LiClO_4/CH_3CN$ to $LiClO_4$/PC.

Both poly[Ni(*salen*)] films showed interesting polyelectrochromic behaviour, exhibiting a yellow colour in reduced state that changes to green and russet in oxidised states. For poly[1], the colour change from yellow to green had the highest optical contrast, while for poly[2] it was the green ↔ russet change. In both cases, the

response times are in order of seconds (8-24 s), revealing the potentiality of these films for application in slow-acting electronic devices. Both films showed superior long-term stability in $LiClO_4$/PC; in this medium, the highest stability was achieved for the yellow ↔ green colour change of poly[1], with a charge loss of 34.3 % after 9000 cycles. The promising EC performance of poly[1] was demonstrated by the assemblage of two electrochromic devices with distinct typologies. The device with the best EC performance showed an optical contrast of ΔT = 88.7 % and a charge loss of 37.0 % upon 3000 redox cycles.

In order to improve the EC properties of the poly[Ni(*salen*)] film with the best performance, poly[1], several nanocomposites were prepared through the electropolymerisation of poly[1] in the presence of (i) WO_3 and (ii) TiO_2 nanoparticles and (iii) nitrogen-doped graphene. The characterisation of the WO_3 and TiO_2 NPs, previously synthesised, confirmed the achievement of crystalline nanomaterials (WO_3: 34-38 nm and TiO_2: 9.7 nm) with quasi-spherical morphologies.

The SEM and XPS results confirmed the presence of the nanomaterials within poly[1] matrix. All nanocomposite films showed similar electrochemical responses to those of pristine film, but higher electroactive surface coverages, which showed the advantage of the incorporation of nanomaterials in poly[1]. The electronic spectra of the nanocomposites and pristine poly[1] also showed similar band profiles and energies, revealing that the electronic structure of poly[1] remains unchanged with the incorporation of nanomaterials. However, according with the nanomaterial employed, differences in the electronic bands ε-values were observed. For WO_3@poly[1] and TiO_2@poly[1] nanocomposites, the differences observed were in the ε-values of bands assigned to charge transitions between the metal and oxidised ligand, that decreased from pristine to nanocomposites (9.0-12.0 % with WO_3 and 3.6-16.2 % with TiO_2), revealing a superior stability of the nanocomposites for over-oxidation processes. For N-FLG@poly[1] nanocomposite, in addition to the decrease of ε-values for CT band (12 %) it was also observed an increase in the ε-values of the bands associated with transitions within band gap (in 19 and 26 %), indicating that this nanomaterial has the additional ability of provide alternative conducting pathways and facilitate the electronic transitions, which are associated with the charge carriers. Furthermore, the nanocomposites prepared with TiO_2 NPs and N-FLG showed an increase in the amount of ClO_4^- incorporated along the redox cycles, in comparison with the pristine film, while for WO_3@poly[1] nanocomposites the ClO_4^- entrapment was less favoured.

Moreover, additional studies performed with TiO_2@poly[1] nanocomposites revealed that high loadings of NPs (above ≈ 15 wt.%) hampered the poly[1] electrodeposition.

The incorporation of nanomaterials in poly[1] resulted in nanocomposites with improvement into some EC properties. The WO_3@poly[1] nanocomposite allowed faster response times, higher optical contrast (≈ + 40 %) and greater colouration efficiency (improvement of 13.1-21.7 %) than the pristine film, but only in $LiClO_4/CH_3CN$. On the other hand, the incorporation of TiO_2 NPs resulted in nanocomposite films with an improvement of 16.7 % of ΔOD and an excellent electrochemical stability, with a charge loss of 7.3 % upon ≈ 10 000 cycles, which corresponds to an increase of 46.7 % in electrochemical stability. Finally, the preparation of N-FLG@poly[1] showed to be the most advantageous, since resulted in the enhancement of all EC properties: the electrochemical stability increased in 71 % (2.7 % of charge loss after ≈ 10 000 cycles), the switching times diminished 71-77 % (τ = 9 / 11 s), the optical contrast increase 38 % (ΔT = 35.9 %) and the colouration efficiency raised 12 % (η = 108.95 $cm^2\ C^{-1}$).

In the context of energy-conversion, activated carbons prepared from sucrose, SC800 and SH800, showed to be efficient metal-free ORR electrocatalysts either in alkaline and acidic media, although the results appeared more favourable in alkaline medium. The electrocatalytic performance was influenced by the textural properties (specific surface areas, porosity and morphology) of the materials. The SH800, which exhibited the highest specific surface area and largest micropores, showed the better ORR electrocatalytic performance, with higher limiting-current density. The materials showed good tolerance to methanol and the SH800 electrocatalyst showed greater long-term stability than the state-of-the-art Pt/C electrocatalyst; however, both ACs were neither selective to 2- or 4-electron ORR processes.

The evaluation of the ORR electrocatalytic activity of the $PMo_{11}V$- and $PMo_{11}V$@carbon-based nanocomposites-modified electrodes revealed a superior performance of the nanocomposites than of the pristine polyoxometalate, which demonstrates the advantage of the immobilisation of the $PMo_{11}V$ onto carbon nanomaterials. Furthermore, the carbon support showed a strong influence on the ORR electroactivity of the nanocomposites, which was clearly demonstrated by the variation of the onset potentials (E_{onset}): $PMo_{11}V$ < $PMo_{11}V$@CBV < $PMo_{11}V$@SWCNT < $PMo_{11}V$@GF. The better performances exhibited by the $PMo_{11}V$@SWCNT and $PMo_{11}V$@GF nanocomposites were explained by the high conductivity of the SWCNT

and GF that improved the charge transport between the modified layer and the GCE electrode and promoted a beneficial synergistic effect with the $PMo_{11}V$.

The modified electrodes also showed activity for the electrocatalytic reduction of hydrogen peroxide, with the $PMo_{11}V$@GF showing the best performance. Thus, modified electrodes with this nanocomposite can be a valuable approach for H_2O_2 sensing.

8.2 Future perspectives

The results described in the thesis provide new insights in the electrochromic behaviour of poly[Ni(*salen*)]-type films and their nanocomposites with metal oxides and nitrogen-doped graphene. The results are encouraging to pursue in the design and preparation of new materials with improved EC properties. Taking into account this goal, the preparation of nanocomposites through the electropolymerisation of poly[1] directly in nanostructured modified electrodes can be a useful tool, once allows to take more advantage of the nanostructures to fine control the morphology of the obtained composite polymer films and to improve the contact between all film components and the electrode and, ultimately, to control the EC properties.

In order to take advantage of the enhancement in EC properties achieved mainly with N-FLG@poly[1] in practical / commercial applications, its employment in the assemblage of electrochromic devices needs to be more explored; other typologies (vertical configuration) and isolation techniques need to be optimised.

With respect to the ORR electrocatalysts, the preparation of activated carbons from natural sources with nitrogen and sulphur elements seems to be adequate to obtained renewable doped carbon-based materials and to study the effect of these dopants in the electrocatalytic mechanism of the ORR. In general, the results reported in literature tend to highlight the advantage of doped materials.

Considering the evident advantage of carbon supports in ORR, other carbon-based nanocomposites can be explored, through the immobilisation of different polyoxometalates or other compounds such as non-noble metal oxides (e.g. iron oxides).

Appendices

Appendix A

Chapters relatively to *Functional electroactive materials: energy saving (Chapters 2 to 5)*

Electrochemical and spectroelectrochemical studies

A1: Electrochemical techniques

The studies were performed using an Autolab PGSTAT 30 potentiostat/galvanostat (EcoChimie B.V.), controlled by a GPES software.

Studies in solution were performed on a three-electrode and single and/or separate compartment cells, enclosed in a grounded Faraday cage, using an Ag/AgCl electrode (NaCl / 1.0 mol dm^{-3}, Metrohm ref. 6.0724.140) as the reference electrode, a Pt wire or a Pt grid (Chapter 2) / foil (Chapters 3-5, for separate compartment cell) as the counter electrode and poly(ethylene terephthalate) coated with indium tin oxide as the working electrode (ITO/PET, Aldrich, resistivity of 60 Ω sq^{-1}).

Coulometric studies used a Pt disk working electrode (area 0.0314 cm^2, BAS), which was previously polished with aluminum oxide of particle size 0.3 μm (Buehler) on a micro-cloth polishing pad (Buehler), then washed with ultra-pure water (resistivity 18.2 MΩ cm at 25°C, Millipore) and CH_3CN.

Chapter 2: All studies were performed on the single compartment electrochemical cell, except the electrodeposition of the films for ECDs assemblage, in which was used the separate compartment cell.

Chapters 3 and 4: All studies were performed on the single compartment electrochemical cell, except the chronoamperometric measurements, in which was used the separate compartment cell.

Chapter 5: All studies were performed on the separate compartment electrochemical cell.

A2: Spectroelectrochemical techniques

Chapters 2-5: The studies were performed *in situ* using an Agilent 8453 spectrophotometer (with diode array detection) coupled to the potentiostat/galvanostat. The experimental apparatus comprised a teflon cell with an Ag/AgCl (NaCl /

3.0 mol dm^{-3}) (Bio-Logic) reference electrode, a Pt grid counter electrode and ITO/PET (typical area 0.785 cm^2) as working electrode.

Particularly in Chapter 2: for ECD monitoring was used a Perkin Elmer Lambda 35 UV/Vis spectrometer, coupled to an Autolab PGSTAT 302N potentiostat/galvanostat (EcoChimie B.V.).

Appendix B

Chapters relatively to *Functional electroactive materials: energy conversion (Chapters 6 and 7)*

Electrochemical characterisation and electrocatalytic studies

B1: Electrochemical characterisation

Chapter 6: Cyclic voltammetry measurements were carried out using an Autolab PGSTAT 30 potentiostat/galvanostat (EcoChimie B.V.), controlled by a GPES software. The studies were performed on a conventional three-electrode compartment cell, using a glassy carbon electrode, GCE, (3 mm of diameter, BAS, MF-2012) as working electrode, a platinum wire (7.5 cm, BAS, MW-1032) as auxiliary electrode and the Ag/AgCl (sat. KCl) (BAS, MF-2052) as reference electrode. The cell was enclosed in a grounded Faraday cage and all studies were carried out at room temperature in deaerated solutions.

Chapter 7: Cyclic voltammetry measurements were carried out using an electrochemical set-up EG & G 273 A, driven by a PC with the M270 software. The studies were performed on a conventional three-electrode compartment cell, using a glassy carbon electrode (GCE, 3 mm diameter, Mersen) as working electrode, a platinum gauze with a large surface area as auxiliary electrode and the saturated calomel electrode (SCE) as reference electrode. All studies were carried out at room temperature and the solutions were previously deaerated for at least 30 min, with pure argon, and kept under a positive pressure of this gas during the experiments.

B2: Electrocatalytic studies

Chapter 6: The cyclic voltammetry and linear sweep voltammetry measurements were carried out using an Autolab PGSTAT 302N potentiostat/galvanostat (EcoChimie B.V.), controlled by NOVA v1.10 software. The studies were performed at room temperature in a three electrode compartment cell, using a rotating disk electrode (RDE) of glassy carbon (3 mm of diameter, Metrohm) as working electrode, an Ag/AgCl (3 mol dm^{-3} KCl, Metrohm) as reference electrode and a glassy carbon rod (2 mm of diameter, Metrohm) as auxiliary electrode.

Chapter 7: In a first step, the ORR performance of materials was evaluated by cyclic voltammetry measurements, carried out using an electrochemical set-up EG & G

273 A, driven by a PC with the M270 software. The studies were performed at room temperature on a conventional three-electrode compartment cell, using a glassy carbon electrode (GCE, 3 mm diameter, BAS, MF-2012) as working electrode, a platinum gauze with a large surface area as auxiliary electrode and the saturated calomel electrode (SCE) as reference electrode. This experimental apparatus was also employed in the studies of the hydrogen peroxide reduction.

In the second stage of the ORR electrocatalytic evaluation, the cyclic voltammetry and the linear sweep voltammetry measurements were carried out using an Autolab PGSTAT 302N potentiostat/galvanostat (EcoChimie B.V.), controlled by the NOVA v1.10 software. A rotating disk electrode (RDE) of glassy carbon (3 mm diameter, Metrohm) was used as working electrode, an Ag/AgCl (3 mol dm^{-3} KCl, Metrohm) as reference electrode and a glassy carbon rod (2 mm of diameter, Metrohm) as auxiliary electrode.

Appendix C: Other characterisation techniques

C1: X-ray photoelectron spectroscopy (XPS)

The analyses were performed at Centro de Materiais da Universidade do Porto (CEMUP, Porto, Portugal). The XPS spectra were deconvoluted with the XPSPEAK 4.1 software, using non-linear least squares fitting routine after a Shirley-type background subtraction. To correct possible deviations caused by electric charge of the samples, the C1s band at 284.6 eV was taken as the internal standard. The surface atomic percentages were calculated from the corresponding peak areas, using the sensitivity factors provided by the manufacturer.

Chapter 2: The measurements were carried out in a VG Scientific ESCALAB 200A spectrometer with non-monochromatised Al Kα radiation (1486.6 eV), using the polymeric films.

Chapters 3, 4 and 5: The measurements were carried out in a Kratos AXIS Ultra HSA spectrometer with a monochromatic Al Kα radiation (1486.7 eV), using the polymeric films or pellets of the nanomaterials (WO_3 and TiO_2 NPs and N-FLG).

Chapters 6 and 7: The measurements were carried out in a Kratos AXIS Ultra HSA spectrometer with a monochromatic Al Kα radiation (1486.7 eV), using pellets of the materials.

C2: Scanning Electron Microscopy / Energy-dispersive X-ray Spectroscopy (SEM/EDS)

Chapters 2, 3 and 5: The analyses were performed at CEMUP (Porto, Portugal) in a high resolution (Schottky) environmental scanning electron microscope FEI Quanta 400 FEG ESEM, attached to an EDAX Genesis X4M X-ray spectrometer.

Chapter 4: The analyses were performed at CEMUP (Porto, Portugal) in a high resolution scanning electron microscope with X-Ray microanalysis and electron backscattered diffraction analysis (JEOL JSM 6301F/ Oxford INCA Energy 350).

C3: Transmission Electron Microscopy (TEM)

Chapter 3: The analyses were performed at HEMS/IBMC – Histology and Electron Microscopy Service – Institute for Molecular and Cell Biology (IBMC) of the Universidade do Porto. The sections were examined under a JEOL JEM 1400 TEM

(Tokyo, Japan) equipped with an EDX Microanalysis System (Oxford Instruments, Abingdon, UK); the images were digitally recorded using a Gatan SC 1000 ORIUS CCD camera (Warrendale, PA, USA). To prepare the sample, a small amount of NPs was dispersed in ethanol under sonication. Afterwards, a carbon-coated 400 mesh copper grid was immersed in the resulting solution, followed by air-drying. After the evaluation of the TEM images, the diameter of 100 particles was measured to generate a histogram and calculate the average particle size distribution.

Chapter 4: The analyses were performed at Departamento de Química, CQ-VR, Universidade de Trás-os-Montes e Alto Douro (Vila Real, Portugal), with a LEO 906E microscope at 120 kV. To prepare the sample, a small amount of NPs was dispersed in ultra-pure water under sonication. Afterwards, a carbon-coated 400 mesh copper grid was immersed in the resulting solution, followed by air-drying. After the evaluation of the TEM images, the diameter of 100 particles was measured to generate a histogram and calculate the average particle size distribution.

C4: Powder X-ray diffraction (XRD)

Chapters 3 and 4: The measurements were performed at Departamento de Química, CQ-VR, Universidade de Trás-os-Montes e Alto Douro (Vila Real, Portugal), at room temperature using a PW 3040/60 X'Pert Pro Röntgen diffractometer with Cu Kα radiation (λ = 1.5418 Å) and $\theta/2\theta$ Bragg-Brentano configuration, over the 2θ range of 15–80º. The system includes the ultrafast PW3015/20 X'Celerator detector and a secondary monochromator. The diffractograms were treated with the Rietveld refinement.

C5: Fourier transformed infrared spectroscopy (FTIR)

Chapters 3, 4 and 7: The spectra were obtained on a Jasco FT/IR Plus Spectrophotometer in the 4000 – 400 cm^{-1} (Chapter 3), 2000 – 400 cm^{-1} (Chapter 4) or 3500 – 500 cm^{-1} (Chapter 7) region, with a resolution of 4 cm^{-1} and 32 scans. The samples were diluted with KBr (99 %, spectroscopic grade, Sigma-Aldrich) and studied as pellets containing 1.4 wt. % (Chapter 3), 1.2 wt. % (Chapter 4) or 0.2 wt.% (Chapter 7) of sample.

C6: Ultraviolet-visible spectroscopy (UV-Vis)

Chapter 4: The spectra were recorded on a Shimadzu UV-3600 spectrophotometer in the 250 -700 nm range, using quartz cells with a path length of 10 mm.

C7: Raman spectroscopy

Chapter 5: The analyses were performed with powder samples in a HR 800 Jobin Yvon Horiba micro spectrometer, using the red line of an argon laser, k = 639 nm, as an excitation source.

C8: CIELAB coordinates

Chapter 4: The CIELAB coordinates were acquired on a reflectance spectrophotometer Konica Minolta Sensing CM-2600d, in the range 350-750 nm. The spectrophotometer performed five sequential measurements, considering an area of 8 mm diameter. The calibration of the spectrophotometer was performed with white and black reference standards.

C9: Adsorption isotherms

Chapter 6: The textural characterisation was made by N_2 and CO_2 adsorption isotherms at -196 ºC and 0 ºC, respectively. The N_2 isotherms were performed in an automatic equipment (Micromeritics ASAP 2010) while the CO_2 adsorption isotherms were obtained on a conventional volumetric apparatus equipped with a MKS-Baratron (310BHS-1000) pressure transducer (0–133 kPa). Before the isotherm acquisition the samples (≈ 50 mg) were outgassed overnight at 120 ºC under a vacuum (pressure < 10^{-2} Pa). From N_2 adsorption data, the apparent surface area, A_{BET}, and microporosity were evaluated through, respectively, the BET equation ($0.05 < p/p_0 < 0.15$)[1] and α_S method, taking as reference the isotherm reported by Rodríguez-Reinoso *et al.*.[2] The micropore size distributions were obtained from the CO_2 adsorption isotherms, according to the method described by Pinto *et al.*.[3]

References

1 Gregg, S. J.; Sing, K. S. W. *Adsorption, Surface Area and Porosity*; Academic Press Inc.: London, **1982**.

2 Rodriguez-Reinoso, F.; Martin-Martinez, J. M.; Prado-Burguete, C.; McEnaney, B. *J. Phys. Chem.* **1987**, *91*, 515.

3 Pinto, M. L.; Mestre, A. S.; Carvalho, A. P.; Pires, J. *Ind. Eng. Chem. Res.* **2010**, *49*, 4726.


U.PORTO
FACULDADE DE CIÊNCIAS
UNIVERSIDADE DO PORTO